Spectroscopic Studies of Size-Selected Ru and Pt Clusters on Titania

by

Liam Howard-Fabretto

Thesis
Submitted to Flinders University
for the degree of

Doctor of Philosophy

College of Science and Engineering

July 2021

TABLE OF CONTENTS

ABSTRACT

Metal clusters are small groups of bound metal atoms which can have distinctly different electronic and catalytic properties, unique from those of a bulk sample of the same metal. The main motivation for research on clusters is their potential for use in catalysis and photocatalysis. The physical and chemical properties of metal clusters are dependent on size, as well as the cluster-substrate interaction. It is difficult to predict the properties of a cluster/substrate pair if studies have not been performed on that specific combination. Fundamental measurements into cluster properties have previously been performed on a range of cluster/substrate combinations, where Au clusters and $TiO_2(110)$ surfaces have received a large focus. However, there are many important cluster and substrate materials which have not had their surface properties measured, which is vital for the informed design of efficient catalytic materials.

The original contribution to knowledge in this field is through the novel experimental measurements and analysis of the surface properties and electronic properties of 3-atom Ru_3 clusters supported on radio frequency (RF)-sputter deposited titania substrates (RF-TiO_2). Ru_3 was chosen due to its potential catalytic and photocatalytic applications. RF-TiO_2 is a cost-effective alternative to the commonly used $TiO_2(110)$ substrate and was chosen due to its ease of production and applicability to industrial applications. The aims were to determine details about the cluster-surface interaction and temperature stability of the clusters, in addition to measuring their electronic density of states (DOS). Additional cluster and substrate systems were analysed for comparison to Ru_3/RF-TiO_2. This study provides a strong basis for future work on the catalysis of RF-TiO_2-supported Ru_3.

Ru_3 clusters were deposited onto RF-TiO_2 and analysed using temperature programmed desorption (TPD) to probe Ru-CO binding sites, and X-ray photoelectron spectroscopy (XPS) was used to provide chemical information. Differences in cluster-support interactions were compared for bare Ru_3 deposited using an ultra-high vacuum (UHV) cluster source (CS), and the chemical vapor deposition (CVD) of ligated $Ru_3(CO)_{12}$ clusters. For CS-deposited Ru_3, heating to 800 K caused partial oxidation of clusters on both non-sputtered and sputter-treated RF-TiO_2. Furthermore, on sputter-treated RF-TiO_2 all Ru-CO binding sites on the clusters were blocked immediately after deposition for CS-deposited Ru_3, but for CVD-deposited $Ru_3(CO)_{12}$ the clusters were protected by their ligands and the Ru-CO binding sites were only blocked once the sample had been heated to 723 K. The mechanism for complete blocking of Ru-CO binding sites on sputtered RF-TiO_2 could not be directly

determined from this first study.

To further probe the $Ru_3/RF-TiO_2$ system, additional temperature-dependent (TD) measurements were performed to analyse the effects of heat treatment. Samples were analysed with TD-XPS, angle-resolved (AR) XPS, and low energy ion scattering spectroscopy (LEIS). Ru_3 was deposited onto $RF-TiO_2$ using 3 methods: solution submersion of $Ru_3(CO)_{12}$, CVD-deposition of $Ru_3(CO)_{12}$, and CS-deposition of bare Ru_3. TD-XPS showed that after heat treatment the Ru 3d BE was very similar between the methods suggesting the cluster oxidation state was the same. TD-LEIS showed the encapsulation of CVD $Ru_3(CO)_{12}$ on sputter-treated $RF-TiO_2$ by a titania overlayer after heat treatment. The average overlayer thickness was calculated to be 0.35 nm ± 0.08 nm, which is thin enough that there is the potential for catalytic or photocatalytic reactions to occur. The encapsulation of the clusters help explain the mechanism behind the complete blocking of Ru-CO sites, suggesting CO is sterically hindered from accessing Ru by the overlayer.

The electronic DOS for Ru_3 on sputter-treated $RF-TiO_2$ was measured using ultraviolet photoelectron spectroscopy (UPS) and metastable impact electron spectroscopy (MIES). Bare Pt_3 clusters were CS-deposited for the purpose of comparison to a different cluster of the same size. Measurements both Ru_3 and Pt_3 were after sample heat treatment. UPS measures the top several layers while MIES has perfect surface sensitivity and measures only the top atomic layer. The electronic DOS of Ru_3 was very similar for Ru_3 deposited using solution submersion and CVD of $Ru_3(CO)_{12}$. UPS suggests that $RF-TiO_2$-supported Ru_3 clusters have metallic characteristics and Pt_3 clusters have non-metallic characteristics. MIES suggests that the encapsulating layer above Ru_3 clusters is composed of reduced titania with a bonding structure such as Ru-Ti-O, while Pt_3 was not encapsulated. The mechanism for the encapsulation of Ru_3, but not Pt_3, is possibly an energetic benefit for Ru_3 encapsulation in terms of the minimisation of surface energy.

As an extension of previous studies, the effects of changing the supported Ru_n cluster size by a single atom was studied by depositing size-selected Ru_4 clusters onto sputter-treated $RF-TiO_2$ and comparing results to previous experiments. Clusters were CVD-deposited with $H_4Ru_4(CO)_{12}$ and analysed using TD-XPS, TPD, and UPS. Based on TD-XPS, $H_4Ru_4(CO)_{12}$ begins to lose ligands at a slightly lower temperature than $Ru_3(CO)_{12}$, most likely related to the loss of H bridging ligands at low temperatures. Other results were very similar between the clusters. CO-TPD showed that after heat-treatment all Ru-CO binding sites were blocked, caused by encapsulation of the clusters. UPS provided evidence that the

encapsulated Ru_4 clusters have metallic properties, and the valence DOS was similar for both Ru_3 and Ru_4. This suggests that the resultant properties of CVD-deposited Ru_4 after heat treatment are very similar to Ru_3, and that both clusters have the same potential catalytic and photocatalytic benefits when supported on $RF-TiO_2$.

DECLARATION

I certify that this thesis does not incorporate without acknowledgment any material previously submitted for a degree or diploma in any university, and that to the best of my knowledge and belief, does not contain any material previously published or written by another person except where due reference is made in the text.

_____

Liam James Armando Howard-Fabretto, 2021

ACKNOWLEDGEMENTS

I would not have been able to complete my PhD studies without the help of a number of people and groups who will be mentioned and thanked below, all of which have dedicated time and effort to helping me.

My supervisor Prof. Gunther Andersson has been with me the whole way. He was able to assist whenever issues arose in the lab and provide fruitful discussions on experimental design, data analysis, and interpretations. Prof. Andersson has provided me many opportunities including travelling to Tsukuba, Japan for the NIMS workshop, travelling to Salt Lake City, USA to collaborate with The University of Utah, allowing me to operate and perform maintenance on ultra-high vacuum instrumentation, and allowing me to work as a leader in teaching PhD, masters, and undergraduate students to use the instrumentation.

My co-supervisor Prof. Sarah Harmer has helped with a number of fruitful discussions and was always open to organising meetings to help with my PHD progression.

Prof. Jamie Quinton was my co-supervisor for the beginning of my candidature and has helped by proudly showing his passion for physics. He inspires interest in students with his humour and approachability, and I will always remember his first year physics lectures with his bold demonstration of quantum tunnelling.

The entire Gunther Andersson research group has been important to my progression. My office colleagues: Chris, Sunita, Anand, and Abdul, have been friendly to work with to talk to during long PhD days. Additionally, Jesse, Ben, Yanting, Altaf, and Gowri have worked alongside me and have been supportive to bounce ideas off and collaborate with. The teamwork shown by the group when working on lab equipment maintenance helped everyone to progress with their experiments using smoothly running instruments.

Prof. Scott Anderson's research group at The University of Utah, including PhD students Tim Gorey and Guangjing Li, were extremely welcoming in my study exchange to their university. They taught me valuable lessons about their instrumentation, methods, and data analysis procedures, and helped me through these processes.

Prof. Greg Metha's research group at The University of Adelaide have given me

PUBLICATIONS AND CONFERENCES

The following is a list of publications submitted and conference presentations performed during the authors candidature resulting from research presented within the thesis. Publications submitted where the author was a co-author are also listed, but the data from these measurements are not presented in the thesis (see Contextual Statement).

Journal Articles (Primary Author)

L. Howard-Fabretto & G. G. Andersson, Metal Clusters on Semiconductor Surfaces and Application in Catalysis with a Focus on Au and Ru, Advanced Materials, 32 (2019) 1904122.

L. Howard-Fabretto, T. J. Gorey, G. Li, S. Tesana, G. F. Metha, S. L. Anderson, & G. G. Andersson, The interaction of size-selected Ru_3 clusters with RF-deposited TiO_2: probing Ru–CO binding sites with CO-temperature programmed desorption, Nanoscale Advances, 3 (2021) 3537–3553.

L. Howard-Fabretto, T. J. Gorey, G. Li, S. Tesana, G. F. Metha, S. L. Anderson, & G. G. Andersson, Encapsulation of Size-Selected Ru_3 Clusters into RF-Deposited TiO_2, *manuscript submitted for review to the Journal of Chemical Physics at the time of thesis submission*.

Journal Articles (Co-author)

J. Daughtry, A.S. Alotabi, L. Howard-Fabretto, G.G. Andersson, Composition and Properties of RF-Sputter Deposited Titanium Dioxide Thin Films, Nanoscale Advances, 3 (2020) 1077–1086

H. Mousavi, Y. Yin, L. Howard-Fabretto, S.K. Sharma, V. Golovko, G.G Andersson, C. Shearer, G.F Metha, Au 101–rGO nanocomposite: immobilization of phosphine-protected gold nanoclusters on reduced graphene oxide without aggregation, Nanoscale Advances, 3 (2021) 1422–1430.

Conference Oral Presentations

L. Howard-Fabretto, G.G. Andersson, Determination of the electronic structure of titania-supported Ru_3 clusters, College of Science and Engineering Inaugural Research Higher Degree Conference, Flinders University. Adelaide, South Australia, Australia. Nov 29 – Dec 1, 2017.

L. Howard-Fabretto, G.G. Andersson, S.L. Anderson, T.J. Gorey, G.F. Metha, Ru_3 clusters on titania: a comparison of deposition methods, APS March Meeting 2019. Boston, Massachusetts, March 4–8, 2019.

L. Howard-Fabretto, G.G. Andersson, G.F. Metha, Determining the electronic structure of Ru_3 clusters on titania, Flinders Institute for Nanoscale Science & Technology 9th Annual Conference. Adelaide, South Australia, Jun 18, 2019.

L. Howard-Fabretto, G.G. Andersson, The electronic structure and support-interaction of Ru clusters on titania substrates, 3rd College of Science and Engineering Higher Degree Research Conference. Adelaide, South Australia, Nov 26–27, 2019.

Conference Poster Presentations

L. Howard-Fabretto, G.G. Andersson, G.F. Metha, Determination of the electronic structure of titania-supported Ru_3 Clusters, The 7th Annual Flinders NanoCentre Conference, Flinders University, SA, Australia. Jun 13, 2017.

L. Howard-Fabretto, G.G. Andersson, G.F. Metha, Determination of the electronic structure of titania-supported Ru_3 clusters, ICONN 2018 - International Conference on Nanoscience and Nanotechnology, University of Wollongong, NSW, Australia. Jan 29 – Feb 2, 2018.

L. Howard-Fabretto, G.G. Andersson, G.F. Metha, Determination of the electronic structure of titania-supported Ru_3 clusters, The 8th Annual Flinders NanoCentre Conference, Flinders University, SA, Australia. Jun 14, 2018.

L. Howard-Fabretto, G.G. Andersson, G.F. Metha, Determination of the electronic structure of titania-supported Ru_3 clusters, College of Science and Engineering 2nd Annual Research Higher Degree Conference, Flinders University. Adelaide, South Australia, Australia. Nov 27 – Nov 28, 2018.

CONTEXTUAL STATEMENT

The bulk of the results presented in this thesis were from experimental measurements performed at Flinders University in Adelaide, Australia. For these, all measurements, data analysis, and manuscript preparation was performed by the author of this thesis. A number of experiments were also performed at The University of Utah in Salt Lake City, United States of America. This was part of a 6-week collaborative research trip when the author collaborated with the research group of Prof. Scott Anderson. These experiments were designed and performed together with Prof. Anderson, as well as his students Timothy Gorey and Guangjing Li. The measurements were performed collaboratively, and the author was taught to use the group's instrumentation. The data analysis and writing of manuscripts based on these experiments was performed by the author.

Chapter 2 is a reformatted version of a review article published in a peer-reviewed journal, and Chapter 4 is a reformatted version of a manuscript published in a peer-reviewed journal. Chapter 5 is a reformatted version of a manuscript which was submitted for publication to a peer-reviewed journal at the time of thesis submission. A full publication list is provided earlier. For these publications, the author of this thesis was the primary author, designer of experiments, and prepared the manuscripts. For the publication of Chapter 2, Gunther Andersson contributed by helping to revise the manuscript and suggesting ideas for inclusion. For the publication of Chapter 4 and Chapter 5, Gunther Andersson, Scott Anderson, Timothy Gorey, and Guangjing Li helped design and refine the experimental procedures, and also helped with revising the manuscripts for publication. Timothy Gorey and Guangjing Li also contributed to collaborative experimental work performed at The University of Utah. Gregory Metha assisted with revising the manuscripts for publication. Siriluck Tesana prepared the $Ru_3(CO)_{12}$ and $H_4Ru_4(CO)_{12}$ cluster materials.

Experimental work was also performed for two additional publications of which the author of this thesis is a co-author. These are mentioned in the publication list, but the data from these measurements are not presented in this thesis. This is because the content of the measurements served to support the work of collaborating researchers, and it was not directly related to the content of the thesis. The author of this thesis also contributed to revisions for the published versions of these manuscripts.

LIST OF ABBREVIATIONS

AD	Auger de-excitation
AES	Atomic emission spectroscopy
AFM	Atomic force microscopy
ALD	Atomic layer deposition
AN	Auger neutralisation
ARXPS	Angle-resolved X-ray photoelectron spectroscopy
At%	XPS atomic concentration (%)
BE	Binding energy
CS	Cluster source
CVD	Chemical vapor deposition
DFT	Density functional theory
DOS	Density of states
E loss	Energy loss
EXAFS	Extended X-ray absorption fine structure
FWHM	Full width half maximum
HAADF-STEM	High-angle annular dark-field scanning transmission electron microscopy
HDS	High-dose sputtered
HOPG	Highly oriented pyrolytic graphite
HRTEM	High resolution transmission electron microscopy
HSA	Hemispherical analyser
IMFP	Inelastic mean free path
IR	Infrared spectroscopy
ISS	Ion scattering spectroscopy
KE	Kinetic energy
LaVa	Laser vaporisation
LDS	Low-dose sputtered
LEED	Low-energy electron diffraction
LEIS	Low energy ion scattering
MagS	Magnetron sputtering
MIES	Metastable impact electron spectroscopy
ML	Monolayer

NEXAFS	Near-edge X-ray adsorption fine structure
NICISS	Neutral impact collision ion scattering spectroscopy
NMR	Nuclear magnetic resonance
NS	Non-sputtered
PXRD	Powder X-ray diffraction
RBS	Rutherford backscattering spectrometry
RF	Radio frequency
RF-TiO$_2$	Radio frequency-sputter deposited titania
RI	Resonance ionisation
SA	Surface area
SD	Solution-deposited
SEM	Scanning electron microscopy
SMSI	Strong metal-support interaction
SPM	Scanning probe microscopy
STEM	Scanning transmission electron microscopy
STM	Scanning tunnelling microscopy
TD	Temperature-dependent
TEM	Transmission electron microscopy
TGA	Thermogravimetric analysis
TPD	Temperature programmed desorption
TPR	Temperature programmed reaction
UHV	Ultra-high vacuum
UPS	Ultraviolet photoelectron spectroscopy
UV	Ultraviolet
XANES	X-ray absorption near-edge structure
XAS	X-ray absorption spectroscopy
XPS	X-ray photoelectron spectroscopy

Chapter 1   Introduction

1.1 Thesis Chapter Details

Chapter 1 introduces the field of surface science as well as the thesis aims and scope. Chapter 2 is a literature review which gives broad context and outlook on previous research in the field of metal clusters. Chapter 3 details the instrumentation, methodologies, and data analysis procedures used throughout the experimental work. Chapter 4 to Chapter 7 are the results-based chapters, which present the main content and experimental results of the thesis. Chapter 8 summarises the conclusions, and details future research pathways which have opened as a result of these studies. Chapter 9 is the reference section, where the references for all thesis chapters are collated into one global list. Chapter 10 contains the Appendices, which are referred to in the main text when they are relevant.

1.2 Surface Science

Surface science is an area of study which focuses on the very top atomic layer of material surfaces, as well as the interfaces between multiple surfaces. This often overlaps with the field of nanotechnology, which is the study of materials at the nanoscale, typically in the range of 1 - 100 nm [1]. Surface interfaces are important in many physical processes such as catalysis and photocatalysis, and a common goal of surface science is the accurate measurement of the properties of these surfaces, whilst minimising or removing any unwanted effects from atoms below the surface layer. The surface properties may include physical, chemical, electronic, and catalytic properties. Many surface science measurements are performed under ultra-high vacuum (UHV). This serves the dual purpose of allowing many UHV-based surface analysis techniques to operate, as well as allowing experiments to be performed on surfaces free from atmospheric contaminants which can affect surface measurements.

To perform the measurements presented in this thesis UHV systems were used. These feature vacuum chambers with surface analysis and sample mounting instrumentation attached. Measurements were typically performed at base pressures of ~1 x 10^{-10} mbar (note that atmospheric pressure is ~1 x 10^3 mbar). Due to the delicate nature of the instrumentation, UHV systems often needed to be repaired during the PhD project when certain parts were damaged or worn out. The instruments were also modified to suit specific experiments as the equipment needed was not readily available for purchase. Thus, a large aspect of this PhD endeavour which may not be visible in the content of the main results

chapters was the time spent modifying the instrumentation and ensuring it ran smoothly, producing consistent, high quality results. Throughout this project, the thesis author repaired and performed maintenance on a range of UHV instrumentation, and also designed new UHV components to achieve the desired results. This "hands-on" approached allowed for a deeper appreciation and understanding of the analysis techniques which were used. Further information is given in Appendix A, including descriptions of the instrument maintenance and modifications which were performed.

1.3 Aims and Scope

The research performed in this thesis is part of a larger project spanning several collaborating universities, which focusses on small metal clusters supported by semiconducting and insulating materials. Metal clusters are small groups of bound metal atoms, which will be introduced further in Chapter 2. The main application for metal clusters is catalysis and photocatalysis. However, rather than examining catalysis, the research performed in this thesis focuses on the fundamental properties of metal clusters, including temperature stability, physical properties, and electronic properties. A solid understanding of these properties is vital for the design of efficient, cluster-based catalytic materials. The main focus is 3-atom ruthenium clusters (Ru_3) supported on RF-sputter deposited titania (RF-TiO_2), but other types of clusters and surfaces are also studied. All results chapters feature the use of RF-TiO_2 as a substrate and aim to determine the effects of the substrate on supported clusters.

The individual focus of each results chapter will be described briefly herein. Chapter 4 focusses on the temperature stability and availability of Ru-CO binding sites on Ru_3 clusters. Chapter 5 expands on these studies, focusing on the effects of heat treatment on Ru_3 clusters by using a range of complimentary surface analysis techniques. Chapter 6 focusses on surface-sensitive measurements of the electronic density of states of supported Ru_3 and Pt_3 clusters. Finally, Chapter 7 looks at the effects of a small change in cluster size on the resultant properties of supported Ru_n clusters, by depositing Ru_4 clusters and comparing the results to the Ru_3 measurements.

Chapter 2   Literature Review

This chapter is a reformatted and edited version of a manuscript for a review article published in a peer-reviewed journal. See the Contextual Statement section for details on the contribution of the co-author to the published version of the manuscript.

Reference for the published version:

L. Howard-Fabretto & G. G. Andersson, Metal Clusters on Semiconductor Surfaces and Application in Catalysis with a Focus on Au and Ru, Advanced Materials, 32 (2019) 1904122.

2.1 Abstract

Metal clusters typically consist of 2 to a few hundred atoms and have unique properties that change with the type and number of atoms that form the cluster. Metal clusters can be generated with a precise number of atoms, and therefore have specific size, shape, and electronic structures. When metal clusters are deposited onto a substrate, their shape and electronic structure depends on the interaction with the substrate surface and thus depends on the properties of both the clusters and those of the substrate. Deposited metal clusters typically have discrete electron energy levels which differ from the electron energy levels in the constituting individual atoms, isolated clusters, and the respective bulk material. This review covers the properties of clusters, the methods to generate metal clusters, the methods to deposit clusters onto substrate surfaces, the application of clusters in catalysis and photocatalysis, and the methods for characterisation of cluster-modified surfaces.

2.2 Introduction

Metal clusters (also called nanoclusters) are an area of rapidly growing interest [2-11]. These clusters contain a group of metal atoms with the number of atoms ranging from 2 to typically a few hundred. The properties of clusters are different to those of an individual metal atom or their bulk material counterparts [11]. Clusters are smaller than metal nanoparticles and extend down into sub-nanometre sizes. Scientific interest is motivated by their unique electronic and catalytic properties and their resulting technological potential [12]. While bulk metals feature electron energy band structures, clusters typically feature discrete electron energies like that of molecules [13]. As the size of clusters begin to increase past approximately 300 atoms, they lose their cluster-like properties and start to become more metallic entering then into the nano-particulate size regime [11, 14-18].

In order to be used for applications such as catalysis, clusters are typically deposited onto a supporting surface, also called a support or substrate. Clusters can be deposited either as ligand-stabilised coordination complexes (also called ligand-protected clusters), or alternatively by physical gas-phase aggregation deposition using a cluster source (CS) [19]. Recent research on surface-supported metal clusters has focussed on aspects such as their morphology, size, cluster-substrate interaction, catalytic and photocatalytic properties, and electronic structure, with a goal to unravel how these different aspects affect one another [20-39].

Research on metal clusters is currently mostly fundamental in nature. The size-selected clusters produced in a laboratory can be treated as model catalysts for real catalytic systems, where the specific structure and properties of the particles can be very closely controlled to probe the relationship of these properties to catalytic ability [40]. This is a natural extension of a trend in real-world catalysts, where catalytic particles have been moving towards smaller and smaller sizes such as particles in the sub-nano cluster regime as well as the single atom catalyst limit where all the active catalyst exists in the topmost layer [40-42]. This stems from the fact that catalytic activity strongly depends on accessible surface area (SA). Real systems may have less controlled cluster sizes and structures than an experimental system, and even single atom catalyst systems may feature a range of small cluster sizes due to agglomeration, especially with particle coverages which are dense enough to be used [40, 42]. Research on small, size-selected clusters is therefore a key part in simplifying and understanding the mechanisms of catalysis which are occurring in practical single atom and sub-nanometre metal catalyst systems.

The research field of supported metal clusters is too large to be reviewed in a single work, and as such this review focuses mainly on Au and Ru clusters as exemplars, while touching briefly on other cluster types. This is because Au clusters are among the most well-studied, while Ru clusters are given special attention because they the main focus of the experimental work in this thesis.

This introduction in section 2.2 will further describe the real-world uses and applications of metal clusters, and the concept of electronic density of states (DOS) will be explained as this is important for understanding the electronic properties of clusters. Section 2.3 discusses how the cluster composition effects their properties. Section 2.4 discusses how clusters are deposited onto supporting surfaces, focussing on two key methods using ligand-stabilised clusters and a gas-phase aggregation CS. Section 2.5 focuses on how the supporting surface interacts with and effects the clusters. Section 2.6 discusses the catalytic and photocatalytic applications of clusters. Section 2.7 discusses the characterisation of clusters focussing on a range of spectroscopy and microscopy techniques including those used in this thesis. Finally, section 2.8 provides a conclusion to the review and offers an outlook on what the future of cluster research will focus on.

2.2.1 Uses and Applications

A key potential use of clusters is in the catalysts and/or photocatalysis of chemical reactions. Large scale industrial processes often rely on metal and metal oxide particle catalysts, and clusters form an extension of this class of heterogeneous catalysts with abilities often surpassing their bulk metal counterpart. As an example, surface-supported Ru cluster catalysts are among the most active catalysts for the hydrogenation of CO and CO_2, reactions featured in a variety of industry-relevant reactions including Fischer-Tropsch synthesis, ammonia feed purification, and methanation of coal-derived gases [43-55]. Photocatalytic substrates can be modified through the addition of metal clusters as cocatalysts to improve their photocatalytic abilities [4, 10]. The catalytic and photocatalytic abilities of a cluster are highly dependent on its size [22, 33, 35, 56], electronic structure [57], and fluxionality (*i.e.* the inherent changing of morphology on the surface during a chemical reaction) [58]. The concept of fluxionality is described in section 2.3.

2.2.2 Electronic Density of States and Solid Band Structures

Because the electronic properties of clusters vary greatly from that of bulk metals and because they are important for technical applications, measurements to probe these properties including the electronic DOS are of great importance. The electronic DOS of a

material is the number of states available to be occupied by an electron per energy interval, as a function of energy. By multiplying the DOS by the probability of those states being occupied, *e.g.* from the Fermi-Dirac distribution, the number of occupied electronic energy states is determined. This can be demonstrated by Equation 2-1[59]:

$$n_e(E).\, dE = P_e(E) * \rho_{energy}(E).\, dE \qquad\qquad 2\text{-}1$$

Where $n_e(E)$ is the number of occupied electronic energy states, $P_e(E)$ is the probability of those states being occupied, $\rho_{energy}(E)$ is the electronic DOS, and dE is the energy interval. In a single crystal the DOS depends also on the momentum vector (or k-vector). However, due to their small size – especially for sizes considered here, *i.e.* less than a few hundred atoms per cluster – clusters show little periodicity and the DOS dependence on the k-vector does not play a role. Another reason is that small clusters easily change between their various configurations due to their high fluxionality [13]. When the DOS is measured using a technique such as ultraviolet photoelectron spectroscopy (UPS) or metastable impact electron spectroscopy (MIES), it is the occupied DOS ($n_e(E)$) which is measured. Previous research has used UPS to study the electronic structure of size-selected, supported clusters and compared this to theoretical calculations of the DOS [57, 60]. MIES only collects data from the very top layer of a sample, and has been used to measure the DOS of supported clusters such as Au_9 [5] and Au_{13} [3]. Further information on UPS and MIES measurements of DOS is given in section 2.7.1.

Individual atoms and small molecules feature discrete electron energy levels, however in a bulk solid sample the energy levels become closely spaced and can be approximated as continuous rather than as discrete levels. These form energy bands of occupiable states; in a conductor such as a bulk metal, the lower energy valence band and higher energy conduction band overlap one another, which is responsible for the ease of electron flow in conductors. Metal clusters typically feature discrete electron energy levels similar to molecules rather than energy bands which would be expected of a bulk counterpart [13].

For semiconductors there is a band gap between the valence and conduction bands. The Fermi level, defined as the highest energy which can be occupied by an electron in a metal at 0 K, resides between these two bands. This means that for semiconductors there is usually a low occupied DOS at energies close to the Fermi level, while conductors have a higher occupied DOS in that region. In a UPS measurement, this manifests as the DOS signal reducing to zero for semiconductors at the conduction band edge (energies below the Fermi level), while a conductor will reduce to zero at the Fermi level [61].

2.3 Composition and Properties

There are many different physical properties which contribute to the electronic and catalytic properties of a cluster, such as size, morphology (shape), and fluxionality. These properties also depend on the elemental composition of the cluster. A small change in the number of atoms forming the cluster can produce a drastic change in physical properties, particularly the electronic structure, and thus can strongly influence the catalytic efficiency. Most cluster research focuses on mono-metallic clusters, however bimetallic clusters can also be produced which will have their own unique electronic and catalytic properties. A common example is those including both Ru and Au [62]. This review and thesis focuses strongly on mono-metallic clusters; however, several examples of research on bimetallic clusters are also given. The supporting surface for a cluster also effects its properties, which is discussed in detail in section 2.5.

Once the size of clusters reaches the range of hundreds of atoms, they begin to lose their cluster-like properties and turn into metallic nanoparticles with more bulk metal-like properties [11, 14-18]. For TiO_2(110)-supported Au clusters it has been shown that a metal-to-nonmetal transition occurs once the cluster size is decreased below approximately 300 atoms, where the clusters start to feature a gap between occupied and unoccupied energy levels [17]. This also coincided with the onset of their catalytic activity for CO oxidation [17]. A similar result has been shown for TiO_2(110)-supported Pd clusters, where a metal-to-nonmetal transition occurred in a window between 215 and 385 atoms per cluster [18]. As an example of the strong effect cluster size can have on the material properties, Sanchez *et al.* [56] tested the ability of MgO-supported Au_n clusters with $1 \leq n \leq 20$ to catalyse the oxidation of CO. It was found that at temperatures < 250 K, Au_8 catalysed the reaction effectively, however clusters with 7 or less atoms ceased to be catalytically active for the reaction at all.

Fluxionality is an inherent flexibility of clusters on a substrate, where small supported clusters can have multiple isomers [13]. These isometric structures have similar energies as well as low metal-metal coordination, and the supported clusters can thus transition between isomers with a relatively low transition energy [63]. As cluster size increases, the level of fluxionality typically decreases; larger nanoparticles have a crystalline structure, whilst smaller clusters can readily change shape on a supporting surface [63-65]. At room temperature changes in conformation can occur for small clusters of only a few atoms. This has been demonstrated when Qahtani *et al.* [66] measured three unique atomic configurations of ligand-stabilised Au_9 chemically deposited onto TiO_2 nanosheets using

high-angle annular dark-field scanning transmission electron microscope (HAADF-STEM). These images are shown in Figure 2-1. One structure was 3D and was attributed to clusters which were still ligand-stabilised, while the other two were unique de-ligated pseudo-2D structures demonstrating the fluxionality of the cluster [66]. Larger clusters can exhibit fluxionality with a larger input of energy; this has been shown experimentally for Au_{38}, where several structural changes were observed upon repeated measurements of the same cluster also using HAADF-STEM. This was attributed to thermal fluctuations and/or the input of thermal energy from the electrons used in the imaging technique [63]. The potential role of fluxionality in catalysis is discussed in section 2.6.
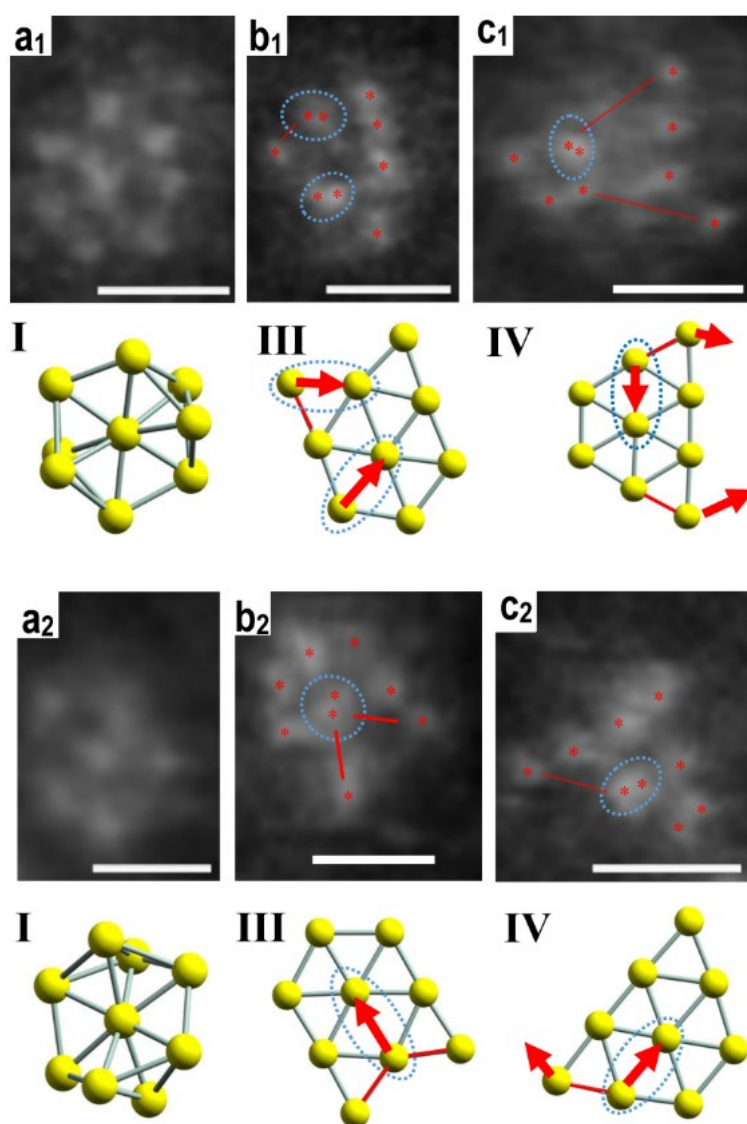
Figure 2-1: High resolution HAADF-STEM images of [Au₉(PPh₃)₈](NO₃)₃ on TiO₂ nanosheets. The scale bar is 0.5nm. Image (a) displays a 3D-like form that is changed into pseudo-2D forms in images (b) and (c). Images I, III, and IV are density functional theory models for three matching isomers of Au₉ [66]. Reprinted with permission of the Journal of Chemical Physics [66].

For experiments on supported clusters a common goal is to produce disperse, bare metal clusters of a single size only on the substrate which maintain size-selected properties. There are however difficulties associated with this; sintering and agglomeration is a common issue which needs to be considered. Agglomeration is the process of smaller clusters coalescing to form larger agglomerates which can change the properties of the clusters or obscure results from an experiment involving size-specific clusters. Agglomeration can occur through Smoluchowski and Ostwald ripening [67]. The first mechanism occurs through migration of clusters over the surface and their collision. The latter mechanism occurs when single atoms diffuse from one cluster to the other [67]. The formation of larger particles through coalescence is driven by the gain in Gibbs free energy [68]. Campbell *et al.* [69, 70] have demonstrated that as nanoparticles decrease in size their chemical potential increases, which results in sintering occurring more readily. There are several types of measurements which can probe clusters to determine whether agglomeration has occurred, including the microscopy techniques scanning tunnelling microscopy (STM) [71] and atomic force microscopy (AFM) [72], as well as observing shifts in core electron binding energies with X-ray photoelectron spectroscopy (XPS) for certain types of clusters [5, 73]. However, the abilities of each of these techniques to measure agglomeration will depend on the particular cluster size. These techniques and their use for probing clusters are discussed in section 2.7.

2.4 Deposition Methods

There are two commonly utilised approaches for preparing size-selected, surface-supported clusters. These are 1) depositing chemically synthesised, ligand-stabilised clusters, and 2) depositing gas-phase aggregated bare clusters. Each of these approaches features multiple distinct methods to perform a cluster deposition which will be discussed. Very few studies have directly compared the cluster properties of identically sized clusters resulting from different deposition methods [74].

2.4.1 Ligand-Stabilised Clusters

Ligand-stabilised clusters feature a central metal cluster which is surrounded by chemical ligands forming a coordination complex. These clusters are chemically synthesised and can be deposited onto a surface by one of two classes of methodologies: solution submersion, or chemical vapor deposition (CVD). After a deposition, the ligands removed (or partially removed) using heat or chemical methods to leave bare, surface-supported particles [3, 5, 74, 75].

An advantage of ligand-stabilised cluster depositions is the ease of scale-up to industrially relevant scales, because complex and expensive equipment such as high vacuum instrumentation is not needed (as is the case with gas-phase aggregation, discussed later). Furthermore, the depositions are atomically precise. When using solution submersion depositions, ligated clusters can also be deposited onto porous support materials covering both the internal and external surfaces, while for gas-phase depositions involving a cluster beam the deposition is line of sight and cannot reach internal surfaces. This is an advantage for depositing clusters onto surfaces such as mesoporous silica [76, 77] and zeolites [78, 79]. Disadvantages are the levels of contamination introduced which can affect measurements, especially for solution submersion depositions where the solvent is introduced to the sample in atmosphere, as well as the extra treatment needed to remove ligands which may change the surface properties. Furthermore, only specific sizes of ligand-stabilised clusters are chemically stable.

2.4.1.1 Structure of Ligand-stabilised Clusters

A range of ligands can be used to stabilise a cluster depending on its size and composition. The metal-metal bonds in these complexes can be separated into two categories; "supported" bonds that have ligands bridging between the metal atoms, and "unsupported" bonds which feature direct metal-metal bonding. One of the most well-studied types of clusters on surfaces are the metal carbonyls; small metal clusters saturated by surrounding carbonyl (CO) ligands [80-83]. Figure 2-2 shows 2 different metal cluster carbonyls: $H_4Ru_4(CO)_{12}$ (1) and $Ru_3(CO)_{12}$ (2). This demonstrates the difference between supported and unsupported metal bonds; (1) features H ligands bridging the Ru atoms and the bonds are therefore supported, while (2) only features outward-facing CO ligands and the bonds are unsupported. Another commonly used ligand is the sulphur-containing thiolates (SR), which can be used to stabilise clusters of a large range of sizes [84-87]. Au thiolates are by far the most studied [86, 87], however other thiolate-stabilised clusters also exist including Ag thiolate [88, 89] and CdS thiolate [90]. By utilising a range of different ligands, Ru, Au, and other clusters can be produced with a variety of sizes and orientations [77, 91-97] and Au [4, 73, 98-102]. While this review mostly focuses on carbonyls and thiolates as common exemplars, there are many other types of ligands which can stabilise clusters including triphenylphosphine (PPh_3) [66, 72, 73, 76, 98, 99, 102-104], and glutathione (GSH) [10, 26], which have been used to stabilise Au clusters among others.
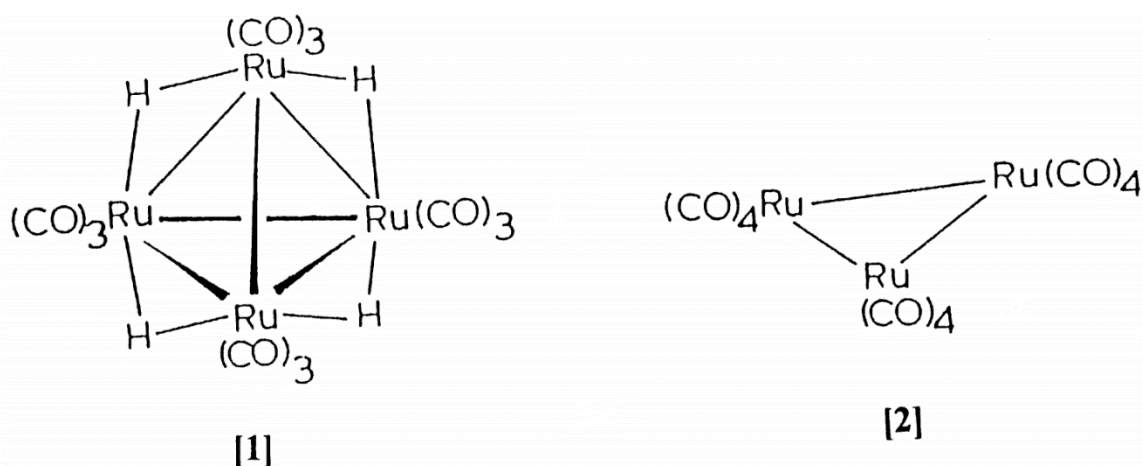
Figure 2-2: Bonding schematic for H₄Ru₄(CO)₁₂ (1) and Ru₃(CO)₁₂ (2). (1) features bridging H ligands meaning the metal-metal bonds are supported, while (2) features unsupported bonds. Adapted from [105]. Reprinted with permission of Inorganica Chimica Acta [105].

Ligand-stabilised clusters can only be made with specific numbers of core atoms; for different metal and ligand combinations different cluster sizes are stable. There has been controversy in the literature regarding explanations of why only certain sized clusters so far have been found to be stable while others not. Some authors have described clusters as resembling "superatoms", where clusters are stabilised according to an electron-shell closing model which is analogous to the electron-shell closure of atoms, that is, valence shells need to be completely filled or remaining valence electrons need to be donated in chemical bonds [106-113]. In this case the superatom is thought to behave like a regular atom in reactions with other molecules [111-113], and superatoms can be treated as the constituents of a periodic table which is differently arranged from the conventional table [114]. However, other studies have shown stable clusters with no superatom-like properties [15, 115-126]. It has been proposed that this model only holds in specific cases rather than in general and that stability is related to effective metal and ligand orbital overlap, and the molecular orbital stabilisation which results from this [15, 115-117].

Metal carbonyls feature bonding between a carbonyl ligand and a metal, which involves π-backbonding. The lone sp-hybridised electron pair (HOMO) on the carbon is donated to the metal to form a sigma bond. The LUMO of the carbon is a pair of π* antibonding orbitals [127]. The d-orbital of the metal overlaps with these orbitals, and donates electrons to the carbon, forming a pair of π bonds and relieving the metal of excess negative charge; this is called π-backbonding and requires a low oxidation state metal to be favourable. The three bonding components (sigma and 2 π-backbonding) form a partial triple bond between the metal and carbon. This can be described by resonance structures, with the share of

electrons distributed between Metal-C-O being dependent on the backbonding power. π-backbonding weakens the bond between carbon and oxygen relative to free carbon monoxide (increases bond length) and strengthens the metal-carbon bond. Density functional theory (DFT) calculations by White *et al.* [128] have demonstrated this by showing that the CO bond length is 1.147 Å for $Ru_3(CO)_{12}$, increasing with decarbonylation (removal of CO ligands) to 1.161 Å for Ru_3CO, while their calculated bond length for free CO is 1.134 Å. This bond weakening can also be seen in measurements of infrared spectrum wavenumber shifts, where the wavenumbers are related to bond energies [83]. The strong bond between the metal and CO due to π-backbonding ensures the stability of the clusters while depositing and contributes to preventing the decomposition or aggregation of the clusters before deposition.

The type of ligand stabilising a cluster can change the overall cluster properties, even for clusters of the same size and species. For example, Negishi *et al.* [129] have synthesised Au-selenolate (SeR) of size $Au_{25}(SeR)_{18}$ (R = $C_{12}H_{25}$ or C_8H_{17}) and compared its resulting bonding nature to thiolate-stabilised $Au_{25}(SR)_{18}$. Their experiment found the SeR ligands had a reduced charge transfer from the Au to the ligand, and that the nature of the metal-ligand bond changed such that the Au-SeR bond was stronger than the Au-SR bond [129]. Furthermore, the SeR ligands improved the stability of the clusters in solution [130]. A follow up experiment found the same phenomenon for Au_{38} clusters [131].

2.4.1.2 Deposition Methodology

A common method to deposit ligand-stabilised clusters is the "solution-based" deposition, also called "solution submersion". This involves producing a solution of the desired clusters in a solvent and immersing the supporting surface into the solution such that clusters can adsorb to the surface. The solvent chosen must be one that prevents aggregation and precipitation in the solution, *e.g.* does not remove the ligands from the cluster core [76]. It also must be easily removed after deposition using mild treatments such as drying in air or vacuum [73, 102, 103] or a gaseous N_2 stream [26]. For a crystal wafer support, the entire sample can be immersed in the solution for a pre-chosen time period [66, 72, 99, 104]. A variant on this method is to drop cast the cluster solution onto the wafer and wait for the solvent to evaporate [63, 104]. Another method involves using a suspension of powdered supports in the solution and stirring, which can then be deposited onto another surface for measurements [10, 73, 100, 102, 103, 132-134].

A different, solvent-free method to deposit ligand-stabilised clusters is to allow the clusters

to vaporise under ultra-high vacuum (UHV) and adsorb to the support, which is known as CVD. Ligated clusters are held in a glass vial which is connected to a UHV system and can be exposed to the sample with a gate valve or equivalent [75, 135]. This method has an advantage over solution-based depositions in that less unwanted surface contaminants are introduced into the system due to contact with atmosphere and solvents. The disadvantages are that a UHV system is needed for deposition (and thus it does not have the same up-scalability), and depositions cannot be effectively performed on the internal surfaces of porous supports. For CVD to be possible the UHV system must reach pressures lower than the vapor pressure of the clusters so that the clusters are the majority of what adsorbs to the surface and do not compete with contaminants from atmosphere. The clusters must also have sufficient stability to vaporise without decomposing. Metal carbonyls are the most reported type of cluster for which this method is used [74, 75, 136, 137]. The deposition of metal carbonyl compounds using CVD has been used to deposit clusters onto a number of substrates such as; metals (*e.g.* Au), metal oxides (*e.g.* TiO_2), non-metal oxides (*e.g.* SiO_2) and others such as zeolites [75, 138-143]. These clusters are highly stable, and due to their relatively low vapor pressure they only require vacuums of 10^{-7} Torr or lower [80] which is achievable by typical UHV systems. The cluster sample can be heated to increase vapor pressure and allow for depositions at higher pressures; however, this is only useful for clusters which need a deposition pressure only slightly lower than the pressure available because heating can decompose the clusters depending on species and temperature. The substrate can be left at room temperature or cooled/heated during vapor depositions, which can affect the resulting adsorption state of the cluster [75, 137].

After a deposition, the ligands are typically removed such that there is contact between the bare metal cluster and the support. This can be done to some extent for some types of ligands by exposure to vacuum [73, 102], however thermal treatment either under vacuum or in the presence of a gas is often needed for complete ligand removal depending on the cluster and ligand types. The risk of ligand removal is that the clusters may agglomerate on the surface and lose their cluster-like properties or catalytic activity, and the difficulty of ligand removal is a key factor in the choice of which ligand-stabilised cluster would be useful for practical catalytic applications. Incomplete de-ligation or a change in the chemistry of the ligands may also occur depending on the cluster species and ligand removal conditions, so careful choice and monitoring of the treatment is important in achieving bare, non-agglomerated clusters [144].

Thermal treatment, also known as heat treatment or calcination, of the sample under UHV

can remove some types of ligands by breaking the bonds between the ligand and the cluster. Ligands are typically transferred into the gas phase, however some can also bind to the substrate surface which has been observed for Au_9 clusters on TiO_2 [73, 102]. Ligand removal can be observed using techniques such as temperature programmed desorption (TPD), which measures desorbing molecules from the surface as the temperature is slowly increased [75]. The use of TPD with metal clusters is described in more detail in section 2.7.3. Heating to 473 K has been reported to fully remove PPh_3 ligands [73, 76, 99, 102]. Thiolate ligands on CeO_2-supported $Au_{25}(SR)_{18}$ have been removed at 523 K [145]. Glutathione ligands have been removed from $Au_{25}(SG)_{18}/BaLa_4Ti_4O_{15}$ at 573 K [146, 147]. For $Ru_3(CO)_{12}$ on TiO_2 full ligand removal has been reported between 700 K and 800 K depending on the nature of the substrate and deposition method [74, 75]. Thermal treatment has also been performed under different atmospheric conditions such as O_2 [102], H_2 [98], and air [85]. However, these conditions have been reported to cause catalytic deactivation and agglomeration [23]. Ozone treatment has been used, but extensive agglomeration was also reported [100, 103].

2.4.2 Gas-phase Aggregation Cluster Source

Gas-phase aggregation is an alternative method of producing metal clusters which utilizes a UHV instrument called a cluster source (CS). This is also referred to as a CS-deposition. Vapor of a specific metal is generated in vacuum by sputtering a sample of the respective metal. Inert gas such as Ar or He is passed through the vacuum chamber containing the metal vapor which thermalizes the sample vapor, *i.e.* lowers the kinetic energy (KE) of the atoms in the gas phase, leading to aggregation of the gas phase atoms into clusters. The initial sputtering to produce the vapor can be achieved through the commonly used methods of magnetron sputtering (MagS) [7, 20, 21, 148, 149] and laser vaporisation (LaVa) [57, 150-154] which have received the largest research interest [8], as well as other less common methods [155, 156]. LaVa is also sometimes referred to as laser ablation. A mass filter such as a quadrupole can be used to size-select clusters based on their mass-to-charge ratio.

CS-depositions have advantages over ligand-stabilised which lend them to be well suited to fundamental experiments on clusters. The whole deposition process can be performed *in situ* without any exposure to atmosphere or ligands, and there are no extra steps required to remove ligands after the deposition which can result in modification of the clusters such as agglomeration. In addition, the cluster sizes are less restricted than for ligand-stabilised clusters, because a CS is not limited by which cluster sizes are stable in ligated complexes [31]. Disadvantages are that the process is difficult to upscale for industrial applications due

to the high vacuum required and small cluster deposition areas [20], and that the size-specificity depends on the resolution of the mass filter used [20, 157]. Furthermore, because the deposition process uses a cluster beam it is line of sight and cannot deposit onto internal surfaces in the case of using a porous support material.

2.4.2.1 Aggregation in the Gas-Phase

A CS typically features an aggregation chamber where the clusters are produced, chamber/s for mass selection, and a final chamber where a substrate is held for cluster deposition. These chambers are differentially pumped vacuum chambers, which reduces the load of the cluster carrier gas at the point of deposition.

MagS sources are based on an idea of Haberland *et. al* [158], and use MagS to produce a vapor of metal which then aggregates to form clusters. A schematic of a typical MagS source is shown in Figure 2-3. These sources can produce charged clusters in large numbers using a relatively simple method. A plasma is ignited using a noble gas, typically Ar, and a magnetic field stabilizes it. A solid sample of the desired metal is mounted close to a permanent axial magnet, and a discharge of metal vapor is initiated by a voltage between the target and a circular electrode. This vapor is then cooled and directed along the length of the instrument by a carrier gas [158]. Water or liquid nitrogen cooling using a shroud around the aggregation chamber can be used to further assist the cooling of the metal vapor. Conducting and semiconducting materials can be sputtered with a source of this type.
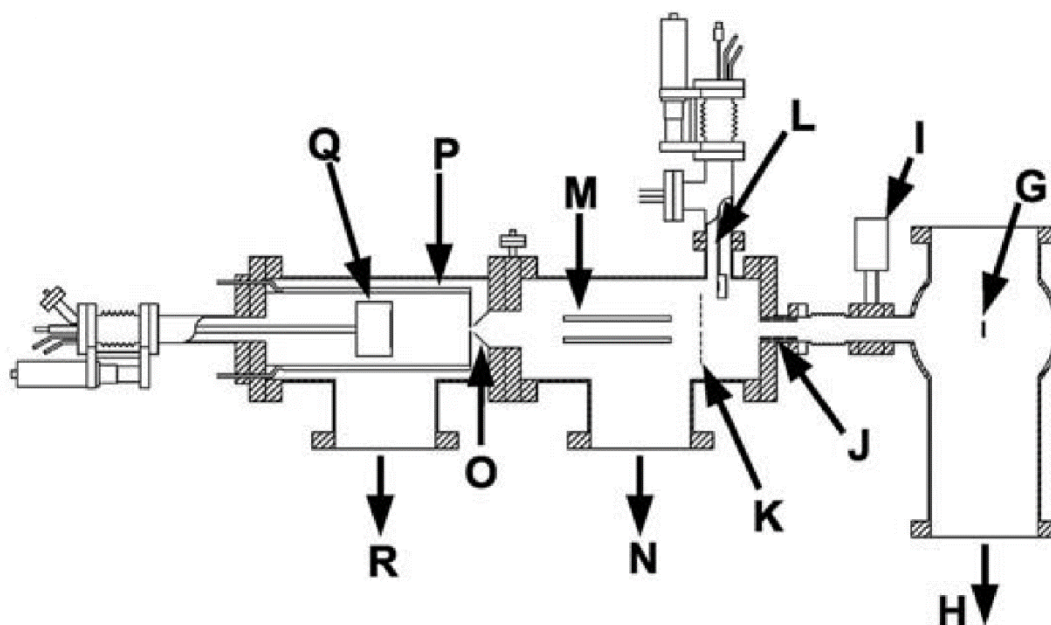
Figure 2-3: Schematic of a magnetron sputtering CS [159]. G) substrate in deposition chamber; H) pumping on deposition chamber; I) gate valve; J) Einzel lenses for focussing beam; K) grid for measuring beam current; L) quartz crystal balance for determining total flux; M) quadrupole mass filter for size-selection; N) pumping on quadrupole chamber; O) skimmer for refining particle beam; P) cooling shroud for aggregation chamber; Q) magnetron sputtering source; R) pumping on aggregation chamber. Reprinted with permission from Surface Science [159].

LaVa sources pulse short, nanosecond bursts of laser light at a rotating target plate or rod of the desired material, using an intensity of 10-100 mJ/pulse which produces a metal plasma plume subsequently carried away by a noble carrier gas [160, 161]. Nd:YAG or Ti:Sapphire lasers are typically used as the light source, and the intensity must be great enough to vaporise the target; almost all solid materials can be vaporised with this type of source. The operation for both MagS and LaVa sources after the initial sputtering step is similar. Both types of CS can also be used to make bimetallic clusters, through the use of a bimetallic alloy target of the desired ratio [162, 163], or simultaneously sputtering two targets [164, 165].

The size distribution of clusters produced in both cases is dependent on the particular source and the conditions used, with particular conditions leading to optimisation for particular size ranges from less than tens to hundreds of atoms [166]. Conditions which can affect the cluster sizes are cluster species nucleation probability, length of the aggregation zone, inert gas species used in the aggregation zone, inert gas flow rate, and sputtering rate [167]. A longer aggregation length means more time for aggregation which leads to larger clusters. Heavier inert gasses result in greater thermalisation and therefore more chance of nucleation leading to larger clusters. Increasing inert gas flow rate results in both greater

thermalisation and less aggregation time which can increase or decrease the size of clusters depending on the rate and species. Increasing the rate of sputtering results in a greater frequency of collisions and therefore larger clusters. These factors are all interactive with one another and optimisation depends on the cluster material and specific CS.

Almost only single atoms are initially present after sputtering, meaning the first step needed for a cluster to form is the formation of a metal dimer from two individual atoms. These form in three-body collisions, where the inert gas lowers the energy of the clustering atoms [158]. For a metal M with argon gas, the clusters form according to the reaction shown in Equation 2-2.

$$M + M + Ar \rightarrow M_2 + Ar \hspace{4cm} \text{2-2}$$

The dimers can continue to cool through further collisions with the Ar and can continue to grow through the addition of atomic monomers. The Ar has simultaneous roles of fulfilling energy and momentum conservation, and stabilising the newly formed dimer [157]. Once the number of monomers present has been reduced, the clusters can continue to grow through coagulation with other clusters [158].

The clusters can begin to aggregate by either homogeneous or heterogeneous nucleation. Nucleation is the initial step in the formation of a new crystal structure by self-assembly. To nucleate, an energy barrier must be overcome. Heterogeneous nucleation occurs at surfaces in the system which form nucleation points, while homogeneous nucleation occurs away from such surfaces and only involves the nucleating species [168]. A gas molecule of an element other than the element forming the metal vapor, such as O_2 or N_2, can function as such a "surface" leading to heterogeneous nucleation. The aggregation process discussed in the previous paragraph featured homogenous nucleation (the Ar gas serves to simply thermalise the clusters). The nucleation energy barrier is reduced in heterogeneous nucleation compared to homogeneous, and as the barrier is reduced the rate of nucleation increases exponentially, meaning heterogeneous nucleation tends to be more rapid [168].

A CS can produce both positively and negatively charged clusters, as well as neutrals [169-171]. The distribution of these will be dependent on the specific source and operation conditions, as well as the species of the clusters [169]. Only around 1 in 1000 atoms sputtered from the target leave charged, however if one atom in a cluster is charged then the whole cluster has that same charge, resulting in a large fraction of the clusters being singly charged regardless of size, with reports ranging from 20-80% [148, 158]. There are

several other mechanisms which result in charged clusters being produced, including Ar^+ ions in the sputtering plasma transferring their charge to clusters due to the high ionisation energy of Ar (when using MagS sources), Penning ionisation, and other mechanisms [158].

A mass filter can be used to size select the singly charged clusters allowing only a narrow range of sizes to reach the substrate, which is possible because once they have passed through the final aperture leaving the aggregation chamber the carrier gas has negligible influence on the clusters after leaving the aggregation chamber [172]. The eventual mass resolution reaching the substrate will depend on the resolution of the mass filter, *i.e.* how well it can discriminate between clusters with a difference in size of only one atom. Tight size selection is able to separate clusters with a precision of 1 u; however, this has only been achieved for a maximum size of a few tens of atoms [157]. Electric bending potentials can also be implemented which will bend the trajectory of charged clusters but not neutrals, allowing only charged particles to reach the surface such that the resultant size resolution will not be broadened by neutrals.

2.4.2.2 Deposition Methodology

The energies of the clusters as they reach the support in a gas-phase aggregation deposition process greatly effects the deposition outcome. A deposition of clusters at high KE will have different results to low KEs [157]. Soft-landing is described as the case when the clusters arrive at the surface with KEs significantly less than the cohesive energy of the cluster constituents, which does not result in cluster fragmentation [7]. The typical upper KE limit for soft-landing has been reported to be from 0.1 eV/atom to 1 eV/atom [21, 157, 173], but this is not a rule which applies to all systems. The substrate impact energy of ionised clusters can be controlled using electrostatic forces by biasing the sample; if positively charged clusters are being deposited onto a substrate, the substrate can be positively biased with a voltage to exert an electrostatic force on the incoming clusters and reduce their energy into the range of soft-landing.

For depositions with increased KEs different phenomena occur. High energy depositions where the deposition energy is larger than the cluster cohesive energy can result in a loss of cluster structure and local damage occurring on the substrate [157, 174]. Figure 2-4 demonstrates the difference between soft-landing (a) and high energy impact (b). This example shows several types of high energy impact damage including cluster deformation and fragmentation, local surface damage, cluster implantation into the surface, and backscattering of fragments. An intermediate regime between soft-landing and the high

energy deposition of clusters is called pinning, where the impact forms defects on the surface and the clusters become trapped at these local defect sites, supressing diffusion of the clusters across the substrate [175, 176]. However, the deposition energy required for pinning varies depending on the cluster species, cluster size, and support material, meaning this regime is not easily controllable. For situations where the cluster size and structure is of importance, soft-landing depositions should be performed because the effects of a high energy deposition will alter the size of the clusters and leave a range of deformed clusters on the surface, thereby removing the ability to relate cluster properties to a particular cluster size.
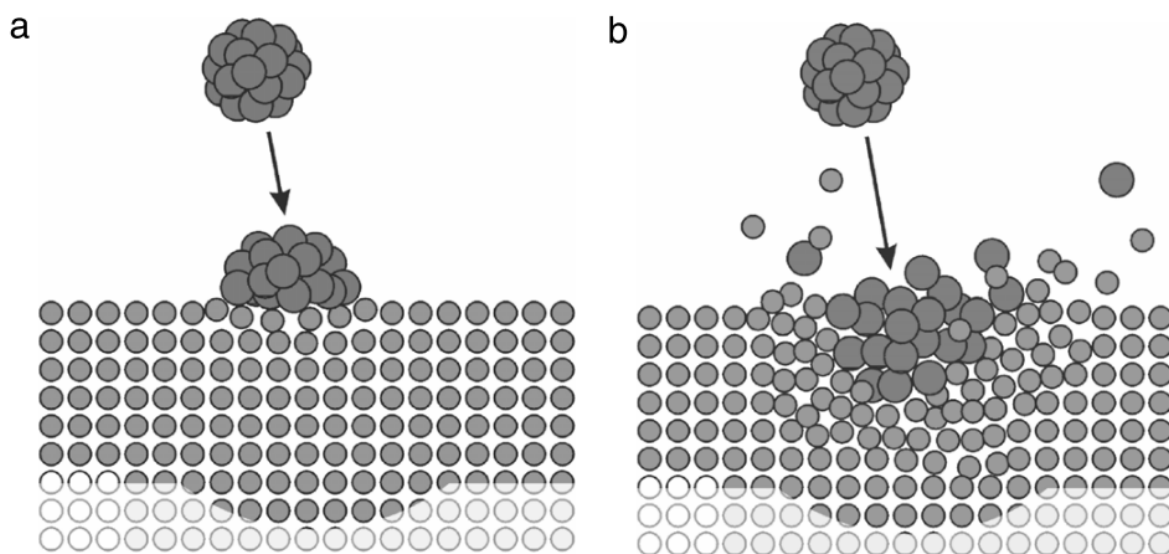
Figure 2-4: Diagram of (a) a cluster soft landing at low energy, and (b) a cluster impacting the surface with high energy [157]. For a high energy deposition both the cluster and substrate are deformed and damaged. Reprinted with permission from Surface Science Reports [157].

2.5 Effects of the Supporting Surface

Supported metal clusters have properties which are affected by the type of supporting surface used, and the choice of support is critical to the catalytic abilities and stability of the system. Cluster-support interaction can affect how strongly the clusters adsorb to the surface, their structure, and their electronic properties [30, 37, 177]. The relationship between supporting material and cluster morphology is entwined with the relationship between the supporting material and catalytic ability, because the structure of the clusters plays a vital role in their catalytic action [58, 177]. The support can offer catalytic benefits for clusters; by example, Au clusters have been shown to catalyse the oxidation of CO when supported on metal oxide surfaces, but not when supported on other substrates [56, 178].

Metal oxides such as titania (TiO_2) and magnesia (MgO) are widely used due to their low fabrication costs and their established benefits including strong bonding between the surface and bare clusters [179]. Metal oxide substrates can be divided into subgroups of: nonreducible oxides, and reducible oxides [180]. Nonreducible oxides including SiO_2, MgO, and Al_2O_3 typically have large bandgaps >3 eV, and the removal of oxygen is not energetically favourable, meaning the materials are stoichiometrically stable and chemically inert [180, 181]. Conversely, reducible oxides such as TiO_2, WO_3, NiO, Fe_2O_3, and CeO_2 are typically semiconductors with band gaps <3eV and can exchange oxygen more readily [180]. When oxygen is removed from the metal oxide, excess electrons are distributed to the metal cations (*e.g.* Ti^{4+} in TiO_2), thereby changing their oxidation state. Carbon-based materials such as graphite are also used as cluster supports for catalytic applications but are reported more often for gas-phase aggregated clusters than chemically synthesised clusters [2, 175, 176, 182]. Chemically synthesised clusters have even been attached to modern carbon-based nanomaterials such as multi-walled carbon nanotubes [183].

TiO_2 is widely used as a support for metal clusters [6, 26, 38, 60, 66, 74, 75, 103, 184-190] as a result of its high stability, photo-activity, ready availability, low cost, and low toxicity [191]. Downsides are that it only supports n-type processes and has a large band gap. The latter is limiting in photocatalytical processes. TiO_2 comes in a variety of different forms which can affect the end properties of the system [66, 72, 73, 75, 102, 103]. Single crystal TiO_2 is well characterised for all the crystal phases of titania; rutile, anatase, and brookite, and is therefore used when uniform and well-characterised supports are required [17, 98, 99, 192]. Atomic layer deposition (ALD) titania is an amorphous but atomically flat variant of titania that has been used due to its benefits for surface imaging techniques, but it has a high synthesis cost so is less suitable for large scale applications [66]. Further variants of titania which have been used as supports include nanoparticulate TiO_2 such as P25, which can features multiple crystal phases based on particle size and phase proportions [193], as well as innovative forms such as TiO_2 nanotubes [26], and thin nanosheets (1.1nm) [72]. Nanosheets are particularly useful for scanning transmission electron microscopy (STEM) imaging, where electrons must pass through the sample.

The morphology of a surface-supported cluster can vary depending on the nature of its supporting surface. To exemplify this, Pacchioni *et al.* [194-196] have done DFT simulations on Au_{20} clusters supported on MgO/Mo(100). They compared the structure of the clusters on MgO films from 2 to 7 monolayers (ML); on a thick film the structure of Au_{20} was pyramidal, which matches its structure in the gas phase, however on a thin film the cluster

formed a planar structure. For the thin film case this is caused by electron transfer to the clusters from the metal substrate, where for that charge state the planar isomer is the most stable structure [194-196]. Figure 2-5 shows the simulation of Au_{20} on a thin film of MgO/Mo(100), with both the less stable pyramidal (a) and more stable planar (b) structures [196]. STM experiments of Au atoms deposited onto MgO/Ag(100) followed by annealing at 210 and 300 K to form non-size selected clusters has shown similar results; for 3 ML MgO, the structure was planar with 2D Au islands, whereas for 8 ML MgO a 3D Au structure was found [197]. Figure 2-6 shows these STM measurements and the height profiles of the measured clusters. Measurements of clusters by STM is further discussed in section 2.7.4.2.
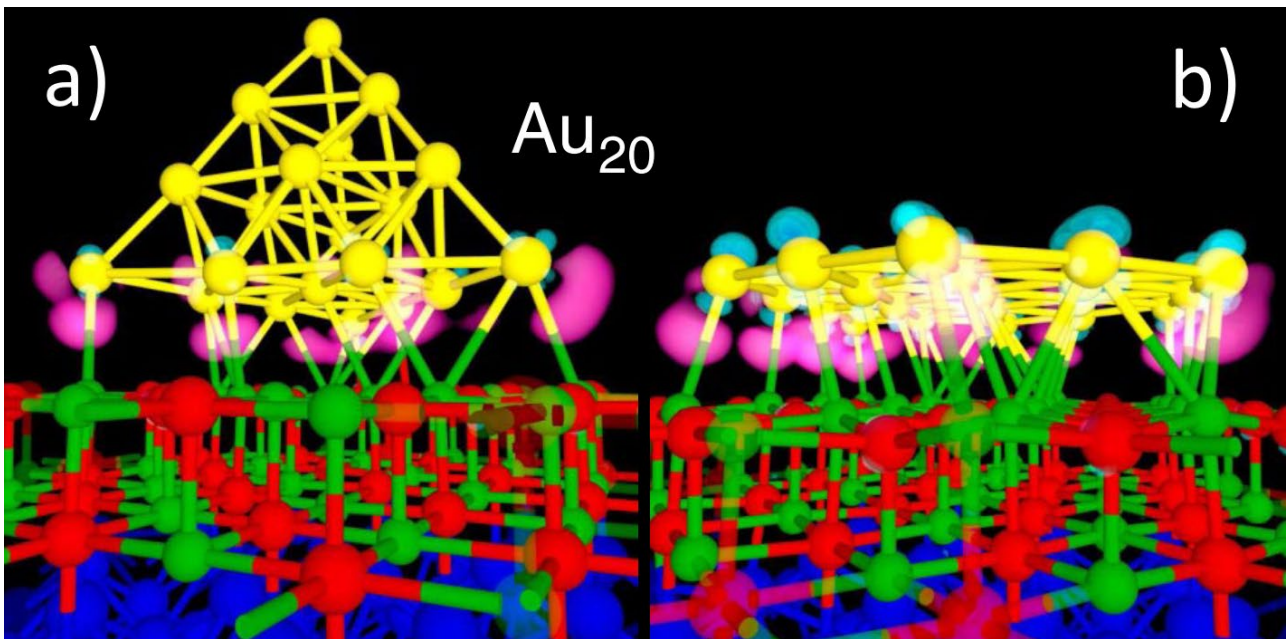
Figure 2-5: DFT simulation of Au_{20} on a thin film of MgO/Mo(100). Left (a) shows the pyramidal (fcc) structure, while right (b) shows the planar structure [196]. In the case of a thin MgO film such as this, the planar structure is more stable by 3.3 eV. Pink represents charge accumulation and light blue represents charge depletion. Yellow, green, red, and dark blue atoms correspond to Au, Mg, O, and Mo, respectively. Adapted from [196]. Reprinted with permission from Physical Review Letters [196].
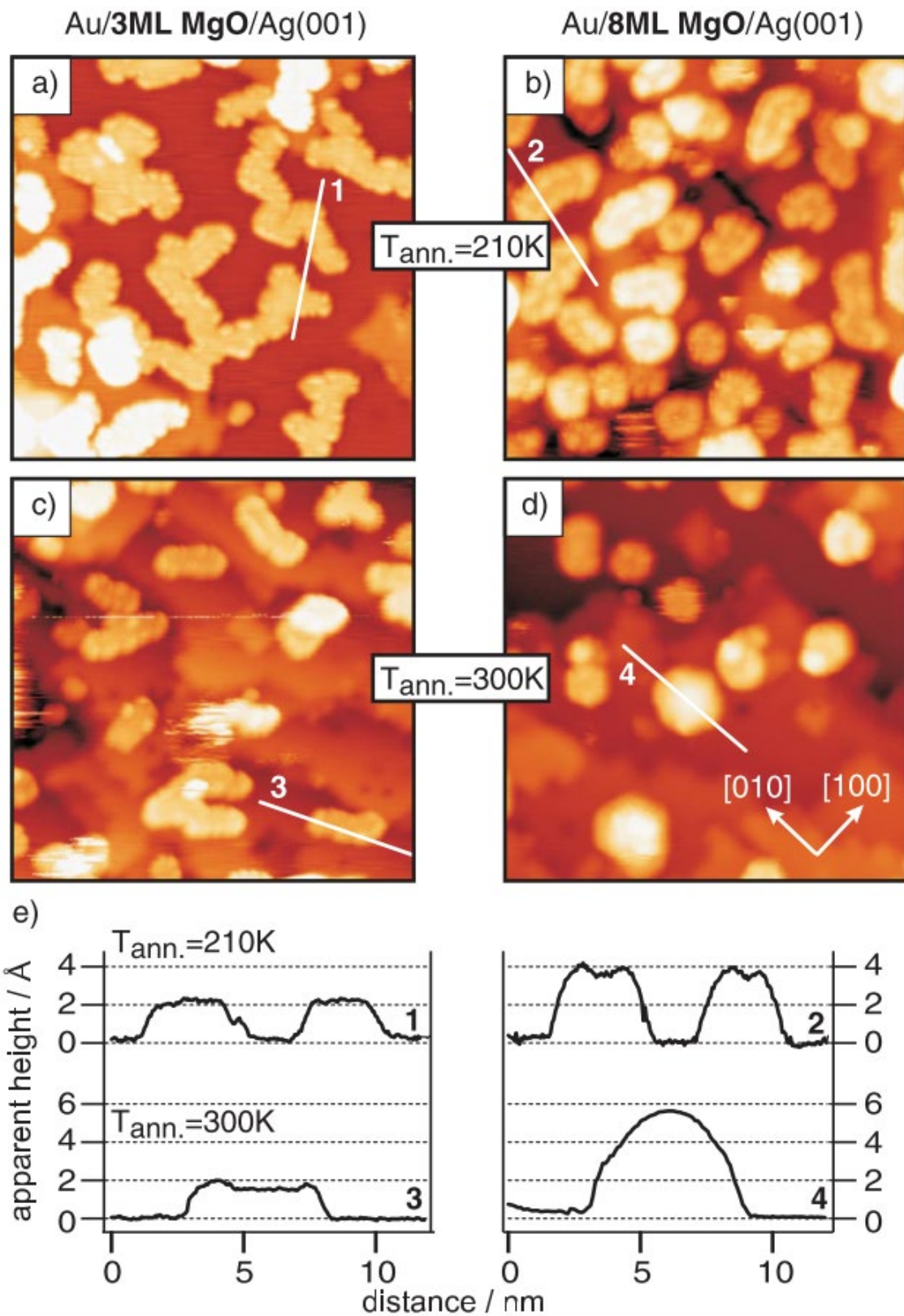
Figure 2-6: 30 nm x 30 nm STM images of Au clusters on MgO/Ag(001) formed by depositing Au atoms and annealing to cause clustering at 210 K (a and b) and 300 K (c and d) [197]. 3ML MgO is shown in (a) and (c) while 8ML MgO is shown in (b) and (d). (e) shows the cluster height profiles for the different systems; on 3ML MgO, the Au forms planar, single layer structures, while on 8ML MgO multilayer Au structures are formed. Reprinted with permission from Physical Review Letters [197].

In some cases, mixing of clusters with the substrate material can occur. Strong metal-support interactions (SMSI) can occur between supported clusters and reducible oxide surfaces such as TiO_2, which can cause changes in cluster catalytic activity [39, 185, 198-200]. The SMSI can involve electronic factors such as cluster oxidation, or a charge transfer between the clusters and the metal oxide [185, 201, 202]. Metals with small work functions (*e.g.* early transition metals and alkali metals) are more typically oxidised compared to their large work function counterparts [185, 203-206]. Additionally, structural effects can occur such as the clusters being covered by a layer of substrate material, which is known as the "encapsulation" or "decoration" model [199, 207]. Depending on the combination of cluster metal and oxide substrate, varying conditions have been required to induce cluster encapsulation, including high temperature reduction in UHV [184-186, 207-214] or in H_2 [198, 199, 215-217], as well as reduction of the substrate by sputtering [185, 186]. Speaking of supported metals in general, studies have shown a variety of metals subject to encapsulation including: Pt, Pd, Rh, Ni and Ir [184-186, 203, 204, 207-213, 216-220], while other metals such as Cu, Ag, A, and CO are known to withstand encapsulation [204]. However, it should be noted that the SMSI is complex and can vary based on substrate treatment, and other factors [185].

An important aspect of the supporting surface that will affect the cluster/surface interaction is whether the surface is pristine or features surface defects. Clusters prefer to adsorb at defect sites or step edges as their surface energy is larger than the corresponding perfect crystal structure [5]. This is beneficial in that the clusters can be more easily attached to a surface, and in some cases their mobility is decreased leading to less cluster agglomeration [3, 5]. Defects can be experimentally introduced onto a substrate by sputtering the surface with Ar ions. This process has been performed on a number of substrates including TiO_2 [5, 75], where the sputtering process can preferentially remove surface oxygen atoms and create defected sites with oxygen vacancies where the Ti is reduced from Ti^{4+} to Ti^{3+} or Ti^{2+} [5, 221]. By combining STM and DFT calculations it was shown that on a rutile TiO_2(110) surface the oxygen vacancies are the strongest binding sites for Au clusters, and that one oxygen vacancy can bind an average of 3 Au atoms [222]. Clusters also preferentially form at defect sites on carbon based surfaces such as highly oriented pyrolytic graphite (HOPG), where small cluster depletion zones occur around the defect [20, 223].

A step edge is a location on the surface where the number of layers changes forming a "step". Like local defects, these edges also have an increased surface energy. Au clusters were shown to nucleate at step-edges preferentially on titania supports [17, 224]. Step

edges on HOPG act as preferential binding zones for clusters and also limit their agglomeration compared to flat terrace regions of the surface, which was demonstrated for large Ag clusters through scanning electron microscopy (SEM) imaging and is shown in Figure 2-7 [225]. It has even been shown that organised nanostructures can be produced with clusters by defecting the substrate in an organised way using a focussed ion beam prior to a CS-deposition [226].
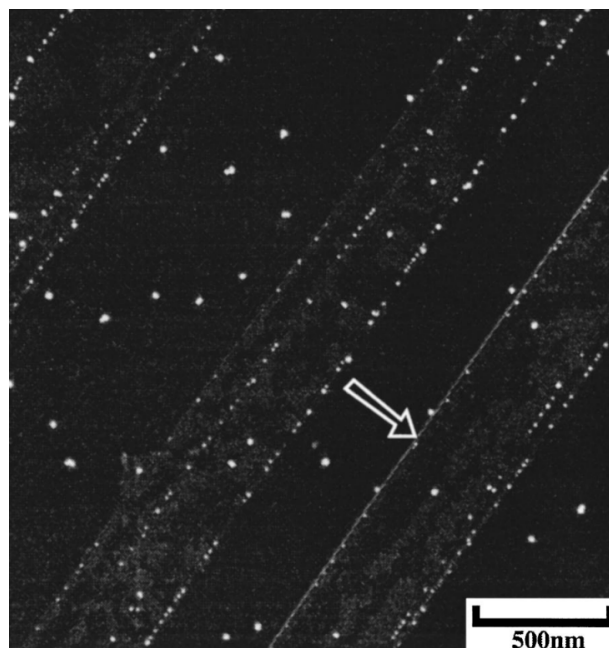
Figure 2-7: SEM image of size-selected Ag$_{400}$ deposited from a CS onto a stepped HOPG surface [225]. The coverage is 4.7 x 10^8 clusters/cm^2. The arrow points to an example of a step edge. The clusters preferentially bind to the step edges and feature less agglomeration (smaller cluster sizes) compared to the particles on the large terrace regions due to their stronger interaction with the defected zones of the surface. Reprinted with permission from Applied Physics Letters [225].

2.6 Catalytic Action

2.6.1 Catalysis

Solid-supported metal clusters have recently attracted interest in catalysis research [25, 227, 228]. The motivation is to increase the SA-to-volume ratio of the catalytically active component, *i.e.* the nanoparticle or cluster, as well as to take advantage of the specific properties of clusters. There is a trend of real-world catalysts moving to smaller sizes such as sub-nanometre clusters and single atom catalysts to exploit the increase in SA [40-42]. Although these practical systems may feature less controlled particle sizes, size-selected clusters can be used to probe the catalytic action of these systems in a controlled way in order to understand how they behave and how to best exploit their properties for catalytic benefit.

The catalytic ability of a cluster is closely related to three main factors: 1) the size of the cluster [32, 57, 154, 229], 2) the morphology and fluxionality [58, 177], and 3) the electronic structure and oxidation state of the cluster [65]. However, the electronic and geometric effects are dependent on one another and are difficult to analyse separately [13]. The cluster-support interface where transfer of charge can occur [230] has also been shown to be of great importance to the catalytic action [56, 178].

Supported Au clusters are among the most researched for catalysis. Due to its nobility gold was previously thought to be a poor catalyst, but has attracted research interest after low temperature CO oxidation was shown by Au nanoparticles in 1989 [231]. Au clusters have been shown to catalyse CO oxidation [22, 56, 65, 85, 99, 100, 154, 232], epoxidation [233, 234], alcohol oxidation [76, 103, 235, 236], C-C bond formation [237], and dye degradation [26], as well as other chemical reactions [238-241]. Among these, CO oxidation (production of CO_2) is the most well-studied reaction [100].

The catalytic activity for CO oxidation by Au clusters supported on MgO has been largely studied, and insight has been provided into its size-dependent catalysis for clusters sized Au_1 to Au_{20} [56, 58, 177, 242]. One study by Sanchez *et al.* [56] used a temperature programmed reaction (TPR) to probe the catalytic CO oxidation by small monodisperse Au_n clusters supported on defect-rich MgO(100), deposited by soft-landing with a size-selected LaVa CS. For sizes of n < 8 the clusters are inert and do not catalyse the reaction, and Au_8 is the smallest catalytically active cluster. For n > 8, the catalytic yield has irregular fluctuations with n, where the overall trend is an increase in yield with n, with Au_{18} being the most vigorous catalyst in the range of $1 \leq n \leq 20$. Figure 2-8 shows this trend in CO oxidation activity with Au cluster size. With help from first principles calculations they found that partial electron transfer between the Au clusters and the substrate, as well as oxygen-vacancy F-centre defects are vital for the catalytic activation of the Au clusters [56]. An O_2 molecule can adsorb at several sites on the Au cluster, and is activated to a peroxo O_2^* molecular state which features a lengthened, weakened bond of 1.41 – 1.46 Å compared to 1.24 Å for the free molecule [56, 243, 244]. Two mechanisms were then proposed, where either a gas phase CO reacts spontaneously in the vicinity of the adsorbed O_2^*, or both O_2 and CO are initially co-adsorbed for a reaction. Both mechanisms result in a CO_2 molecule bound weakly to the cluster with approximately 0.2 eV [56]. Catalysis by oxide-supported Au clusters has also been studied extensively by computational methods, probing different aspects such as the effects of the metal-oxide layer thickness and the role of defects in catalysis [245].
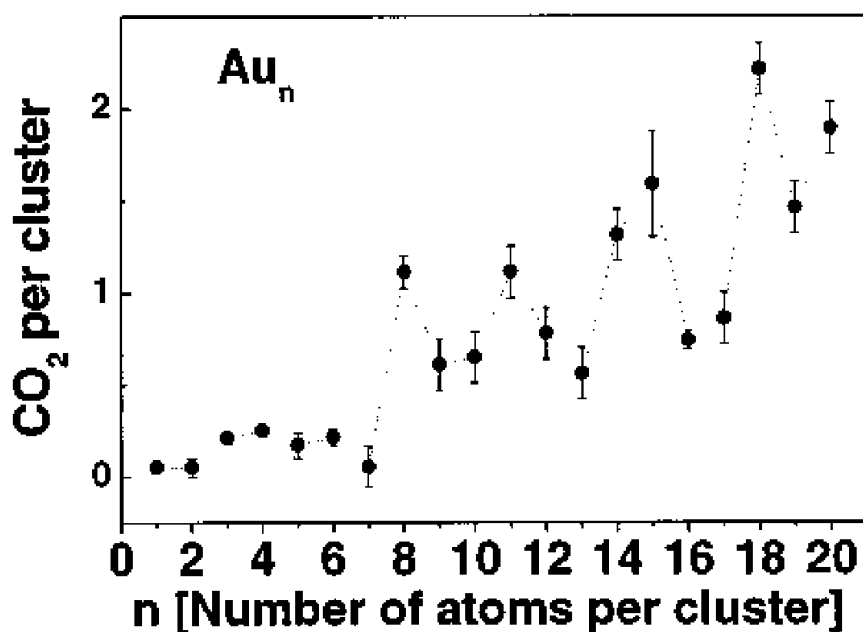
Figure 2-8: Trend in catalytic CO_2 production for Au_n clusters supported on defect-rich MgO(100) [56]. Au_{18} is the most active catalyst in this size range. Reprinted with permission from the Journal of Physical Chemistry A [56].

Tsukuda *et al.* [236] have studied various catalytic reactions with Au clusters. One experiment has looked at aerobic alcohol oxidation catalysed by $Au_{25}(SC_{12}H_{25})_{18}$ thiolate clusters supported on porous carbon nanosheets, after heating to 673-773 K under vacuum for ligand removal. They found that the selectivity for the formation of benzaldehyde was improved with more residual ligands present on the clusters, however this caused the activity to decrease. This was attributed the thiolates functioning in two different ways. Firstly, the thiolates reduce the ability of the Au clusters to oxidise due to electron withdrawal. Extended X-ray absorption fine structure (EXAFS) results supported this by suggesting the cluster cores were more positive when residual ligands were present. Secondly, the thiolates sterically inhibited esterification on the cluster surface due to site isolation. Clusters which were still fully covered by ligands were inert due to complete site blocking by the ligands [236]. In a separate study, they looked at the effect of cluster size on catalytic activity for cyclohexane oxidation by Au_n supported on hydroxyapatite (HAP), an inert support material [246, 247]. The products of this reaction are important intermediates for producing nylon-6 and nylon-66 in industry. All tested cluster sizes (n = 10, 18, 25, 39, and ~85) catalytically converted cyclohexane into cyclohexanol and cyclohexanone, and the catalytic activity followed a volcano-like trend with cluster size which peaked at Au_{39}. The involvement of the Au clusters in this complex oxidation process remain unclear, and this size dependence could not be explained using geometric factors such as cluster SA or the number of low-coordination sites. The authors postulated that the high catalytic activity of Au_{39} may have

26

been due to its unique electronic structure [246, 247].

Studies on Au clusters have been used to provide evidence for the effect of fluxionality on catalysis. The role of fluxionality in Au cluster catalysis has been researched via both calculations and experimental measurements. DFT calculations have shown two isomers of Au_8 supported on MgO(100) which are catalytically different [58, 248]. In a calculation probing the catalytic oxidation of CO by Au_8, O_2 was found to adsorb at the interface between bilayer Au_8 clusters and the support, and after the interaction the clusters changed in structure dramatically. This is important as it was shown that the clusters maintaining their structure would block the adsorption and activation of O_2 [58]. Multiple unique cluster isomers of this nature have been experimentally observed using HAADF-STEM, including Au_9 on TiO_2 nanosheets which is shown in Figure 2-1 [66], as well as ligand-stabilised Au_{38} on Cu grids coated in a film of amorphous carbon [63]. It may be that a cluster can change its isomeric structure during a reaction such that it allows the reaction to occur through an energetically favourable pathway [177]. It has been proposed that an adsorbed molecule could undergo a series of transition states which are favoured energetically and stabilised by the cluster, thereby greatly reducing the reaction activation barrier [13].

Ru clusters are also well-studied for their catalytic abilities. Supported Ru clusters have been shown to catalyse the gas phase hydrogenation of ethylene [249], CO_2, and CO [43, 132, 250, 251], the dissociation of N_2 [27, 252], the dissociation of NH_3 [27, 29], and the oxidation of graphitic carbon into CO [167]. In fact, for CO and CO_2 hydrogenation supported Ru catalysts are among the most active catalysts [43]. For CO_2 hydrogenation, the first step is the dissociation of CO_2 to CO. After this, both CO_2 and CO hydrogenation proceed with the same mechanism, where CO is dissociated to give a highly active carbon surface species which hydrogenates rapidly to methane [43, 46].

While this review focuses on supported clusters, it should also be noted that research has been performed studying cluster catalysis in the gas phase as well as catalysis in solution. These are not covered here in detail as they are outside the scope of this review but are described briefly. In the gas phase, catalysis can be studied by methods such as creating mass-filtered clusters with a gas-aggregation CS and introducing them into an octupole ion trap, where defined amounts of reactants can be introduced. In this arrangement all reactants, intermediates, and products can be analysed with a mass spectrometer following the reaction [253-257]. Such experiments are useful for probing the properties of clusters in the gas phase but are not applicable to industrial heterogeneous catalysis. It also must be

noted that in this type of experiment the contribution of the support to the catalytic activity is missing. For the case of clusters in solution, experiments have been performed on using non-supported ligand-stabilised clusters as homogenous catalysts. For example, recent studies have reported the use of $[Fe_4N(CO)_{12}]^-$ and $[Fe_4N(CO)_{11}PPh_3]^-$ clusters in solution as highly selective homogeneous catalysts for C-H bond formation with CO_2 to produce formate [258-261], an environmentally-relevant reaction for converting excess CO_2 into chemical fuels. This homogeneous catalysis is not unique to Fe clusters, and Ru as well as other clusters have also been used to catalyse reactions in solution [262-265]

2.6.2 Photocatalysis

The photocatalytic abilities of metal clusters have been less well studied than their catalytic abilities and are still relatively unexplored. In photocatalysis, a semiconductor absorbs light with an energy larger than the band gap of the semiconductor. The absorbed light generates electron-hole pairs, so called excitons. These charge carriers separate, and the separated charge carriers migrate to the surface of the semiconductor. Those charge carriers which have not recombined can reduce or oxidise molecular species adsorbed to the semiconductor surface. The presence of co-catalysts such as clusters deposited onto the semiconductor surface can promote the conversion rate. This can be through various mechanisms, amongst them promoting the adsorption and desorption of reactants and products, and by providing sites where the photogenerated electrons and holes are stabilised thus reducing their recombination rate. The concept of photocatalysis has been described by multiple reviews which are recommended for further details [266-269].

The improvement of the reactivity and stability of photocatalytic surfaces through supported nanoparticles acting as co-catalysts has been well established [270], while supported cluster-regime co-catalysts have not been commonly reported. Photocatalytic water splitting is used for hydrogen production and is among the most commonly researched reactions [4, 10, 34, 36, 146, 271]. It is industrially relevant because H_2 is a clean alternative to fossil fuels. A 1983 study by Yesodharan and Grätzel demonstrated that titania-supported Ru and Rh carbonyl clusters improve the photocatalytic splitting of water [272], legitimising the concept of clusters as co-catalysts.

In a recent 2015 study by Negishi *et al.* [10] gold glutathione $Au_n(SG)_m$ clusters of sizes n = 10-39 were deposited onto a photocatalytic $BaLa_4Ti_4O_{15}$ substrate, with the ligands being removed by heating under vacuum. They compared the photocatalytic water splitting to both the bare photocatalyst and to large 10-20 nm Au nanoparticle cocatalysts and found the

small Au_n clusters had an improved activity when highly stable sizes were used. Cocatalysts using $Au_{25}(SG)_{18}$ as a precursor featured an activity 2.6 times greater than that of nanoparticulate cocatalysts. It was argued that in this case the improved photocatalytic activity was due to the ultra-miniaturisation of the cocatalyst, and that the smaller clusters in fact had less activity per surface atom than Au nanoparticles, but this was overcome by the increase in the number of surface atoms [10]. Thus, in this case the effect from increasing the number of surface atoms for clusters outweighed any effects from the change in physical or electronic structure compared to nanoparticles. Another interesting finding was that when ligands were not removed, $Au_{25}(SG)_{18}$ clusters still increased the photocatalytic activity of $BaLa_4Ti_4O_{15}$, meaning charge transfer from the Au to the support was still possible. However, the increase in photocatalytic activity was only 23% of the amount compared to the deligated cocatalyst. Thus either the electron transfer efficiency or the Au cluster catalytic performance was decreased [10]. This phenomenon has also been previously reported for other $Au_n(SG)_m$ clusters [189, 273-275].

Back-reactions can negatively affect the efficiency of photocatalytical processes by removing the desired products which have been produced [276, 277]. Thus, research has been performed on reducing the occurrence of these back-reactions. Negishi *et al.* [4] have further refined the Au cluster photocatalytic process by developing a new method for forming a Cr_2O_3 shell on $BaLa_4Ti_4O_{15}$-supported Au_{25}. This work follows on from previous work by Domen and co-workers, which demonstrated the suppression of contact between the cocatalyst and O_2 for the case of larger nanoparticles [278-281]. The Cr_2O_3 was first loaded onto the $BaLa_4Ti_4O_{15}$ photocatalyst by photodeposition in an aqueous K_2CrO_4 solution, and $Au_{25}(SG)_{18}$ was adsorbed after. The Cr_2O_3 forms a shell which serves to enhance the photocatalytic water-splitting by supressing the reverse O_2 photoreduction reaction, because the Cr_2O_3 shell is permeable to H^+ but impermeable to O_2 [4, 282]. This suppression of the back reaction improved the water-splitting activity by approximately 19 times compared to the same system without the Cr_2O_3 shell. In addition to improving activity, it was shown using EXAFS that the Cr_2O_3 also stabilised the Au_{25} on the surface by supressing aggregation during light irradiation. Because the Au_{25} was embedded in the shell it does not move readily on the surface, and only a small particle size increase was found after 10 hours of the water-splitting reaction [4].

2.7 Characterisation and Electronic Structure Measurements

There are many characterisation techniques which can be used in elucidating information

about supported metal clusters. Each provides unique information, and they are often complimentary to one another. In this section, a number of the main characterisation techniques for clusters are described, and particular emphasis was placed on the applications of the techniques to supported metal clusters as well as specific examples of use. These techniques are divided into; electron spectroscopy, ion scattering spectroscopy (ISS), temperature programmed desorption/reaction, and microscopy. A number of the characterisation techniques were used in the experimental methodologies of this thesis (refer to section 3.6 in the Instrumentation and Methodologies chapter for more details). However, this section also reviews a larger range of techniques which have been used successfully in literature.

2.7.1 Electron Spectroscopy

Electron spectroscopy is a vital technique for the analysis of metal clusters, and commonly used techniques are XPS and UPS. MIES is a less used yet powerful electron spectroscopy technique. X-ray absorption spectroscopy (XAS) is another different type of spectroscopy useful in cluster analysis which is split into two energy ranges: X-ray Absorption Near-Edge Structure (XANES), which is also called Near-edge X-ray Absorption Fine Structure (NEXAFS), and EXAFS, where EXAFS focuses on higher KEs.

2.7.1.1 XPS

XPS is one of the most used electron spectroscopy techniques [66, 72, 73, 102-104], which measures the binding energy (BE) of core-level electrons. This works by utilising the photoelectric effect due to incident X-ray photons; electrons are ejected from the surface and their KEs are measured and converted into BE. These BEs are unique to each element, and XPS can determine quantitative elemental concentrations as well as chemical information about a surface. Chemical information such as oxidation states of surface species can be determined because the BE depends on the chemical state of the respective atoms [283]. Due to the finite inelastic electron mean free path the information depth of XPS is typically around 5 nanometres. Thus the information in a XPS experiment is related to the top several nanometres rather than purely the outermost layer [284]. Two reviews of XPS by Seah are available for a deeper analysis of the technique [285, 286].

For metal cluster modified surfaces XPS is useful for quantitatively determining their elemental composition, determining whether deposited species are in the cluster or bulk regime, and following the removal of ligands. BEs have been found to shift for some clusters when compared to the BE of a bulk sample. As an example, for ligand-stabilised Au clusters

BE shifts of between +0.8 and +1.4 eV compared to bulk Au have been reported for the Au $4f_{7/2}$ peak [66, 72, 73, 102]. Based on this, the Au peak position has been used to relate the XPS BE to the size of a cluster [73, 98, 102, 287, 288]. Attached ligands also influence the BE, and ligand removal can result in a positive or negative BE shift depending on whether the ligands are electron donors or acceptors. In Au-PPh$_3$ clusters the ligands are electron donors, and removal results in a positive BE shift; for example $[Au_6(PPh_3)_6][BF_4]_2$ on TiO_2 was reported to shift by +0.4 eV upon removal of the PPh$_3$ ligands [73, 98]. Alternatively, for $Ru_3(CO)_{12}$ on TiO_2 there is a negative shift in the Ru $3d_{5/2}$ peak associated with the removal of ligands, with a -0.6 eV shift for partially deligated clusters and a total -1.3 eV shift for fully deligated but agglomerated clusters [75].

Shifts in BE can occur due to initial and final state effects which depend on the cluster size and metal forming the cluster, as well as the substrate-cluster interaction [73, 102, 230, 289]. The initial state effects are related to the energy of the electron orbital relative to the vacuum level. For example, the positive BE shifting for an oxidised metal compared to an elemental metal is an initial state effect, because the metal donates charge to the oxygen which reduces the screening of the nucleus, reduces the core state energy, and increases the electron BE. These shifts in BE can be in the order of several electron volts. Final state effects are changes in BE related to the difference in the sample after an electron is ejected. After an electron is removed its vacancy will be stabilised by the chemical environment, but whether the relaxation occurs before or after the photoelectron has escaped and fully decoupled from the system will affect the BE. If a single atom is bound to a surface the result will be a localised hole where the atom cannot easily relax electronically, but for a metal cluster the hole produced can be delocalised across the atoms in the cluster which will lower the energy in the final state and lower the electron BE [60]. By the same mechanism, a bulk sample will have a lower BE energy again due to a greater ability to electronically relax after ionisation. The shift in BE of the Au $4f_{7/2}$ peak for clusters compared to bulk has been attributed to final state effects [66]. Initial and final state effects are difficult to deconvolute from one another but work has shown that for certain systems this can be done, mainly using Auger electron spectroscopy [290, 291]. The problem of separating initial and final state effects has also been approached theoretically using DFT calculations [289].

### 2.7.1.2 Valence Electron Spectroscopies: UPS and MIES

The measurement of the electronic DOS is important for clusters as it gives information on their valence electronic structure and can show whether materials are behaving like clusters or more typical bulk metals. The electronic structure of a cluster also plays an import role in

its catalysis, and this information is crucial for the design of effective catalysts [292]. Furthermore, comparisons between measured and calculated DOS are key to determining whether current theoretical models for how the clusters are structured are accurate.

UPS is a common way to measure the DOS for catalysts such as metal clusters [6, 60, 71, 161, 166]. UPS works based on the photoelectric effect similarly to XPS, however ultraviolet photons are used in place of X-ray photons. UPS measures the BE of outer valence electrons which are not as strongly bound to the nucleus as the inner core electrons, and can be used to measure the electronic properties of a solid surface such as the occupied valence DOS and work function [293]. UPS features an information depth of approximately 2-3 nm [284]. Two reviews of UPS are referenced for a deeper analysis of the technique [294, 295].

UPS can also be used to follow changes in the DOS when modifying the clusters or surface. A trend has been found for the d-band shape of UP spectra to become more narrow and triangular for clusters when compared to a bulk sample of the same metal, such as in a study comparing mass-selected Ag_{55} to larger clusters [71], as well as further experiments [24] and calculations [296]. One study measured UP spectra of titania-supported Pd_n clusters of various sizes between n = 1 and n = 25 [6]. The authors found that the DOS in the titania band gap was decreased when CO was adsorbed to the clusters, while O_2 adsorption did not decrease the density. These UP spectra are shown in Figure 2-9 for Pd_{20}. This was an unexpected result because oxygen is more electronegative. This means that the positive charge on the clusters should be greater when oxygen is adsorbed than CO, and the electrons should have greater BEs. However combining these experimental measurements with DFT calculations they found that there is final state stabilisation when an O atom is bound to the top of the clusters, which restores the DOS in the band gap and accounts for this opposition to the simplified picture considering electronegativity [6].
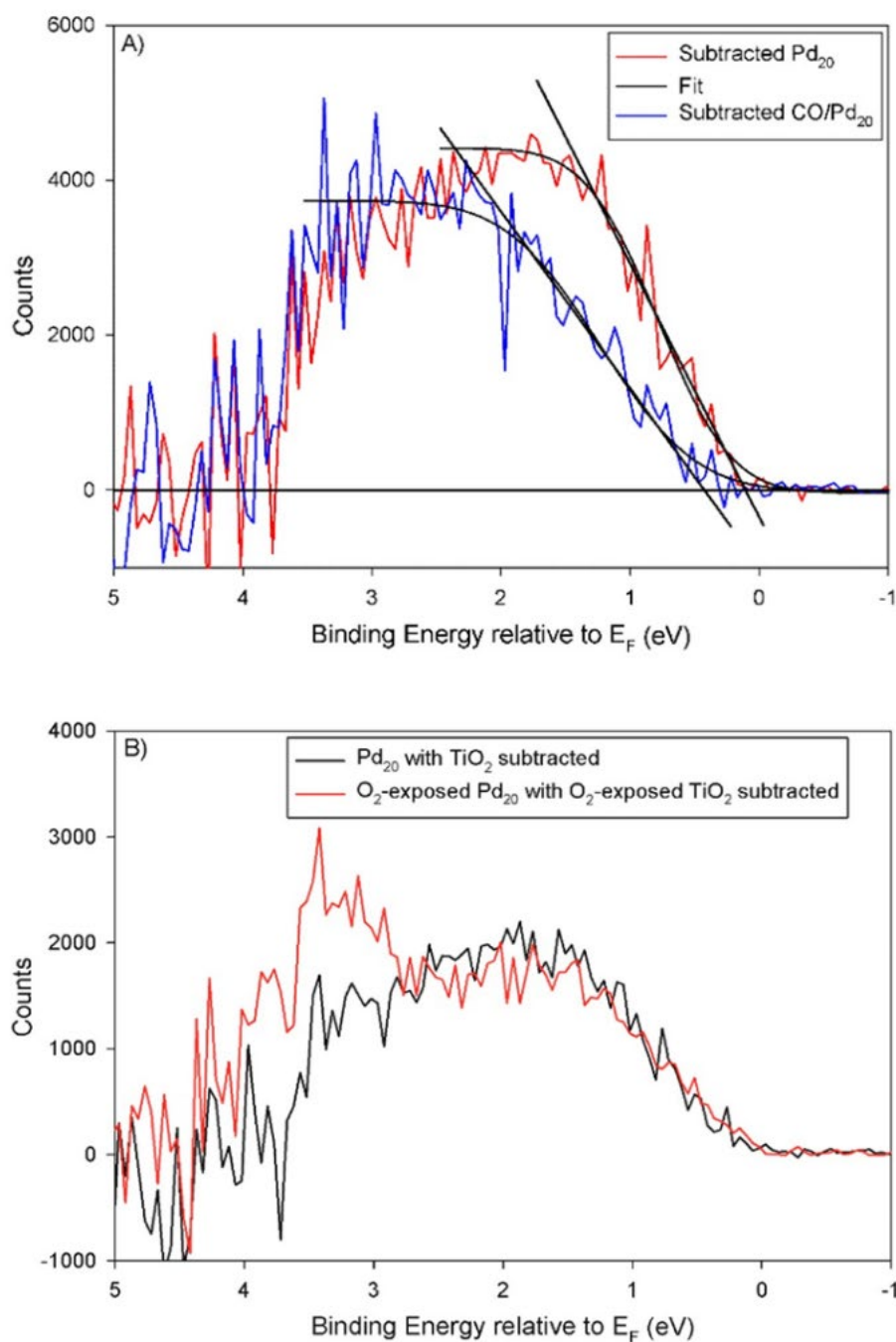
Figure 2-9: A) UP spectra for Pd$_{20}$ on TiO$_2$ before (red) and after (blue) CO exposure. The contribution from the support has been subtracted. Tangent lines in the fits estimate the onset energy. B) UP spectra for Pd$_{20}$ on TiO$_2$ with (red) and without (black) 10 L O$_2$ dose. The contribution from the support has been subtracted, and for the dosed sample O$_2$-dosed TiO$_2$ was subtracted. Adapted from [6]. Reprinted with permission from the Journal of Physical Chemistry C [6].

MIES measures the valence electronic structure of the surface, also allowing the measurement of DOS and work functions [297]. However, rather than irradiating the sample with photons like UPS, metastable helium atoms (He*) are used. The He* which feature an excitation energy of 19.8 eV are directed to the surface, and a de-excitation or neutralisation process occurs, resulting in the emission of an electron. The result of a He* probing the

surface is like that of XPS and UPS: electrons are ejected from the surface and their KEs are measured.

The major advantage of MIES over other techniques is that it is purely surface sensitive (XP and UP spectra are averages over the information depth of the respective methods). He* reaches the surface with low, thermal energy and de-excitation occurs at a distance of a few angstroms from the surface. The He* therefore cannot penetrate into the bulk of the sample. This gives MIES a distinct advantage when accurate measurements of surface properties are required, because the data from MIES is purely based on the topmost layer of atoms in the material [104, 297]. This is beneficial for cases such as supported clusters which reside only on the surface. A disadvantage of MIES is that more than one electron de-excitation mechanism is possible, which makes data analysis more complicated. For ordinary metals and small band gap semiconductors, metastable atoms deexcite through resonance ionisation (RI) followed by Auger neutralisation (AN), while for larger band gap semiconductors and molecular materials Auger de-excitation (AD) occurs [297]. The AD process is more directly comparable to UPS results, while RI+AN has broadened features which are less easy to interpret and relate to the electronic DOS, so in general MIES is more useful for insulators. A detailed article on surface characterisation using MIES is available from Morgner [298].

While MIES is a powerful tool for cluster analysis due to its surface sensitivity, it is reported less often in the literature than the more common UPS. However, several publications exist using MIES to probe surface supported clusters. One study by Andersson *et al.* [104] has deposited $Au_9(PPh_3)_8(NO_3)_3$ clusters onto ALD titania and silica using solution-based deposition and removed the ligands by heating. Results were compared between the two substrates using both MIES and synchrotron XPS [104]. They found that on the titania when heating the PPh_3 ligands react with the oxygen in the titania and bond to the surface, and that this only occurs when the Au clusters are present (not for straight PPh_3). For depositions from cluster solutions of 0.02 mM to 0.75 mM they achieved small, non-agglomerated Au clusters, whereas at higher loadings they only found agglomerated clusters. Singular value decomposition was used to separate the measured MIE spectra into reference spectra corresponding to the substrate, the ligands bound to the surface, and small Au clusters interacting with the surface, which they could directly compare to previous UPS measurements. On silica substrates they only found agglomerated clusters and could not elucidate a MIE spectrum for the Au clusters, and there was also no interaction between the ligands and silica [104].

Andersson *et al.* [5] in a later study deposited the same Au_9 clusters on defect-rich sputtered ALD titania, which strongly reduced cluster agglomeration due to the surface defects. Using an SVD calculation they found two reference spectra in their MIES measurement. One spectrum can be assigned to the substrate and one to the presence of Au clusters bound to the surface. The Au_9 DOS measured by MIES was comparable to those calculated using DFT [5]. These MIES measurements are shown in Figure 2-10; A shows the measured MIE spectra for ligand-removed Au_9 on TiO_2, while B shows the 2 calculated reference spectra. This demonstrates a MIE spectrum for supported clusters being determined by using a range of spectra with varying cluster surface concentrations. In yet another study, they deposited Au_{13} from $(Au_{13}(dppe)_5Cl2)Cl_3$ (dppe = 1,2-bis(diphenylphosphino)ethane) onto similarly sputtered ALD titania using a similar deposition process. Using MIES it was found that the DOS for the reference spectrum associated with the Au_{13} clusters shifted by 0.1 eV closer to the Fermi level than for Au_9 [3].
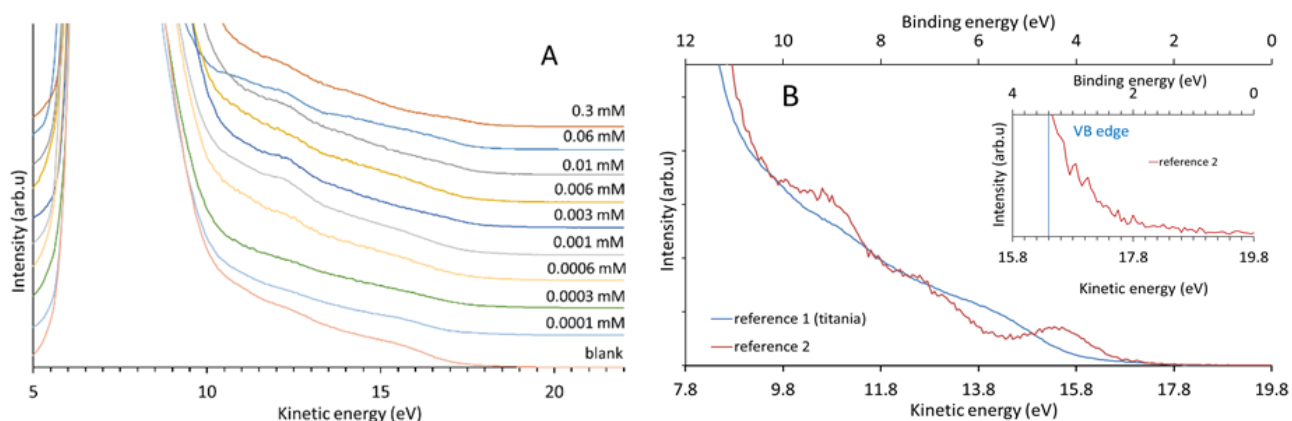
Figure 2-10: A) MIE spectra of Au₉ on ALD TiO₂ with varied concentrations, after heating to remove ligands; B) calculated reference spectra after heating. Reference 1 is attributed to the substrate and reference 2 is attributed to the Au clusters, potentially as well as ligands which have attached to the surface [5]. The inset shows the valence band edge region more closely for reference 2. Adapted from [5]. Reprinted with permission from the Journal of Physical Chemistry C [5].

2.7.1.3 X-ray Absorption Spectroscopy: XANES and EXAFS

XAS is elementally specific and provides information on the electronic structure and local geometry (coordination environment) of matter. This technique measures the absorption of incident X-rays onto the sample as a function of energy, which correspond to core electron excitations to an unoccupied state below the ionisation threshold, or more often excitation to the continuum above this threshold [299]. The spectra feature a sudden increase in absorption while scanning through the X-ray energy range corresponding to X-ray absorption by a specific core electron type (*e.g.* 1s), which is called the absorption edge. The shape of the adsorption edge allows determining bond length to the next neighbours

surrounding the element causing the absorption edge. Typically, synchrotron radiation is used, and the technique can be divided into two regions: XANES, and EXAFS. XANES refers to the structure found within 50 eV of the absorption edge, and the region above this extending to 1000 eV or more above the edge is referred to as EXAFS [300]. The EXAFS region has an oscillatory structure due to interference between ejected and backscattered photoelectron waves. A thorough review on high resolution XAS is available from F. De Groot [301].

In the field of nanocatalysts XAS is commonly used to elucidate information on the atomic structure of catalysts and their adsorbates. A series of EXAFS studies has been performed probing the adsorption of CO onto Ru clusters prepared from heating $Ru_3(CO)_{12}$ deposited onto a variety of substrates. It was found in EXAFS that the adsorption of CO onto Ru supported on Al_2O_3 or MgO resulted in the Ru-Ru bonds being disrupted, and new species being formed with the Ru bound to a surface oxygen as well as CO molecules, but not to other Ru atoms. However, upon heating to remove the CO the original Ru-Ru bonds were reformed [133, 134, 302, 303]. When depositing the clusters onto SiO_2 or TiO_2, there was no evidence that the Ru-Ru bonds were broken upon dosing with CO. The particle sizes were larger for these substrates, so it was suspected that this difference may be related to cluster structure and size differences resulting from different surface interactions [134]. This same disruption of metal-metal bonds had also been previously found by a different research group using EXAFS for small, Al_2O_3-supported Rh clusters when dosed with CO [304, 305].

Grazing-incidence XANES has been used to compare the structure and valence states of Cu_5 and Cu_{20} clusters to that of bulk Cu [7]. By comparing the XANES measurements from the clusters to a range of bulk Cu standards with differing valence states including Cu foil, Cu_2O, CuO, and $Cu(OH)_2$, linear combinations of the bulk measurements could be used to determine the average valence states of the two clusters; 2 for Cu_5 and 1.85 for Cu_{20} [7]. This is shown in Figure 2-11. Recent developments in near-ambient-pressure XANES allow absorption experiments to measure before, during, and after catalysis, and this real-time data allows a more precise elucidation of catalytic mechanisms [306]. One study has utilised this development to follow the structure of Pt nanoparticle catalysts as they sinter and redisperse (which is a harmful problem reducing the catalytic ability of the Pt) while catalysing high-temperature reactions relevant to automotive catalytic conversion [307]. This allowed for determining a mechanistic model for the process; by combining their results with *in situ* transmission electron microscopy (TEM) they found the most likely mechanism for sintering/redispersion was the dissociation of molecular or atomic species from the Pt

crystallites, and subsequent capture of these by the support (redispersion) or other Pt particles (sintering) [307].
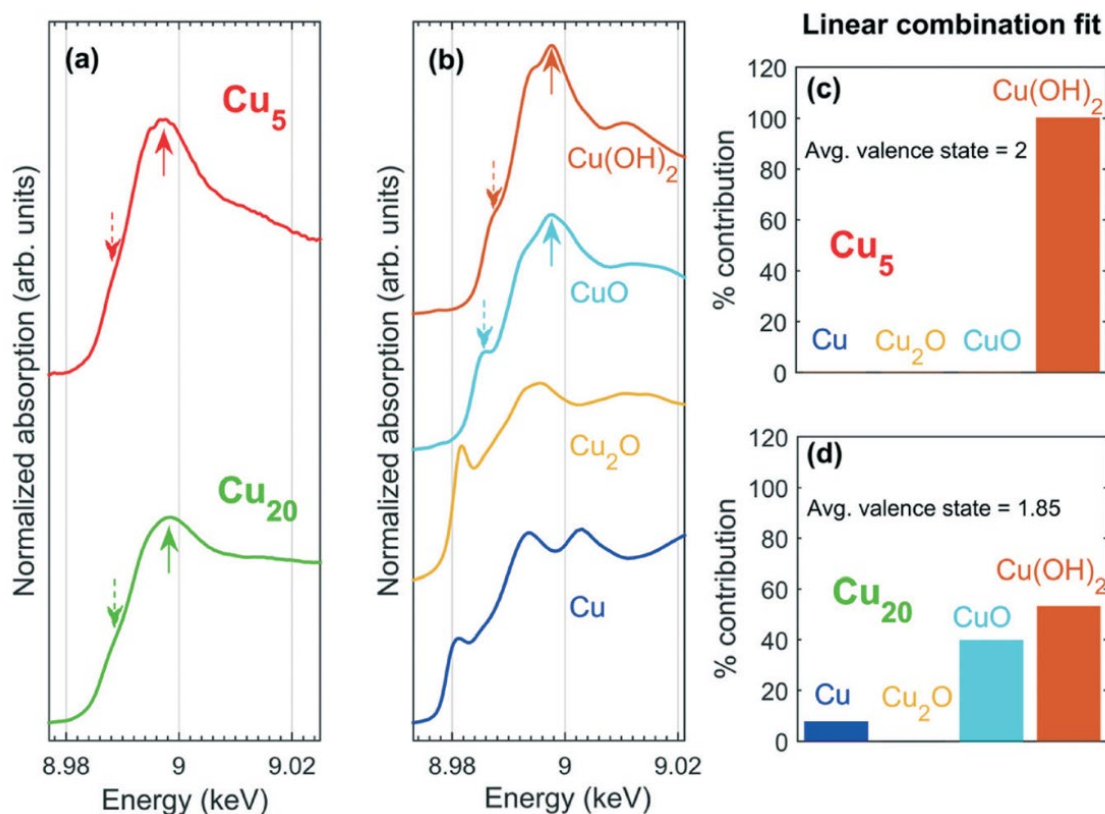
Figure 2-11: a) XANES spectra of Cu₅ and Cu₂₀ supported on ultrananocrystalline diamond after exposure to air; b) spectra of bulk Cu standards: Cu foil, Cu₂O, CuO and Cu(OH)₂; c and d) linear combination analysis for Cu₅ and Cu₂₀ respectively, showing the individual component fractions and the calculated average valence states [7]. Reprinted with permission from Catalysis Science & Technology [7].

2.7.2 Ion Scattering Spectroscopy

ISS is a class of spectroscopy in which a surface is bombarded with ions of known energy, and the energies of backscattering ions and/or neutrals are measured (depending on the technique). For surface-supported clusters one of the most commonly used variants [6, 9, 57, 60, 208, 308-326] is low energy ion scattering (LEIS, also simply referred to as ISS). This is a variant of Rutherford backscattering spectrometry (RBS) which bombards the surface with low energy, 0.5 to 10 keV ions (He⁺, Ne⁺, or Ar⁺) and measures only backscattered ions. High energy ion scattering has also been less commonly used for cluster research [185]. The strength of LEIS for cluster research lies in its sensitivity to the topmost layer of the surface. The low energy range of the ions in addition to the detection of backscattered ions allows for the measurement of the atomic composition of the topmost atomic layer, and provides depth information about the atomic distribution in the region 0-10 nm below the surface layer (depending on the ion energy used) [327]. Two review articles

37

have been written by Brongersma *et al.* [327, 328], further describing the LEIS technique.

A change in the number of surface-layer atoms present results in a change in LEIS peak height for that element. LEIS can therefore be used to give information about the structure of supported clusters; one such example of this is determining the number of layers present in the clusters [315, 318]. For example, Anderson *et al.* [315] used LEIS on Pd_n clusters (2 ≤ n ≤ 25) supported on alumina, and found that the Pd_n clusters changed from single to multi-layer at sizes larger than n = 5. Both cluster agglomeration as well as the complete encapsulation of clusters by metal oxide substrate materials have been supported using LEIS in a similar way, where the encapsulation results in the complete loss of the metal surface peak [208, 308, 319]. For example, Ovari *et al.* [308] showed that Rh clusters were agglomerated on TiO_2(110) between 500 K and 700 K, but were completely encapsulated by the substrate after heating to 900 K. LEIS has also been used to show the absorption gas molecules to clusters and provide information about their binding locations, which is useful for probing catalytic reactions [314, 315]. Lastly, LEIS has been used for a number of studies on bimetallic clusters, and has provided structural information about the arrangement of the different metal atoms in the bimetallic clusters on supporting surfaces [316, 320-326].

2.7.3 Temperature Programmed Desorption/Reaction

TPD is a useful technique for probing the chemistry of surface-supported clusters. In brief, gasses are dosed onto supported clusters at a reduced temperature, and the temperature is then ramped while monitoring the desorbing gasses [329]. This gives information about the binding sites for adsorbed gasses on the clusters, and when multiple TPD cycles are performed in series information is gained about cluster thermal stability. An extension of TPD is TPR; this is where one or more reactive gasses are dosed onto the sample, and several different products may be desorbed simultaneously. TPR can give kinetic data and insight into reaction mechanisms [329]. A thorough review on the use of TPD and TPR for catalysts is available by Falconer and Schwarz [329].

A significant amount of work has been done by Anderson *et al.* [6, 57, 292, 309-315, 330, 331] using TPD and TPR, commonly using CO gas to probe bare, CS-deposited metal clusters. While studying small Pt_n cluster on SiO_2, in two separate studies the used CO binding sites on the clusters as a probe to show; the suppression of Pt cluster agglomeration due to heating by alloying the clusters with Sn [311], and the ALD of an overcoat of alumina onto Pt clusters [310]. CO-TPD was used in these cases because CO binds well to Pt but

not to the substrate SiO_2. CO was used in TPR to test the catalytic oxidation of CO for CS-deposited Pt_n/alumina/Rh(0001) [57] and Au_n/TiO_2 [154]. Aside from CO gas dosing, they have performed TPR studying the catalytic ethylene dehydrogenation of small Pt_n clusters on Al_2O_3, observing the size dependence of the catalytic reaction [314] as well as the effect of Sn-modification of the Pt clusters [309].

For ligated clusters which are deposited onto supporting surfaces, TPD can be used to monitor the de-ligation with increasing temperature. This provide insight into the cluster-substrate interaction and be used as a reference for ligand removal temperatures corresponding to a particular cluster/substrate combination. By example, this process has been used to study the de-ligation of $Ru_3(CO)_{12}$ clusters on different substrates and shown that the de-ligation profiles are difference for each substrate, and even for different forms of TiO_2 [74, 75, 332]. This further emphasises the importance of the cluster-support interaction (discussed in section 2.5).

2.7.4 Microscopy

Microscopy is vital to cluster research as it provides a direct visual representation of the morphology and size of supported clusters, and their distribution on a surface. Because the electronic properties are dependent on both the morphology and size, microscopy can probe this dependence. Microscopy techniques generally employed for use with clusters include electron microscopies such as STEM, TEM, and scanning probe microscopies (SPMs) such as STM, and AFM. The imaging technique that will work most effectively depends on and is limited by the substrate being used, the size of the clusters, and the information desired from the measurement.

2.7.4.1 Electron Microscopy

TEM and STEM are techniques commonly applied to clusters [10, 21, 43, 66, 76, 333]. Both techniques direct electrons with a KE of a few tens of keV at the sample which are then transmitted through the sample. The techniques are similar, but the main difference is that STEM uses pre-focussing and rastering of a small electron beam, whereas TEM uses a large electron beam over the sample which is focussed after transmittance [334]. A limitation to these techniques is that not all types of supports can be measured. They both need a flat, thin substrate to function because electrons need to transmit through the surface [334]. Clusters supported on nanoparticulate supports can also be measured with STEM. In addition to this, electron irradiation can transfer energy to the sample which can damage samples, and cause clusters to break or agglomerate [335, 336]. A book and review article

are referenced for more information on TEM and STEM [337, 338].

TEM has been used effectively in the size determination of metal clusters [10, 21, 43, 66], with recent studies being able to identify individual clusters on several different substrates [333]. STEM is responsible for producing remarkable images of metal clusters, and can determine cluster size range and dispersion on the surface at scales of less than a nanometre [76]. For very small cluster sizes, counting particles using conventional TEM and STEM can be difficult as there is poor contrast between the clusters and support [339, 340]. Z-contrast microscopy is a technique which helps with this issue, and it well suited to measurements of high-Z clusters on low-Z supports (where Z is the atomic number) [340]. HAADF-STEM is a Z-contrast microscopy technique which detects electrons differently to conventional STEM, by using an annular detector to detect only very high angle, incoherently scattered electrons. Higher Z elements scatter more electrons at higher angles due to their greater electrostatic interaction with the electron beam, and so higher Z elements receive greater signal [341]. This technique enables imaging of a single metal atom on a surface. HAADF-STEM also has the advantage of using the dependence of scattering intensity on particle diameter to determine nanoparticle shapes from 2D images [339, 342, 343]. Aberration-corrected HAADF-STEM has been used to detect several different morphologies of $Au_9(PPh_3)_8$ clusters on thin TiO_2 nanosheet supports for the first time at an atomic resolution, which is shown in Figure 2-1 [66].

2.7.4.2 Scanning Probe Microscopy

SPM uses a physical probe with a very sharp apex scanning across and interacting with the surface to produce an image. Common SPM types include STM, where a voltage is applied between the tip and sample and the quantum tunnelling current is the measured interaction, and AFM, where the force between the tip and sample is the interaction. Both techniques can be run in constant height mode or constant current/force mode, and AFM has yet another mode called tapping mode where the probe is oscillated, reducing lateral forces on the sample and lessening surface damage [344]. A limitation for these techniques is that they need a very flat substrate, and additionally for STM the substrate also must be conductive, which may mean a desired supporting surface cannot be used. An advantage of SPMs compared to EM is that in principle SPMs can obtain images without effecting the distribution of clusters on the surface, as opposed to the damage that can occur from the electron beam in EM, however this is easier for systems with a strong cluster-surface interaction [345]. SPM instruments can also be used in ambient conditions, as opposed to EM which much be performed under high vacuum. Several reviews on STM and AFM are

referenced for more information on the techniques [346-349].

Both AFM [20, 350] and STM [17, 21, 38, 71, 159, 175] have been used in determining the geometric properties such as size and distribution of supported metal clusters. Both suffer from tip-convolution effects due to the tip curvature, and the lateral resolution is often larger than the size of small clusters resulting in an overestimation of particle width [21]. SPM therefore cannot always resolve individual clusters laterally, however they can provide extremely accurate results for measurements of particle height [21, 72]. Typically the resolution of STM is better than AFM as the tunnelling current utilised in STM is exponentially dependent on sample to probe distance [72, 351]. AFM has been effectively used to characterise the height distribution of $Au_9(PPh_3)_8(NO_3)_3$ clusters on titania, and follow this distribution with agglomeration after heating [72]. It has also been used in demonstrating where particles are located on a surface, such as in demonstrating that clusters preferentially bond to step edges [20]. Using STM, cluster coverage and height has been measured for a variety of cluster/substrate combinations such as Ag_{55} clusters on clean HOPG where 30 clusters per 100 x 100 nm^2 was found to be a low enough coverage to prevent agglomeration at 50 K [71]. This measurement is shown in Figure 2-12. STM has been used to image Ru clusters deposited from both ligand-stabilised clusters [74] and magnetron-sputtered gas-aggregation depositions [21]. STM has also been used to assist in probing the catalytic activity of gas-phase deposited Pt_n clusters of n = 4, 7-10, 15 on TiO_2. It was found that the structure of the clusters changed from single layer to multilayer at n = 8, and at that same size the CO oxidation activity also stopped increasing with cluster size [352, 353].
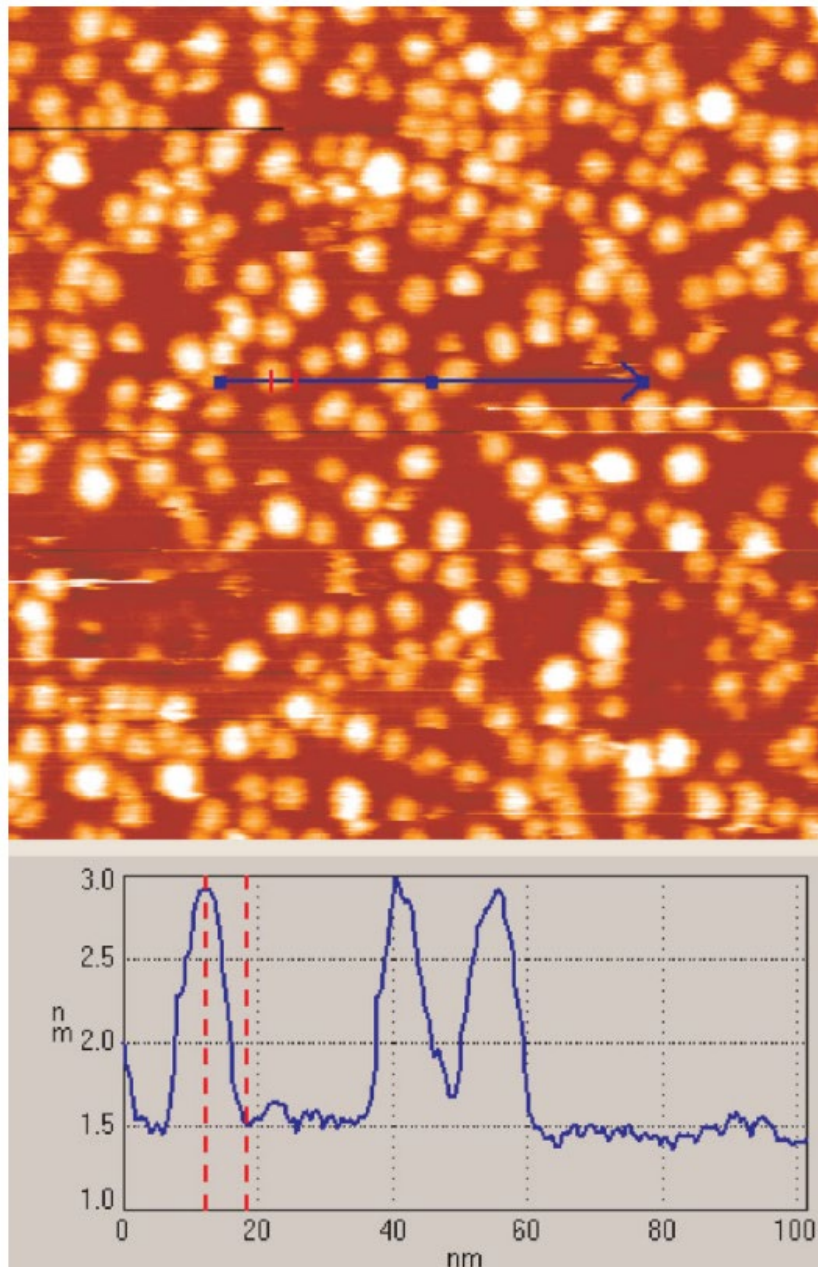
Figure 2-12: 200 x 200 nm² STM image of Ag₅₅ on HOPG covered in 1 ML Xe to fix the clusters to the surface, with a total of 7.5 x 10¹⁰ clusters. The lower image is the line profile for particle height across the line drawn on the STM image, measured at 5 K [71]. Reprinted with permission from Physica Status Solidi B [71].

It is difficult to image supported, isolated clusters with atomic resolution using SPM as the results are effected by tip convolution, as well as interactions between the tip and clusters which can move or pick up clusters in some cases [354]. However, atomic resolution can indeed be obtained using STM. For example, Piednoir *et al.* [355] condensed an atomic vapor beam of Pd onto an MoS_2 substrate, and imaged a 1.5 nm isolated Pd_{27} cluster using STM. Lin *et al.* [356] have performed a similar feat by imaging small Au clusters on thin MgO/Ag(001) films. In this case, Au atoms were evaporated from an Au wire onto the substrate and aggregated into clusters. The authors produced an STM image of an Au

cluster with close-to-atomic resolution, and when this was combined with extensive DFT screening the geometric structure could be determined to be a planar Au_{18} cluster [356]. It should be noted that in both cases the clusters were not size-selected, and the STM images were from surfaces featuring clusters agglomerated into a variety of sizes.

2.8 Conclusion and Outlook

Supported metal clusters have a vast range of potential applications which are still largely untapped. When deposited onto semiconductor substrates they show inspiring catalytic and photocatalytic results when compared to their respective bulk materials. This gives cluster modified semiconductor surfaces the potential for applications in large-scale chemical industry. The electronic and catalytic properties of metal clusters can vary greatly depending on size, morphology, and interaction with the supporting surface, which are focuses for current research. Ligand-stabilised cluster depositions have an advantage over gas-phase aggregated clusters due to the ease of scale-up to industrial scales. However, gas-phase aggregated clusters offer an advantage for fundamental research in that the method is very clean in terms of contamination and no additional steps are required to remove ligands and expose the cluster core. Significant challenges in research on cluster modified surfaces are the prevention of cluster agglomeration, and the measurement of structural and electronic properties for size-selected clusters. An understanding of these properties is necessary as they relate to catalytic ability, and designing an efficient catalyst which fully exploits the unique properties of metal clusters for industrial and other applications relies on a strong fundamental understanding of material properties.

Chapter 3   Instrumentation and Methodologies

The instrumentation and methodologies used throughout this thesis will be described herein. Note that only methods and techniques which were used in more than one experimental chapter are discussed in this chapter, while those used in one chapter only are described within the relevant chapter.

3.1 Substrate Details

The main substrates used were radio frequency (RF)-sputter deposited TiO_2 and Si(100). These substrates came as 10 cm x 10 cm circular wafers. For analysis they were cut into smaller pieces using a diamond cutting tool, while being careful to not contaminate the surfaces.

3.1.1 SiO₂ Substrate

P-type, boron-doped Si (100) wafers were purchased from MTI Corporation and used without further modification. The boron doping makes the wafers conductive and suitable for electron spectroscopy. These substrates are herein referred to as SiO_2; due to the fact that they have an oxidised SiO_2 (silica) surface layer [312], which is the layer the clusters interact with.

3.1.2 RF-TiO₂ Substrate

RF-sputter deposited TiO_2 substrates, shortened herein to RF-TiO_2, were prepared by RF magnetron-sputtering onto an SiO_2 wafer using a 99.9% pure TiO_2 ceramic target. This was using an HHV/Edwards TF500 Sputter Coater at a pressure <2 x 10^{-5} mbar, while using 10 sccm Ar for sputtering the TiO_2 surface. The power was ramped up at 50 W per minute to 500 W, and a shutter was then removed from the target for 50 minutes, allowing the deposition of material onto the rotating wafer. This process was performed in a separate instrument to all other depositions and measurements. The thickness of the RF-TiO_2 was approximately 150 nm, which is thick enough that the SiO_2 wafer beneath would not affect any measured electron spectra. This thickness was estimated based on SEM measurements previously performed on wafers prepared on the same instrument by using a similar method [358]. RF-TiO_2 has been shown to have a nanoparticulate film structure with spherical-shaped grains, where the grain size is 25-45 nm as-made but enlarges upon annealing [357-360].

3.2 Cluster Materials

Clusters were prepared by the deposition of both ligated clusters and bare clusters. The ligated clusters used were based on two ruthenium carbonyl compounds: $Ru_3(CO)_{12}$ and $H_4Ru_4(CO)_{12}$. The structural formulae of $Ru_3(CO)_{12}$ and $H_4Ru_4(CO)_{12}$ are shown in Figure 2-2 in the Literature Review. These were synthesised as powdered samples by collaborators at the University of Canterbury, according to synthesis procedures reported by Eady *et al.* [361] for $Ru_3(CO)_{12}$ and by Bruce *et al.* [362] for $H_4Ru_4(CO)_{12}$. The clusters were used without further modification. Measurements were performed by Siriluck Tesana which confirmed the composition and lack of contamination of the synthesised clusters (see Appendix B). For bare clusters, both Ru_3 and Pt_3 were deposited using a cluster source (CS). The source metals were 99.9% pure metal targets of Ru and Pt respectively, and clusters were prepared by laser vaporisation (LaVa) according to the methods in section 3.5.3.

3.3 UHV Systems

All main surface analysis techniques were performed under UHV. Vacuum chambers with turbomolecular pumps were used to achieve UHV conditions. Individual samples were attached to molybdenum sample mounting plates for loading into the UHV system. Experiments were performed at both Flinders University and The University of Utah; and each had UHV system which was used for sample preparation and analysis. Various deposition and analysis techniques were available on each system, with some such as XPS being available on both. Both UHV systems had ion guns for sample sputtering using Ar^+, as well as procedures to heat and cool samples while monitoring their temperature under UHV. Additional measurements were performed at the Australian Synchrotron; these are unique to Chapter 5 and the methodologies are discussed in that chapter.

In situ analysis of clusters was performed where possible. That is, the cluster samples were analysed in the same instrument that they were deposited in, thus avoiding the need expose the samples to atmosphere. This is the desirable and optimum condition for surface science experiments because it minimises the possibility of surface contamination or modification by contact with the atmosphere. Due to experimental limitations, some measurements were performed *ex situ*, where the clusters were analysed in a different instrument from where the deposition was performed. This is mentioned and discussed where relevant.

3.3.1 Flinders University System

The Flinders University UHV system was used to perform XPS, UPS, MIES, and LEIS. A simplified diagram of the system is shown in Figure 3-1. The main UHV analysis chamber is able to operate at a base pressure of <2 x 10^{-10} mbar and includes electron bombardment heating and Ar^+ sputtering. The electron bombardment heats the sample by applying an 800-1000 V potential between the sample holder and a filament underneath the holder. A current is passed through the filament and electrons are ejected and bombard the back of the sample holder, increasing the temperature of the sample holder and sample itself. Temperatures were monitored using a Type-K thermocouple attached to a metal tab which touched the edge of the sample. Chemical vapor depositions (CVD) of ligated clusters were only performed on this instrument, in the loading chamber (with a base pressure of <8 x 10^{-8} mbar). Substrates were cut to 10 mm x 10 mm for attachment to the sample holders.
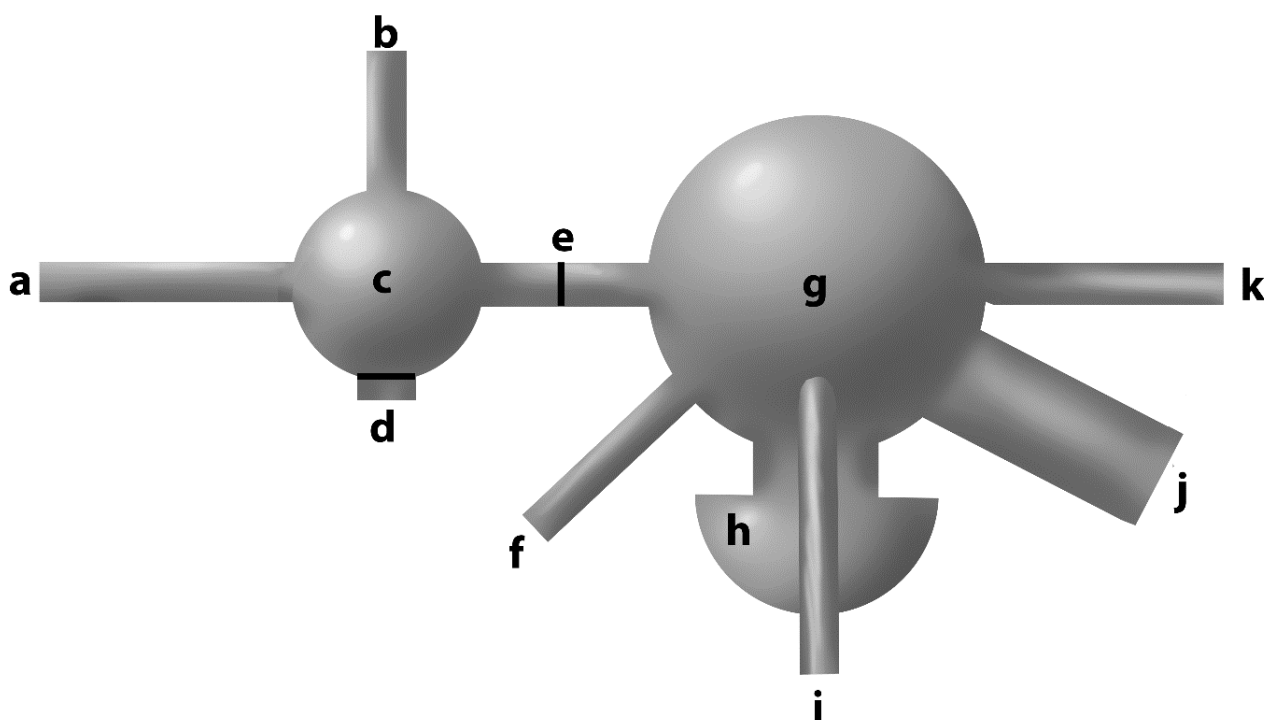
Figure 3-1: Simplified diagram of the Flinders University UHV system, viewed top-down. a) sample manipulator arm, b) CVD rig, c) loading chamber, d) loading chamber door, e) gate valve, f) X-ray source, g) main UHV analysis chamber, h) hemispherical analyser, i) ion gun (He⁺ or Ar⁺), j) metastable He* and UV light source, k) sample stage manipulator. Note that (i) is pointing out of the page, with a 45° angle to (h).

3.3.2 The University of Utah System

The University of Utah UHV system was utilised during a study exchange to Utah, where work was conducted in their laboratory with the assistance of Professor Scott Anderson and two PhD students; Tim Gorey and Guangjing Li. A simplified diagram of the system is shown

in Figure 3-2. A key feature of this UHV system is the LaVa CS; this was used to deposit bare metal clusters onto surfaces under UHV. Details on the CS are given in section 3.5.3. The analytical techniques used on the instrument were XPS, CO-TPD, and LEIS. The main analysis chamber operated at a base pressure of <2 x 10^{-10} mbar and featured an ion gun for Ar^+ sputtering and LEIS. Samples were located in the main analysis chamber when depositing clusters using the CS. The instrument allowed for liquid N_2 cooling by means of piping which touched the sample holder under vacuum, as well as heating by passing a current through a resistive wire element to heat the sample holder and sample. A C-type thermocouple was spot welded to the backing plate of the sample holder to monitor the temperature. The instrument allowed for continuous temperature control and automatic temperature ramping, which were used for TPD. Wafers were cut to 14 mm x 10 mm for attachment to the sample plates.
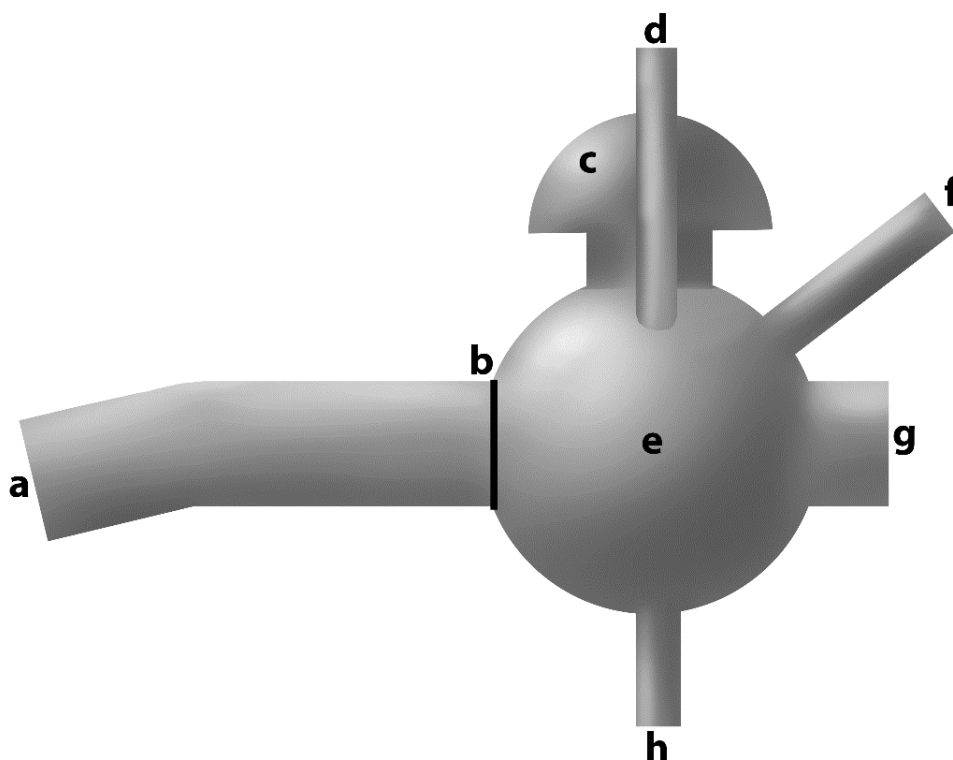
Figure 3-2: Simplified diagram of the University of Utah UHV system, viewed top-down. a) LaVa cluster source with ion bending unit, b) gate valve, c) hemispherical analyser, d) ion gun (He⁺ or Ar⁺), e) main UHV analysis chamber, f) X-ray source, g) quadrupole mass spectrometer. Note that (d) is pointing out of the page, with a 45° angle to (c). There is also a loading chamber below (e), and sample manipulation arm above (e) (not shown in diagram).

3.4 Ar$^+$ Sputtering

In many cases, as part of an experimental procedure substrates were sputtered with Ar$^+$ ions using an ion gun. In a sputtering procedure Ar was leaked into the UHV chamber using a leak valve, where it was ionised, and then accelerated towards the sample using a potential difference. Sputter dosages are given in the units of ions/cm^2. Ar$^+$ dosages per area were determined using the size of the ion beam area, the sputter neutralisation current measured during the sputtering process, and the sputtering time.

On the Flinders University system, the Ar$^+$ ion energy was 3 keV/ion and sputtering was performed by an ion beam which rastered over the entire sample surface continuously. On The University of Utah system, the ion energy was 2 keV/ion, and the entire sample was covered by the sputter beam. Due to the slightly higher Ar$^+$ impact energy at Flinders University, the defects may extend deeper into the bulk for samples prepared on this instrument [185, 186]. This was not corrected for when comparing samples prepared using the different instruments, however it must be noted that the variation in defects on the substrate was not noticeable with the characterisation techniques used and was deemed not to be of critical importance for the experiments.

3.5 Cluster Deposition Methods

3.5.1 Ligated Clusters: Chemical Vapor Deposition

CVD was previously introduced in the Literature Review, section 2.4.1.2. CVD was performed in the loading chamber of the Flinders University UHV system. For each deposition (or series of depositions) a sample vial was loaded with ~2.0 mg of $Ru_3(CO)_{12}$ or $H_4Ru_4(CO)_{12}$. ~2 mL of dichloromethane was added to the vial which was ultrasonicated for 1 minute to ensure the clusters were dissolved. Dichloromethane was chosen as it is a suitable solvent for dissolving both cluster types without causing degradation or agglomeration. The dichloromethane was left to evaporate for ~30 minutes in a fume hood leaving a film of ligated clusters coated on the inside wall of the vial. The outside of the vial was then cleaned with ethanol before being loaded into the vacuum chamber on a manipulator arm which could be positioned such that the vial faced the substrate <1 cm away during depositions. The deposition time was used as a control for the number of clusters deposited; times ranged from 5 minutes to 120 minutes, and specific details are given in the individual experimental chapters. Further details on the designing and building of the CVD setup at Flinders University are given in Appendix A, section 10.1.2.

Due to their high vapor pressures, metal carbonyl clusters only typically require vacuum in the range of 10^{-7} mbar or lower to vaporise at room temperature [80]. From in-house testing, pressures of approximately 4×10^{-6} mbar or lower were found to be suitable for depositions to proceed at a fast enough rate. $Ru_3(CO)_{12}$ depositions were performed with the clusters and substrate at room temperature, however $H_4Ru_4(CO)_{12}$ has a lower vapour pressure and the clusters and substrate were both heated to 353 K to increase the deposition rate. The heating of the substrate was not necessary for increasing the deposition rate but was necessary due to equipment limitations.

3.5.2 Ligated Clusters: Solution Submersion

The deposition of ligated clusters using a solution submersion process is discussed in Literature Review section 2.4.1.2. Here-in, the phrase "solution-deposition", or "SD" will be used for shorthand to refer to the solution submersion process. To perform a deposition a sample was submerged into a cluster solution for 30 minutes. In this case, SD was performed using a solution of $Ru_3(CO)_{12}$ in dichloromethane. The concentration of the solution was used as a method to control the number of clusters deposited (further details are given in the relevant experimental chapters). Due to the nature of the deposition procedure, the substrate was exposed to atmosphere before and after submerging. Due to this, special care was taken to move the samples from the vacuum chamber to the cluster solution and back again quickly, in order to reduce the total time exposed to atmosphere and minimise the extent of atmospheric contamination.

3.5.3 Bare Clusters: Cluster Source

The University of Utah UHV system featured a LaVa CS used which has been described in several previous works [309, 310, 312]. A detailed description of the operation of a CS is available in the Literature Review section 2.4.2. A schematic diagram of the CS is given in Figure 3-3. The clusters were produced under UHV by pulsed LaVa of a 99.9% pure metal target. A Ru target was used to prepare Ru_3 clusters, and a Pt target was used to prepare Pt_3 clusters. The target was set to raster during LaVa to achieve even target ablation. Vaporised target atoms were pulsed into a helium gas flow, immediately followed by supersonic expansion of the metal atoms into the vacuum. A RF quadrupole ion guide was set to collect only positively charged clusters, and the cluster beam was angled by 20° to remove neutral clusters. The beam passed through several differential pumping stages, before reaching a quadrupole mass filter which selected for a specific mass/charge ratio. Because most clusters are singly charged [148, 158] this can be treated as a cluster size selection process where only a single size of cluster is selected for passing through the

quadrupole.

Following size-selection, the clusters passed through an aperture into the main UHV chamber where they were deposited onto a substrate. A 2 mm diameter aperture positioned 1 mm from the surface ensured the cluster spots were ~2 mm in diameter. A positive retarding potential was applied to the substrates during deposition to reduce the impact energy of the clusters, which is critical to prevent cluster fragmentation on impact [157]. The retarding potential was calibrated for soft-landing by determining the minimum potential needed to stop all clusters, and then set to ~1 eV/atom. Previous studies of the deposition of small Ir clusters onto TiO_2 and SiO_2 showed that impact energies in the tens of eV/atom are required to embed the clusters into these substrates (*e.g.* at least 10 eV/atom for small Ir clusters on TiO_2) [331, 363]. Thus, the ~1 eV/atom deposition energy is considered suitable to not cause cluster damage or embedding during depositions of Ru and Pt clusters.

During CS-depositions, samples were liquid N_2 cooled to 180 K, followed by a quick temperature flash to 700 K to remove any adventitious hydrocarbons which may have adsorbed to the sample. After the flash heating the depositions were started at 300 K, and continued as the samples cooled further to 180 K. Clusters were neutralised when deposited due to the conductivity of both the RF-TiO_2 and the SiO_2 substrates. The neutralisation current was measured during each deposition to ensure the amount of deposited cluster material was consistently 1.5×10^{14} atoms/cm^2 (or in terms of clusters, 0.5×10^{14} clusters/cm^2). This nominal value assumes that all clusters which neutralised at the surface also adsorbed onto the surface.
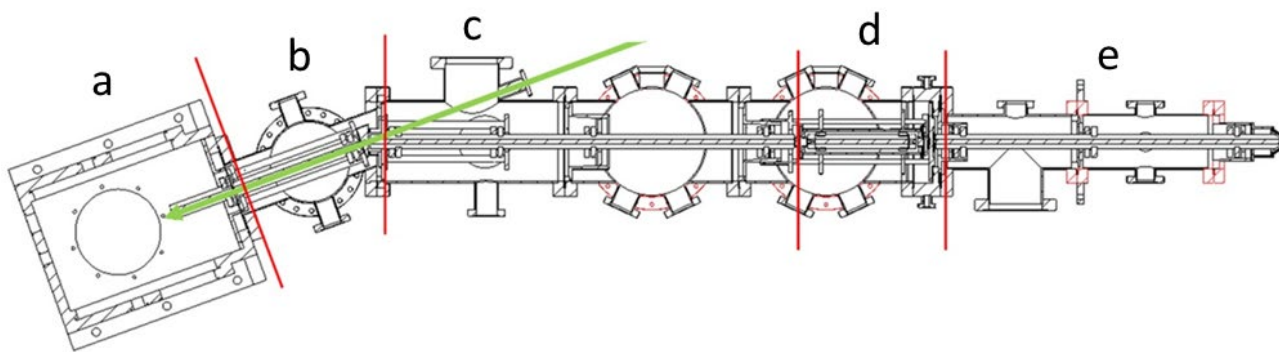
Figure 3-3: Schematic diagram of the UHV laser vaporisation cluster source. The green arrow represents the incoming laser photons. There are multiple quadrupole ion guide chambers featuring vacuum pumps, which serve to reduce the pressure by differential pumping while directing the clusters along the path. The red lines represent the pressure decreasing at each chamber. Describing the chambers from left to right; a) source chamber (contains the metal target, generates clusters), b) quadrupole ion guide and bending lens (collects the clusters, removes neutral and negative particles), c) quadrupole ion guide, d) quadrupole mass filter (selects a single cluster mass to pass through), e) quadrupole ion guide. After the final quadrupole ion guide the clusters enter the analysis chamber (not shown) where a sample is placed for deposition. Image adapted from diagram produced by Anderson, S. [364].

3.6 Analytical Techniques

This section describes the analytical techniques which were used in multiple chapters. For each technique, information will be given on the background, instrument details and settings, and the data analysis procedures used.

3.6.1 XPS

3.6.1.1 XPS: Background

XPS is a spectroscopic technique which gives compositional and chemical information about a surface. Soft X-ray photons are fired at a surface, which excite electrons and can cause those in the core shells to be ejected from the sample as photoelectrons. This process is demonstrated in Figure 3-4. The kinetic energies (KEs) of these ejected electrons are measured and counted by a detector such as a hemispherical analyser (HSA). The binding energy (BE) of the core level electrons can be calculated from the KE using the photoelectric equation, which is a modified version of Einstein's equation [365], shown in Equation 3-1.

$$BE = E_p - KE - \Phi \qquad\qquad 3\text{-}1$$

Where E_p is the energy of the incident X-ray photon, BE is the binding energy of the ejected photoelectrons, and Φ is the work function of the spectrometer (also shown in Figure 3-4).
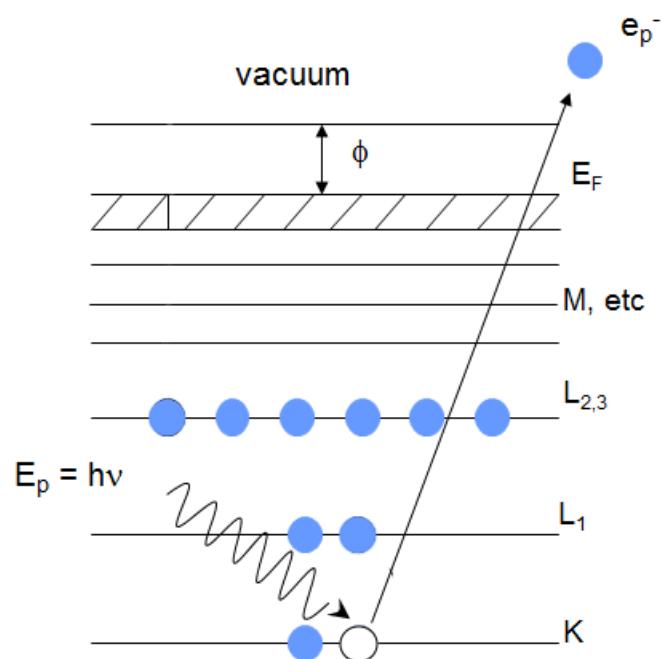
Figure 3-4: Diagram of the photoejection of a core shell electron in XPS. E_p is the incoming photon energy, e_{p^-} is the ejected photoelectron, Φ is the work function of the spectrometer, E_F is the Fermi energy, and K, L, M, *etc.* refer to electron shells. Adapted from Harmer, S. [366].

The data from an XPS measurement are presented as a spectrum of photoelectron BE vs. counts (*i.e.* the number of electrons emitted at that energy). The BEs of core electrons are dependent on the element being measured, so peaks are found at BEs corresponding to specific elements. These peaks are named based on the shell location of the electrons which contribute to that peak; for example, the carbon 1s peak is a result of the photoelectric ejection of a 1s core electron in carbon. Due to this, XPS can be used to determine the elemental composition of a surface by comparison between measured and reference data [367]. Chemical information such as oxidation states or cluster size can also sometimes be determined by slight shifts in BE [283][73]. In XPS the X-ray photons can penetrate into the surface and electrons can escape from a depth of ~5 nm into the sample. This means that the information from XPS is based on the top several nanometres rather than the surface layer alone [284]. This is called the information depth and is based on the electron inelastic mean free path (IMFP), which varies for different samples and photon energies and can be experimentally determined [284].

3.6.1.2 XPS: Instrumentation and Methods

The applications of XPS to supported metal clusters are discussed in the Literature Review section 2.7.1.1. At Flinders University, a non-monochromatic X-ray source with an Mg anode was used for photon generation. This produced Kα radiation with a photon energy of $E_p = 1253.6$ eV [368], at a 54.7° incidence angle to the surface. A Phoibos 100 HSA (SPECS,

Germany) was used to measure the ejected photoelectrons orthogonal to the surface. A pass energy of 40 eV was used to survey the samples, and 10 eV was used for high resolution scans.

At The University of Utah, a non-monochromatic X-ray source with an Al anode was used. This produced Al Kα radiation with photon energy of E_p = 1486.6 eV. The difference between excitation wavelengths on the two systems can change the line shapes of XPS peaks, which is mentioned where relevant. An HSA made by Physical Electronics was used, featuring an area-selective lens with a 1.1 mm diameter analysis area which was optimised to measure cluster spots of 2 mm in diameter without any XPS signal from the surrounding bare substrate. The geometry of the instrument and pass energy settings used were identical to Flinders University.

For each XPS measurement, a survey was typically first performed to identify all elements present on the surface. This is a fast, low resolution scan. Once the regions of interest were identified, high resolution measurements were performed on these regions. For the high resolution measurements each region was scanned multiple times and then averaged to provide greater resolution and reduce the effects of random errors. The number of scans per region required for sufficient resolution varied depending on the particular element and surface concentration. The work functions of the spectrometers were calibrated and set-up for automatic inclusion by the XPS software.

3.6.1.3 XPS: Data Analysis

The program CasaXPS was used to model XPS spectra. Shirley backgrounds were subtracted from each raw spectrum when integrating the fitted peaks; information about Shirley backgrounds can be found in reference [369]. Individual component peaks are added to the spectra and fitted using typically the symmetrical GL(30) line shape, which is a convolution of Gaussian and Lorentzian line shapes. Peaks were then adjusted to fit the experimental data based on peak area, full width half maximum (FWHM) and peak location in BE. The peak area is related to the elemental concentration, while the FWHM is related to the instrument resolution (but can also sometimes be influenced by composition). The BE axis was calibrated to C 1s = 285.0 eV, which is commonly used and accepted. This was chosen in preference to other commonly reported calibration values (such as C 1s = 284.8 eV) in order to remain consistent with the BE calibrations in previous work published by our research group. The uncertainty in reported BEs is ± 0.2 eV, while for comparing BE differences for the same sample before and after a sample treatment the uncertainty is ± 0.1

eV. When modelling an XPS peak, as a constraint each peak added must be justified with a physical meaning, and the least number of reasonable peak components was chosen in each situation when performing data analysis.

All sample surfaces will have some carbon contamination, either from adventitious carbon in atmosphere or present in the sample structure itself. Thus, every XPS spectrum featured C 1s peaks to some extent. Two peaks were always present; these were due to C-C or C-H bonding at 285.0 eV, and C=O or C-O-C bonding at 287.0 eV. A third carbon peak likely due to O=C-O bonding at 289.4 eV was sometimes present but was most often removed by UHV heat treatment and/or sputtering. These results were comparable to previously reported assignments for carbon contamination on SiO_2 substrates [370].

Care was paid when fitting the Ru 3d doublet for clusters, because the 285.0 eV adventitious C 1s peak overlapped with the Ru 3d doublet. There was often partial overlap with the Ru $3d_{5/2}$ peak, while the Ru $3d_{3/2}$ was typically completely covered. To aid with fitting the covered Ru $3d_{3/2}$ peak, a metallic Ru reference metal was analysed with XPS and used as a fitting model for cluster spectra (results shown in section 4.4.2.1). When comparing the $3d_{5/2}$ and $3d_{3/2}$ peaks, the peak separation was 4.17 eV, peak area ratio was 3:2, and FWHM ratio was 1:1.15. For Ru cluster XPS peak fitting, these values were used to lock the size and shape of the $3d_{3/2}$ peak to the $3d_{5/2}$ peak which can be more easily fitted. The reason the FWHM of the Ru $3d_{3/2}$ peak was larger than the $3d_{5/2}$ was due to a Coster-Kronig broadening effect for the $3d_{3/2}$ peak [371, 372].

It is typical for transition metals such as Ru to feature asymmetrical line shapes for the 3d core electrons, and work has been done by Morgan [372] investigating the best way to fit this asymmetry for Ru in different chemical environments. The extent of asymmetry is dependent on the chemical nature of Ru, and the measured asymmetry may also be effected by the resolution of the XPS instrumentation [371-373]. A modified version of the line shape used by Morgan for metallic Ru was used to fit the metallic Ru reference XPS, where Ru $3d_{5/2}$ was LF(0.8,1.3,500,180) and Ru $3d_{3/2}$ was LF(1.15,1.5,500,50). The LF line shape corresponds to a "Lorentzian asymmetric line shape with tail damping" in CasaXPS. To the best of the author's knowledge, there are no published asymmetry results for Ru in cluster form, and thus the line shapes published by Morgan were used as a starting point and were altered to best fit the line shape seen for the Ru clusters on each instrument. These line shape parameters are shown in Table 3-1 below. A special case was made for the as-deposited ligated Ru clusters; these were fitted with symmetrical GL(30) line shapes.

Table 3-1: Line shapes used for fitting Ru 3d peaks from XPS in different scenarios. LF means Lorentzian asymmetric line shapes with tail damping, while GL means a convolution of Gaussian and Lorentzian line shapes.

Measurement	XPS Instrument	Ru 3d$_{5/2}$ line shape	Ru 3d$_{3/2}$ line shape
Metallic Ru reference sample	Flinders University	LF(0.8,1.3,500,180)	LF(1.15,1.5,500,50)
Ru clusters	Flinders University	LF(0.75,1.25,500,250)	LF(0.8,1,500,250)
Ru clusters	The University of Utah	LF(0.7,1.8,25,280)	LF(0.7,1.8,25,280)
As-deposited, Ligated Ru clusters	All	GL(30)	GL(30)

Atomic concentrations in percentage (At%) were determined using XPS by fitting all the peaks and integrating them to determine their area, and then calibrating the areas by dividing them by XPS sensitivity factors found in the Handbook of X-ray Photoelectron Spectroscopy [367]. These were C 1s = 0.296, O 1s = 0.711, Ti 2p = 2.001, Ru 3d = 4.273, and Pt 4f = 5.575. The atomic ratio was determined by dividing the calibrated peak area for each element by the total calibrated peak area for all elements present. This was then multiplied by 100% to determine the At%. The At% represents an average of the atomic concentration over the top several layers of the sample, with the average being weighted towards upper layers for which there are a higher probability of photoelectrons reaching the detector.

The relative resolution for At% varied depending on the size of the peaks, and whether they overlapped with other peaks. For example, a smaller peak which is overlapping a larger peak is not able to be fitted as accurately as the larger peak which dominates the spectrum. Due to this, the relative fitting uncertainty in At% for each peak of interest was estimated by determining the largest range of peak areas which resulted in what was considered to be a reasonable fitting of the measured spectra. The relative uncertainty for At% of deposited cluster peaks was ~4% for both Ru 3d and Pt 4f. For substrate materials, the relative At% uncertainty is ~1% for Ti^{4+} 2p, O 1s, and Si 2p in SiO_2 and RF-TiO_2. The defects in RF-TiO_2 substrates are present as Ti^{3+} and Ti^{2+} 2p peaks (these, when summed, are referred to as Ti^{defects}), and each have a relative uncertainty of ~24%; this is greater than Ti^{4+} 2p because they are located on a shoulder of the larger Ti^{4+} peak. The fitting procedure was kept consistent for all Ti 2p spectra to minimise the relative error, and as such it was estimated

that the relative uncertainty in the $Ti^{defects}$ At% when comparing between the samples was lower at ~15%.

Ratios between the calibrated peak areas for different XPS spectra features are often presented. For $Ti^{defects}/Ti^{Total}$ ratios, the ~15% $Ti^{defects}$ 2p fitting uncertainty was taken to be the dominant uncertainty. When C/Ru ratios are presented, the uncertainty in the fitting of C was considered to be small compared to Ru, and the relative uncertainty was taken as ~4%. In some chapters CO/Ru atomic ratios are discussed, which have a summed uncertainty of ~13%. Due to this fitting uncertainty as well as the CO contaminant baseline subtractions which were necessary, as well as any possible differences between the XPS handbook atomic sensitivity factors and the true factors for the instruments used, the absolute error in CO/Ru atomic ratio for supported clusters was estimated to be ± ~0.5 (where the maximum ratio is 4 for $Ru_3(CO)_{12}$, for example).

The surface coverage of cluster material was estimated for each cluster deposition where XPS was performed. The surface coverages are presented in units of % ML, which is the percentage relative to an entire monolayer (ML) of coverage. This estimation was done using a calculation procedure similar to that used by Eschen *et al.* [374], except for the difference that Eschen *et al.* used multiple XPS detection angles. This calculation solved for the surface concentration required to achieve the measured XPS At% for the cluster metal (Ru or Pt). The clusters were assumed to be present in only a single ML on the surface with negligible stacking of atoms and no mixing of cluster and substrate layers. The bulk interatomic distance for each metal was used to estimate the layer thickness for deposited Ru and Pt clusters, where Ru-Ru is 0.265 nm, and Pt-Pt is 0.278 nm [375]. The contribution of individual atoms to the XPS spectra is reduced as the depth of the atom into the surface increases, which was factored into the calculation by using the IMFP of electrons in TiO_2, 1.8 nm [376]. The IMFP changes with excitation wavelength as well as substrate material, however for consistency this was kept at 1.8 nm for all calculations including those based on measurements using an SiO_2 substrate.

A range of factors contribute to the uncertainty in surface coverage estimations. These include errors in the calculated XPS At% for the clusters, differences between atomic sensitivity factors in our detector setup and in the XPS handbook [367], and any inaccuracy in the IMFP of electrons in the substrate. Inaccuracies in the IMFP could be based on structural differences between the $RF-TiO_2$ used in this study and the reference study for IMFP, differences between the IMFP between $RF-TiO_2$ and SiO_2, and differences in the

exact excitation wavelength used. Based mainly on the uncertainty of the IMFP, the absolute error in surface coverages was assumed to be ~100%. However, the relative error comparing between samples only comes from the cluster At% uncertainty and was ~4%. While the ~100% error can be considered high, the surface coverage estimation was intended to give the scale of the surface coverage of clusters used in the experiments, rather than determining the exact coverage.

3.6.1.4 TD-XPS

In Chapter 5 and Chapter 7 temperature-dependent XPS (TD-XPS) measurements are performed. For TD-XPS measurements, the temperature of a sample is increased in a stepwise manner while XPS is performed at each discrete temperature. This has the ability to yield information about how the surface changes physically or chemically as a result of heat treatment. Samples are held at each temperature for 10 minutes, then the heating is turned off and XPS is performed as the sample slowly cools. XPS instrument settings and procedures were performed as per the standard procedures described above.

3.6.2 UPS and MIES

Although the techniques differ from one another, the results and data analysis of UPS and MIES are similar and for this reason they will be discussed together. Both were used to measure the valence electronic structure of supported cluster systems. MIES has been used by other authors under acronyms including MDS (Metastable De-excitation Spectroscopy), MQS (Metastable Quenching Spectroscopy), and MAES (Metastable Atom Electron Spectroscopy) [298].

3.6.2.1 UPS and MIES: Background

UPS functions in a similar way to XPS. Incident ultraviolet (UV) light causes electrons to be ejected from the sample as photoelectrons due to the photoelectric effect. The key difference is that UPS uses UV light which has a lower excitation energy compared to X-rays. The electrons which are ejected in this process are outer valence electrons, which are not as strongly bound to the nucleus as the inner core electrons. Importantly, valence electrons are responsible for the electronic properties of a material [377]. UPS can be used to measure the electronic properties of a surface such as the occupied density of states (DOS) [293], featuring information depth of ~2-3 nm [284].

Metastable impact electron spectroscopy (MIES) measures surface electronic properties such as DOS [297] in a manner similar to UPS. However, MIES functions in a different way to XPS or UPS. Rather than firing photons at the surface, metastable helium atoms (He*)

with an excitation of 19.8 eV and a lifetime of ~9000 s [297] are used which bombard the surface, resulting in a He* de-excitation or neutralisation process and the emission of an electron. Similar to XPS and UPS, electrons are ejected from the surface and their KEs are measured using an HSA. These are not photoelectrons however, and the ejection process will be described in more detail below. The major advantage of MIES over other techniques is that it is purely surface sensitive, unlike XPS and UPS which have information depths. Thus, MIES is advantageous when accurate measurements of surface properties are needed. He* are not able to exceed the Van der Waals interactions at the surface of the substrate and He* de-excitation occurs at a distance of a few angstroms from the surface, providing true surface sensitivity [297, 298]. UPS and MIES are complementary when used together, where UPS observes the top 2-3 nm of the sample and MIES observes only the top layer.

The mechanism by which an electron is emitted from the surface in MIES is not unique. Electron emissions can occur by two known individual de-excitation pathways; these are resonance ionisation (RI) followed by Auger neutralisation (AN), and Auger de-excitation (AD) [298, 378]. These two pathways are shown in Figure 3-5a and Figure 3-5b respectively.
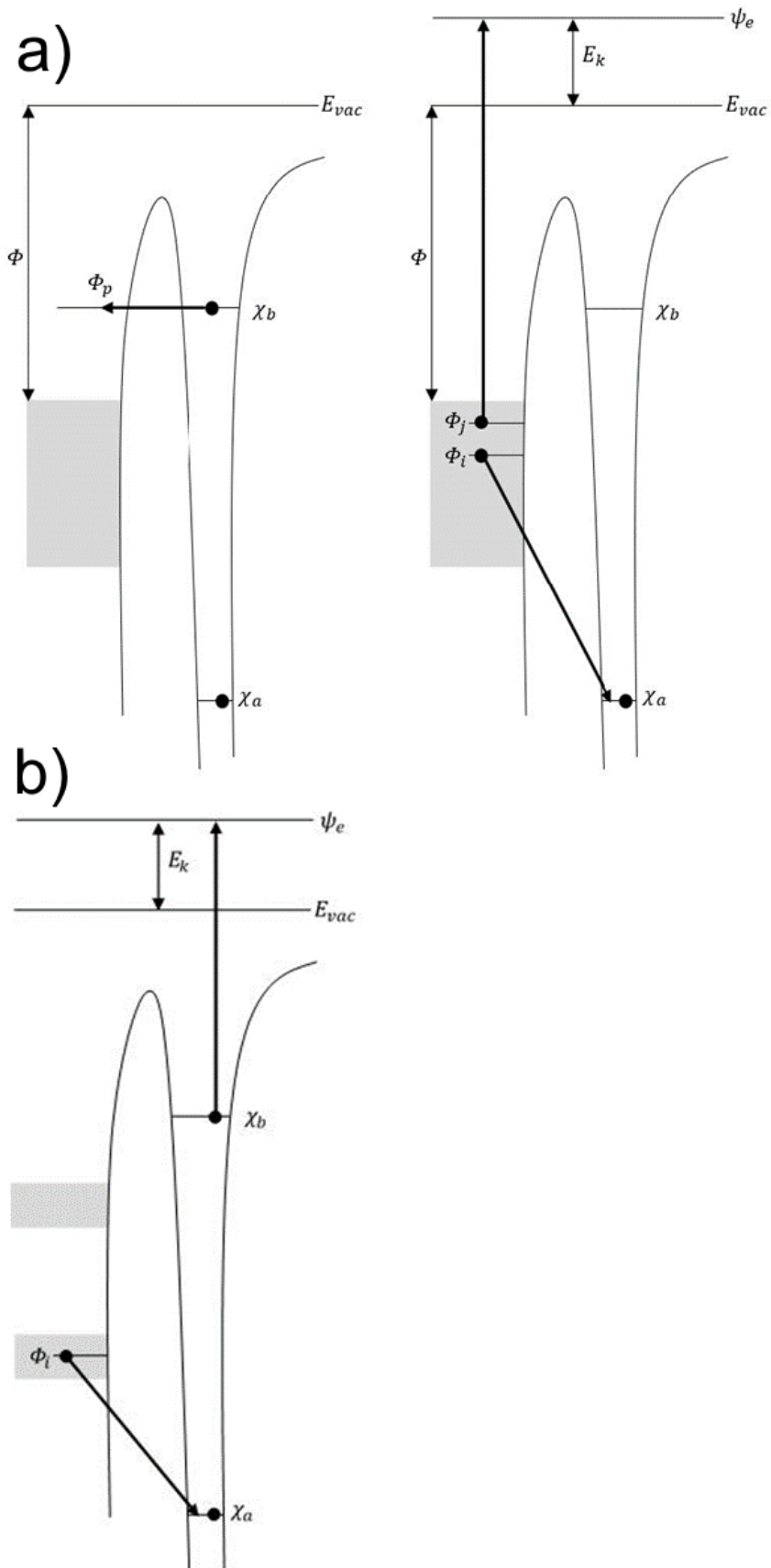
Figure 3-5: a) Resonance ionisation (left) and Auger neutralisation (right) process. b) Auger de-excitation process. Images modified from Harada *et al.* [297].

For the case where the surface has an unoccupied state Φ_p, RI will occur; and the excited electron in the He* outer orbital χ_b will tunnel into the surface. This results in a He$^+$ ion, and the surface gains an extra electron. Following this, the He$^+$ is neutralised by AN; a surface electron fills the empty state χ_a neutralising He$^+$, and the surface gains the difference in energy which results in the ejection of an electron from the surface with kinetic energy E_k. It is possible that there are multiple unoccupied surface states, *e.g.* Φ_i and Φ_j, which leads to features being broadened in the RI/AN spectra [297, 298]. When RI does not occur, the AD process occurs instead. AD features a surface electron in the state Φ_i transferring to the vacant χ_a orbital for He*. The excited He* electron in the orbital χ_b is then ejected with energy E_k [297]. AD results in sharper features than RI/AN, and the resulting spectra are directly comparable between UPS and the AD components of MIES, where both show the same features, but relative sizes may be different [298].

Any measurement may be some combination of AD and RI/AN to varying degrees depending upon the composition and temperature of the surface [298]. RI is hindered by surfaces with an absence of unoccupied states Φ_p which the excited He* electron in the χ_b orbital can tunnel to [297]. Thus, typically RI/AN is supressed for non-metallic samples while it dominates for high work function metals. Conversely, the AD process dominates for semiconducting, organic, and insulating surfaces, as well as surfaces with very low work functions [298, 379].

3.6.2.2 UPS and MIES: Instrumentation and Methods

The application of UPS and MIES to supported metal clusters is discussed in the Literature Review section 2.7.1.2. UPS and MIES were measured on the Flinders University UHV system. UV light and He* were generated simultaneously by a two-stage cold cathode He discharge lamp manufactured by MFS (Clausthal-Zellerfeld, Germany). The UV photons were from the He I emission line with an excitation energy of 21.2 eV. The metastable He* was excited with 19.8 eV energy [297]. Both UV photons and He* were fired at the surface simultaneously, and a chopper spinning at 2000 Hz split the signal into discrete pulses. This allowed both UPS and MIES spectra to be measured simultaneously, due to the velocity difference between photons (the speed of light) and He* (velocity of the gas in UHV). The He* arrived at the surface after the UV light, which caused individual pulses of electrons to be ejected which were then attributed to UPS or MIES based on the time of detection. These electrons were detected with a Phoibos 100 HSA using pass energy of 10 eV. Typically, 5 scans were taken and averaged for UPS and MIES measurements to improve the signal-to-noise ratio.

During UPS/MIES measurements, a bias of -10 V was applied to the samples to assist the low energy secondary electrons in reaching the detector. In the measurements, the KEs of ejected photoelectrons were measured in the low BE region of 0 eV to ~20 eV. As with XPS, the measured KE was subtracted from the UV or He* excitation energy to calculate the BE. However, the -10 V bias was also taken into consideration. As such, Equation 3-1 for XPS must be modified to include this bias, as shown in Equation 3-2.

$$BE = E_p - KE - \Phi - 10\ eV \qquad\qquad 3\text{-}2$$

In this case, E_p can represent the incoming energy due to a UV photon, or He*. This assumes an AD process is occurring for MIES; as described earlier, if RI/AN occurs the electron ejection process is more complicated and features a broadening mechanism.

In each UPS and MIES measurement, a series of samples were analysed. These will be referred to as a UPS/MIES series. Each UPS/MIES series featured samples with one changing variable, for example, the coverage of clusters on the surface or the level of surface defects. Additionally, each also featured a blank measurement. This allowed the valence electronic DOS to be determined due to the changing component (see section 3.6.2.3 below for details). Due to the nature of this style of measurement series, several repeated measurements, with consistent results, are necessary to determine an averaged DOS due to one changing variable. Thus, repeated measurements for verifying the reliability of the resulting DOS are built into the methodology.

3.6.2.3 UPS and MIES: Data Analysis

The data processing required to determine the UPS and MIES spectra due to a changing component in a UPS/MIES series will be described. These determined spectra will be referred to as "difference spectra". The most common case in this thesis of determining the Difference Spectrum due to deposited clusters will be used as an example.

Data above a BE of 10 eV were truncated and not considered in the analysis procedures as the low BE region of the spectrum from 0 to 4-6 eV is of most interest and gives information about the metallic properties of the material. Additionally, data above a BE of ~15 eV are related to secondary electrons which are inelastically scattered resulting in a loss of KE, further complicating the analysis. A linear background was subtracted from each spectrum. Spectra were then normalised by multiplying each spectrum by a linear multiplication factor to achieve the same count rate, typically normalised so all spectra have the same intensity as the blank spectrum within experimental uncertainty. The normalisation procedure

eliminates variations in the intensity of UV light and He* source.

To determine the Difference Spectrum due to the addition of clusters, the assumption was that the measured spectra were a linear combination of the substrate spectrum, and a spectrum related to the supported clusters according to Equation 3-3.

$$measured\ spectrum(C) \qquad\qquad 3\text{-}3$$
$$= A(C) * cluster\ spectrum + B(C) * susbtrate\ spectrum$$

Where C is the surface coverage of clusters, and A and B are weighting factors that vary with C. A diagram showing the effect of cluster coverage on the weighting factors is shown in Figure 3-6. The cluster spectrum and substrate spectrum do not vary with C, and therefore the assumption was that the cluster surface loading did not affect the DOS of the clusters. Such an assumption is reasonable, considering all cluster-loaded surfaces were <20% ML, and similar assumptions for MIES spectra have been found to hold for several systems including solid surfaces partially covered by adsorbates [298].
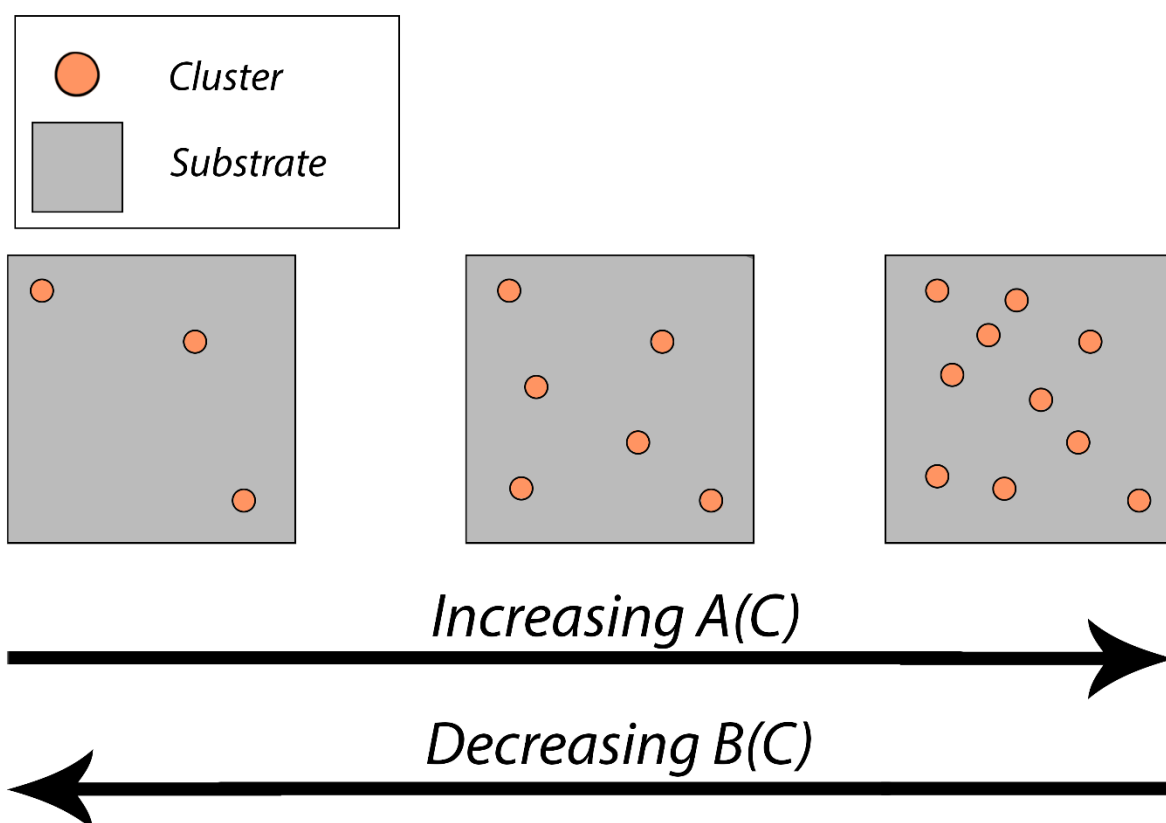
Figure 3-6: Diagram showing the effect of the cluster surface coverage on the variables A(C) and B(C) in Equation 3-3.

For the blank sample in each UPS/MIES series A(C) = 0. Based on this, the blank substrate

spectrum was subtracted from each spectrum of cluster-loaded samples multiplied by linear scaling factors. The scaling factors used were determined by minimising the differences between the resultant Difference Spectra for each sample in a UPS/MIES series in Excel using the Solver function. The Difference Spectra for each sample were then averaged to determine an average Difference Spectrum. It is these spectra which are shown in the experimental chapters for each UPS/MIES series.

Weighting factors for UPS and MIES were determined by linearly combining the substrate spectrum and the averaged Difference Spectrum as per Equation 3-3, and using Solver to determine the weighting factors A(C) and B(C). Weighting factors were determined by minimising the sum of differences between the linear combinations of the component spectra and the measured spectrum for each sample. These were then normalised so that the sum of weighting factors for UPS and MIES was unity, *i.e.* A(C) + B(C) = 1. The uncertainty in weighting factors was estimated to be ± 0.05. If the spectrum related to a cluster deposition increased in weighting factor as the cluster surface coverage increased, this provided evidence that the determined spectrum was indeed related to the presence of the clusters.

3.6.3 CO-TPD

3.6.3.1 CO-TPD: Background

TPD is a UHV procedure where a catalyst sample is dosed with a gas which adsorbs onto the surface, and the temperature is then increased at a steady ramping speed while the molecules desorbing are counted using a quadrupole mass spectrometer (QMS) [329]. As the catalyst is increased in temperature, adsorbed gasses desorb and may also potentially decompose. A diagram of gas molecules adsorbing and desorbing from metal clusters in a typical TPD experiment is shown in Figure 3-7. As the sample temperature is increased the rate of desorption increases until a maximum, and then decreases to the baseline as the adsorbed gas is depleted [329]. TPD spectra are presented as desorption rate vs. temperature. The shape and position of the peak features in these spectra give information about how the gas was adsorbed on the catalyst, such as the number of binding sites and their relative binding energies [329, 380]. Higher temperature peaks are related to sites with higher binding energies, requiring more energy for gas desorption to occur. However, because the TPD measurements are performed with continuously ramping temperatures it can be problematic to relate a desorption peak to an exact temperature of desorption.
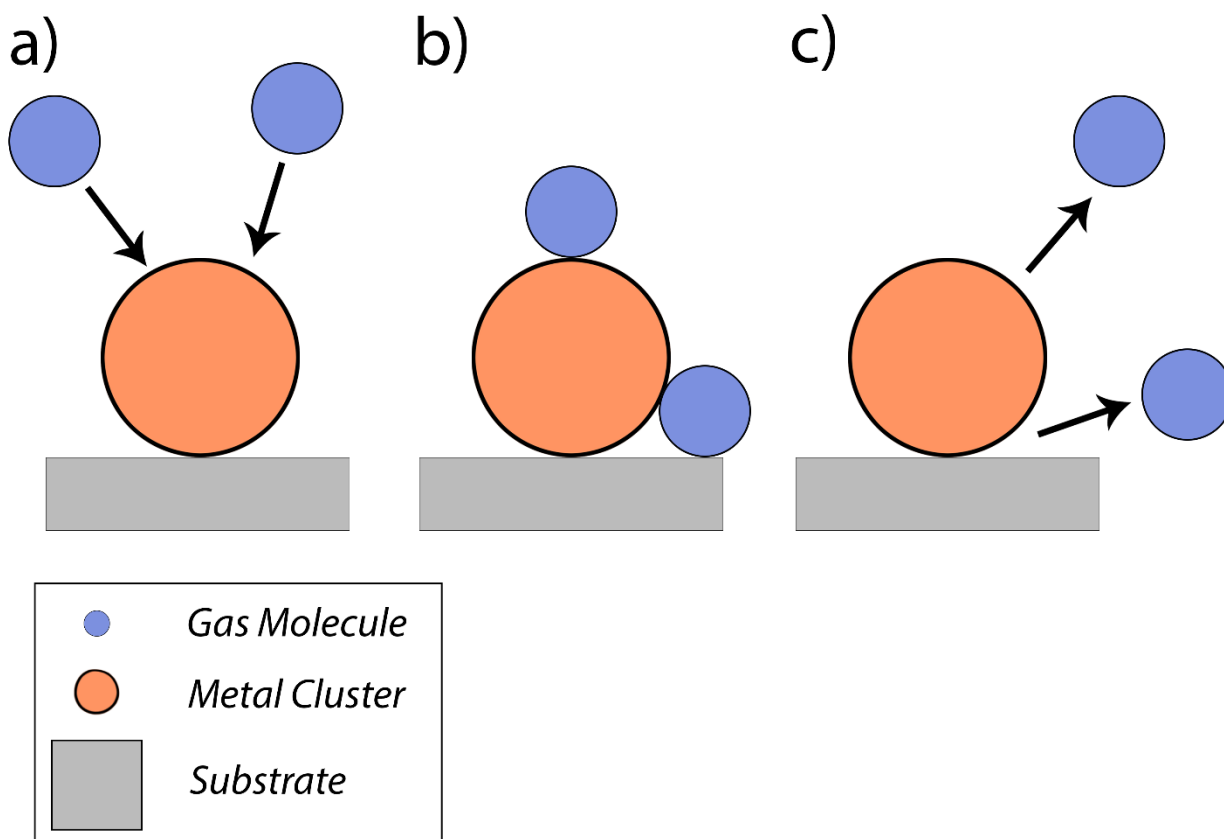
Figure 3-7: Diagram showing the binding of gas molecules to metal clusters in a typical TPD measurement. The same metal cluster at three points in time is shown. a) gas molecules are dosed onto the surface under vacuum. b) Gas molecules adsorb to the metal cluster, where 2 example binding sites are shown. c) As the temperature is increased, the gas molecules desorb when the temperature reached is sufficient to overcome their binding energy.

CO-TPD refers to TPD focussing on the desorption of CO molecules. This typically involves dosing a saturating amount of CO onto the clusters at a reduced temperature before temperature ramping is initiated. The technique can also be used to analyse the de-ligation of clusters with CO ligands such as $Ru_3(CO)_{12}$ [45, 74, 75]. When the CO dosing and temperature ramping procedure is repeated for multiple cycles, CO-TPD can show the effect of heating on the available CO binding sites on the surface, which can give insights into cluster/substrate interactions.

3.6.3.2 CO-TPD: Instrumentation and Methods

The application of CO-TPD to research on supported metal clusters is discussed in the Literature Review section 2.7.3. CO-TPD was performed on The University of Utah UHV system. A diagram of the sample and experimental system used is shown in Figure 3-8. A CO-TPD procedure is performed by dosing the sample with isotopically labelled ^{13}CO (mass 29) at 180 K and ramping the temperature at a rate of 3 K/s while measuring the amount of

desorbing ^{13}CO using a QMS made by UTI. ^{12}CO (mass 28) is the most commonly occurring isotope, and thus using ^{13}CO allows for separation of any background CO in the chamber from the desorbing CO signal. For each substrate used, CO-TPD measurements were performed before and after cluster depositions to determine the spectra due to the blank substrates. This is for all samples except CVD samples which were not deposited *in situ* (discussed below). After a deposition, the TPD procedure was initiated as quickly as practicable to avoid additional adventitious hydrocarbons in the vacuum chamber from adsorbing onto the sample. CO exposure was through a dosing tube which terminated approximately 2 cm from the surface of the substrate (see Figure 3-8); this increased the gas flux at the surface by a factor of approximately 10 compared to dosing the gas into the chamber without the tube. This increase factor was determined previously by The University of Utah research group as per the method described by Kaden *et al.* [330].

The standard procedure for CO-TPD measurements is as follows. Samples were cooled to 180 K and exposed to 10 L ^{13}CO, which was above the saturation dose. After CO dosing, the sample was cooled to 170 K and positioned at a distance of 0.5 mm from the differentially pumped QMS entrance, which is a 2.5 mm diameter aperture in a skimmer cone (see Figure 3-8). The temperature was then ramped from 170 K to 800 K, while masses corresponding to CH_3, O, H_2O, ^{12}CO, ^{13}CO, O_2, $^{12}CO_2$, $^{13}CO_2$ were monitored in 50 ms total cycles by the QMS. Masses aside from ^{12}CO and ^{13}CO were monitored for irregularities or reaction products. Between 700 K and 750 K the sample holder "degassed" CO resulting in a sharply increased background, and data points beyond this temperature and up to 800 K were not considered for analysis. A linear background was subtracted from each measured spectrum. CO-TPD measurements were repeated 3 or 4 times in cycles. After all CO-TPD cycles were completed, samples were retracted away from the entrance of the QMS in the vacuum chamber and 3×10^{-8} mbar of CO was introduced into the chamber. This allowed for the calibration of QMS detector counts to a known flux of CO entering the QMS.
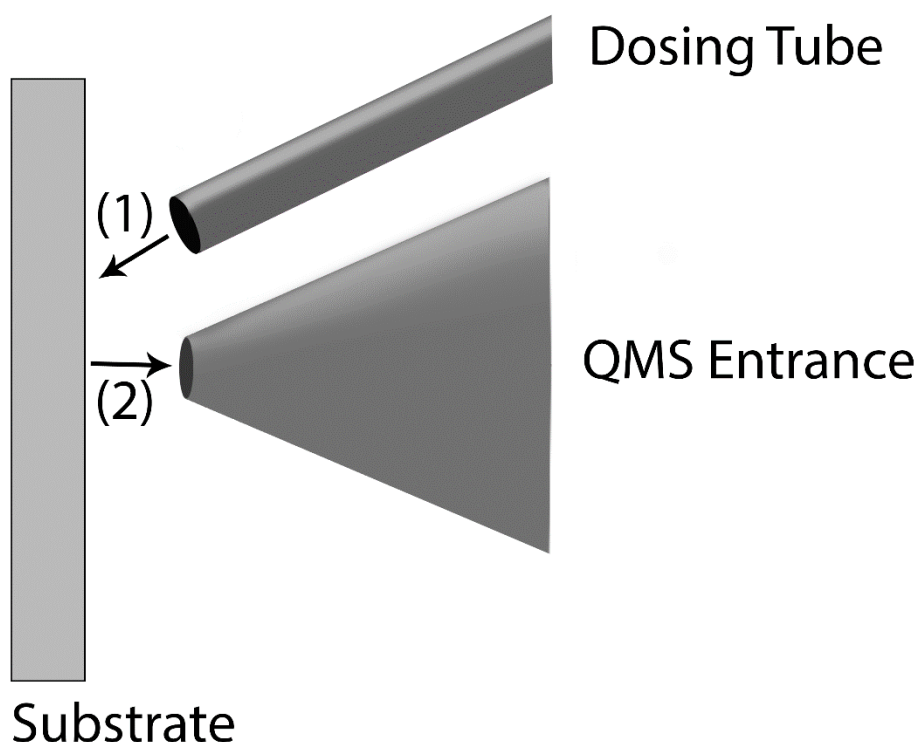
Figure 3-8: Diagram of the UHV experimental setup used for CO-TPD measurements. In step (1), CO is dosed onto the surface of the substrate through a dosing tube. In step (2), the substrate is heated while monitoring the gasses which desorb and enter the QMS entrance.

CS-deposited samples were analysed by CO-TPD *in situ*. Conversely, ligated cluster samples, featuring depositions of ligated $Ru_3(CO)_{12}$ (Chapter 4) or $H_4Ru_4(CO)_{12}$ (Chapter 7) were prepared on the Flinders University UHV system and analysed on University of Utah UHV system. As these samples had been exposed to atmosphere before measurements, there may have been a small component of the CO-TPD signal which was due to the desorption of adsorbed CO contamination. This was not corrected for but due to the large number of CO ligands measured desorbing in the 1st CO-TPD cycles, any effects from contamination were deemed minimal in comparison to the signal strength.

The CO-TPD procedure for the mentioned ligated samples was slightly different to the standard procedure; the samples were cooled to 180 K and the CO-TPD heat ramping process was initiated with no further treatment. For these samples, the temperature was only ramped to 723 K on the 1st CO-TPD cycles, not 800 K. The clusters were already saturated with ^{12}CO ligands, and thus for the 1st cycle no ^{13}CO was dosed, and ^{12}CO was the mass of interest. ^{13}CO was dosed as per the standard procedure for the CO-TPD on the 2nd and 3rd cycles. An additional complication for the ligated samples was that on the 1st

cycle for each measurement, the CO desorption rate reached the maximum count limit of the QMS which caused two effects; the ^{12}CO spectrum was distorted due to saturation, and the measured ^{13}CO signal clearly was actually due to overlap of the adjacent ^{12}CO mass peak signal. This detection of a small fraction of the overlapping ^{12}CO signal at mass 29 allowed us to correct the ^{12}CO spectrum for saturation by scaling the ^{13}CO spectral intensities so that they matched the ^{12}CO signal at low temperature, where the signal was well below the saturation level. Note that after the 1st TPD on the CVD samples, and in all TPD experiments with CS clusters, the ^{12}CO signal was small, and unsaturated.

3.6.3.3 CO-TPD: Data Analysis

The QMS counts were calibrated to quantitatively determine the CO desorption rate; that is, the number of CO molecules desorbing from the sample per unit time in molecules/second. This calibration used the QMS counts resulting from a known flux of CO added to the chamber at the end of each experiment. It was performed according to the procedure reported by Li *et al.* [309]. The real measurement time for each mass (duty factor) during the QMS cycles was considered. The fact that the skimmer cone was 2.5 mm in diameter and the cluster spot was 2 mm in diameter contributed an uncertainty to the calculation, as angular distribution effects may have changed the efficiency of detection depending on the distance of the sample to the aperture. Due to this it was estimated that the accuracy of the absolute TPD intensity calibration was ~50%, while the relative uncertainty between samples was ~15%.

A procedure was used to integrate the CO-TPD desorption spectra over time, to determine the total number of CO molecules desorbed. The integration performed by dividing the desorption spectrum into many thin, right angle trapezoids and calculating the total area. For CS-depositions a known number of cluster atoms were deposited, and the total CO desorbing per cluster atom was determined. However, for CO-TPD spectra of Ru clusters on RF-TiO$_2$ substrates the largest Ru-CO desorption feature overlapped with a background signal due to the sample holder degassing at ~750 K. Thus, these spectra could not be integrated without assuming their shape beyond 750 K. The only CO-TPD measurement for which the integration was performed was for CS-Ru$_3$/SiO$_2$ in Chapter 4. The absolute error in the reported CO desorbing per Ru atom was assumed to be the same as the CO desorption rate; ~50% absolute error and ~15% relative error when comparing between measurements.

Chapter 4   The interaction of size-selected Ru$_3$ clusters with RF-deposited TiO$_2$: probing Ru-CO binding sites with CO-TPD

This chapter is a reformatted and edited version of a manuscript published in a peer-reviewed journal. See the Contextual Statement section for details on the contributions of co-authors to the published version of the manuscript.

Reference for the published version:

4.1 Abstract

Small Ru clusters are efficient catalysts for chemical reactions such as CO hydrogenation. In this study 3-atom Ru$_3$ clusters were deposited onto radio frequency (RF)-sputter deposited TiO$_2$ (RF-TiO$_2$) which is an inexpensive, nanoparticulate form of TiO$_2$. TiO$_2$ substrates are notable in that they form strong metal-support interactions (SMSI) with clusters. Using temperature programmed desorption (TPD) to probe Ru-CO binding sites, and X-ray photoelectron spectroscopy to provide chemical information on clusters, differences in cluster-support interactions were studied for Ru$_3$ deposited using both a cluster source as well as chemical vapor deposition of Ru$_3$(CO)$_{12}$. SiO$_2$ was compared as a substrate to RF-TiO$_2$ with a range of pre-deposition sputter treatments.

For cluster source-deposited Ru$_3$, heating to 800 K caused cluster agglomeration on SiO$_2$ and oxidation on non-sputtered RF-TiO$_2$. For cluster source-deposited Ru$_3$ on sputter-treated RF-TiO$_2$ substrates all Ru-CO binding sites were blocked as-deposited, and it was determined that for the binding sites to be preserved the sputter treatment cannot be applied. Conversely, for Ru$_3$(CO)$_{12}$ on sputter-treated RF-TiO$_2$ the clusters were protected by their ligands and Ru-CO binding sites were only blocked once the sample was heated to 723 K. The mechanism for complete blocking of Ru-CO sites on sputter-treated RF-TiO$_2$ could not be directly determined. Comparisons to the literature indicate that possible mechanisms for the blocking of the CO adsorption sites is cluster encapsulation into the TiO$_x$ layer reduced through sputtering as well as the partial oxidation of the clusters.

4.2 Introduction

Metal clusters are generally defined as groups of metal atoms with sizes less than ~300 atoms [11, 14-18]. They often possess unique electronic and catalytic and/or photocatalytic properties which are highly tuneable, such that the addition or subtraction of just one atom to a small cluster can be a deciding factor on whether it functions as a catalyst or not [56]. For this reason, experiments often focus on a single cluster size. Ru clusters in particular have been shown to be among the most active catalysts for industry and environment-relevant reactions such as CO and CO_2 hydrogenation [43-47, 49-51, 53, 54] which are relevant to both ammonia production as well as the conversion of pollutants into liquid fuels. Two of the main ways to deposit Ru clusters onto substrates is through the preparation of bare clusters under ultra-high vacuum (UHV) using a cluster source (CS), or through depositing ligand-stabilised clusters such as $Ru_3(CO)_{12}$ using chemical vapor deposition (CVD) [74, 75, 135-137] or a solution-based deposition [332]. This process of depositing metal carbonyl compounds using CVD is well explored in the literature and has been used to deposit clusters onto a number of substrates such as; metals (*e.g.* Au), metal oxides (*e.g.* TiO_2), non-metal oxides (*e.g.* SiO_2) and others such as zeolites [75, 138-143]. When depositing ligand-stabilised clutters, extra post-deposition surface treatments such as heating are needed to remove the ligands if bare metal clusters are desired on the substrate.

TiO_2 is a photocatalytically active substrate [204] and is a common choice as a substrate for the deposition of clusters [6, 26, 38, 60, 66, 74, 75, 103, 184-190]. In typical surface science experiments, the rutile $TiO_2(110)$ single crystal is the most commonly used form of TiO_2 because it has a well-defined crystal structure and allows for easy comparison to previous research. However, for the application of clusters in real-word catalysis and/or photocatalysis, a single crystal surface such as $TiO_2(110)$ would be unlikely to be used due to the cost and nature of producing the crystals. Here we use RF-sputter deposited TiO_2 (RF-TiO_2) as a substrate. It is a nanoparticulate form of TiO_2 made by UHV magnetron RF-sputtering a ceramic TiO_2 wafer onto a substrate (sputter deposition), in the present case Si(100). This process produces a dense, uniform, stoichiometry-controlled layer of TiO_2 more cheaply and readily than $TiO_2(110)$ [357].

A key problem of clusters deposited onto surfaces is maintaining the properties of size-selected clusters by preventing them from agglomeration, in particular at elevated temperatures [67]. One method to help with this is to induce defects on the substrate surface prior to cluster deposition [5, 221]. Clusters are known to preferentially bind to defect sites, as their surface energy is greater than the corresponding perfect crystal structure [5]. As a

specific example regarding TiO_2 substrates, a study by Krishnan et al. [5] showed that for Au_9 clusters supported on atomic layer deposition (ALD) TiO_2, sputter-treating the surface with Ar^+ prior to cluster deposition was able to help prevent cluster agglomeration. The anchoring of clusters to defect sites on TiO_2 has also been demonstrated by DFT calculations of Au clusters on $TiO_2(110)$ [222]. However, the cluster-substrate interaction, and therefore agglomeration characteristics, will be different for each cluster/substrate combination. To the best knowledge of the author this type of defect experiment has not been previously performed for Ru clusters on TiO_2.

There are two main types of defects: oxygen vacancies and interstitial titanium ions both resulting in the presence of Ti^{3+} in the TiO_2 [204]. The transport of each in the substrate can be explained by vacancy and interstitial models respectively [204, 381-383]. Interstitials are atoms present within crystal lattice locations where they should not normally be present. Ar^+ sputtering removes O atoms more preferentially than Ti atoms from the surface, and the main surface defect sites from sputtering are predominantly vacancies in the bridging oxygen rows of the TiO_2 [204, 384]. These defect sites act as electron donors to clusters because the oxygen removal leaves behind two electrons which previously occupied O_{2p} valence band levels [204, 385].

Previous studies on the effects of heating systems of small, size-selected Ru clusters on TiO_2 have often focussed on Ru deposited using $Ru_3(CO)_{12}$: two separate studies by Zhao et al. and Rizzi et al. [75, 136] have been performed on $Ru_3(CO)_{12}$ deposited by CVD onto $TiO_2(110)$, using XPS and/or CO-temperature programmed desorption (CO-TPD). Both studies found that there is partial decomposition of $Ru_3(CO)_{12}$ when deposited onto room-temperature $TiO_2(110)$ [75, 136]. Furthermore, Zhao et al. [75] demonstrated using XPS and TPD that heating to 700 K under UHV yielded almost pure Ru particles on the surface, but heating to 600 K while dosing O_2 resulted in oxidised Ru. The latter point was also supported in the Rizzi et al. study using XPS [136]. The specific cluster-substrate interaction can have a large effect on the state of supported clusters, even for differing forms of TiO_2; CO-TPD spectra have been shown to have different CO desorption features for $Ru_3(CO)_{12}$ deposited onto varying forms of TiO_2, such as $TiO_2(110)$ [75], polycrystalline P25 TiO_2 [332], and $TiO_2/Mo(110)$ [74]. Other studies have used differing Ru/TiO_2 systems with different thermal stability results, including one study by Komaya et al. [386] for large Ru particles deposited with $Ru(NO)(NO_3)_3$ onto P25 nanocrystalline TiO_2, where heating to 573 K resulted in the encapsulation of Ru by an amorphous titania layer. These studies show that it is unclear how Ru clusters interact with the substrate when deposited onto titania, in particular when

heating of the cluster/substrate system is involved. It is therefore important to test the interaction and stability of Ru clusters on RF-TiO$_2$ because studies performed on differing TiO$_2$ forms cannot predict the results for this substrate. Of particular interest is agglomeration of the clusters and encapsulation into the substrate.

The aim of this study was to determine whether defects induced in RF-TiO$_2$ substrates help to avoid agglomeration of bare Ru$_3$ and Ru$_3$(CO)$_{12}$ clusters upon deposition, and how the clusters interact with RF-TiO$_2$ substrates upon heating to ~800 K. The clusters were deposited both from a CS (bare Ru$_3$) and evaporation of Ru$_3$(CO)$_{12}$ via CVD. To the knowledge of the authors no previous studies exist for size-selected Ru deposited by a CS onto TiO$_2$, and thus comparison between the results of these two common deposition methods is of critical importance. CO-TPD was used to probe the available CO adsorption sites on the metal clusters, as well as for probing the removal of ligands with heating in the case of CO-stabilised clusters [57, 74, 75, 310, 312, 313, 330]. XPS was used to analyse the composition of the surface and to determine concentration depth profiles.

4.3 Methodology

4.3.1 Substrates

See section 3.1 for information on the RF-TiO$_2$ and SiO$_2$ substrates used. Ru$_3$ was deposited onto four different types of substrates: two RF-TiO$_2$ substrates modified by Ar$^+$ ion sputtering (prior to the deposition of Ru clusters) at two different sputter doses, non-sputtered TiO$_2$, and non-sputtered SiO$_2$ for comparison. The different sputtering dosages for RF-TiO$_2$ have been designated as follows: "low-dose sputtered RF-TiO$_2$" was treated with 4 x 10^{13} Ar$^+$/cm^2, and "high-dose sputtered RF-TiO$_2$" was treated with 6 x 10^{14} Ar$^+$/cm^2. Additionally, a "non-sputtered RF-TiO$_2$" sample was used. In the text these will be abbreviated to LDS-RF-TiO$_2$, HDS-RF-TiO$_2$, and NS-RF-TiO$_2$, respectively. A list of the substrates and their abbreviated names are given in Table 4-1. Deposition of Ru$_3$ from CS was performed on all 4 substrates. However, deposition of Ru$_3$ from CVD was only undertaken on an HDS-TiO$_2$ substrate. 5 samples were analysed with CO-TPD overall, and blank measurements CO-TPD were performed prior to the deposition of Ru clusters. Additional samples were prepared for further XPS analysis, and thus the XPS measurements in some cases were of samples prepared with an identical method, rather than the same sample as was analysed with CO-TPD.

Table 4-1: Summary of the different supporting substrates used in this study. The designated sample names are given as well as abbreviated names for the RF-TiO$_2$ substrates.

Substrate Material	Ar$^+$ Sputter Dose (ions/cm^2)	Designated Sample Name	Abbreviated Name
RF-TiO$_2$	None	Non-Sputtered RF-TiO$_2$	NS-RF-TiO$_2$
RF-TiO$_2$	4 x 10^{13}	Low-Dose Sputtered RF-TiO$_2$	LDS-RF-TiO$_2$
RF-TiO$_2$	6 x 10^{14}	High-Dose Sputtered RF-TiO$_2$	HDS-RF-TiO$_2$
SiO$_2$/Si(100)	None	SiO$_2$	SiO$_2$

4.3.2 Instrumentation

Depositions and analysis were performed in two separate UHV instruments; laser vaporisation (LaVa) CS depositions were performed at the University of Utah UHV system, where Ar$^+$ sputtering, CO-TPD, and XPS were performed *in situ*. The CVD of ligated Ru$_3$(CO)$_{12}$ clusters was performed at the Flinders University UHV system. Due to instrument limitations CO-TPD was only available on the University of Utah system, while CVD depositions were only possible at Flinders University. The CVD sample was transported from Flinders University to the University of Utah for CO-TPD analysis. This means that the

ligated clusters were not deposited *in situ*, however the CO ligands serve to stabilise the clusters when exposed to atmosphere, which decreased the likelihood of a change in the clusters occurring due to atmospheric exposure. The Ar$^+$ sputter guns differed between the instruments; Flinders University experiments used 3 keV Ar$^+$ and University of Utah experiments used 2 keV. This was discussed in section 3.4 and was deemed not to be of critical importance for this experiment.

4.3.3 Cluster Depositions

4.3.3.1 Cluster Source

CS-depositions were performed by LaVa CS. The instrument details and deposition procedure are given in section 3.5.3. In short, the clusters were produced under UHV by pulsed LaVa of a 99.9% pure Ru metal target and deposited onto the substrates *in situ*. A 2 mm diameter aperture positioned 1 mm from the surface ensured the cluster spot was approximately 2 mm in diameter. A retarding potential was used to ensure a deposition energy of ~1 eV/atom, to prevent fragmentation upon cluster impact [157]. For each CS deposition 1.5×10^{14} Ru atoms/cm^2 were deposited. Samples were deposited while being cooled with LN$_2$ to 180 K.

Each CS deposition followed the same procedure, except for the pre-deposition treatment process. RF-TiO$_2$ samples were heated under UHV to 723 K for 10 minutes to remove surface hydrocarbons. The surface was then Ar$^+$ sputtered to the required dosage (except for NS-RF-TiO$_2$ which was not sputtered), and clusters were deposited with the CS. For the deposition onto SiO$_2$ the initial heating step was different; SiO$_2$ was heated to 700 K for 20 minutes under an atmosphere of 7×10^{-6} mbar O$_2$ to preserve the surface oxide layer, followed by a further 2 minutes of heating under UHV.

4.3.3.2 Chemical Vapor Deposition

The deposition by CVD of Ru$_3$(CO)$_{12}$ clusters onto RF-TiO$_2$ was described in section 3.5.1. The full CVD measurement procedure was performed as follows: RF-TiO$_2$ was heated under UHV to 723 K for 10 minutes then sputtered with Ar$^+$ at 6×10^{14} ions/cm^2. Ru$_3$(CO)$_{12}$ was deposited in the loading chamber for 120 minutes, where the starting pressure was $<7 \times 10^{-7}$ mbar. The cluster-deposited sample was then removed from the vacuum for transferring to the University of Utah.

4.3.3.3 List of Samples

A list of all cluster samples analysed in the study is given below in Table 4-2. All samples were prepared at the University of Utah except for CVD-deposited Ru$_3$(CO)$_{12}$/HDS-RF-TiO$_2$,

which was prepared at Flinders University. All CO-TPD and XPS measurements were performed in Utah. Some samples were analysed with both CO-TPD and XPS, while some were analysed by one technique only. Multiples of the same sample were prepared in some cases to allow for further XPS testing. For CO-TPD, blank measurements were performed on each substrate prior to cluster depositions, except for CVD $Ru_3(CO)_{12}$/HDS-RF-TiO_2. The treatment of the samples for the XPS measurements are shown in the table. The blank XPS measurements in the XPS Results were performed on same cluster samples, prior to cluster depositions.

Table 4-2: List of samples analysed with CO-TPD and XPS.

Deposition	Substrate	Analysis Techniques	XPS Measurements Performed
CS Ru_3	SiO_2	CO-TPD	N/A
CS Ru_3	SiO_2	XPS	No treatment, and 800 K
CS Ru_3	NS-RF-TiO_2	CO-TPD and XPS	No treatment, and 800 K
CS Ru_3	NS-RF- TiO_2	XPS	No treatment, and after CO dose
CS Ru_3	LDS-RF-TiO_2	CO-TPD	N/A
CS Ru_3	HDS-RF-TiO_2	CO-TPD and XPS	800 K, and after CO dose.
CVD $Ru_3(CO)_{12}$	HDS-RF-TiO_2	CO-TPD and XPS	No treatment, 800 K heating, and after CO dose.

4.3.4 CO-TPD Measurements

The measurement, data analysis, and error analysis procedures for CO-TPD are given in given in the Instrumentation and Methodologies section 3.6.3. For each substrate type, CO-TPD measurements were performed before and after CS cluster depositions to gauge the CO adsorption to the blank substrates. Each CO-TPD procedure was repeated for a total of 3 cycles, except the SiO_2 sample which was repeated for 4 cycles as there were noticeable changes between the 2nd and 3rd cycles.

As discussed in section 3.6.3.2, for the CVD $Ru_3(CO)_{12}$/HDS-RF-TiO_2 sample the 1st CO-TPD cycle measured the desorbing ^{12}CO ligands without dosing ^{13}CO. This was because the CO bonding sites for the $Ru_3(CO)_{12}$ are saturated before heating due to the ^{12}CO ligands. As this had been exposed to atmosphere before measurements, there may have been a small component of the CO-TPD signal which was due to the desorption of adsorbed CO contamination. This was not corrected for, but due to the large number of CO ligands

measured desorbing in the 1st CO-TPD cycle, any effects from contamination were deemed minimal in comparison to the signal strength.

The desorption spectra were integrated over time to determine the total number of CO molecules desorbed, and subsequently total CO desorbing per Ru atom. CS Ru$_3$ on SiO$_2$, was the only CO-TPD sample where the total number of CO desorbing could be determined, because the desorption rate returned to the baseline level before the background signal increased at ~750 K. The uncertainty in the total number of CO desorbing was assumed to be the same as that of the CO desorption rate (see section 3.6.3.3).

4.3.5 XPS Measurements

The experimental, data analysis, and error analysis procedures for XPS measurements were given in section 3.6.1. Details on the XPS peak fitting are given, including particular details about fitting Ru peaks using asymmetrical line shapes, as well as the estimation of Ru surface coverages. Details on the two UHV systems used for measurement are given in section 3.3.

An XPS spectrum of an Ru reference material was measured on the Flinders University UHV system XPS instrument. A Mg Kα source was used with a 10 eV pass energy. The Ru reference sample was taken from a 99.9% pure Ru metal sample cut to 1 cm x 1 cm to accommodate the sample mounting plate. A measurement was first taken with no surface treatment, and then again after heating to 1073 K for 10 minutes and sputtering with 3 keV Ar$^+$ for 1 hour to remove the surface Ru oxide layer and any hydrocarbon contamination. The BE scale for these measurements was calibrated to the C 1s peak for the pre-treatment XPS spectrum before hydrocarbon removal. The peak fitting parameters for Ru cluster XPS peaks were based on this reference measurement; see section 3.6.1.3 for details.

For XPS measurements of cluster-deposited samples, the Ru 3d/C 1s and O 1s regions were measured for each sample, while the Ti 2p and Si 2p regions were additionally measured for RF-TiO$_2$ and SiO$_2$ substrates, respectively. The University of Utah UHV system was used to record all XPS measurements *in situ* (except for CVD Ru$_3$(CO)$_{12}$/HDS-RF-TiO$_2$), using an Al Ka source and 10 eV pass energy for the HSA. No evidence for charging was found for any sample.

4.4 Results and Discussion

4.4.1 CO-TPD Results

4.4.1.1 CO-TPD of CS Ru_3/SiO_2

Figure 4-1 shows CO-TPD measurements of blank SiO_2 and CS Ru_3/SiO_2. CO-TPD is an analysis technique useful for probing the available CO adsorption sites on metal clusters, as well as for probing the removal of ligands with heating in the case of CO-stabilised clusters [57, 74, 75, 310, 312, 313, 330]. When discussing peaks in CO-TPD figures, they will be labelled based on the temperature corresponding to the peak CO desorption rate. Due to the continuous temperature ramping of the CO-TPD measurements the temperature at the peak CO desorption rate is typically greater than the minimum temperature required for CO desorption to occur for that particular binding site. SiO_2 was used for reference measurements because it is a nonreducible oxide substrate that is stable at the temperatures being used and does not form a strong metal support interaction (SMSI) with clusters under typical conditions [180, 181, 387]. SMSI is a general term to explain changes in catalytic activity for metals on reducible oxide supports after high temperature reduction [185, 198, 199], which can be contributed to by oxidation [185, 201, 202] and/or the clusters being covered by a layer of reduced support material, which is known as the "encapsulation" or "decoration" model [199, 207].
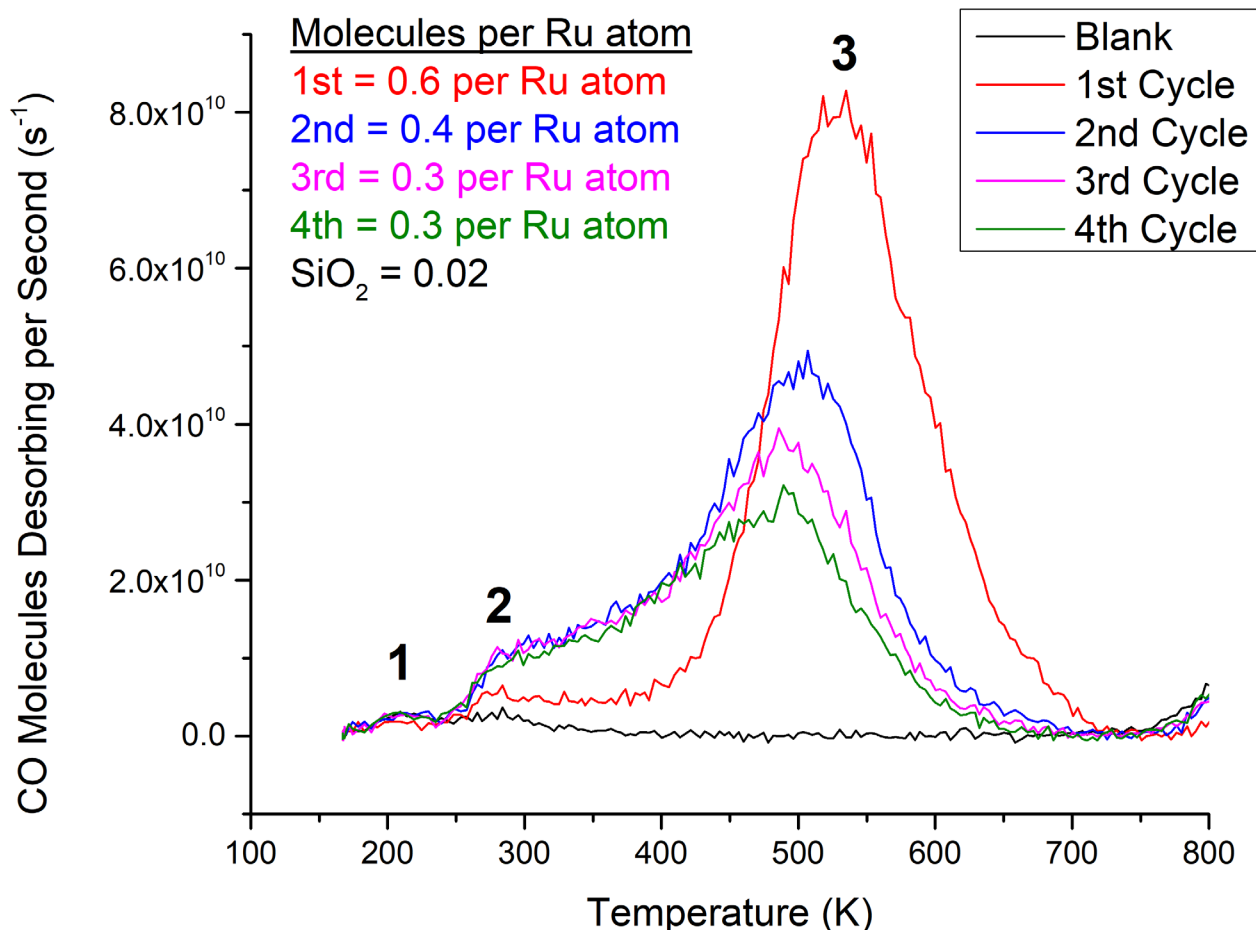
Figure 4-1: ^{13}CO-TPD from CS Ru₃/SiO₂ and blank SiO₂ (before Ru₃ deposition). Quantification of CO molecules desorbing per Ru atom is shown in the top left corner. Three peaks were identified at 210 K (1), 260 K (2), and 530 K (3), where peak (3) decreases in temperature with successive heating cycles (discussed in the main text). The blank SiO₂ CO-TPD is an average of 3 cycles where there were no noticeable changes. For comparison purposes the quantified blank SiO₂ desorption assumes the same number of Ru atoms were deposited as the cluster-loaded measurements.

Figure 4-1 shows that very little CO has desorbed from blank SiO₂, with two small features centred at 210 K and 285 K. Furthermore, there was no change between the blank measurements over 3 repeated TPD cycles (traces not shown in figure), indicating the affinity of the surface for CO was not strongly affected or changed by heating to 800 K. The 1st CO-TPD cycle for CS Ru₃/SiO₂ features a small peak at 210 K, which is related to desorption of CO from the SiO₂ substrate. The remaining features in the spectrum are due to CO desorbing from Ru-CO binding sites. Notably, there is a small peak at 260 K and then a large, main desorption peak at 530 K. In this study, these two features will be treated as the reference Ru-CO desorption peaks for CO desorbing from supported Ru clusters which have not chemically reacted with the substrate or formed an SMSI state.

In the 2nd to 4th cycles, the 260 K desorption feature increased in size (Figure 4-1). Also, the

largest ~530 K CO peak changed shape with successive CO-TPD cycles decreasing in size and shifting to lower temperatures. By the 4th cycle the main desorption peak was at 500 K, and the total number of CO molecules desorbing had had decreased to half the value in the 1st cycle. The decrease in total CO desorbing cannot be explained by the clusters detaching or travelling into the substrate. First, once the clusters have adsorbed they are not likely to detach due to heating to 800 K as the bulk Ru boiling point is 4423 K [388]. Second, the clusters are unlikely to travel into the substrate because SiO_2 is fairly inert and does not interact strongly with supported clusters [204] or typically form an SMSI with supported metals at these temperatures and conditions [387].

The decrease in CO desorption peak size with successive CO-TPD cycles (Figure 4-1) can be explained by cluster agglomeration. When clusters form larger aggregates the ratio of surface atoms to internal atoms for the clusters is reduced, thereby reducing the total number of CO binding sites on Ru clusters and agglomerated Ru clusters available in the system. A decrease in CO peak size due to cluster agglomeration has similarly been seen in other CO-TPD studies, such as studies by Anderson et $al.$ on CS-deposited Pt_7/alumina and various sized Pt_n/silica [311, 314]; in these studies the CO-TPD spectra changed in shape with repeated TPD cycles to 700 K in a similar manner, where the higher temperature binding site decreased in peak size and temperature, while the lower temperature binding site increased in peak size slightly. The agglomeration of Ru on SiO_2 was not surprising, and was most likely due to a weak cluster-surface interaction of Ru with SiO_2; previous studies have also shown agglomeration of small clusters on SiO_2 at temperatures below 800 K [9, 331].

In addition to aggregation of the Ru clusters, there was most likely also a change in either the cluster structure beyond the agglomeration or cluster-surface interaction with repeated CO-TPD cycles; this is evidenced by the peak CO desorption temperature decreasing with each CO-TPD cycle, meaning CO was adsorbing less strongly to the clusters after agglomeration. This is also supported by earlier studies by Anderson et $al.$ [57, 311, 314], where it was shown that for both Pt_n/alumina ($2 \leq n \leq 18$) and Pt_n/silica ($n = 4, 7, 12, 24$), the intensity of the high temperature CO-TPD peak increased as cluster size increased, but that repeated CO-TPD cycles caused the peak decrease in intensity and shift to lower temperatures. This provided evidence in the case of small Pt clusters that agglomeration produces different structures than those produced by deposition of larger size-selected clusters.

By making reasonable assumptions, the increase in cluster size over the four CO-TPD cycles was estimated. The 4th cycle had 0.3 CO desorbing per Ru atom compared to 0.6 CO per Ru atom in the 1st cycle. Total CO desorption is proportional to the number of CO binding sites. The simplest case was assumed employing a model which disregarded the individual atoms forming the clusters, using hemispherical clusters pinned to the substrate where the number of binding sites was assumed to be proportional to the surface area (SA). If the bottom half of a hemispherical cluster is bound to the substrate and not available for binding to CO, then the available SA of the clusters would be given by Equation 4-1 for the SA of a hemisphere.

$$SA_{(hemisphere)} = 2\pi r^2 \qquad\qquad \text{4-1}$$

Utilising the number of CO desorbing per Ru atom in each cycle, and the assumption that available binding sites are proportional to available SA, the increase in cluster radius was calculated as per Equations 4-2 and 4-3. Subscripts correspond to the SA or radius of clusters in the 1st or 4th cycle.

$$\frac{0.6\ molecules/atom}{0.3\ molecules/atom} = \frac{SA_{(1st)}}{SA_{(4th)}} \qquad\qquad \text{4-2}$$

By substituting in the relationship between SA and radius for each cycle from Equation 4-1 and simplifying the expression, the change in radius was estimated.

$$r_{(4th)} = 1.4 * r_{(1st)} \qquad\qquad \text{4-3}$$

The Ru cluster radius increased by an estimated factor of 1.4 after 4 CO-TPD cycles. Given that there would be a range of aggregated cluster sizes, this should be treated as an average size. The diameter of supported Ru_3 is estimated to be 0.265 nm based on the interatomic Ru-Ru distance (bond length) [375], and the clusters therefore increased to an average diameter of 0.37 nm after the 4th CO-TPD cycle. The assumptions made in this calculation are rather simplified and needs to be taken with caution. The assumption of a hemispherical cluster is a rather simple model and likely deviates from the true structure of the supported clusters and also ignores the finite size of the atoms forming the clusters. The calculation also ignores any effects of the cluster structure and size, or the number of binding sites available per SA.

4.4.1.2 CO-TPD of CS Ru$_3$/RF-TiO$_2$

Figure 4-2 shows the CO-TPD of CS Ru$_3$ and blank measurements on three differently prepared RF-TiO$_2$ substrates; a) NS-RF-TiO$_2$, b) LDS-RF-TiO$_2$, and c) HDS-RF-TiO$_2$. This allows for the comparison of the desorption spectra between RF-TiO$_2$ and the SiO$_2$ substrate used in Figure 4-1. The use of the three different RF-TiO$_2$ substrates allows for determining the effect of pre-deposition substrate sputtering on the available Ru-CO sites on the clusters, which can provide information about the effect of surface defects on the cluster-surface interaction.
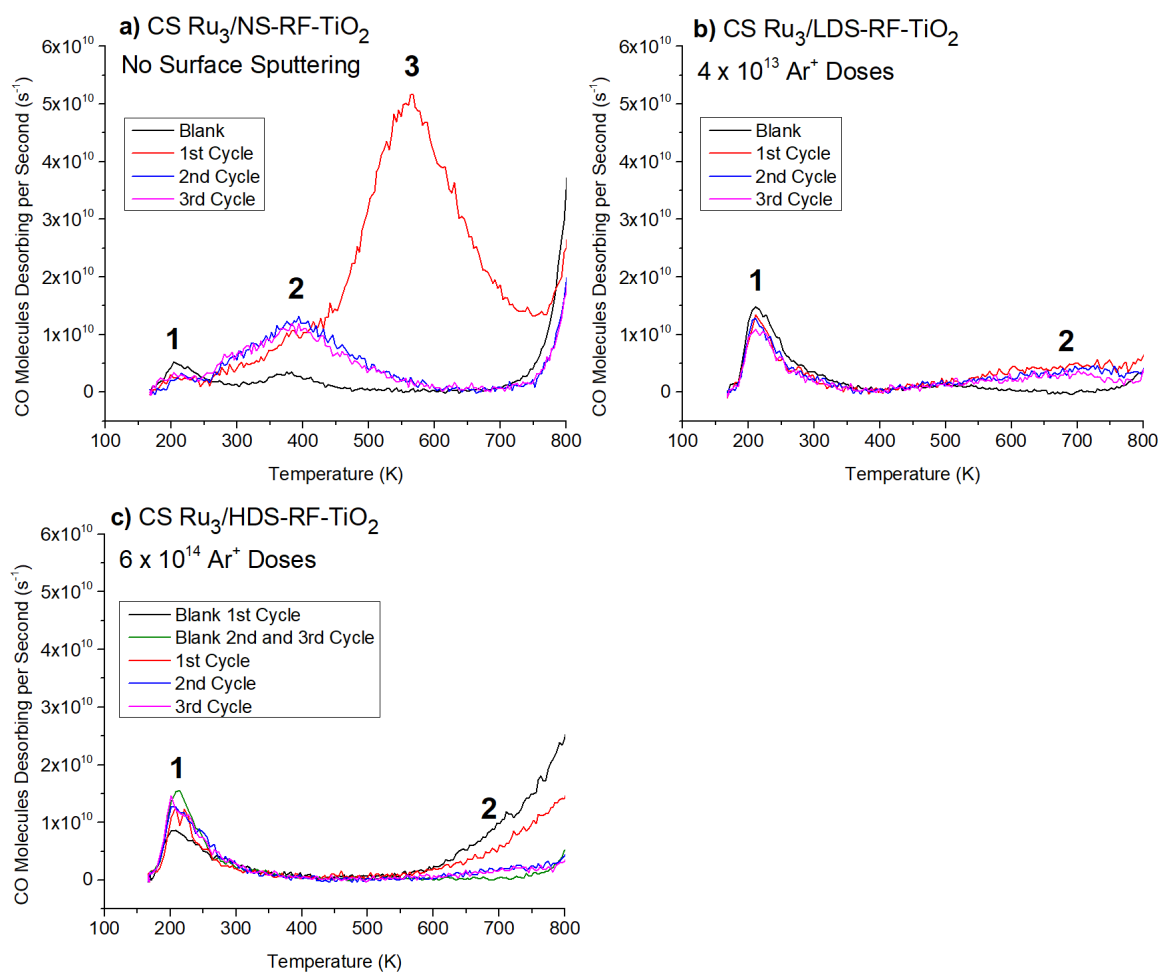
Figure 4-2: **^{13}CO-TPD of CS Ru$_3$ on RF-TiO$_2$ substrates with varying pre-deposition sputtering treatments. Blank measurements are included for each substrate (before Ru$_3$ deposition). a) CS Ru$_3$/NS-RF-TiO$_2$; peaks identified at 210 K (1), 380 K (2), and for the 1st cycle only at 560 K (3). b) CS Ru$_3$/LDS-RF-TiO$_2$; peak identified at 210 K (1), and a broad feature is present at (2). c) CS Ru$_3$/HDS-RF-TiO$_2$; peak identified at 210 K, and a broad feature is present at (2). The blank CO-TPD measurements for NS-RF-TiO$_2$ and LDS-RF-TiO$_2$ are averages of 3 cycles where there were no noticeable changes. For HDS-RF-TiO$_2$ two blank measurements are shown: the 1st cycle and an average of the 2nd and 3rd cycles. These are shown because there was a change in the blank spectrum after the 1st cycle. This is presumably because the HDS-RF-TiO$_2$ blank featured more hydrocarbons adsorbing from the vacuum before the CO-TPD cycle was started, because defected TiO$_2$ is more reactive than pristine TiO$_2$ [204].**

For the NS-RF-TiO$_2$ substrate (Figure 4-2a), the blank measurement shows 2 desorption features at 210 K and 380 K (Figure 4-2a). The 1st CO-TPD cycle for the cluster-loaded CS Ru$_3$/NS-RF-TiO$_2$ features a similar CO-TPD spectrum to the 1st cycle on SiO$_2$ (Figure 4-1). The peak at 210 K due to the blank NS-RF-TiO$_2$ substrate was still present when clusters were on the surface but was reduced in size by approximately half. This was a result of the Ru$_3$ binding to and covering these low energy CO binding sites on the substrate. In addition, a shoulder feature at 380 K and a large desorption peak at 560 K (the main peak) were present. These appeared to be shifted versions of the 260 K and 530 K peaks present for CS Ru$_3$/SiO$_2$.

The 2nd and 3rd heating cycles for CS Ru$_3$/NS-RF-TiO$_2$ (Figure 4-2a) have a consistent CO desorption shape which is different to that of the 1st cycle. They still have the 380 K feature from the 1st cycle, with a slightly increased height and width, but the 560 K main desorption peak has been completely removed. Thus, heating to 800 K caused the loss of the most strongly-binding and most numerous CO binding site on the Ru clusters. The increase in desorption of the 380 K peak after heating was not proportional to the loss in signal of the 560 K peak, indicating that after heating there was less CO binding sites available overall. The changes in the CO-TPD spectra cannot be associated with cluster agglomeration alone, because the result would be a CO desorption shape more like that of CS Ru$_3$/SiO$_2$ on the 2nd to 4th CO-TPD cycles (Figure 4-1), where agglomeration occurred but the peak was not lost completely. As such, agglomeration was ruled out as the sole cause for the change in CO desorption after the 1st cycle. The XPS results for the XPS samples provided further insights into the loss of the main desorption peak, by providing evidence that heating to 800 K caused a change in oxidation state of the clusters. It is likely that the clusters were oxidised by the surface when heated, which blocked the main Ru-CO binding site. This is discussed further in detail in in section 4.4.3.2, after the discussion of the XPS results. Some agglomeration may have also contributed to the loss of the peak, which cannot be ruled out with this data.

The blank CO-TPD spectra for the sputtered substrates, namely LDS-RF-TiO$_2$ and HDS-RF-TiO$_2$ (Figure 4-2b and Figure 4-2c respectively) feature one main peak at 210 K, which was larger than that of the blank NS-RF-TiO$_2$ (Figure 4-2a). Because the CO desorption rate for the 210 K peak increased for sputtered RF-TiO$_2$, it is likely that this peak was related to CO adsorbed to defected surface regions on the blank RF-TiO$_2$. The second, 380 K peak present for the blank NS-RF-TiO$_2$ was not present on blank LDS-RF-TiO$_2$ or HDS-RF-TiO$_2$; however, the LDS-RF-TiO$_2$ spectrum has a second, wider desorption feature at 500 K which

may be a shifted version of the 380 K peak seen for blank NS-RF-TiO$_2$. For the blank HDS-RF-TiO$_2$ spectrum (Figure 4-2c) there is no such desorption feature, which may indicate the 380 K feature for blank NS-RF-TiO$_2$ was from CO binding sites on non-defected, pristine RF-TiO$_2$ regions, and the binding site was modified by sputtering (for LDS-RF-TiO$_2$) before being lost completely at a higher sputter dosage (for HDS-RF-TiO$_2$).

The CO-TPD spectrum for the CS Ru$_3$/LDS-RF-TiO$_2$ sample (Figure 4-2b) features a broad CO desorption peak for all cycles which was not seen for the blank sample, with a deviation from blank at 550 K. For CS Ru$_3$/HDS-RF-TiO$_2$ (Figure 4-2c) there was a similar deviation from the blank sample (2nd and 3rd cycle) above 550 K, although the exact shape was not the same. In both cases this may have been due to desorption from cluster-modified titania binding sites, or the desorption of background contamination. None of the characteristic CO desorption features seen in the CS Ru$_3$/SiO$_2$ sample were present for Ru$_3$ on either sputtered RF-TiO$_2$ substrate. This means the clusters were interacting with the sputtered RF-TiO$_2$ in such a way that all Ru-CO binding sites were blocked, both before and after the sample was heated for CO-TPD. Although agglomeration and/or oxidation may have contributed to the loss of Ru-CO binding sites, the complete loss of all sites suggests a different mechanism for the blocking of sites on LDS- and HDS-RF-TiO$_2$ substrates. The cause of site-blocking for these samples was most likely that the clusters were not present in the outermost layer, as a result of being covered by substrate material. This is expanded upon in detail in the Discussions section 4.4.3.3. There was good repeatability between the three CO-TPD cycles for both CS Ru$_3$/LDS-RF-TiO$_2$ and CS Ru$_3$/HDS-RF-TiO$_2$, showing the resultant Ru/TiO$_2$ systems were stable and not changed significantly by heating to 800 K.

4.4.1.3 CO-TPD of CVD Ru$_3$(CO)$_{12}$/HDS-RF-TiO$_2$

The 1st cycle CO-TPD desorption shape for CVD Ru$_3$(CO)$_{12}$/HDS-RF-TiO$_2$ (Figure 4-3) features a smaller peak at 300 K and a larger peak at 600 K. The CO-TPD shape is very similar to the 1st cycle of both CS Ru$_3$/SiO$_2$ (Figure 4-1) and CS Ru$_3$/NS-RF-TiO$_2$ (Figure 4-2a). The peak CO desorption rate from the 1st cycle in Figure 4-3 was 6.0 x 10^{11} molecules/s, which is ~12 times greater than that of CS Ru$_3$ on NS-RF-TiO$_2$, which had a maximum of 5.2 x 10^{10} molecules/s (Figure 4-2a) and ~7 times greater than CS Ru$_3$/SiO$_2$ which had a maximum of 8.3 x 10^{10} molecules/s (Figure 4-1). This higher desorption rate was due to a greater number of CO molecules per Ru atom on the ligated clusters, in addition to a ~3 times greater Ru surface coverage for the CVD Ru$_3$(CO)$_{12}$ sample (see Table 4-4 in section 4.4.2.3 below). For the 2nd and 3rd cycles, the shape and intensity of the ^{13}CO desorption changes significantly from ^{12}CO in the 1st cycle (Figure 4-3), and has a

shape unique from that of the earlier CS-deposited samples. No characteristic Ru-CO binding sites are present which indicates the Ru-CO sites are being blocked, but there is a broad CO desorption peak from 180 K to 650 K, which retains the same shape and intensity between the 2nd and 3rd cycle.
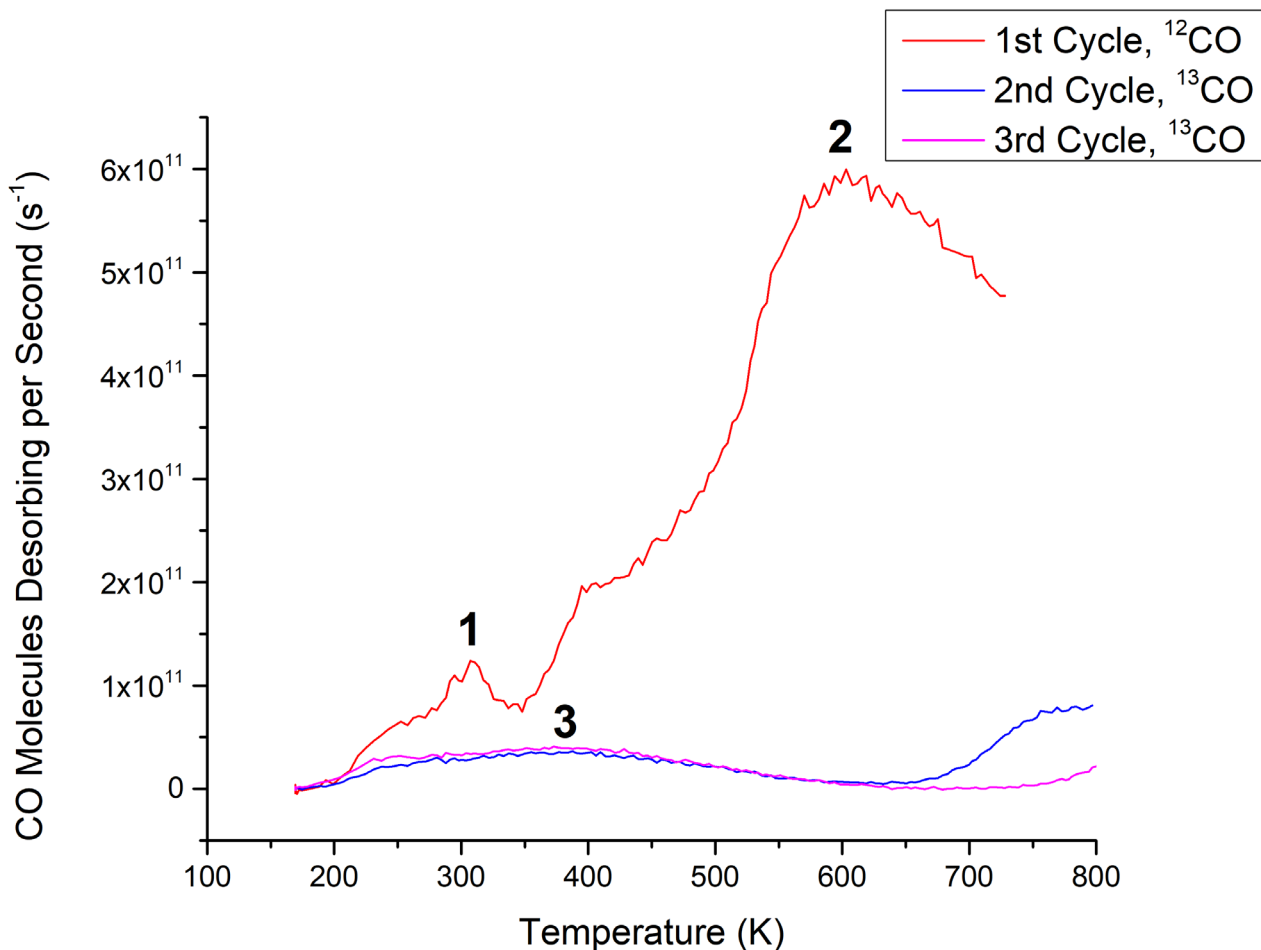
Figure 4-3: CO-TPD for CVD Ru₃(CO)₁₂/HDS-RF-TiO₂. The ¹²CO spectrum (related to CO ligands) is shown for the 1ˢᵗ cycle and ¹³CO spectra (related to *in situ* dosed CO) are shown for the 2ⁿᵈ and 3ʳᵈ cycles. ¹³CO was only dosed in vacuum for the 2ⁿᵈ and 3ʳᵈ cycles (see section 4.3.4 for more details). Peaks were identified for the 1ˢᵗ cycle at 300 K (1) and 600 K (2), while a broad desorption feature (3) was identified for the 2ⁿᵈ and 3ʳᵈ cycles.

There are differences between the 1ˢᵗ cycle CO desorption spectra of CVD Ru₃(CO)₁₂/HDS-RF-TiO₂ (Figure 4-3) and the 1ˢᵗ cycle spectra of the previously discussed CS-deposited samples; CS Ru₃/SiO₂ (Figure 4-1) and CS Ru₃/NS-RF-TiO₂ (Figure 4-2a). The CVD Ru₃(CO)₁₂/HDS-RF-TiO₂ sample low temperature peak was at 300 K, while CS Ru₃/SiO₂ and CS Ru₃/NS-RF-TiO₂ featured desorption peaks at 260 K and 380 K, respectively. Another difference between the 1ˢᵗ cycle CO-TPD spectra of the samples is the temperatures of the main, higher-temperature desorption peaks: 600 K for CVD

Ru$_3$(CO)$_{12}$/HDS-RF-TiO$_2$, 560 K for CS Ru$_3$/NS-RF-TiO$_2$, and 530 K for CS Ru$_3$/SiO$_2$. This indicates that although the Ru-CO binding sites were similar in these cases, the highest binding energy site was strongest for CVD Ru$_3$(CO)$_{12}$, followed by CS Ru$_3$/RF-TiO$_2$, then CS Ru$_3$/SiO$_2$. However, the main peak starts at ~400 K for each of these samples, and because the CVD Ru$_3$(CO)$_{12}$/HDS-RF-TiO$_2$ sample extends to the highest temperature this may indicate it has a slightly wider range of binding sites with differing energies that were not individually resolved in the spectra. The difference in peak desorption temperatures for the large peak between the samples may be due to a combination of multiple effects. Firstly, the direct contact of clusters to the substrate for the bare CS Ru$_3$ may alter the electron density in the clusters and weaken the bond with CO compared to the ligated sample. Secondly, this could be due to less CO binding to the CS clusters, which effected the Ru-CO binding energy. Lastly, because CS Ru$_3$/SiO$_2$ had the lowest peak temperature, it follows that the strong interaction between Ru$_3$ and RF-TiO$_2$ stabilised the Ru-CO bonding when compared to the less strongly interacting SiO$_2$ substrate.

The 1st cycle CO-TPD spectrum of CVD Ru$_3$(CO)$_{12}$/HDS-RF-TiO$_2$ (Figure 4-3) is similar to what Zhao *et al*. [75] previously measured for Ru$_3$(CO)$_{12}$ on TiO$_2$(110) when deposited by CVD at 300 K. However, in this case the large main peak featured a lower temperature shoulder at ~550 K not seen in Figure 4-3, and additionally the relative heights and specific peak locations of the features were slightly different. It is likely these differences are related to differences in cluster-surface interaction between the TiO$_2$(110) used in that study and HDS-RF-TiO$_2$ used in this study.

A key difference comparing the full set of CO-TPD cycles for CVD Ru$_3$(CO)$_{12}$/HDS-RF-TiO$_2$ (Figure 4-3) to CS Ru$_3$ on sputtered RF-TiO$_2$ (CS Ru$_3$/LDS-RF-TiO$_2$ and CS Ru$_3$/HDS-RF-TiO$_2$, see Figure 4-2) was that for the CS samples, Ru-CO binding sites were completely blocked for the as-deposited samples, but for CVD Ru$_3$(CO)$_{12}$ the sample needed to be heated in the CO-TPD procedure before Ru-CO sites were blocked. It would appear that the CO ligands on CVD Ru$_3$(CO)$_{12}$ prevented the Ru-CO sites from being blocked by the HDS-RF-TiO$_2$ substrate until the ligands were removed by the heating process during the 1st CO-TPD cycle. That is to say, the cluster-substrate interaction which blocks the Ru-CO sites does not preferentially replace ligands which are already present on the clusters. The mechanism for this site blocking is discussed below in detail together with the CS-deposited samples in section 4.4.3.3. Since the clusters will pin to the defect sites on sputtered TiO$_2$ [5, 222], these ligated Ru clusters were likely to be well-pinned to the substrate and present as unique, monodispersed cluster complexes before the ligands were removed due to

heating. An additional difference is that the CVD $Ru_3(CO)_{12}$/HDS-RF-TiO_2 was the only sample deposited *ex situ* and exposed to atmosphere. This caused the passivation of defect states in the titania due to interaction with atmospheric gasses (shown and discussed below in XPS Results section 4.4.2.2). This most likely accounts for the differences in shape between the 2nd and 3rd cycle CO-TPD spectra between CS Ru_3/HDS-RF-TiO_2 (has a small feature at high temperature) and CVD $Ru_3(CO)_{12}$/HDS-RF-TiO_2 (has a much broader desorption feature starting at a lower temperature); even after the ligand removal, the differing cluster-surface interaction between the Ru and titania due to the passivated defects of the CVD sample changed the resultant available CO sites on the modified substrate.

4.4.2 XPS Results

4.4.2.1 Metallic Ru Reference Sample

Figure 4-4 shows the XPS spectrum for the Ru 3d region of a Ru reference sample, which was fitted with one asymmetrical Ru doublet. The Ru $3d_{5/2}$ peak is located at 279.7 eV ± 0.2 eV and the doublet peak separation is 4.17 eV. This is comparable to the Ru $3d_{5/2}$ BE reported by Morgan [372] for metallic Ru at 279.75 eV. The $3d_{5/2}$ BE serves as a reference point for comparison to the BE of the Ru cluster samples. This spectrum was also used as a reference model for fitting the Ru 3d/C 1s regions for cluster samples, as discussed in section 3.6.1.3.
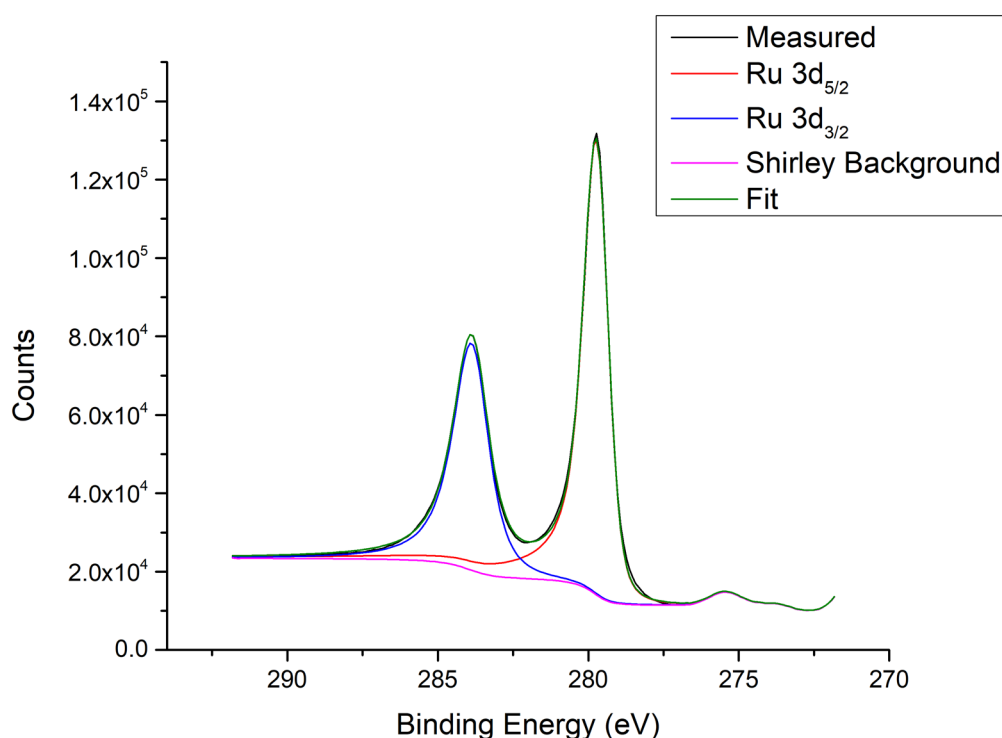
Figure 4-4: XPS results for Ru metallic reference sample - Ru 3d region peak fitting. Measurement was after heating the sample to 1073 K and sputtering for 1 hour to remove hydrocarbon contamination and surface Ru oxides.

4.4.2.2 Ti 2p Region – Surface Defects

The Ti 2p regions were measured for RF-TiO$_2$ substrates and fitted using two sets of peak doublets, as shown in Figure 4-5a for NS-RF-TiO$_2$ and Figure 4-5b for HDS-RF-TiO$_2$ as examples. The doublets correspond to the Ti^{4+} and Ti^{3+} oxidation states; for the 2p$_{3/2}$ state the former is found at 459.4 eV ± 0.2 eV, and the latter at 457.8 eV ± 0.2 eV. A higher Ar$^+$ sputter dose will yield more Ti^{3+}, which is related to titania defect states. The fitting of Ti 2p is complicated by a changing background signal between the lower and higher BE peaks of the Ti doublets, which led to a consistent discrepancy between the measured and the fitted spectra for all samples in the region between the peaks. To reduce the relative uncertainty of the result of the fitting, the fitting and analysis procedure was kept consistent for all Ti 2p measurements.
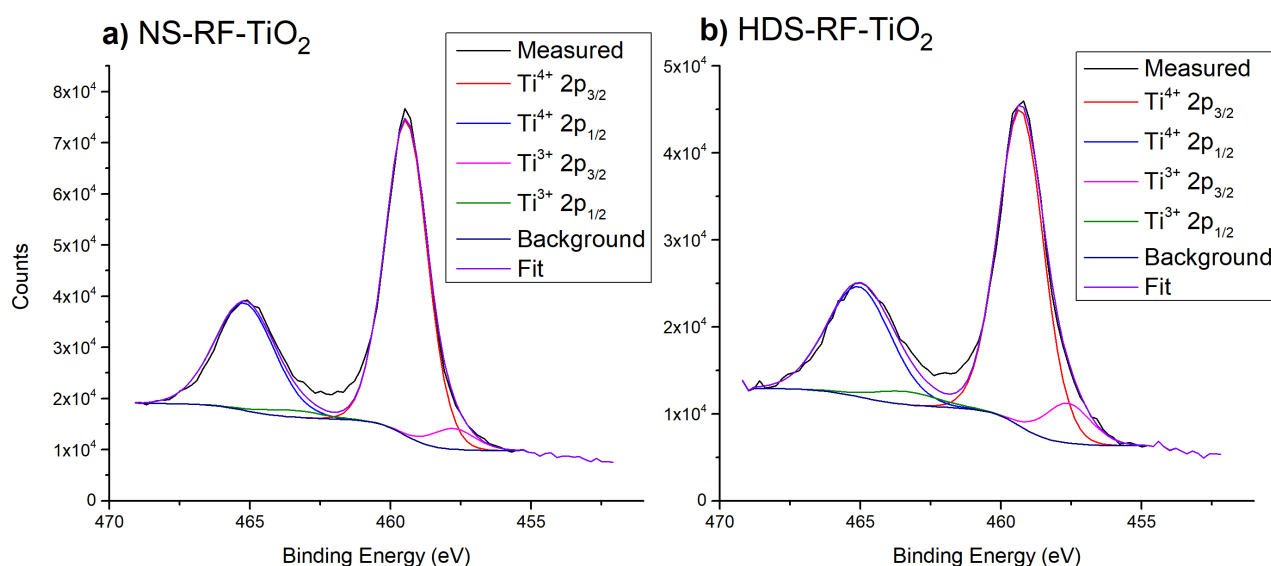
Figure 4-5: Example peak fittings for Ti 2p region, after heating samples to 800 K. a) NS-RF-TiO$_2$. b) HDS-RF-TiO$_2$.

The results from the XPS fitting procedure are shown in Table 4-3. Ti^{Total} is the sum of both peak areas, and the ratio of Ti^{3+}/Ti^{Total} was used as an approximation for the concentration of surface defects for each substrate. In the case of this discussion, less than 5% Ti^{3+}/Ti^{Total} is considered as negligible surface defects. The uncertainty in the Ti^{3+}/Ti^{Total} ratio was estimated and discussed in section 3.6.1.3. The Ti^{3+}/Ti^{Total} ratio is 6% ± 15% for the blank NS-RF-TiO$_2$ sample after heating to 800 K. This shows that defects were present to some extent on non-sputtered TiO$_2$. The level of defects in the blank NS-RF-TiO$_2$ at 800 K was greater than when CS Ru$_3$ was deposited on the same type of substrate; this can be attributed to the clusters preferentially binding to the Ti^{3+} defect sites on the surface [5, 222], which decreases the amount of Ti^{3+}. There is no significant change in the Ti^{3+}/Ti^{Total} ratio for

CS Ru$_3$/NS-RF-TiO$_2$ upon heating to 800 K. The Ti^{3+}/Ti^{Total} ratio of CS Ru$_3$/HDS-RF-TiO$_2$ at 800 K was 11% ± 15%, greater than that of all other samples. The greater number of defects was expected due to the pre-deposition Ar$^+$ sputtering process. For CVD Ru$_3$(CO)$_{12}$/HDS-RF-TiO$_2$, the Ti^{3+}/Ti^{Total} ratio was only 4% ± 15% after heating to 800 K; this was lower than expected for CS Ru$_3$ on the same type of substrate. This was likely due to a combination of the ~3 times greater Ru surface coverage of CVD Ru$_3$(CO)$_{12}$ (see Table 4-4) passivating the Ti^{3+}, in addition to some defect passivation from atmospheric exposure which could not be reversed by heating to 800 K.

Table 4-3: Summary of At% for Ti^{4+} and Ti^{3+} for blank and Ru cluster-loaded RF-TiO$_2$ samples. The Ti^{3+}/Ti^{Total} ratio in % is calculated according to $\frac{100\% \times At\%(Ti^{3+})}{At\%(Ti^{Total})}$. The uncertainty is ± 1% for Ti^{4+} At%, and ± 15% for both the Ti^{3+} At% and Ti^{3+}/Ti^{Total} ratio.

| Deposition	Substrate	Sample Treatment	Ti^{4+} At%	Ti^{3+} At%	Ti^{3+}/Ti^{Total} ratio (%)
Blank	NS-RF-TiO$_2$	800 K heating	24.1	1.6	6
CS Ru$_3$	NS-RF-TiO$_2$	As deposited	22.2	0.8	3
CS Ru$_3$	NS-RF-TiO$_2$	800 K heating	23.1	0.8	3
CS Ru$_3$	HDS-RF-TiO$_2$	800 K heating	23.4	2.9	11
CVD Ru$_3$(CO)$_{12}$	HDS-RF-TiO$_2$	As deposited (*ex situ*)	16.9	0.3	2
CVD Ru$_3$(CO)$_{12}$	HDS-RF-TiO$_2$	800 K heating	23.2	1.0	4

4.4.2.3 Ru 3d/C 1s Region – Clusters

The peak location of Ru 3d$_{5/2}$ was dependent on the deposition method, substrate, and additional sample processing such as heating or dosing CO under UHV. No carbon was present in the stoichiometry of the substrate or clusters (excepting for ligated Ru$_3$(CO)$_{12}$), and thus all carbon present was contamination on the surface or in the bulk structure of RF-TiO$_2$. Figure 4-6 shows an example of the peak fitting for the Ru 3d and C 1s region of a cluster-loaded sample, and Figure 4-7 shows XPS results for Ru clusters on SiO$_2$ and RF-TiO$_2$ after deposition of the Ru$_3$ clusters and specific treatments. Figure 4-7 shows overlayed XPS spectra without peak fitting applied. The intent of this is to show whether the Ru 3d peak has shifted as a result of heat treatment (or other sample treatments) for the different samples. These BE shifts are then summarised in Table 4-4. More details on peak fitting are provided in section 3.6.1.3, including the assigning of the three C 1s peaks.
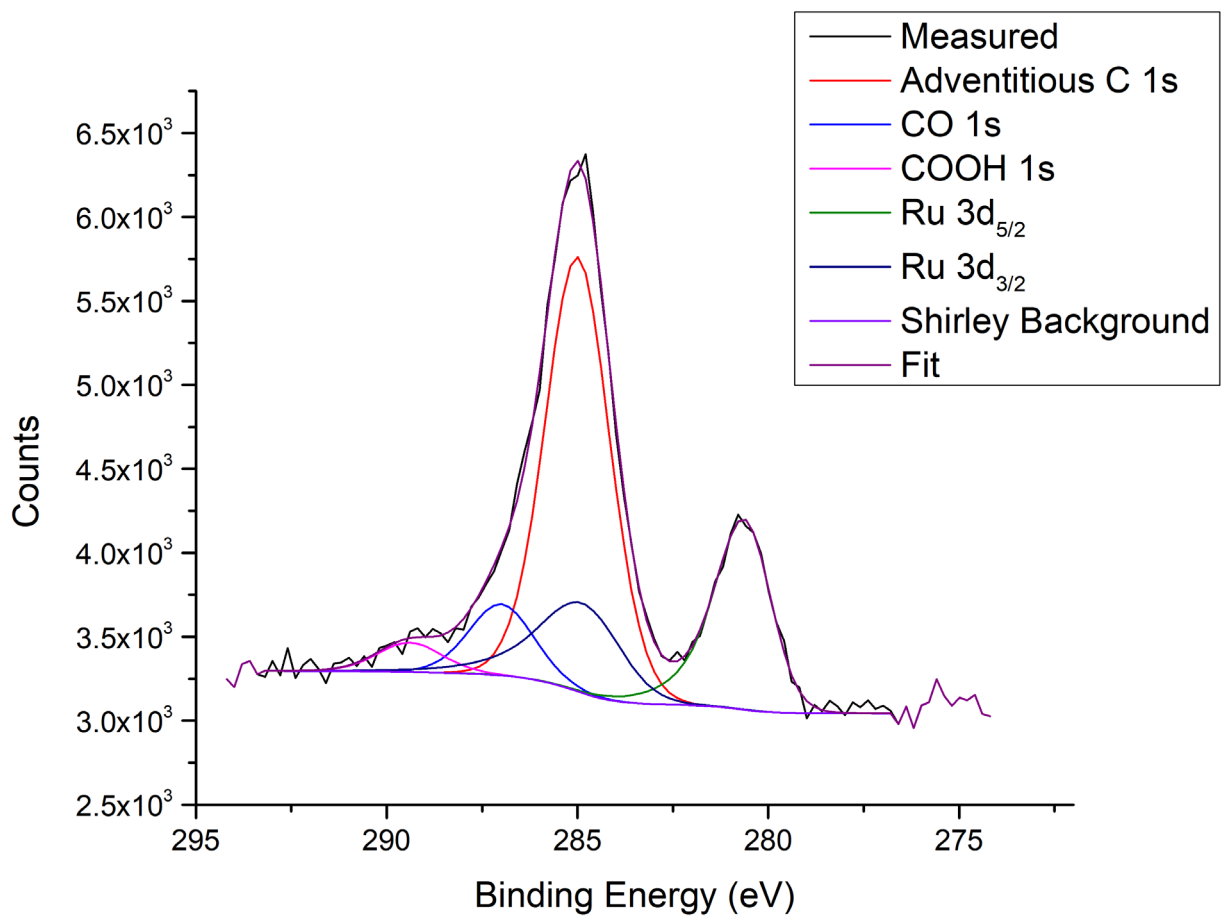
Figure 4-6: Example fitting for the Ru 3d/C 1s region; measurement of CS Ru$_3$/HDS-RF-TiO$_2$ after heating to 800 K.
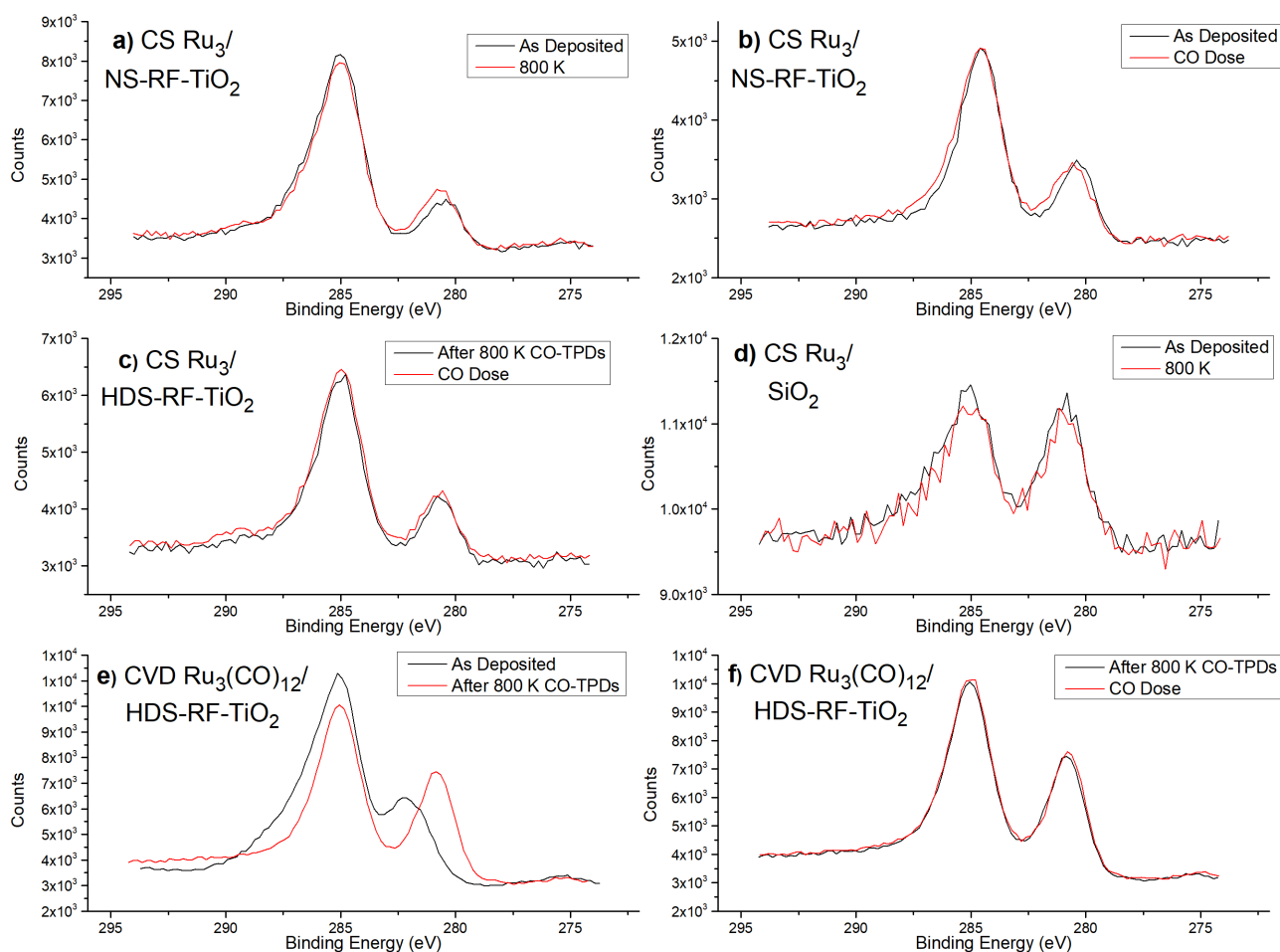
Figure 4-7: XPS spectra of Ru 3d/C 1s region for CS Ru3 (a-d) and CVD Ru3(CO)12 (e-f) on various substrates. Different surface treatments are being compared with XPS to show whether they cause a shift in the Ru 3d peak, and some spectra are repetitive. The lower BE peaks at 280.2-282.0 eV are from Ru 3d5/2 and are the peak of interest for peak shifting. a) CS Ru3/NS-RF-TiO2 – as-deposited, and after heating to 800 K. b) CS Ru3/NS-RF-TiO2 – as-deposited, and after CO dose. c) CS Ru3/HDS-RF-TiO2 – after CO-TPD to 800 K, and after CO dose. d) CS Ru3/SiO2 – as-deposited, and after heating to 800 K. e) CVD Ru3(CO)12/HDS-RF-TiO2 – as-deposited, and after CO-TPD to 800 K. f) CVD Ru3(CO)12/HDS-RF-TiO2 – after CO-TPD to 800 K, and after CO dose (performed in series with the measurement in e).

A summary of all XPS measurements is shown in Table 4-4. These are analysis results from the spectra shown in Figure 4-7, and the key details are the Ru surface coverage for each sample, as well as the extent of Ru 3d BE shifting due to the sample treatments (such as heating or CO dosing) which gives information about the oxidation properties of the clusters. The Ru surface coverage was greater for CVD $Ru_3(CO)_{12}$/HDS-RF-TiO2 than for all CS-deposited samples; for example, it is ~3 times greater than CS Ru3/HDS-RF-TiO2. However, all samples had only a fraction of a monolayer (ML) coverage (10.7% ML maximum). Due to the low coverages, it was assumed any cluster-cluster interactions were negligible and the differences in cluster loading would not have significantly affected the properties of the clusters when making comparisons between samples.

Table 4-4: Comparison of XPS results for different treatments of CS Ru₃ and CVD Ru₃(CO)₁₂ clusters on different substrates. Data is from peak fitting of the XPS spectra in Figure 4-7. Ru 3d$_{5/2}$ BE and Ru surface coverage are shown. Each row features XPS measurements before and after a sample treatment step, which have been separated into "Method 1" and "Method 2" (the method number only indicates the order of applying a treatment). Where none is shown for a method, this means the sample was as deposited. Surface coverage values are from Method 1. For samples with an "800 K + CO Dose" method, the sample was cooled to 180 K before dosing. Both CVD Ru₃(CO)₁₂ measurements were performed on a single sample. The uncertainty in BEs is ± 0.2 eV, while for BE differences the uncertainty is ± 0.1 eV. The absolute error in the Ru surface coverage is ~100% while the relative uncertainty is based on the Ru At% and is ± 4%.

Deposition	Substrate	Ru Surface Coverage (% ML)	Method 1		Method 2		BE Shift (eV)
			Method	BE (eV)	Method	BE (eV)	
CS Ru₃	SiO₂	4.0	None	280.7	800 K	280.7	0.0
CS Ru₃	NS-RF-TiO₂	3.1	None	280.2	CO Dose	280.4	0.2
CS Ru₃	NS-RF-TiO₂	3.0	None	280.3	800 K	280.5	0.2
CS Ru₃	HDS-RF-TiO₂	3.1	800 K	280.5	800 K + CO Dose	280.5	0.0
CVD Ru₃(CO)₁₂	HDS-RF-TiO₂	10.7	None	282.0	800 K	280.6	-1.4
CVD Ru₃(CO)₁₂	HDS-RF-TiO₂	10.7	800 K	280.6	800 K + CO Dose	280.6	0.0

For as-deposited CS Ru₃/NS-RF-TiO₂, the Ru 3d$_{5/2}$ peak is found at 280.3 ± 0.2 eV, and after heating to 800 K it is found at 280.5 ± 0.2 eV, thus shifting by +0.2 eV ± 0.1 eV (see Table 4-4 and Figure 4-7a). It should be noted that the relative error in peak position for the same sample before and after heating is smaller than the error for the absolute peak position. The positive BE shift indicated the clusters had become more positively charged, and the BE moved further away from the value for metallic Ru 3d$_{5/2}$ which is 279.7 eV ± 0.2 eV. The BE after heating is comparable to studies in the literature [75, 136] where O₂ was dosed onto Ru₃(CO)₁₂ on TiO₂(110) while heating to purposely form oxidised clusters. In these cases similar BE shifts were measured, and absolute values for Ru 3d$_{5/2}$ were reported as 280.6 eV by Zhao *et al.* [75] and 280.8 eV by Rizzi *et al.* [136]. The similarity between these and the present study provides context for the previously discussed loss of the main 560 K CO desorption peak for CS Ru₃/NS-RF-TiO₂ after heating to 800 K (Figure 4-2a). The

XPS peak shifting and CO-TPD results both point towards the oxidation of the Ru clusters, presumably due to an interaction with the oxygen in the supporting RF-TiO$_2$ because O$_2$ was not dosed onto on the clusters. Based on this, the shifted Ru 3d$_{5/2}$ XPS peak was assigned to a partially oxidised form of the clusters.

When referring to oxidised Ru clusters in this study the exact oxidation state is not known, because the stoichiometric arrangement of the oxidised Ru clusters cannot be easily determined from the data. Thus, when discussing oxidised Ru clusters, no explicit statement is made about the oxidation state. Ruthenium has only a small BE shift when oxidised compared to some metals; Morgan [372] has reported a shift of +1.62 eV for bulk RuO$_2$ compared to bulk metallic Ru. In both the present and referenced studies the Ru 3d$_{5/2}$ BEs for oxidised Ru clusters were lower than those typically reported for oxidised bulk Ru such as RuO$_2$ [372]. This is likely because the stoichiometric ratio for oxidised clusters had less oxygen than RuO$_2$. However, the starting BE was higher for the supported Ru clusters than for bulk Ru, and the differences in core electron properties between bulk samples and small, supported clusters may also have contributed to the small BE shift upon oxidation.

Figure 4-7b shows XPS spectra for as deposited CS Ru$_3$/NS-RF-TiO$_2$ before and after dosing with CO. The Ru 3d$_{5/2}$ peak shifted from 280.2 eV to 280.4 eV but is still lower than the as-deposited CVD Ru$_3$(CO)$_{12}$; 282.0 eV ± 0.2 eV (see Table 4-4). In Figure 4-7c XPS spectra are shown for CS Ru$_3$/HDS-RF-TiO$_2$ after performing CO-TPD cycles to 800 K, and then after dosing with CO ligands. For this sample there was no Ru 3d$_{5/2}$ BE shift (within the resolution of the XPS instrument). It follows that CO does most likely not bind to the clusters for CS Ru$_3$/HDS-RF-TiO$_2$ (to an extent which could be observed in the XPS results). This is supported by the earlier CO-TPD results showing that there was no Ru-CO binding sites available for CS Ru$_3$/HDS-RF-TiO$_2$ (Figure 4-2c). As-deposited XPS was not measured for this sample, however the BE for Ru 3d$_{5/2}$ at 800 K was 280.5 eV ± 0.2 eV (see Table 4-4). This BE is comparable to oxidised CS Ru$_3$/NS-RF-TiO$_2$, which had an identical BE of 280.5 eV ± 0.2 eV. Thus, the clusters were most likely also oxidised by the RF-TiO$_2$ surface by heating to 800 K on sputtered, HDS-RF-TiO$_2$ in the same way as the non-sputtered, NS-RF-TiO$_2$.

For as-deposited CS Ru$_3$/SiO$_2$ the Ru 3d$_{5/2}$ BE was at 280.7 eV ± 0.2 eV (see Table 4-4 and Figure 4-7d) and slightly higher than for the CS Ru$_3$ on RF-TiO$_2$ in this study. The CO-TPD results for the same type of sample do not suggest the higher Ru 3d$_{5/2}$ BE was due to cluster oxidation; if oxidation occurred the ~530 K peak would have most likely been lost, as was

the case for the ~560 K peak for CS Ru_3/NS-RF-TiO_2. The higher Ru $3d_{5/2}$ BE of as-deposited CS Ru_3/SiO_2 was more likely related to a difference in cluster/substrate charge transfer between RF-TiO_2 and SiO_2 supports. There was no noticeable Ru 3d BE shift when heated from to 800 K. It was previously argued that Ru clusters were agglomerated on SiO_2 due to the heating process (see Figure 4-1 and discussion in section 4.4.1.1), and thus the fact that there was no shift in BE indicated that the Ru 3d peak location is not particularly sensitive to cluster size (in the range of approximately 3-atom clusters). This means information on cluster agglomeration was not easy to determine based on XPS peak shifting for Ru, which differs from the case for some other metal clusters such as Au, where the cluster size has been shown to affect core electron BE [66, 72, 73, 102] and it was possible to relate XPS BE to cluster size [73, 98, 102, 287, 288].

For the CVD $Ru_3(CO)_{12}$/HDS-RF-TiO_2 (see Table 4-4 and Figure 4-7e-f), the Ru 3d peak shifted by -1.4 eV ± 0.1 eV to a BE of 280.6 eV ± 0.2eV after heating, due to the loss of CO ligands. The BE for Ru $3d_{5/2}$ after heating to 800 K is the same within experimental uncertainty as the CS Ru_3/NS-RF-TiO_2 and CS Ru_3/HDS-RF-TiO_2 samples, indicating that the CVD clusters were also oxidised by the RF-TiO_2 substrate after heating. When dosing CO onto the clusters after the 800 K heating process, there was no discernible shift in the Ru 3d binding energy (BE). If there was Ru-CO binding occurring one would reasonably expect a positive BE shift, as was the case for dosing CO onto CS Ru_3/NS-RF-TiO_2 (Figure 4-7b). The lack of shift indicates that the Ru-CO binding sites were completely blocked by the substrate after heating to 800 K. This is supported by the earlier CO-TPD data which showed no characteristic Ru-CO desorption peaks for CVD $Ru_3(CO)_{12}$/HDS-RF-TiO_2 after the 1st CO-TPD cycle (Figure 4-3).

4.4.3 Discussions

As a brief summary of the results, the adsorption of CO to CS-deposited Ru_3 clusters was completely blocked when clusters were deposited onto LDS-RF-TiO_2 or HDS-RF-TiO_2, but this was not the case for SiO_2 or NS-RF-TiO_2. After Ru_3/SiO_2 was heated to 800 K for a TPD cycle there was a decrease in peak temperature and size for the high temperature peak in the CO-TPD spectrum which was associated with agglomeration, while for Ru_3/NS-TiO_2 heating caused the complete loss of the high temperature CO desorption peak. In XPS the Ru 3d BE for Ru_3/NS-TiO_2 shifted to slightly higher energies after heating to 800 K, which is associated with a change in oxidation state of the clusters. The higher energy BE after heating to 800 K is shared is position by both Ru_3 and $Ru_3(CO)_{12}$ on HDS-TiO_2.

4.4.3.1 Assigning binding sites to CO-TPD features

Differences in temperature for CO desorption could be due to CO binding to chemically different parts of the cluster (*i.e.* a different binding site) or due to differing cluster-substrate interactions affecting the cluster-CO binding. The shape of the CO desorption trace between successive CO-TPD cycles can provide information about the location of the Ru-CO binding sites on the clusters. This has been attempted in similar experiments including a study by Labich *et al.* [213] of Rh particles supported on TiO_2/Mg where on-top (away from the substrate, highest temperature) and two-fold coordinated bridge (cluster-substrate bridging, medium temperature) positions, as well as a third high-coverage state were identified (low temperature). This study did not have sufficient TPD resolution to identify exact peak positions for the desorption features, but highlights the fact that when on a substrate, cluster-substrate μ_2 bridging bonds are also a possibility. This was also shown by Lee *et al.* [154] for Au_3 clusters on TiO_2(110), who argued that CO was bound to the cluster-substrate interface when dosed under UHV because the LEIS signal for Au was not attenuated by CO adsorption. Regarding the nature of Ru-CO bonds, White *et al.* [128] suggested via a DFT study that the optimised structure for $Ru_3(CO)_1$ features a 1.50 eV terminal μ_1 bond (CO bound to one Ru atom) while $Ru_3(CO)_2$ features an additional bridging μ_2 bond (CO bound to two Ru atoms) with a higher average Ru-CO bond energy of 1.79 eV. This calculation was performed in the gas phase and although not directly comparable to supported clusters, it importantly indicates that μ_1 and μ_2 bonding are possible.

The peaks will first be assigned for the CS Ru_3/SiO_2 sample, which was treated as the baseline for comparisons. As mentioned in the section 3.6.3.3, the accuracy of the absolute TPD intensity calibration is estimated to be ~50%. Figure 4-1 shows that in the 1st cycle there was an average of 0.6 CO adsorbed per Ru atom, or 1.7 CO per Ru_3 cluster. Given the ~50% estimated accuracy, it is likely that most clusters had 2 adsorbed CO per cluster after dosing. The clusters were agglomerated on SiO_2 with each successive CO-TPD cycle, and the main 560 K CO desorption site decreased in size successively while the smaller 260 K desorption feature increased in size after one cycle and then stabilised. As the clusters agglomerate the total number of CO "edge sites" available where the cluster meets the substrate is expected to decrease. Understanding this helps to assign the two main features in Figure 4-1. The 560 K peak was most likely from a μ_2 cluster-substrate bridging site on the cluster edges; this is supported because the CO-TPD peak size decreased with agglomeration, which would preferentially decrease the number of edge sites (as discussed above), and because the higher binding energy of the site supports the likelihood of CO bonding to both the cluster and substrate. This peak also decreased in temperature, which

provides evidence that the adsorption energy of CO to the cluster-substrate bridging sites decreased as clusters agglomerated, which may have been related to a change in cluster charge density. The 260 K feature was most likely from an on-top binding site with μ_1 and/or μ_2 bonding with Ru. The increase in the 260 K peak size after the 1st cycle may indicate that some amount of agglomeration promoted the number of on-top sites compared to edge sites.
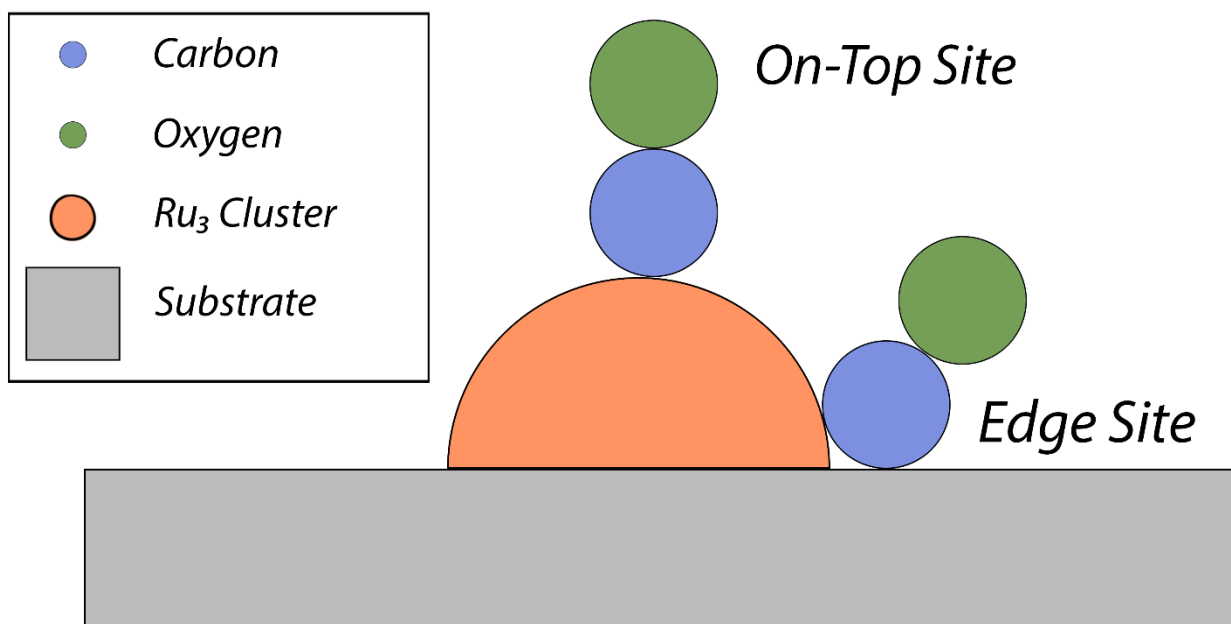
Figure 4-8: Diagram showing the bonding geometry of on-top sites and edge sites for CO molecules adsorbed to Ru$_3$ clusters.

Regarding the CO-TPD samples on TiO$_2$ substrates, for CS Ru$_3$/NS-RF-TiO$_2$ the CO-TPD spectrum (Figure 4-2a) is very similar to CS Ru$_3$/SiO$_2$ in the 1st cycle. The assignment of peaks is therefore the same as for CS Ru$_3$/SiO$_2$, but the peaks were shifted in temperature. For CS Ru$_3$ on sputtered RF-TiO$_2$ surfaces (Figure 4-2b-c), no Ru-CO peaks were observed and there were no CO binding sites to assign. For CVD Ru$_3$(CO)$_{12}$/HDS-RF-TiO$_2$ the high temperature peak (at 600 K) is also assigned to cluster-substrate bridging sites. As previously discussed, this peak is wider in temperature than for the large desorption peak of either CS Ru$_3$/NS-RF-TiO$_2$ or CS Ru$_3$/SiO$_2$, which may indicate a wider range of binding energies are present for bridging sites in this sample, possibly as a result of the larger number of CO molecules per Ru atom. The peak at 300 K (Figure 4-3) is assigned to on-top CO with μ_1 and/or μ_2 bonding, the same as for the other samples.

4.4.3.2 Oxidation of Ru Clusters

For all measured RF-TiO$_2$ substrates, Ru clusters were partially oxidised by heating to 800 K. The CO-TPD peak which was blocked for CS Ru$_3$/NS-RF-TiO$_2$ after the 1st cycle was assigned to cluster-substrate bridging sites, and thus oxygen is either binding to these sites or sterically hindering the access of CO to the sites. The increase in oxidation state can also be a reason for making Ru less attractive for binding to CO ligands. Conversely, when supported on SiO$_2$, the oxidation state of the clusters did not increase by heating to 800 K. This indicated that the change in oxidation state of Ru clusters is not universal for oxygen-containing substrates and was related to the cluster-surface interaction present for the RF-TiO$_2$-supported clusters. Evidence of the substrate-dependent oxidation of clusters has been shown in other studies, and oxidation is typical of the SMSI for clusters on metal-oxide supports [185, 201, 202]. The lack of change in Ru oxidation state on SiO$_2$ is most likely due to the fact that it is a non-reducible oxide, while TiO$_2$ is a reducible oxide [180]. The removal of O^{2-} from non-reducible oxides such as SiO$_2$ is energetically unfavourable and they are more stoichiometrically stable and less reactive [180, 181].

It is likely that the mechanism of cluster oxidation on RF-TiO$_2$ is related to the minimisation of surface energy, where there was an energetic benefit for the system from the oxidation of Ru. The surface free energy of Ru at 298 K has been determined experimentally as 3.409 J/m^2 [389], while the surface free energy of RuO$_2$ was calculated in a separate DFT study as 1.1 J/m^2 for RuO$_2$(110) and 1.4 J/m^2 for RuO$_2$(100) [390]. These two studies used different calculation methods and are not quantitatively comparable for determining the precise change in surface free energy, however the lower surface free energy of RuO$_2$ than Ru provides evidence for the surface-energy minimisation benefit of Ru oxidation. The reduction of free surface energy due to oxidation has been shown more explicitly using calculations for other transition metals [391]. This mechanism can also be considered in terms of the negative enthalpy of formation for oxidised Ru; the energy of formation of transition metal oxides is typically negative, meaning there is an energetic benefit for oxidation and the clusters would lose energy to their surroundings when an oxide is formed [392, 393]. Both the surface energy and the enthalpy considerations have the same meaning.

Heating is required for Ru cluster oxidation on NS-RF-TiO$_2$. The Ru$_3$ clusters on NS-RF-TiO$_2$ showed the lowest oxidation state based on the XPS results, but the oxidation state increased upon heating to 800 K, even after the temperature was reduced. It is probable that for oxidation the transport of O^{2-} anions on the substrate must be activated by heating

such that they are mobilised and can be transported to the clusters; the idea of bulk TiO$_2$ defects becoming mobile at elevated temperatures and interacting with supported metals has been suggested previously [185, 204, 394].

Zhao *et al.* [75] have previously deposited Ru$_3$(CO)$_{12}$ by CVD onto TiO$_2$(110). After heating and ligand removal the authors found that the Ru 3d$_{5/2}$ peak was located at 279.90 eV, which is comparable to bulk Ru. They found by dosing 400 L O$_2$ under UHV at 600 K that the Ru peaks shifted higher to 280.60 eV, which they associated with oxidation of the clusters. This reported BE is comparable to the results for (partially) oxidised Ru in this study, but the necessity for dosing O$_2$ contrasts the results on NS-RF-TiO$_2$ in this study where the clusters were oxidised only after heating to 800 K under UHV. This serves to demonstrate the fact that the SMSI interaction depends greatly on the combination of cluster and substrate, even including different forms of the same material such as TiO$_2$(100) in the work of Zhao *et al.* [75] and RF-TiO$_2$ in this study. Zhao estimated that the cluster coverage was 5% to 25% of a ML, which is comparable to this study, so surface coverage cannot be the reason for the difference in results [75]. It is most likely that the different outcome is related to the differences between nanoparticulate RF-TiO$_2$ and single crystal TiO$_2$(110) substrates; it is possible that TiO$_2$(110) is not as easily reducible as RF-TiO$_2$, or that the surface energy is lower meaning there is less of a driving force for cluster oxidation in terms of surface energy minimisation.

4.4.3.3 Mechanism for Complete Blocking of Ru-CO Binding Sites

The CO-TPD measurements for Ru$_3$ on RF-TiO$_2$ indicate that all Ru-CO binding sites are completely blocked such that no CO is able to adsorb to the clusters when dosed under UHV. For CS Ru$_3$ on RF-TiO$_2$, this phenomenon occurred only when pre-deposition Ar$^+$ sputtering was performed on the substrate. It is seen from TPD that Ru-CO sites are present on NS-RF-TiO$_2$, but completely blocked on LDS-RF-TiO$_2$ and HDS-RF-TiO$_2$. For Ru$_3$(CO)$_{12}$/HDS-RF-TiO$_2$, the Ru-CO sites were present in the 1st CO-TPD cycle (before the ligands were desorbed) but were completely blocked in the 2nd and 3rd cycles after heating to 800 K. This is in contrast to the previously mentioned study by Zhao *et al.* [75], where XPS peak shifting was used to show that for Ru$_3$(CO)$_{12}$ on non-sputtered TiO$_2$(110) that Ru-CO binding was not blocked by the substrate after the sample was heated to 700 K and the ligands were removed.

The fact that Ru-CO sites were only completely blocked if RF-TiO$_2$ was sputter treated, in addition to the differences between depositions onto RF-deposited TiO$_2$ in this study and

TiO$_2$(110) in other studies [75], raises a question about the mechanism for the site-blocking. The Ru-CO blocking cannot be associated with agglomeration only as this would result in CO-TPD spectra like that of CS Ru$_3$/SiO$_2$ (Figure 4-1), or oxidation as this would result in CO-TPD spectra like that of CS Ru$_3$/NS-RF-TiO$_2$ (Figure 4-2a). Encapsulation is another phenomenon separate from oxidation, which can occur for metals supported on a reducible oxide like TiO$_2$. This involves the mass transport of substrate material to the top of the clusters, effectively covering them. This has been shown in the literature for several types of clusters on TiO$_2$ substrates, including the study by Fu *et al.* [185] of 1.5 nm Pd clusters grown on TiO$_2$(110) as well as many other examples over the past few decades [184, 186, 207, 208, 210-213, 386]. Encapsulation leads to the formation of an SMSI state, and there are various proposed reaction mechanisms for encapsulation in the literature, including thermodynamic drive to minimise the total surface energy of the system [185, 203, 207, 210, 211, 213], which has also been considered as a balancing between the metal-metal bonding of the clusters and the metal-oxide bonding of the clusters to the substrate [207, 211]. This mechanism is most likely to occur when the surface energy of the metal is greater than the surface energy of the supporting oxide layer [185, 203, 210, 213], which is the case for TiO$_2$ and Ru, the surface energies of which have been calculated at 1.78 J/m^2 for TiO$_2$(110) [363, 395] and 3.409 J/m^2 for metallic bulk Ru [389]. As such, it is possible that the complete loss of Ru-CO binding sites is due to cluster encapsulation by the substrate material, possibly in combination with other phenomena such as oxidation and/or agglomeration. However, which mechanism is at play is not entirely clear because the data does not directly show the encapsulation, only the blocking of Ru-CO sites. A diagram visualising the geometry of the proposed cluster encapsulation, as well as the oxidation state of the clusters before and after heat treatment, is shown for non-sputtered and sputter-treated RF-TiO$_2$ in Figure 4-9. Further insight into the covering of the clusters by substrate material will be shown in Chapter 5.
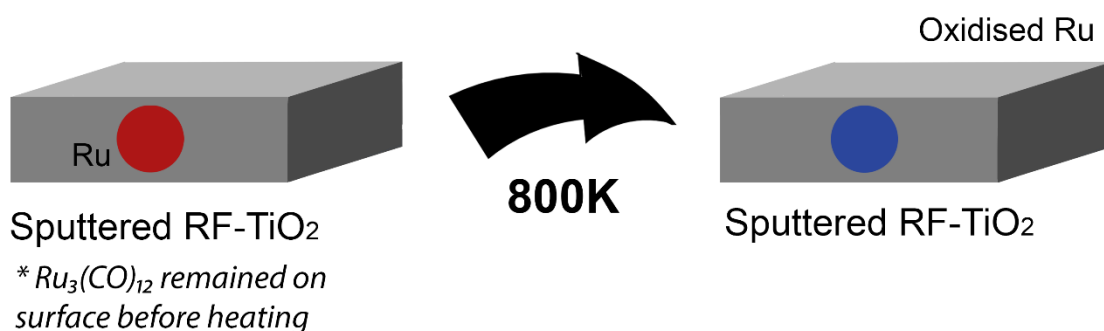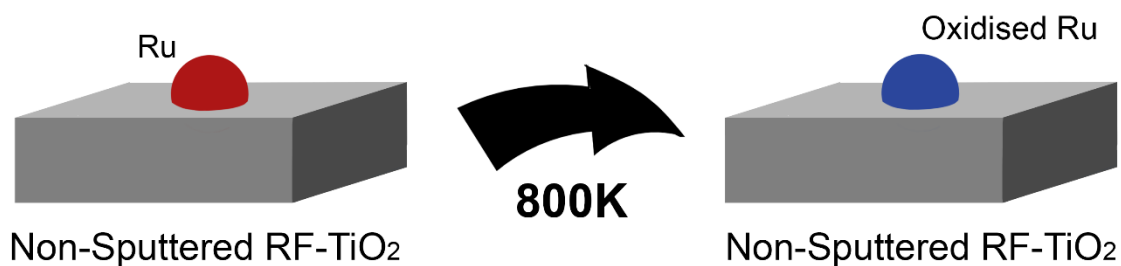
Figure 4-9: Summary of results regarding the encapsulation and oxidation of Ru₃ clusters on non-sputtered RF-TiO₂ (top) and sputtered RF-TiO₂ (bottom), before and after heat treatment. For this diagram, compete blocking of Ru-CO binding sites is interpreted to mean the clusters have been covered by substrate material (encapsulation), and reside beneath the surface layer.

While it is not directly shown by this data, the assumption of encapsulation of the Ru clusters by TiO_2 is supported by similarities to previous findings. A similarity between the study presented here and previous studies on $TiO_2(110)$-supported Pd clusters [185] and Rh nanoparticles [186], is the effect of substrate sputtering on the results. Pd clusters were not encapsulated by non-sputtered $TiO_2(110)$ but were encapsulated by the same substrate with heavier pre-deposition sputtering at 1 keV for 10 minutes [185], and similar results were shown for Rh nanoparticles [186]. This mirrors the present study where Ru-CO binding sites were only completely blocked for CS Ru₃ on sputtered RF-TiO₂. However, a key difference is that in the cases of Pd and Rh on $TiO_2(110)$, heating was required before encapsulation occurred [185, 186], starting for example at ~553 K for Pd [185]. This was interpreted by the researchers as heating activating the mobility of Ti interstitials in the substrate, which outwardly diffused and moved onto the clusters. This was also supported for Rh nanoparticles by Berkó *et al.* [186]. Conversely, in the present study Ru-CO blocking occurred for as-deposited samples, with no heating required.

The lack of heating required for the loss of Ru-CO sites of CS Ru₃ on sputtered RF-TiO₂

points towards an interpretation that the mechanism may have been different to the Pd study, and was not based on the activation of Ti interstitial mobility by heating. Varying conditions have been reported to induce cluster encapsulation, which typically require reduction of the oxide substrate and include high temperature reduction in UHV [184-186, 207-214, 363] or in H_2 [198, 199, 215-217]. The results presented in this study cannot directly provide evidence on the exact mechanism, however mechanisms can be proposed based on results and comparisons to literature. One possible mechanism is that the sputtered RF-TiO_2 was more mobile than the TiO_2(100) used in other studies such as that of Fu *et al.* [185], such that substrate material could migrate to encapsulate the clusters even without additional energy input from heating. However, this seems unlikely as RF-TiO_2 mobility is typically only shown at elevated temperatures [185, 204, 394]. An alternate mechanism could be that sputtering was causing increased surface roughness and surface energy, such that there may have been small, oxygen-deficient pores for the clusters to enter. Ar^+ sputtering at 3 keV has been shown to cause defects in subsurface regions [186], so it is possible that the clusters enter such pores and pin to defect sites. Based on the fact that the surface energy of Ru is higher than that of TiO_2 [363, 389, 395], such pores would be preferred sites for Ru clusters deposited onto sputtered TiO_2. Another driving force for the clusters to enter the subsurface region is the oxygen deficiency of the sputtered TiO_2, where subsurface oxygen is likely more readily available for the Ru_3 than surface oxygen. It should be noted that based on the experimental results shown here it is not possible to determine the size of Ru clusters after heating.

To the best knowledge of the author, there have been no measurements for the encapsulation of size-selected Ru clusters on TiO_2 in the literature, though some studies using similar materials have been conducted. One study by Komaya *et al.* [386] deposited large Ru particles from the $Ru(NO)(NO_3)_3$ organometallic complex onto P25 nanocrystalline TiO_2, and used transmission electron microscopy (TEM) to show that the encapsulation coverage over the particles by an amorphous titania layer increased as the temperature was increased from 573 K to 773 K. Encapsulation has also been shown for Ru clusters supported on surfaces other than metal oxides; Sham *et al.* [396] showed using X-ray Absorption Near-Edge Structure (XANES), atomic emission spectroscopy (AES), and low-energy electron diffraction (LEED), that for $Ru_3(CO)_{12}$ aggregates deposited by a 45 L CVD onto Cu(111), bimetallic clusters with an Ru core and Cu shell were formed by heating to 723 K. Rh particles (neighbouring element to Ru on the periodic table) have also been encapsulated by P25 TiO_2 [216], and TiO_2/Mo [213].

The blocking of cluster-CO binding sites is not generally desired for catalytic purposes because CO adsorption capacity is reduced, which was the case for some samples in this study as well as other works in the literature [185, 186, 213]. As such the results discussed can provide a framework for how to achieve Ru clusters with available Ru-CO binding sites on RF-TiO$_2$ supports for the catalysis of reactions such as CO hydrogenation. While it is possible that conserving Ru-CO binding sites is important for catalytic activity, it should be noted that there are studies which have shown that for thin enough covering layers some combinations of cluster and covering layer can have an electronic structure which is suitable for catalysis and/or photocatalysis, without direct reactant-cluster contact [4, 397, 398]. In these cases, there can be extra benefits for catalysis such as increasing resistance to cluster agglomeration [4, 397], increasing catalytic reaction selectivity [398], or improving catalytic activity by hindering back reactions which remove reaction products [4]. As such catalysis measurements are necessary for experimental verification of this framework.

4.5 Conclusions

When Ru_3 was CS-deposited onto SiO_2, heating the clusters to 800 K caused cluster agglomeration. Conversely, when CS-deposited onto NS-RF-TiO_2, the clusters remained on the surface with all Ru-CO binding sites as-deposited but were oxidised by the substrate when heated to 800 K resulting in the loss of the main CO binding site. This indicated oxygen either bound to the same sites as CO or bound in such a way that CO was sterically hindered, or Ru was less attractive for binding to CO due to an increase in oxidation state. When the RF-TiO_2 substrate was sputtered before CS-depositions the Ru-CO binding sites on the clusters were completely blocked by the substrate as-deposited. For CVD $Ru_3(CO)_{12}$/HDS-RF-TiO_2, the clusters retained their Ru-CO sites as-deposited, but after heating to 800 K the ligands were removed, and the Ru-CO sites were completely blocked. It is possible given the lack of Ru-CO binding sites that the catalytic abilities of the small Ru clusters will be reduced when supported on sputtered RF-TiO_2.

We have developed a set of deposition criteria for Ru_3 clusters to retain their Ru-CO binding sites when supported on RF-TiO_2. For CS depositions the Ru-CO sites will be blocked if the substrate is sputter treated prior to deposition, but when depositing $Ru_3(CO)_{12}$ by CVD the CO ligands are retained on a sputtered substrate. In both cases heating to 800 K will cause cluster oxidation (a partial loss of CO sites) and/or complete Ru-CO blocking. The mechanism for complete Ru-CO blocking on sputtered RF-TiO_2 could not be precisely determined from the presented results, but comparisons to similar studies of metal/TiO_2(100) interfaces [184-186, 207, 208, 210-213, 386] suggested an interpretation that the clusters may have been encapsulated by layer of substrate material. To address the remaining question about the Ru-CO blocking mechanism, Chapter 5 further explores Ru cluster/RF-TiO_2 systems and focusses on temperature-dependent measurements of surfacer properties.

Chapter 5　　The interaction of size-selected Ru₃ clusters with RF-deposited TiO₂: a temperature-dependent XPS, ARXPS, and LEIS study

This chapter is a reformatted and edited version of a manuscript which was submitted for review to a peer-reviewed journal at the time of thesis submission. See the Contextual Statement section for details on the contributions of the co-authors to the journal version of the manuscript.

Reference for the journal version:

L. Howard-Fabretto, T. J. Gorey, G. Li, S. Tesana, G. F. Metha, S. L. Anderson, & G. G. Andersson, Encapsulation of Size-Selected Ru₃ Clusters into RF-Deposited TiO₂, manuscript submitted for review to The Journal of Chemical Physics.

5.1 Abstract

In this study 3-atom Ru₃ clusters were deposited onto radio frequency (RF)-sputter deposited TiO₂ (RF-TiO₂) substrates by both solution submersion and chemical vapor deposition (CVD) of $Ru_3(CO)_{12}$, as well as CS depositions of bare Ru₃. TiO₂(100) and SiO₂ were also used as substrates with differing cluster-surface interactions. Temperature-dependent XPS, angle-resolved XPS, and temperature-dependent low energy ion scattering (TD-LEIS) were used to probe how the cluster-surface interaction changes due to heat treatment. Bare Ru₃ supported on SiO₂ remained on the surface layer but was agglomerated by heating. Conversely, when supported on sputter-treated RF-TiO₂, bare Ru₃ was encapsulated by a layer of titania substrate material as-deposited. Ligated $Ru_3(CO)_{12}$ was covered by a layer of titania only after heat treatment when supported onto sputter-treated RF-TiO₂. TD-LEIS was used to measure the encapsulation of CVD $Ru_3(CO)_{12}$ clusters on sputter-treated RF-TiO₂, and the substrate overlayer thickness was calculated. The overlayer was thin enough that there was potential for catalytic or photocatalytic reactions to occur.

5.2 Introduction

In section 4.2, other studies involving Ru_3 clusters deposited on titania substrates such as $TiO_2(110)$ were examined and their catalytic potential was discussed. The advantages and disadvantages of $RF\text{-}TiO_2$ as a substrate for clusters compared to $TiO_2(110)$ were discussed; in short, $RF\text{-}TiO_2$ is cheaper to produce and has a rougher nanoparticulate structure [357] which is more comparable to supporting substrates used for industrial purposes. The nature of defects and defect mobility in TiO_2 substrates was discussed, and the concept of cluster encapsulation by reducible substrates was introduced.

Two commonly utilised approaches to depositing metal clusters onto substrates are: 1) depositing gas-phase aggregated, bare clusters using a cluster source (CS), and 2) depositing ligand-stabilised clusters. Furthermore, (2) can be split into two classes of methodologies: solution submersion or chemical vapor deposition (CVD). These were introduced in detail in the Literature Review, section 2.4. Each of these methods have different advantages with respect to experimental and industrial applications. They can also affect the resultant cluster properties, however very few studies have directly compared the cluster properties of identically sized clusters resulting from different deposition methods [74]. Thus, it is important to understand how the deposition procedure affects the resulting properties of the clusters.

CS and CVD depositions are both performed *in situ* and are typically suited to experimental work. However, both are difficult to upscale for industrial applications due to the high vacuum required and small cluster deposition areas [20]. Solution submersion depositions, also referred to as solution-based depositions, are advantageous in this area due to the ease of upscale to industrially relevant scales; complex and expensive equipment is not needed, and the volume of cluster solution can be scaled to suit large substrate surfaces [66, 72, 99, 104]. A secondary advantage of solution submersion is that it allows for cluster deposition onto the inside surfaces of porous substrates such as mesoporous silica [76, 77] and zeolites [78, 79], while CS and CVD are line of site. However, solution-based depositions introduce the possibility of extra contamination to the samples due to exposure to atmosphere and the solvent. For both types of ligated cluster depositions (*i.e.* CVD and solution), the ligands are typically removed after deposition using heat or chemical methods to leave bare, surface-supported particles [3, 5, 74, 75].

Clusters can form a strong metal-support interaction (SMSI) with reducible oxides, and in some cases may be covered by a layer of support material [185, 215]. This is known as

"encapsulation" or "decoration" of the clusters [199, 207]. Depending on the combination of cluster and substrate, varying conditions have been required to induce cluster encapsulation, including reduction of the oxide by sputtering prior to cluster depositions [185, 186], and high temperature reduction of the cluster/oxide system in ultra-high vacuum (UHV) [184-186, 207-214]. If a sufficient amount of cluster material is present, these changes are typically measurable using XPS; encapsulation increases the concentration of reduced Ti at the surface which causes a low-BE shoulder in the Ti 2p peak [185, 203].

The encapsulation of clusters can greatly reduce their catalytic and/or photocatalytic ability by means of steric hindrance, where reactant molecules are prevented from reaching the clusters [185, 186, 213]. However, if the covering layer is thin enough some combinations of clusters and covering layer can have an electronic structure which is suitable for catalysis and/or photocatalysis without direct reactant-cluster contact [4, 397, 398]. In these cases there can be benefits such as increasing resistance to cluster agglomeration [4, 397], increasing reaction selectivity [398], or improving activity by hindering back reactions which remove reaction products [4]. As an example, the water splitting photocatalytic activity of $Au_{25}/BaLa_4Ti_4O_{15}$ was increased 19-fold due to cluster encapsulation by 0.8-0.9 nm thick Cr_2O_3, which was attributed to the blocking of the O_2 photoreduction back reaction as well as stabilising the clusters from agglomeration due to UV light [4]. Thus, knowledge about cluster encapsulation is important for catalytic and photocatalytic applications.

Depth profiling techniques are relevant to clusters for measuring the occurrence of cluster encapsulation and thickness of the overlayer. There are various analytical techniques which can be used to depth profile. Angle-resolved XPS (ARXPS) and LEIS are used in this chapter, but others also exist including high resolution transmission electron microscopy (HRTEM) [4]. ARXPS is commonly used for non-destructive depth profiling [399, 400], but is known to be less reliable for surfaces which are non-monotonic or show significant roughness [400]. LEIS is one of the most commonly used ISS variants for supported clusters [6, 9, 57, 60, 208, 308-326]. It allows for measuring the atomic composition of the topmost layer, and can provide depth information about the atomic distribution over the range 0-10 nm below the surface layer depending on the ion energy used [327]. Cluster encapsulation can be detected by LEIS and results in the complete loss of the metal surface peak [208, 308, 319]. One study showed that Rh clusters were completely encapsulated by $TiO_2(110)$ after heating to 900 K [308]. LEIS can determine film thicknesses for surface layers by using calculation methods such as those described by Brongersma *et al.* [401], which has previously been applied to determining the overlayer thickness for functionalised Au

nanoparticles [402, 403].

In this study, size-selected Ru$_3$ clusters were deposited onto RF-TiO$_2$ surfaces using 3 different deposition methods: solution-based, CVD, and CS. Based on the results in the Chapter 4 it was postulated that the encapsulation of small Ru clusters may be the mechanism behind the complete blocking of Ru-CO sites on sputter-treated RF-TiO$_2$. To further explore this, sputter-treated RF-TiO$_2$ substrates were primarily used in this study. The aims were to elucidate how heat treatment affects the cluster-surface interactions between Ru$_3$ and RF-TiO$_2$ and to determine whether the deposition method had any effect on the resultant surface properties after heat-treatment. An additional aim was to directly measure the encapsulation of Ru$_3$ and determine the temperature at which this occurs, in order to elucidate potential catalytic and photocatalytic benefits of the cluster/substrate system. TiO$_2$(110) and SiO$_2$ were used as comparison substrates to assist with analysis. TiO$_2$(110) is the most commonly used form of TiO$_2$ for experiments on supported clusters due to its high stability, photo-activity, ready availability, low cost, and low toxicity [191], and SiO$_2$ was useful for comparison because it does not interact as strongly with the clusters [204].

5.3 Methodology

5.3.1 Substrates

RF-TiO_2, TiO_2(110), and SiO_2 were used as substrates for depositions of Ru_3 by solution submersion and CVD of $Ru_3(CO)_{12}$, as well as CS depositions of bare Ru_3. See section 3.1 in the Instrumentation and Methodologies for information on the RF-TiO_2 and SiO_2 substrates. Similar to Chapter 4, RF-TiO_2 was prepared using 3 different pre-deposition sputtering treatments: namely, NS-RF-TiO_2 (non-sputtered), LDS-RF-TiO_2 (low-dose sputtered, treated with 4 x 10^{13} Ar^+ ions/cm^2), and HDS-RF-TiO_2 (high dose-sputtered, treated with 6 x 10^{14} Ar^+ ions/cm^2). TiO_2(110) was also used as a substrate in this chapter and is described in detail below. A list of the substrates used, and their abbreviated names are given in Table 5-2.

A 99.99% pure single crystal of rutile TiO_2(110) purchased from MTI Corporation was used. It was initially treated by heating to 1050 K for 1 hour under UHV, which has been previously shown to induce oxygen defects in the bulk of the TiO_2(110) turning it blue and making it conductive [330, 382, 404]. The induced conductivity allowed XPS to be performed without the sample charging. Before each experiment, the sample was sputtered with 3 keV Ar^+ for 20 minutes then heated to 900 K for 20 minutes. These procedures followed those used in recent publications by Anderson *et al.* where TiO_2(110) was used as a substrate for metal clusters [6, 60].

Table 5-1: Summary of the different supporting substrates used in this study. The designated sample names and abbreviated names are given.

Substrate Material	Ar^+ Sputter Dose (ions/cm^2)	Designated Sample Name	Abbreviated Name
RF-TiO_2	None	Non-Sputtered RF-TiO_2	NS-RF-TiO_2
RF-TiO_2	4 x 10^{13}	Low-Dose Sputtered RF-TiO_2	LDS-RF-TiO_2
RF-TiO_2	6 x 10^{14}	High-Dose Sputtered RF-TiO_2	HDS-RF-TiO_2
Rutile TiO_2(110) Single Crystal	6 x 10^{14}	TiO_2(100)	TiO_2(110)
SiO_2/Si (100)	None	SiO_2	SiO_2

5.3.2 Instrumentation

Depositions and analysis were performed on 3 separate UHV systems. These included the

University of Utah UHV system used for CS depositions and Flinders University UHV system used for CVD and solution-based depositions (both described in section 3.3). Additionally, ARXPS measurements were performed at the Australian Synchrotron soft X-ray UHV beamline. For these measurements CVD was performed *in situ,* while a CS-Ru$_3$/HDS-RF-TiO$_2$ sample was prepared at the University of Utah and analysed *ex situ*. All 3 systems featured XPS and *in situ* Ar$^+$ sputtering, and LEIS was available on all, except at the Australian Synchrotron.

Flinders University and Australian Synchrotron experiments used 3 keV impact energy for Ar$^+$ sputtering while University of Utah experiments used 2 keV. The defects may extend deeper into the bulk for CVD samples prepared with 3 keV impact energy due to the greater impact energy of the Ar$^+$ [185, 186]. This was not corrected for, with a slightly variation in defects on the substrate deemed not to be of critical importance for this experiment.

5.3.3 Cluster Depositions

5.3.3.1 Chemical Vapor Deposition

CVD was performed *in situ* at both Flinders University and the Australian Synchrotron. Ru$_3$(CO)$_{12}$ clusters were deposited onto HDS-RF-TiO$_2$ substrates. Prior to cluster depositions, RF-TiO$_2$ was heated under UHV to 723 K for 10 minutes then sputtered with Ar$^+$ at 6 x 10^{14} ions/cm^2. The deposited clusters covered the entire sample areas in an approximately even manner. At Flinders University the CVD procedure followed the method described in the Instrumentation and Methodologies section 3.5.1; Ru$_3$(CO)$_{12}$ was deposited in a loading chamber, and deposition times were 120 minutes for RF-TiO$_2$ and 30 minutes for TiO$_2$(110). At the Australian Synchrotron, the clusters were deposited using a modified version of the same procedure. The Ru$_3$(CO)$_{12}$ vial was a greater distance from the sample at the Australian Synchrotron, and due to this the Ru$_3$(CO)$_{12}$ vial was heated to 313 K to increase the deposition rate to a usable level. Clusters were deposited for 90 minutes.

5.3.3.2 Solution Submersion

The solution submersion procedure is described in the Instrumentation and Methodologies section 3.5.2. Ru$_3$(CO)$_{12}$ was deposited *ex situ* onto an HDS-RF-TiO$_2$ substrate, which was analysed with temperature-dependent XPS (TD-XPS). In this chapter clusters which were solution-deposited (SD) are referred to as SD-Ru$_3$(CO)$_{12}$. Prior to removing the substrate from UHV to perform the deposition, RF-TiO$_2$ samples were heated under UHV to 723 K for 10 minutes, then Ar$^+$ sputtered with 6 x 10^{14} ions/cm^2. A concentration of 0.2 mM was used for the Ru$_3$(CO)$_{12}$ solution in dichloromethane. The deposition process coated the whole

surface with an approximately even layer of clusters. Due to the *ex situ* nature of the deposition the substrate and clusters may have been affected by the adsorption of atmospheric gasses which is discussed where necessary.

5.3.3.3 Cluster Source

CS depositions were performed *in situ* by a laser vaporisation CS onto RF-TiO$_2$ and SiO$_2$. The instrument details and standard deposition procedure are given in the Instrumentation and Methodologies section 3.5.3. Prior to cluster depositions, RF-TiO$_2$ samples were heated under UHV to 723 K for 10 minutes, then Ar$^+$ sputtered to the required dosage (except for NS-RF-TiO$_2$ which was not sputtered). SiO$_2$ was heated to 700 K for 20 minutes under an atmosphere of 7 x 10^{-6} mbar O$_2$ to preserve the surface oxide layer, followed by a further 2 minutes of heating under UHV. For CS deposition nominally 1.5 x 10^{14} Ru atoms/cm^2 was deposited. Cluster spots were 2 mm in diameter. A retarding potential was used to achieve a deposition energy of ~1 eV/atom to prevent fragmentation [157].

5.3.4 TD-XPS Methods

The TD-XPS measurement procedure is described in section 3.6.1.4. TD-XPS of solution and CVD-Ru$_3$(CO)$_{12}$ samples were measured at Flinders University using an Mg X-ray anode, while CS-Ru$_3$ samples were measured at the University of Utah XPS using an Al X-ray anode. Differences between the excitation energy and HSA of the two instruments contributed to a difference in line shapes for elements in some cases. The At% and estimated Ru surface coverages for TD-XPS represent averages over all temperatures for each sample. See section 3.6.1.3 for a discussion on errors and uncertainties in the XPS measurements.

TD-XPS measurements were also performed for blank samples corresponding to SD-Ru$_3$(CO)$_{12}$/HDS-RF-TiO$_2$, CVD-Ru$_3$(CO)$_{12}$/HDS-RF-TiO$_2$, and CVD-Ru$_3$(CO)$_{12}$/TiO$_2$(110). For each of these samples, a measurement was performed as per the procedure for a cluster deposition, but no clusters were deposited. This assisted with differentiating when changes in the substrate were due to the presence of clusters. The blank sample for SD-Ru$_3$(CO)$_{12}$/HDS-RF-TiO$_2$ was submerged in dichloromethane solvent for 30 minutes. The blank samples for CVD-Ru$_3$(CO)$_{12}$/HDS-RF-TiO$_2$ and CVD-Ru$_3$(CO)$_{12}$/TiO$_2$(110) were each held in the loading chamber for 5 minutes with no cluster deposition vial present.

5.3.5 ARXPS

ARXPS measurements were performed at the Australian Synchrotron soft X-ray beamline. Two samples were analysed; CVD-Ru$_3$(CO)$_{12}$/HDS-RF-TiO$_2$ deposited *in situ*, and CS-

Ru$_3$/HDS-RF-TiO$_2$ deposited *ex situ* at the University of Utah.

5.3.5.1 ARXPS: Background

Depth information about a surface can be determined using ARXPS by changing the observation angle of the emitted photoelectrons. This varies the distance electrons are able to travel through the sample matter, which affects the depth from which photoelectrons are likely to escape and reach the detector. XPS is typically conducted with the sample normal to the analyser, defined as an observation angle of 0˚. For each ARXPS measurement, XPS scans were taken at observation angles of 0˚, 30˚, 45˚, 55˚, and 60˚. According to work by Baschenko and Nesmeev [405], these angles are within the range which avoids severe angle effects related to the elastic scattering of photoelectrons. Figure 5-1 illustrates how the observation angle affects the measured XPS intensity for a surface elemental species. For increasing observation angles the shortest path for an electron to reach the detector increases in distance through the sample, increasing the chance of re-adsorption events (represented in Figure 5-1 by arrows with square ends). To determine a depth profile from an ARXPS measurement, a model must then be made and fitted to the experimental data for At% measured at each observation angle.
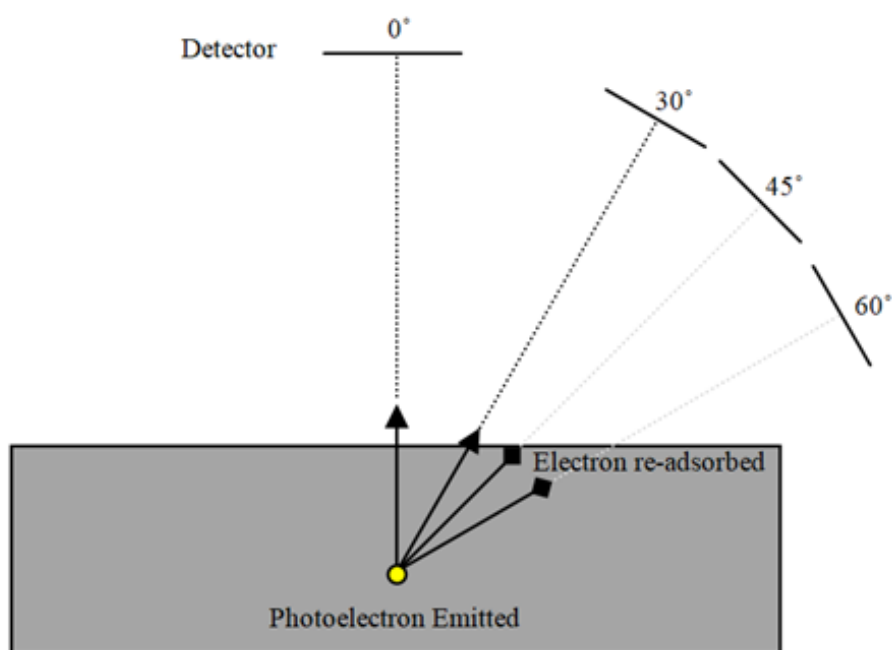
Figure 5-1: Schematic diagram showing different observation angles in ARXPS, allowing for surface sensitivity and depth profiling. Observation angles from 0˚ to 60˚ are shown. Image produced by Chambers, B.A. [406].

5.3.5.2 ARXPS: Instrumentation and Methods

Each individual ARXPS measurement was performed with the sample at 5 temperatures between room temperature and 723 K. The synchrotron X-ray excitation energy was

controllable, and 720 eV was used which was confirmed to not cause any overlapping satellite peaks with the peaks of interest. The beamline was equipped with a Phoibos 150 HSA (SPECS, Germany), using a 10 eV pass energy. The synchrotron beam strength could be varied by varying the entrance slit size; the standard size was 20 μm and the X-ray flux at the sample scaled linearly with the slit size. The beam size at the sample was ~0.1 mm^2. The total beam at the sample was measured using a GaAs detector, where the energy per GaAs electron-hole pair energy was taken as 4.18eV [407]. Assuming the entirety of each 720 eV photon was transferred into electron-hole pairs, the beam flux was 7 x 10^{14} photons/cm^2/s for a 20 μm slit.

For the CVD-Ru$_3$(CO)$_{12}$/HDS-RF-TiO$_2$ sample it was noticed that synchrotron X-rays removed CO ligands from Ru$_3$(CO)$_{12}$. The sample damage by the beam was further investigated by performing a series of XPS measurements on a single spot at room temperature. Furthermore, an ARXPS measurement was performed on a cluster spot which was irradiated 3.95 x 10^{18} photons/cm^2. To avoid sample damage by the beam for the main ARXPS measurements, the CVD-Ru$_3$(CO)$_{12}$/HDS-RF-TiO$_2$ sample was scanned in a grid such that each angle and temperature measurement was on an unaffected area of the sample.

5.3.5.3 ARXPS: Peak Fitting

In general, the standard XPS data analysis procedures described in the Instrumentation and Methodologies section 3.6.1.3 were used. Differences from the standard procedure will be noted here. It was found that the adventitious C 1s peak location was affected by the X-ray beam, so this was not used to calibrate the BE scale. The Ti 2p peak was stable and was used as the BE reference. The Ti^{4+} 2p was referenced to its location when C 1s = 285.0 eV for the first XPS scan before the C 1s was significantly affected by the beam. To determine atomic sensitivity factors for 720 eV excitation energy, a sample was scanned at both 720 eV and 1253.6 eV (the Mg Kα excitation energy) to find the peak area ratios between them. When determining the Ru At%, C 1s peaks were ignored in the calculations to minimise effects of hydrocarbon contamination on the results.

Ru 3d peaks in all ARXPS spectra were fitted with only one doublet. The lineshape used for fitting Ru 3d on the Flinders University XPS instrument was modified to suit the lineshape of the Australian Synchrotron XPS. All ARXPS Ru peaks were fitted using the same asymmetrical line shape, where Ru 3d$_{5/2}$ was fitted with LF(1.2,1.8,500,250) and Ru 3d$_{3/2}$ was fitted with LF(1,1.8,500,250). One exception to this procedure was as-deposited

$Ru_3(CO)_{12}$; this featured a less asymmetrical line shape which was best fitted by using LF(1.2,1.8,500,250) for Ru $3d_{5/2}$ for and LF(1,1.8,500,250) for Ru $3d_{3/2}$ (discussed in section 5.3.5.3).

Fitting uncertainties were estimated in the same manner as the laboratory-based XPS fitting uncertainties (see Chapter 3 section 3.6.1.3). The increased resolution and count rate of the Australian Synchrotron XPS instrument improved the fitting uncertainties; Ru At% was ± 2%, CO At% was ± 2%, and CO/Ru atomic ratio was ± 4%. The absolute error for CO/Ru atomic ratio was estimated to be higher at ~10% due to the CO baseline subtractions which were necessary, as well as any differences between the XPS atomic sensitivity factors used and the true factors for XPS [367]. The fitting accuracy for Ru 3d peak locations was ± 0.05 eV when comparing different measurements of the same sample performed in series, or ± 0.1 eV when comparing different samples.

5.3.5.4 ARXPS: Model Calculation

A similar evaluation algorithm was used in determining concentration depth profiles as used by Eschen *et al.* [374], and more recently Andersson *et al.* [400]. In this procedure the measured Ru At% at each angle was fitted to a model, using the concentration of Ru at various sample depths as a fitting parameter. The difference between the measured and modelled At% at each angle was minimised to determine the concentration depth profile. The Excel solver function was used to minimise the differences. The solver function is less robust than the genetic algorithm used in [374] and [400] because the starting parameters are not automatically varied and must be close to the final solution. This limits the range of possible solutions, but for the purpose of the ARXPS model minimisation it was deemed acceptable. The ratio of $\frac{|measured\ At\% - modelled\ At\%|}{measured\ At\%}$, herein called the "Model Difference Ratio", was used as a measurement for the difference between the modelled and measured results for Ru At%. The mean free path of electrons in the sample material depends on the composition of the sample and will influence the distance photoelectrons can travel through the sample, which was factored into the calculation and taken as 1.2 nm for 720 eV photons [376].

The following assumptions are inherent in the modelling process: a) The observation depth varied with the cosine of the emission angle, θ. b) Once beyond a finite depth from the surface into the bulk, the sample has a consistent, homogeneous composition. c) Possible variations in sample density which effected the composition are neglected. d) The inelastic mean free path (IMFP) was constant from the bulk to the surface. e) the distance from the

surface into the depth of the sample was modelled as a number of finite layers, each having a homogenous composition.

For the ARXPS depth profiles, the values of layer concentration (%) in each depth layer were estimated to have an uncertainty of ± 20%. This was estimated by manually altering the depth profile to determine the range of results which produced an acceptable comparison between the calculated and measured Ru At% values. For these results the important aspect was the shape of the depth profile rather than the exact values, and thus a better estimation of the error bars was not necessary. The resolution of the Ru penetration depth for ARXPS was ± 0.3 eV, based on half the defined layer width used in the calculation.

5.3.6 Optical Microscopy

Optical microscopy was used on an SiO_2 sample to assist with determining the He^+ beam size for the Flinders University LEIS beam (results shown in section 5.4.3.1). A Nikon Eclipse LV100 POL Petrographic microscope was used to take a high resolution digital image of the sample following extended exposure to the He^+ beam. The processing software ImageJ was then used to calculate the area of the beam spot. The scale was calibrated based on the scale bar of the microscopy, and a defined polygonal shape was created around the area of beam damage to determine the damaged surface area; $12.1mm^2 ± 0.15\ mm^2$.

5.3.7 LEIS Methods

5.3.7.1 LEIS: Background

LEIS, sometimes called ISS, is a variant of Rutherford backscattering spectrometry (RBS). LEIS allows for measuring the atomic composition of the outer, topmost atomic layer of the sample. It provides depth information about the atomic distribution in the region 0-10 nm below the surface layer (depending on the ion energy used) allowing the analysis of thin layers atop a surface [327]. This makes LEIS a well-suited technique for the analysis of supported metal clusters. A drawback is that the surface is bombarded with keV ions which can lead to the sputtering of atoms from the surface layer, and thus the ion dose must be moderated in LEIS measurements [327].

In LEIS a sample is bombarded with 0.5 to 10 keV low energy ions (He^+, Ne^+, or Ar^+). The ion beam is incident on the surface with angle α, and ions are backscattered at angle θ [327, 328]. A schematic of this process is shown in Figure 5-2. Over 99% of He^+ bombarding the surface is neutralised or implanted into the surface, and the remaining ions that backscatter with an angle θ are detected [327, 408]. The ions lose energy when backscattered, and the energy loss increases as the mass of the target atom being scattered from decreases. The

result of a LEIS measurement is a spectrum where surface peaks are present at specific locations related to the masses of the outer surface elements, except for H and He which cannot be measured. However, the analysis of only charged particles is thought to prevent the quantitative analysis of surface concentrations, and composition results from LEIS are treated as qualitative [327]. LEIS does not typically have matrix-effects, meaning the chemical nature of the surface atoms does not affect the LEIS results [328] except in rare cases [409].
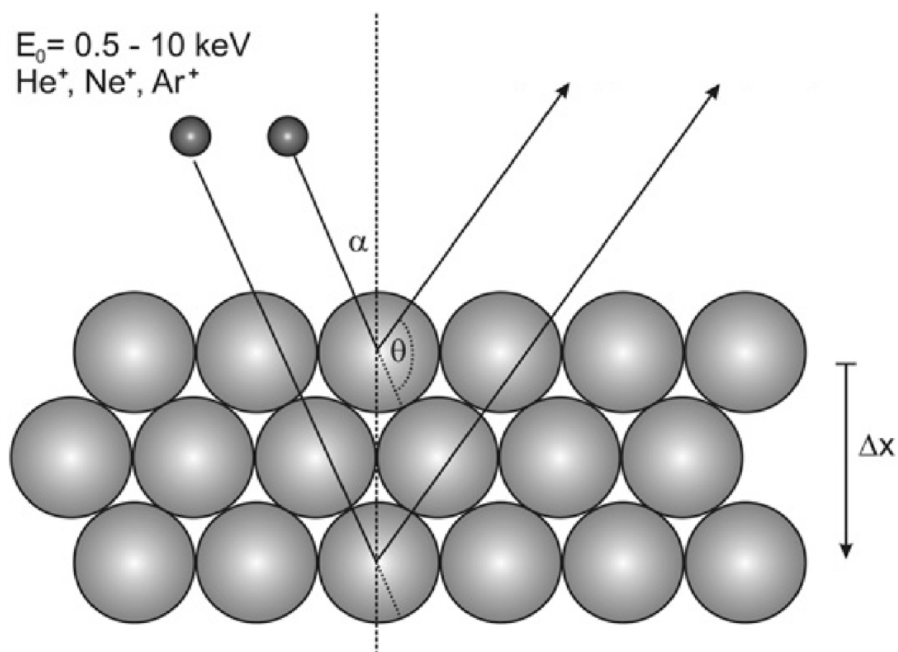
Figure 5-2: Schematic of the ion scattering process for LEIS [328]. Two backscattering processes are shown: one from a surface atom, and one from a sub-surface atom Δx below the surface. Reprinted with permission from Surface Science Reports [328].

Backscattering of ions from atoms below the topmost layer, such as the event shown with the ion backscattering from a depth of Δx in Figure 5-2, is suppressed. This is due to a combination of shadowing (upper atoms shielding lower atoms from He^+), blocking (backscattered He^+ being shielded due to sample geometry), and the reduced ion survival probability due to the increased time of interaction between the projectile and sample. The latter gives LEIS its ability to distinguish between ions scattered from the topmost atomic layer and from sub-surface atoms [309]. A single monolayer (ML) of impurities can dramatically affect the results of a LEIS experiment [328]. Ions scattered from thin layers below the surface may still be detected, and feature shifted peak locations due to the stopping power of the sample material. A mix of surface and subsurface atoms results in a tail to lower energies, while a full overlayer will result in a shift in peak location [328]. The peak shift was used to determine the depth of thin layers on the surface; the stopping power

of the overlayer and the onset half-maximum energy of a sub-surface peak were compared to reference measurements for the target atom [328].

5.3.7.2 LEIS: Instrumentation and Methods

LEIS measurements were performed on *in situ* samples at both Flinders University and the University of Utah. Both of the LEIS instruments used were set up with the same settings. 1 keV He$^+$ ions were produced using ion guns, which were incident on the sample at α = 45° and detected orthogonal to the sample where θ = 135° (see the ion geometry shown in Figure 5-2). The backscattered He$^+$ ions were detected with the same HSA detectors which were used on each UHV system for XPS; namely a Phoibos 100 HSA (SPECS, Germany) at Flinders University and a Physical Electronics HSA at the University of Utah. Ion energies were measured in steps of 5 eV. Backscattered counts were plotted against the ratio E/E_0, where E is the backscattered energy and E_0 is the incident ion energy. Higher E/E_0 values result from He$^+$ scattering from heavier surface elements.

The two LEIS measurement procedures used were "temperature-dependent LEIS" (TD-LEIS), and "series LEIS". TD-LEIS measurements were performed stepwise as the sample temperature was increased to determine the effects of heating (method described below), while series LEIS measurements were performed repeatedly on the same sample area without further modification, to determine the effects of the He$^+$ beam on the sample.

Each TD-LEIS measurement was performed on a unique sample, separate from those analysed using TD-XPS or ARXPS. Clusters were deposited as per the methods discussed in section 2.4 and LEIS was performed *in situ*. LEIS measurement was first performed at the deposition temperature. Following this, the He$^+$ beam was stopped, and the sample was heated at 3 K/s to the next temperature. Heating was stopped as soon as the target temperature was reached, and another LEIS measurement was performed. This process was repeated for regular temperature intervals until 900 K. For each TD-LEIS sample, XPS was performed after the TD-LEIS measurements and used to determine Ru surface coverage (see section 3.6.1.3 for the calculation process).

The reproducibility of results from the University of Utah LEIS was well known prior to this study because repeated experiments using the instrument had been performed on as-deposited Pd$_{20}$/alumina samples which indicated the instrument had high reproducibility [315], and the system had been used in numerous studies after this [6, 9, 60, 309-314]. Conversely, previous work had not been performed using LEIS at Flinders University. In testing the reproducibility of the spectra and consistency of the ion beam, RF-TiO$_2$ was

scanned 20 times in one day and no differences in the results were found. To determine the locations of the most important peaks related to Ru, Ti, and O, blank RF-TiO$_2$ and metallic Ru were measured which are shown in Figure 2-1.

Due to the potential damaging nature of LEIS measurements on surfaces, ion doses were minimised by using the lowest scan time to achieve reasonable resolution and only bombarding the surface while scans were running. Additionally, ion doses were estimated for each sample to estimate the level of surface damage due to the He$^+$ beam. The neutralisation current at the sample and scan times were used to determine the total ion doses for each sample. The neutralisation current was a good measurement for the number of incoming clusters because >99% of incoming He$^+$ ions were neutralised [327, 408].

5.3.7.3 LEIS: Data Analysis

The surface peaks in LEIS spectra were integrated to determine cluster/substrate peak area ratios. These ratios, *e.g.* Ru/(Ti+O) for Ru clusters on TiO$_2$, were used as a measure of the concentration of Ru accessible to LEIS. The uncertainty in Ru peak area ratios was estimated as ± 8% based on the data spread of a LEIS measurement of CS-Ru$_3$/SiO$_2$ which was repeated in series on the same cluster spot. For CVD-Ru$_3$(CO)$_{12}$/HDS-RF-TiO$_2$ the penetration depth of clusters into the substrate was calculated based on TD-LEIS data. The calculation process is described in the relevant Results and Discussion, section 5.4.4.3. The stopping power of titania was needed to relate the energy loss of backscattered particles to substrate depth. This was calculated using the software package SRIM [410] for 1.10 keV He$^+$ in TiO$_2$ to be 29.74 eV/nm ± 2.97 eV/nm. SRIM calculations were according to Bragg's rule [411], and thus any effect of the specific structure of RF-TiO$_2$ on the stopping power was neglected.

5.3.7.4 LEIS: Estimating Surface Damage

For each TD-LEIS sample the total cumulative surface damage caused by the He$^+$ beam was estimated using the percentage of Ru which was sputtered from the surface. It was assumed all Ru was on the topmost layer, and that the LEIS signal was directly proportional to the Ru surface coverage. The sputter rate of Ru from an SiO$_2$ surface, R, was determined in the Results and Discussion section 5.4.3.3 to be R = -1.2 x 10^{-2} atoms/ion. This sputter rate was determined experimentally, and any instrumentation effects are included. The packing density of an Ru ML, D, was estimated in order to calculate the surface damage in terms of Ru MLs. Ru unit cells are close packed hexagonal, and if we slice the top off the unit cell (to make a surface layer) there are 2 Ru atoms per unit cell at the surface, and the

length of a hexagonal side is 0.27 nm [412]. Based on the area of a hexagon the area of the unit cell face was determined to be 1.89 x 10^{-15} cm^2. The face features two atoms, and thus the estimated packing density, D, of an Ru ML was ~9.47 x 10^{-16} cm^2/atom.

The estimated surface damage was determined using the same method for all TD-LEIS measurements, and these are shown in Table 5-4 in the Results and Discussion. Here, an example calculation is provided for the CVD-Ru$_3$(CO)$_{12}$/HDS-RF-TiO$_2$ sample. The cumulative Ru dose per area for this measurement was 5.95 x 10^{15} ions/cm^2 (ion doses for each measurement are provided in Table 5-4). The ion dose per area was multiplied by R to determine the number of Ru atoms being removed per area; 7.14 x 10^{13} atoms/cm^2 (this assumed a full ML of Ru was present).This was then found in terms of MLs of Ru removed, by multiplying by D; ~6.8 x 10^{-2} ML of Ru was sputtered by the beam, or 6.8% ML. Because all cluster depositions were < 1 ML, this result was treated as the estimated percentage of Ru sputtered from the surface. That is, if 6.8% of a Ru full ML were to be removed, 6.8% of a partial ML would also be removed (relative to the initial coverage of that partial ML).

5.4 Results and Discussion

5.4.1 TD-XPS Results

TD-XPS measurements were performed on 5 different Ru_3-deposited samples, listed in Table 5-2. For each of the $Ru_3(CO)_{12}$ depositions, blank measurements were performed on the same substrates to determine the effects of the solution-based and CVD deposition procedures on the amount of surface Ti defects and adsorbed CO contamination. In this section the samples were first summarised with their TD-XPS temperature ranges and key XPS results related to the Ru clusters (see Table 5-2). The spectra and fitting of the Ru 3d/C 1s and Ti 2p regions were then discussed and the main TD-XPS results were presented.

5.4.1.1 TD-XPS Sample Summary

Table 5-2 displays the Ru At% and estimated Ru surface coverage determined for each TD-XPS sample. The TD-XPS temperature ranges are shown for each sample; measurements started at a lower temperature for CS-Ru_3 than $Ru_3(CO)_{12}$ samples due to the clusters being deposited at reduced temperatures while the $Ru_3(CO)_{12}$ was deposited at room temperature in both methods. The as-deposited Ru $3d_{5/2}$ BE and heat-treated BE are shown for each sample.

Table 5-2: Summary of Ru At% and Ru $3d_{5/2}$ BE for each TD-XPS cluster deposition. At% are averaged from all temperatures for each sample, and Ru surface coverages are determined according to the method in section 3.6.1.3. The as-deposited BE was at the deposition temperature, while the heat treated BE was at 723 K for SD and CVD samples, and 800 K for CS samples. Errors and uncertainties are discussed in section 3.6.1.3. The fitting uncertainty for Ru At% is ~4%. The absolute error in Ru coverage is ~100%, while the relative uncertainty between the experiments is based on the Ru At% fitting uncertainty and is ~4%. Absolute errors in BE are ± 0.2 eV, while the relative uncertainty when comparing measurements of the same sample is ± 0.1 eV.

Deposition	Substrate	Ru At% (%)	Ru Surface Coverage (% ML)	TD-XPS Range (K)	As-Deposited BE (eV)	Heat-Treated BE (eV)
SD-$Ru_3(CO)_{12}$	HDS-RF-TiO_2	0.44	3.2	298 - 723	282.0	280.5
CVD-$Ru_3(CO)_{12}$	HDS-RF-TiO_2	1.11	8.0	298 - 873	281.6	280.6
CVD-$Ru_3(CO)_{12}$	TiO_2(110)	2.41	17.2	298 - 873	281.2	280.5
CS-Ru_3	NS-RF-TiO_2	0.44	3.2	190 - 800	280.3	280.5
CS-Ru_3	SiO_2	0.51	3.7	190 - 800	280.7	280.7

The Ru surface coverages in Table 5-2 show that the coverage ranged from 3.2% ML to 17.2 % ML. Since all samples were a small fraction of a ML, any cluster differences related to surface coverage (*i.e.* due to cluster-cluster interactions) were considered negligible. The rate of CVD deposition for $Ru_3(CO)_{12}$ was greater when depositing onto $TiO_2(110)$ than RF-TiO_2; approximately double the attached Ru surface coverage, although the deposition pressure was the same and deposition time was shorter (30 minutes compared to 120 minutes for RF-TiO_2). The RF-TiO_2 deposition concentration was typical for this type of deposition, which provided evidence that $Ru_3(CO)_{12}$ bonded more readily to single crystal $TiO_2(110)$ than the nanoparticulate RF-TiO_2.

5.4.1.2 Fitting Ru 3d/C 1s Region

Details on the assigning of the C 1s peaks were given in the Instrumentation and Methodologies section 3.6.1.3. Ru $3d_{5/2}$ peaks were used as the main reference for the Ru BE position because there is less peak overlap with C 1s features than Ru $3d_{3/2}$. The TD-XPS results for the $Ru_3(CO)_{12}$ samples are shown in Figure 5-3. A minimum of 5 temperatures were measured per sample, however for readability the results are only shown at room temperature, 373 K, and 723 K.
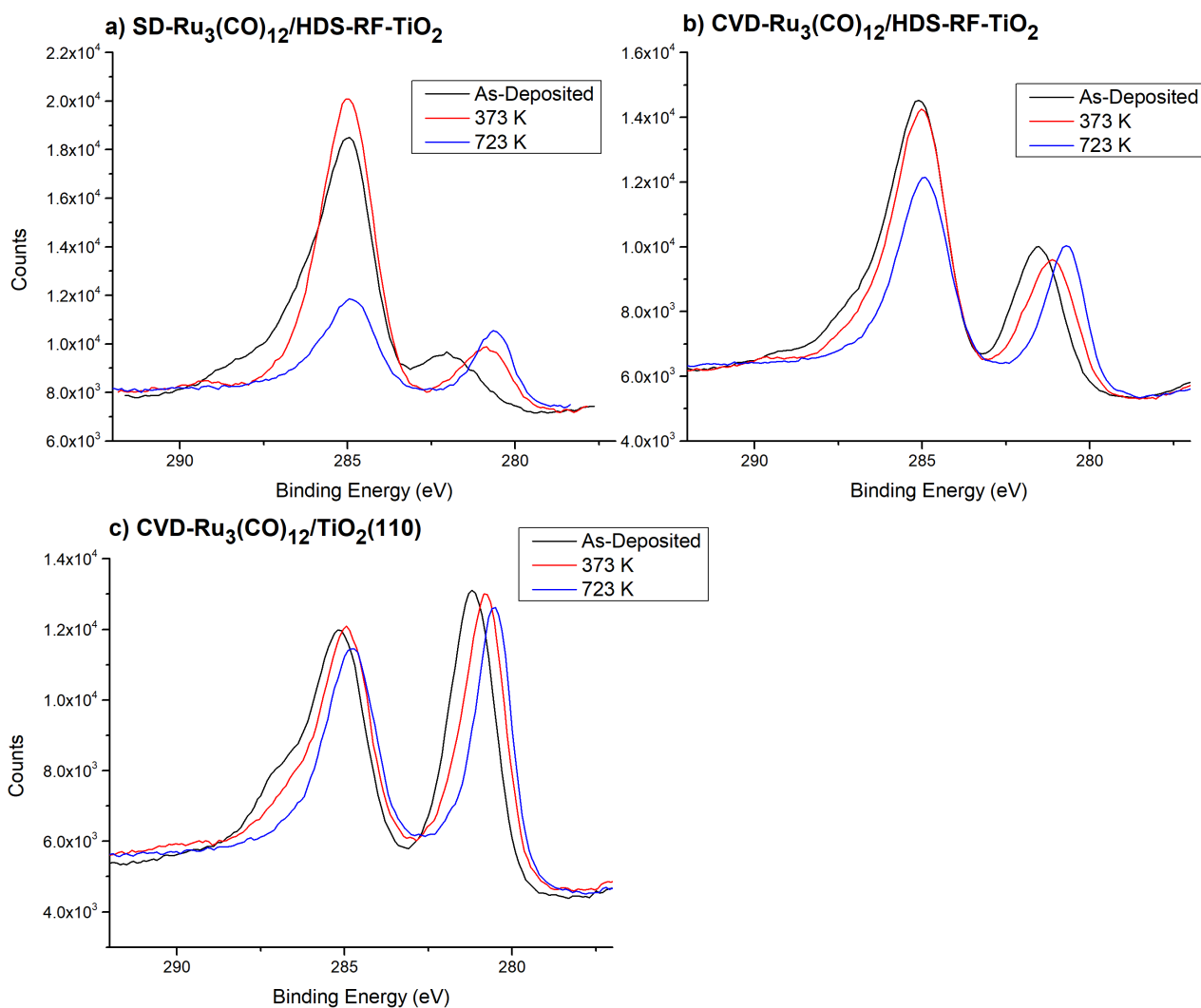
Figure 5-3: TD-XPS spectra of the Ru 3d/C 1s region for Ru$_3$(CO)$_{12}$ samples as-deposited, at 373 K, and at 723 K. a) SD-Ru$_3$(CO)$_{12}$/HDS-RF-TiO$_2$. b) CVD-Ru$_3$(CO)$_{12}$/HDS-RF-TiO$_2$. c) CVD-Ru$_3$(CO)$_{12}$/TiO$_2$(110).

For all spectra in Figure 5-3 the lower BE features were related to Ru 3d$_{5/2}$ and the higher BE features were related to the overlap of Ru 3d$_{3/2}$ and C 1s. The amount of C 1s was reduced by heating due to the desorption of adventitious hydrocarbons. This was most significant for the SD-Ru$_3$(CO)$_{12}$/HDS-RF-TiO$_2$ sample, because this deposition was not performed *in situ* and thus more hydrocarbons had adsorbed to the surface. For each sample, heating to 373 K and 723 K successively reduced the BE of the Ru doublet. Examples of the XPS peak fitting for Ru$_3$(CO)$_{12}$-deposited TD-XPS samples are shown in Figure 5-4. Both asymmetrical and symmetrical line shapes were used for fitting the Ru 3d doublets depending on the state of the clusters which will be described below.
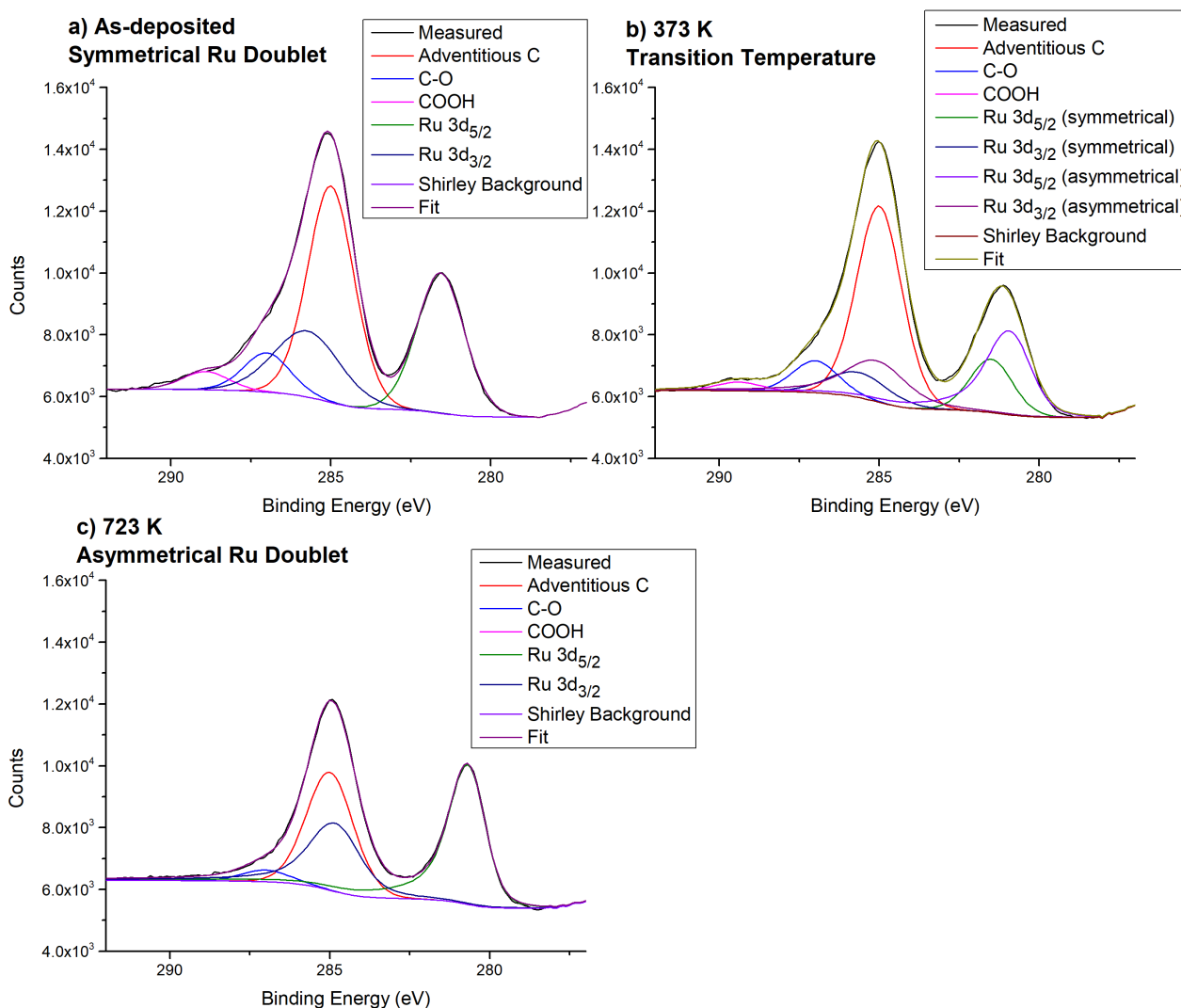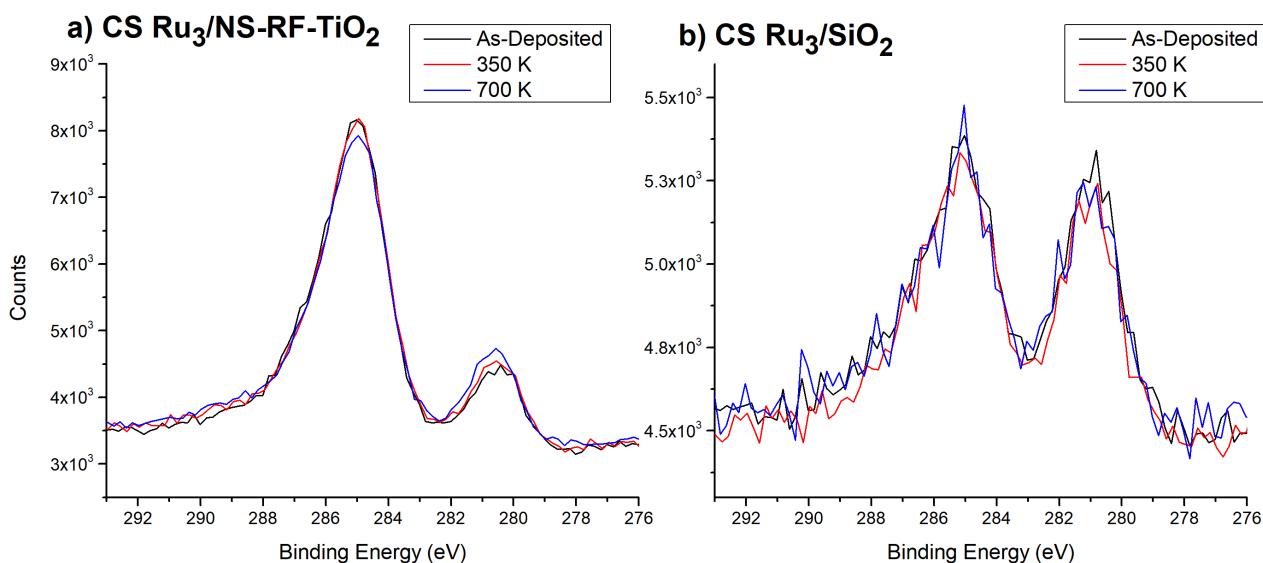
Figure 5-4: Example fittings of the Ru 3d/C 1s XPS region for the TD-XPS of CVD-Ru₃(CO)₁₂/HDS-RF-TiO₂. a) As-deposited at room temperature. b) Heated to 373 K. c) Heated to 723 K. The fitting procedure is identical for CVD-Ru₃(CO)₁₂/TiO₂(110) and SD-Ru₃(CO)₁₂/HDS-RF-TiO₂.

Figure 5-4 shows that the Ru 3d doublet related to the $Ru_3(CO)_{12}$ clusters were fitted with a symmetrical line shape as-deposited (before heating), but the peak changed to an asymmetrical shape by heating to 423 K. At 373 K the Ru was transitioning between states, and both symmetrical and asymmetrical doublets were required for an accurate fitting in the model. An asymmetrical line shape is typical for the Ru 3d peak from bulk, metallic Ru [372]. Due to this, the change of line shape with heating provides evidence for a shift towards more metallic properties for the Ru, associated with the removal of the CO ligands due to heating. Clusters typically have non-metallic properties with discrete electron energies like that of molecules [13], and become more metallic entering then into the nano-particulate size regime as their size increases past approximately 300 atoms [11, 14-18]. Thus, it is notable that the small Ru clusters are most likely in a metallic state on the surface; this may be an intrinsic property of the Ru clusters, or due to the cluster-surface interaction. This is

examined in more detail in Chapter 6 where UPS and MIES were performed on Ru$_3$/RF-TiO$_2$, and further details on the cluster valence electronic properties are discussed.

The TD-XPS results for CS-deposited Ru$_3$ samples are shown in Figure 5-5. For readability, the results are only shown at room temperature, 373 K, and 723 K for each sample. There was a slight shift towards higher Ru 3d$_{5/2}$ BE due to heating, for CS-Ru$_3$/NS-RF-TiO$_2$, while there was very little change in BE for CS-Ru$_3$/SiO$_2$. Examples of the peak fitting for the CS-deposited TD-XPS samples are shown in Figure 5-6, and the results are discussed further below.

Figure 5-5: XPS Spectra of the Ru 3d/C 1s region for CS-Ru$_3$ TD-XPS samples, as-deposited, at 350 K, and at 700 K. a) CS-Ru$_3$/NS-RF-TiO$_2$. b) CS-Ru$_3$/SiO$_2$.
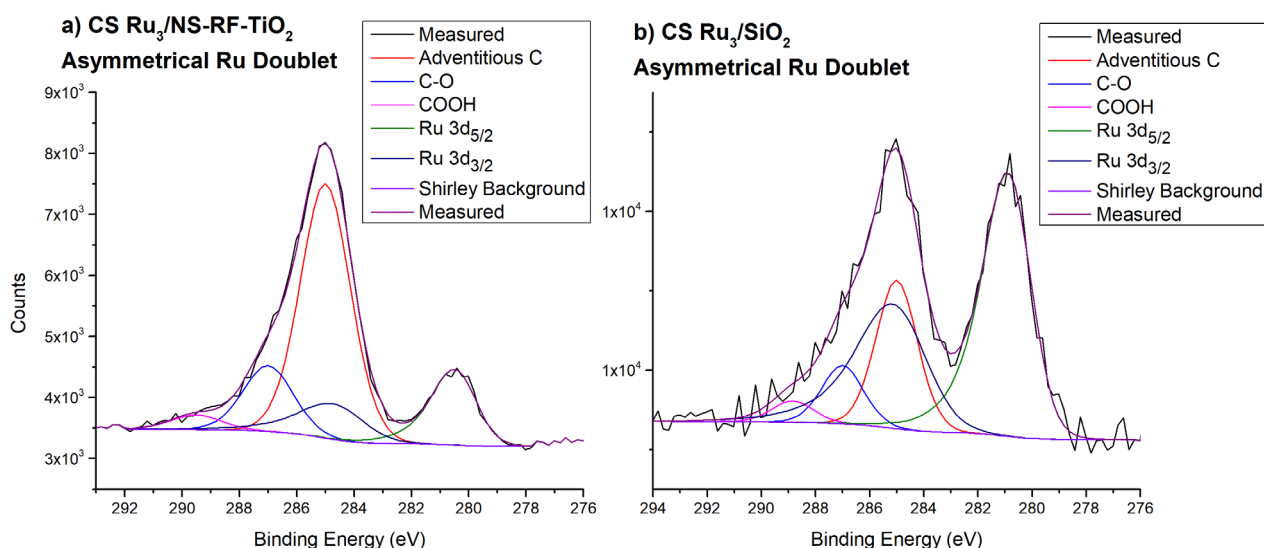
Figure 5-6: Example fitting of the Ru 3d/C 1s XPS region for CS-Ru₃ TD-XPS samples. a) CS-Ru₃/NS-RF-TiO₂ as deposited. b) CS-Ru₃/SiO₂ as deposited. Asymmetrical Ru doublets are used at all temperatures for both samples.

For CS-Ru$_3$, the Ru peak shape was asymmetrical at all measured temperatures for both samples. This is in contrast to the ligated Ru$_3$(CO)$_{12}$ samples, where the Ru peak shape was symmetrical at room temperature. This aligns with the interpretation that the presence of CO ligands was influencing the asymmetry of the peaks. After heating, the Ru$_3$(CO)$_{12}$ clusters had some or all of their ligands removed and were likely more similar in properties to the bare CS-deposited clusters. It is worth mentioning the asymmetrical line shape used was slightly different on CS-deposited and Ru$_3$(CO)$_{12}$-depsoited samples. This was due to the fact that the measurements were performed on different XPS instruments which featured slightly different line shapes. This change in line shape was discussed in the Instrumentation and Methodologies section 3.6.1.3, but did not significantly affect the results and was neglected in analyses.

5.4.1.3 Fitting Ti 2p Region

Three examples of fitted spectra are shown for the Ti 2p XPS region in Figure 5-7. These show the Ti 2p regions for CVD-Ru$_3$(CO)$_{12}$/HDS-RF-TiO$_2$, CVD-Ru$_3$(CO)$_{12}$/TiO$_2$(110), and CS-Ru$_3$/NS-RF-TiO$_2$, and were given as examples because they represent the three types of TiO$_2$ substrates used in TD-XPS measurements. Peak fitting for all other measurements of the Ti 2p region followed these models.
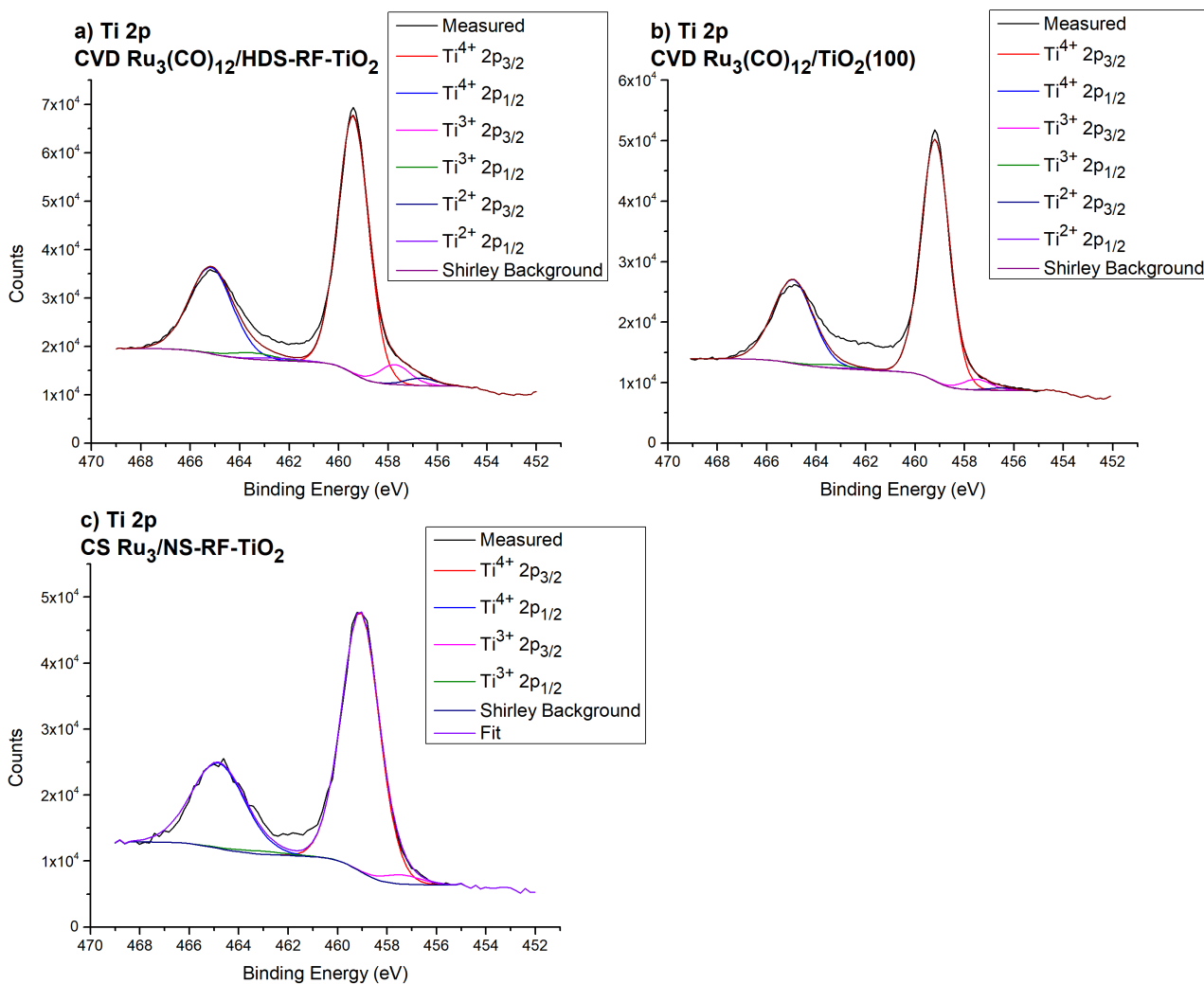
Figure 5-7: Example Ti 2p XPS region fittings for substrates with as-deposited clusters. a) CVD-Ru₃(CO)₁₂/HDS-RF-TiO₂. b) CVD-Ru₃(CO)₁₂/TiO₂(110). c) CS-Ru₃/NS-RF-TiO₂. (a) and (b) were measured with an Mg Kα excitation energy while (c) was measured with Al Kα. This resulted in different line shapes for the spectra (see section 3.6.1.3 for discussion on this). There is a consistent under-fit between the Ti doublet peaks due to a changing background signal (this was discussed in Chapter 4, section 4.3.5).

There was a difference in Ti 2p fitting procedures between Figure 5-7a-b and Figure 5-7c. This difference was due to the slightly different line shapes for the Flinders University XPS (used for ligated samples) and the University of Utah XPS (used for CS-deposited samples). All TiO₂ samples measured on the Flinders University XPS instrument had some signal present in the location of Ti^{2+} which was not visible at The University of Utah; the Ti^{2+} was most likely not actually present on the surface, and was just an artefact of the intrinsic line shape related to the detector. The differences between the systems were discussed in more detail in section 3.3, but suffice to say the key change was the difference between Mg Kα excitation and Al Kα excitation, which are known to effect the line shape [367].

Figure 5-7a and Figure 5-7b were fitted very similar to one another. Three unique Ti doublets

were modelled, corresponding to Ti^{4+}, Ti^{3+}, and Ti^{2+}. The Ti 2p peaks were present at 459.6 eV, 457.9 eV, and 546.8 eV, respectively. These show that the Ti 2p fitting procedure was identical for ligated $Ru_3(CO)_{12}$ depositions onto both RF-TiO_2 and $TiO_2(100)$. For CS-Ru_3 depositions, the Ti 2p fitting procedure was performed according to Figure 5-7c; only two doublets were used corresponding to Ti^{4+} and Ti^{3+}. For the purpose of this study Ti^{3+} and Ti^{2+} were summed and referred to as $Ti^{defects}$. Due to the larger number of Ti defect peaks the relative concentration of defects may have been slightly increased when measuring on the Flinders University XPS. However, this only applied when comparing different samples; each individual sample was analysed consistently and the change in surface defect concentration due to heating could be followed using TD-XPS in each case. Thus, for these purposes the Ti 2p fitting differences are considered negligible to the result.

5.4.1.4 TD-XPS Analysis and Discussion

A range of peak fitting results provided different chemical information about the samples. The Ru At%, Ru $3d_{5/2}$ BE, CO/Ru atomic ratio, and Ti^{Defect}/Ti^{Total} atomic ratio were all individually plotted against temperature to determine how they were affected. The Ru At% TD-XPS results are shown first in Figure 5-8.
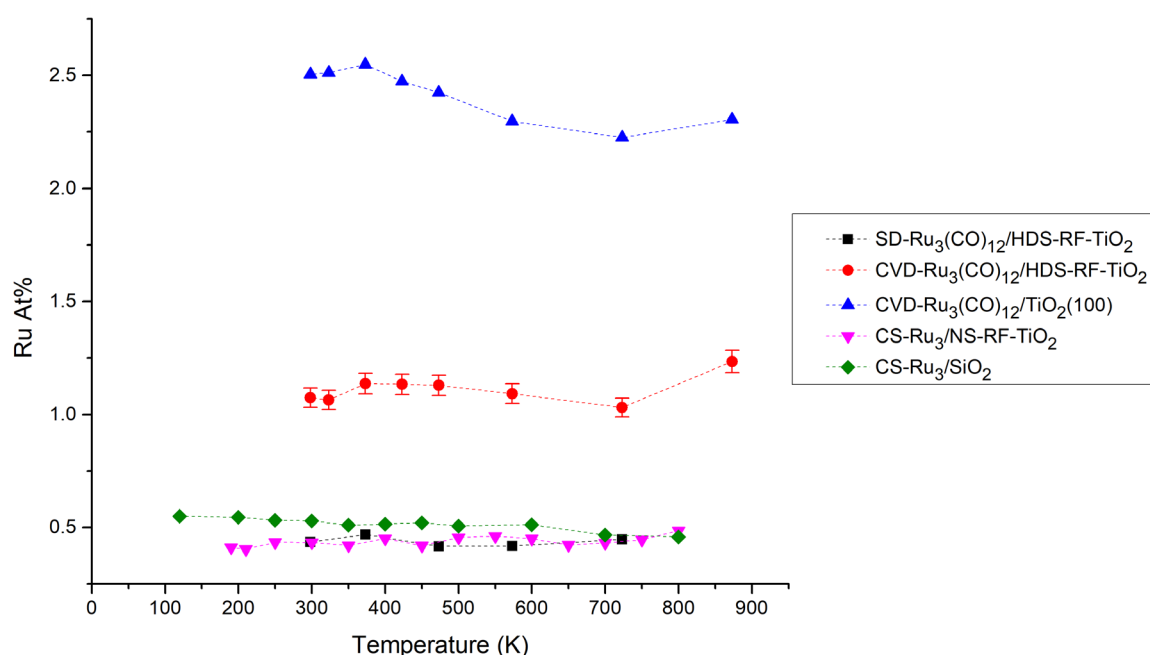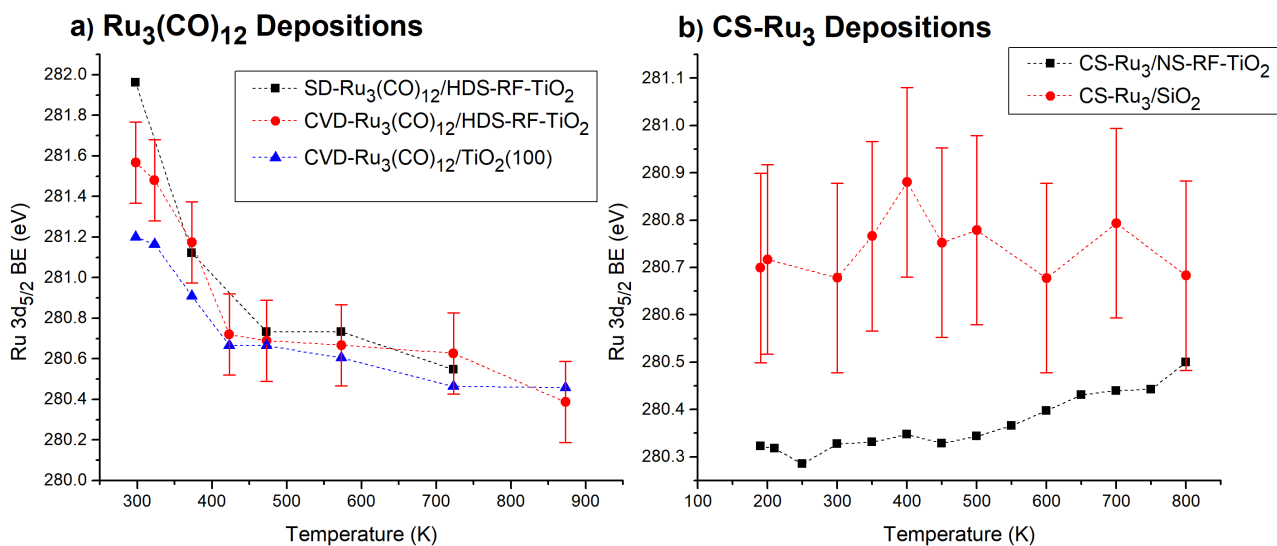

Figure 5-8: TD-XPS results for Ru At%. The uncertainty in Ru At% is ~4% which is shown in the error bars. Error bars are the same for all samples but are only displayed for one to prevent overlapping.

Figure 5-8 shows that there was no overall Ru At% trend between all samples, as temperature was increased. The SD-$Ru_3(CO)_{12}$/HDS-RF-TiO_2, CS-Ru_3/NS-RF-TiO_2, and

CS-Ru$_3$/SiO$_2$ samples featured no change in At%. From the CO-TPD results in Chapter 4 it was postulated that for CVD-Ru$_3$(CO)$_{12}$/HDS-RF-TiO$_2$ the clusters may be encapsulated by substrate material when heat treated at 723 K, however there was no noticeable decrease in At% for Ru associated with heating; this sample had a slight increase in At% greater than the error bars at 873 K, perhaps related to a decrease in surface contamination due to heating. The lack of decrease in Ru At% means that if the clusters were indeed encapsulated by substrate material, the penetration into the substrate was only of a short scale (*i.e.* less than 1 nm), otherwise the XPS signal would have noticeably been attenuated. The CVD-Ru$_3$(CO)$_{12}$/TiO$_2$(110) sample did begin to decrease in Ru At% to an extent greater than the error bars starting at ~423 K. This may be an indicator of cluster encapsulation which was noticeable in XPS due to the higher Ru surface coverage on the TiO$_2$(110) substrate. Cluster encapsulation is discussed in more detail in section 5.4.6.

TD-XPS results for Ru 3d$_{5/2}$ BE are shown in Figure 5-9. The results from Ru$_3$(CO)$_{12}$ depositions and CS depositions cannot be directly compared; for Ru$_3$(CO)$_{12}$ there was a significant decrease in BE due to the removal of CO ligands with heating [74, 75] which did not occur for CS-Ru$_3$ samples. Due to this the results were plotted separately in Figure 5-9a and Figure 5-9b.

Figure 5-9: TD-XPS results for Ru 3d$_{5/2}$ BE. a) Ru$_3$(CO)$_{12}$ depositions. b) CS-Ru$_3$ depositions. Note the BE scale is smaller in (b) because the peak shifting occurs to a lesser extent. When fitting Ru$_3$(CO)$_{12}$ at the transition temperature, 373 K, the average of the two Ru 3d$_{5/2}$ peak locations is shown. The absolute error in BE is ± 0.2 eV which is shown in the error bars, but the relative uncertainty is ± 0.1 eV for peak shifting of an individual sample. See section 3.6.1.3 for discussion on errors and uncertainties. Error bars are the same for all samples but are only displayed for one sample per figure to help readability.

In Figure 5-9a the initial BE varied between the Ru$_3$(CO)$_{12}$ samples. As the temperature was increased there was a sharp decrease in BE followed by a shallower decrease; the change in slope occurred between 423 and 473 K. The initial sharp decrease in BE was due to the loss of CO ligands from the clusters. From this data alone, it was not clear whether the change in slope was due to the removal of all ligands, or the direct attachment of Ru clusters to the substrates following ligand removal. This will be discussed below with extra insight from CO/Ru atomic ratios given in Figure 5-10.

In Figure 5-9b the TD-XPS of CS-Ru$_3$/NS-RF-TiO$_2$ showed a slight BE increase with heating which begins at 500 K. The peak shifted further with increased temperature until the total BE shift at 800 K was 0.2 eV ± 0.1 eV. This shift was most likely due to the oxidation of Ru clusters by the RF-TiO$_2$ substrate, which was previously suggested in Chapter 4, section 4.4.3.2. The increase in BE at 500 K indicated a temperature of at least 500 K was needed for oxidation to occur, which could not be determined in Chapter 4. However, similar to that chapter the exact stoichiometry of the oxidised Ru clusters on the substrates could not be determined. For CS-Ru$_3$/SiO$_2$ the BE was not greatly affected by the heating process. The measurement at 400 K increased in BE by ~0.1 eV, however this appeared to be a random error because the CS-Ru$_3$/SiO$_2$ has less BE consistency than the other samples. This was because the Ru 3d region signal-to-noise ratio was the lowest for CS-Ru$_3$/SiO$_2$ (see Figure

126

5-6b), but it was not clear why this occurred in the experiment. Comparing the two CS samples, the Ru 3d BE was higher for CS-Ru$_3$/SiO$_2$ both as-deposited (280.7 eV ± 0.2 eV) and after heat treatment (280.7 eV ± 0.2 eV). This indicated that the cluster-surface interaction between titania and Ru lowered the core Ru 3d BE of the clusters when compared to SiO$_2$, which was most likely due to the greater extent of charge transfer between the clusters and substrate and/or the formation of an SMSI with RF-TiO$_2$ [204].

In Figure 5-9b CS-Ru$_3$/SiO$_2$ showed no change in Ru BE larger than the uncertainty at any temperature between 190 K and 800 K. It was shown using CO-TPD in Chapter 4 section 4.4.1.1 that heating to 800 K caused agglomeration for CS-Ru$_3$/SiO$_2$, which indicates that the cluster agglomeration is not effecting the XPS BE. This result differs from reports for other metal clusters such as Au, where the cluster size has affected core electron BE [66, 72, 73, 102] and it has been possible to relate XPS BE to cluster size [73, 98, 102, 287, 288].

Comparing the data from Figure 5-9a and b, the BEs for all Ru$_3$ clusters supported on TiO$_2$ (both RF-TiO$_2$ and TiO$_2$(110)) were similar after heat treatment, varying only by ± 0.1 eV which was less than the uncertainty for comparing different samples. For TiO$_2$-supported samples, the initial, as-deposited Ru 3d BE was different between the samples but the difference lessened as the temperature was increased. This suggests that the initial state of the clusters was noticeably affected by the deposition method and substrate type, but after heat treatment to 723-823 K the Ru chemical state became very similar between all TiO$_2$-supported samples (280.5 eV to 280.6 eV). This suggests the Ru$_3$ had similar oxidation states after heating. This implies that for the use of Ru$_3$ supported on TiO$_2$ in catalysis, the particular deposition method is most likely not as important if a heat treatment process is applied. This could be considered if a sample were to be heated for industrial catalytic reactions; the solution submersion deposition method could be preferentially used due to its ease of scalability and the lack of difference in cluster oxidation state between the deposition methods after heating.

Figure 5-10 displays the TD-XPS results for CO/Ru atomic ratios for each ligated Ru$_3$(CO)$_{12}$ sample. This provided a representation of the CO ligands being removed by the heating procedures. The CO/Ru atomic ratio was determined at each temperature by calculating the ratio between the calibrated peak areas for CO 1s ligands and Ru 3d. For CO 1s, a background level of CO contamination was always present on the samples, even without clusters, and the pre-deposition CO area was subtracted in each case to reduce the effects

of contamination on the results. Also shown are blank, room temperature measurements for CO/Ru atomic ratios (discussed in section 5.3.4).
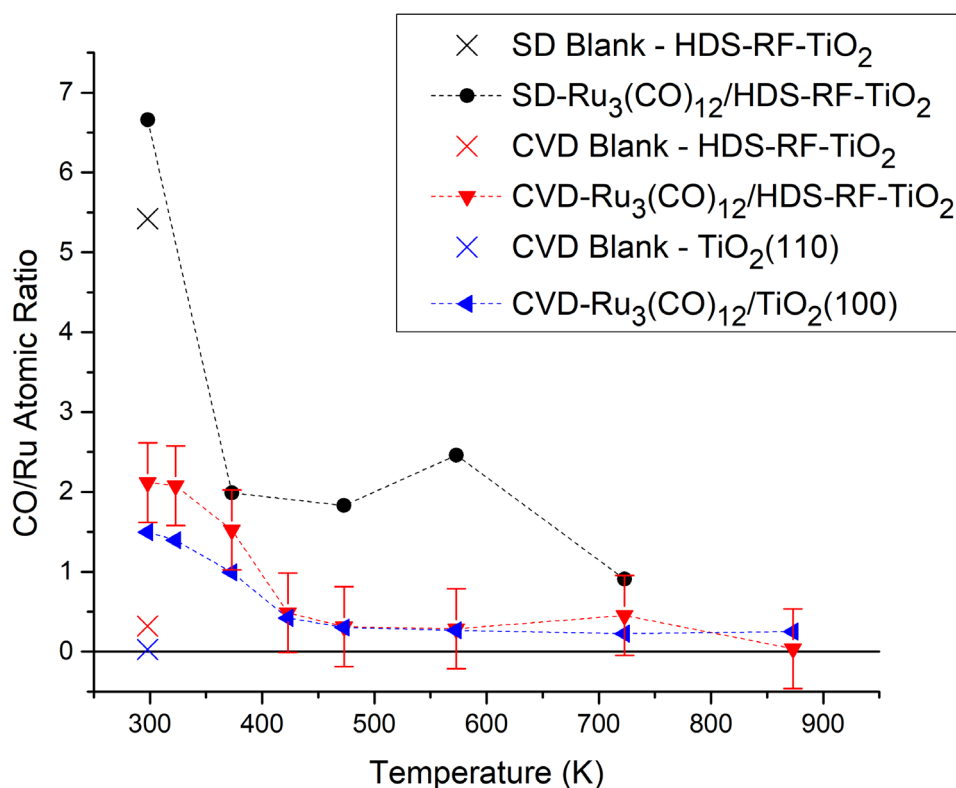
Figure 5-10: TD-XPS Results - CO/Ru atomic ratios for $Ru_3(CO)_{12}$ depositions. Ratios are determined using XPS At%. For blank, room temperature measurements (marked by X's) the CO/Ru atomic ratios are calculated using the Ru At% of the equivalent loaded depositions. The fitting uncertainty in CO/Ru atomic ratios is ~13% when comparing between samples, which is reflected in the error bars. The absolute error in the CO/Ru atomic ratio is estimated to be higher at ~0.5 (see section 3.6.1.3). Error bars are the same for all samples but are only displayed for one sample to increase readability.

Figure 5-10 shows that the blank substrate measurements for the two CVD depositions had very little CO adsorbed onto the HDS-RF-TiO_2 or $TiO_2(110)$ substrates after being exposed to CVD conditions with no clusters present. This indicated that the CO/Ru atomic ratios for the CVD-$Ru_3(CO)_{12}$ samples were not affected significantly by any contamination added during the deposition processes. Conversely, the SD blank measurement for HDS-RF-TiO_2 showed an equivalent ratio of CO/Ru = 5.4. This was greater than the maximum theoretical ratio of 4 for $Ru_3(CO)_{12}$ and indicated a significant amount of CO was adsorbed during the solution-based deposition process, due to both the *ex situ* nature of the process and the adsorption of dichloromethane solvent.

Observing the as-deposited Ru/CO atomic ratios for the cluster-loaded samples in Figure 5-10, the initial CO/Ru atomic ratio for SD-Ru$_3$(CO)$_{12}$/HDS-RF-TiO$_2$ was 6.7 ± ~0.5; this was greater than the maximum theoretical value of 4, and was indicative of CO contamination remaining on the surface from exposure to the atmosphere. Due to this the CO/Ru atomic ratio for the SD-Ru$_3$(CO)$_{12}$/HDS-RF-TiO$_2$ was not a reliable indicator of the true CO/Ru atomic ratio. This issue was not present when using the *in situ* CVD deposition method. The initial CO/Ru atomic ratio was 2.1 ± ~0.5 for CVD-Ru$_3$(CO)$_{12}$/HDS-RF-TiO$_2$, and 1.5 ± ~0.5 for CVD-Ru$_3$(CO)$_{12}$/TiO$_2$(110). This implied an approximate as-deposited chemical formulae of Ru$_3$(CO)$_{6.3}$ and Ru$_3$(CO)$_{3.0}$ for the clusters in each sample respectively, meaning some ligands were lost in the CVD-procedures. CVD-Ru$_3$(CO)$_{12}$/HDS-RF-TiO$_2$ also had a higher Ru 3d BE than CVD-Ru$_3$(CO)$_{12}$/TiO$_2$(110), which supported the interpretation that more ligands were lost on TiO$_2$(110). This aligned with previous measurements by Zhao *et al*. [75], where it was found ligands were desorbed when depositing Ru$_3$(CO)$_{12}$ onto TiO$_2$(110) by CVD at room temperature, where the average atomic ratio was Ru$_3$(CO)$_{10}$. There thus may be some mechanism for the removal of ligands by TiO$_2$ at room temperature.

The trends in CO/Ru atomic ratio for the 3 Ru$_3$(CO)$_{12}$ samples in Figure 5-10 were similar to one another, and also similar in shape to the trend in Ru 3d$_{5/2}$ BE for the same 3 samples in Figure 5-9a. There was a sharp decrease upon heating as the ligands began to desorb, and then the slope decreased. It appears that for the CVD depositions the trend flattens between 423 K and 473 K, which matched the temperature where the BE trend flattened. The similarity of the trends between the CO/Ru atomic ratio TD-XPS and Ru 3d BE TD-XPS provides support for the interpretation that the initial large decrease in BE with heating, for ligated samples was due to the loss of CO ligands. For SD-Ru$_3$(CO)$_{12}$ the CO/Ru atomic ratio flattened at 373 K compared to 473 K for Ru 3d BE, which may have been due to experimental inconsistencies in the thermocouple measurement. By approximately 423 K the majority of CO ligands had desorbed regardless of the type of TiO$_2$ substrate or deposition method. For the CVD depositions, at 423 K and above the CO/Ru flatlined to an average of ~0.27. This suggests the majority of the ligands had been removed, however it is difficult to confirm the complete deligation within the uncertainty (see error bars). The value of 0.27 may be related to the last ~1 or few ligands. This is supported by the literature where complete deligation has been reported for Ru$_3$(CO)$_{12}$ on different forms of TiO$_2$ at between 700 K and 800 K depending on the nature of the substrate and deposition method [74, 75], implying 423 K is not a high enough temperature to remove all CO ligands.

The TD-XPS results for Ti^{Defect}/Ti^{Total} atomic ratio for each sample are shown in Figure 5-11.

Blank measurements for substrates without deposited clusters were also performed and are displayed on the same axes. These results only applied to the TiO_2 substrates, and the CS-Ru_3/SiO_2 data were not included due to the lack of Ti.
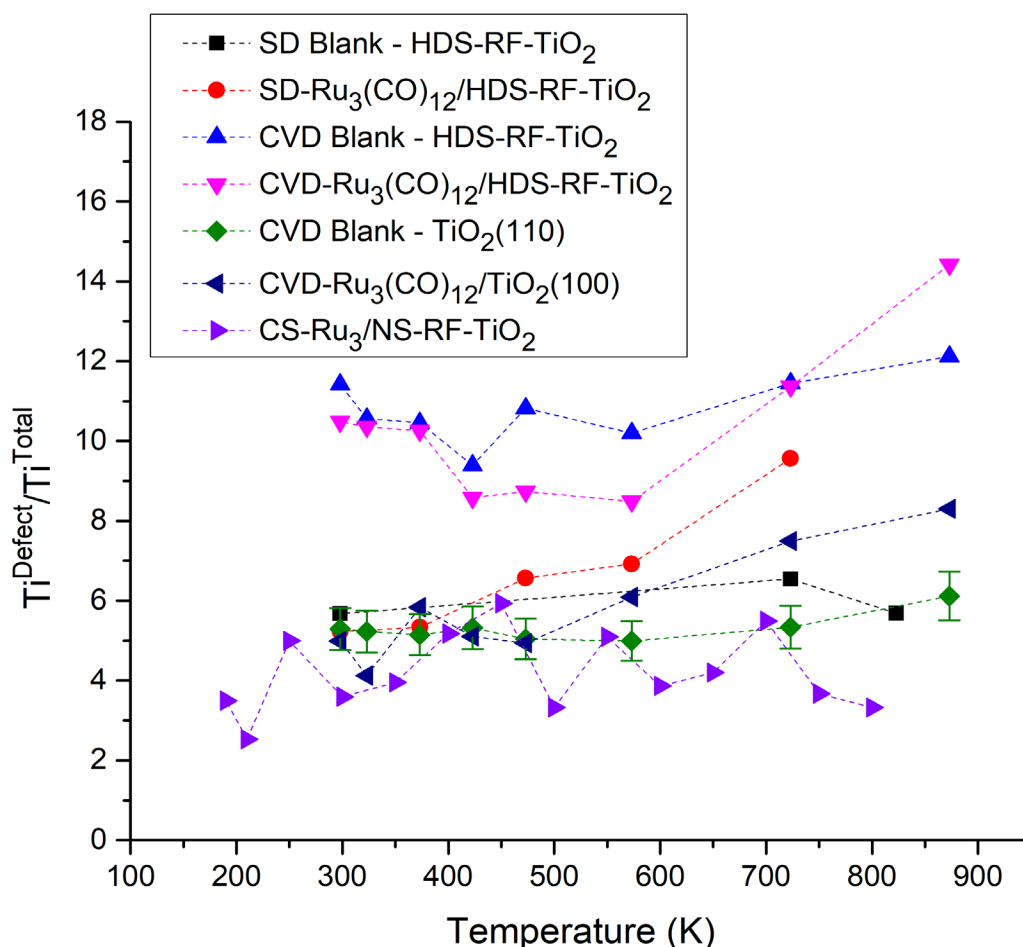
Figure 5-11: TD-XPS Results - Ti^{Defect}/Ti^{Total} atomic ratio. Ratios are determined using XPS At%. Blank measurements where no clusters were deposited are included for the solution-based and CVD depositions. The uncertainty in the fitting of Ti defect ratios is ± 10%, which is shown in the error bars (see section 3.6.1.3 for discussion on errors and uncertainties). Error bars are the same for all samples but are only displayed for one per figure to increase readability.

Figure 5-11 shows that blank HDS-RF-TiO_2 and blank $TiO_2(110)$ for CVD depositions featured small increases in surface defects due to heating, starting at 600 K. The blank measurement for SD-$Ru_3(CO)_{12}$ only featured 298 K and 723 K measurements, and also showed a small increase in defects due to heating. However, all $Ru_3(CO)_{12}$-loaded samples in Figure 5-11 increased in Ti defects to a greater extent, beyond the level of blank samples. For CVD-$Ru_3(CO)_{12}$ this started at 573 K on HDS-RF-TiO_2 and at 473 K on $TiO_2(110)$, while for SD-$Ru_3(CO)_{12}$/HDS-RF-TiO_2 this started at 373 K. The difference in Ti defect ratio between the loaded and blank samples after heat treatment was larger than the error bars for SD-$Ru_3(CO)_{12}$/HDS-RF-TiO_2 and CVD-$Ru_3(CO)_{12}$/$TiO_2(110)$, but for CVD-$Ru_3(CO)_{12}$ the

defects increased beyond the blank but there was some overlap in error bars (not shown in the figure). Because there was still an increase, and the difference was above the error bars for the other two CVD-$Ru_3(CO)_{12}$ samples, it is assumed that the increase above the blank sample was significant for CVD-$Ru_3(CO)_{12}$/HDS-RF-TiO_2 even with the overlapping error bars.

The increase in Ti defects with temperature was at least partially due to heating of the substrate for the cluster-deposited samples; heating-induced defects for TiO_2 under UHV are well-known and have been reported in previous studies [204, 207, 413]. However, because the sample defects increased even above the level of the blank samples, evidence is provided that the clusters were involved with the increase in surface defects by reducing the substrate (or conversely the substrate was oxidising the clusters). The SD-$Ru_3(CO)_{12}$/HDS-RF-TiO_2 and corresponding blank sample both had less total defects than either the CVD-blank or CVD-$Ru_3(CO)_{12}$/HDS-RF-TiO_2 samples, even though the surface loading was less and there was thus less clusters present to passivate defects (see Table 5-2). This was presumably because of the exposure to atmosphere and dichloromethane solvent passivating the surface defects before the sample was analysed.

In the literature, Ti defects increasing for substrates loaded with clusters has previously been associated with clusters being oxidised or encapsulated [184-186, 203, 207, 210-212], and this lends support to the fact that cluster encapsulation and/or oxidation was occurring for the $Ru_3(CO)_{12}$ samples due to heating. Conversely, CS-Ru_3/NS-RF-TiO_2 did not have an increase in surface defects related to heating. From the CO-TPD and XPS results in Chapter 4, CS-Ru_3 was expected to be oxidised after heating, which would hypothetically increase the number of Ti defects in the surface as the substrate was reduced. Because no increase in TiO_2 surface defects was detected for this sample, it is possible that the effect was too small to detect, perhaps due to a combination of lower Ru surface coverage of the CS-Ru_3/NS-RF-TiO_2 compared to CVD-$Ru_3(CO)_{12}$/HDS-RF-TiO_2 (see Table 5-2).

5.4.2 ARXPS Results

ARXPS measurements were performed on 2 samples; CVD-$Ru_3(CO)_{12}$/HDS-RF-TiO_2 (deposited *in situ*) and CS-Ru_3/HDS-RF-TiO_2 (deposited *ex situ*). In addition to the main ARXPS results, fitted Ru 3d/C 1s region XPS spectra are shown for each sample and the effect of the synchrotron X-ray beam on the clusters is discussed.

5.4.2.1 Ru 3d Peak Fitting and Estimating Surface Coverages

The Ru surface coverage of the ARXPS samples were estimated according to the Instrumentation and Methodologies section 3.6.1.3, and are shown in Table 5-3. The Ru surface coverage for both samples was low (< 5% ML), and thus cluster-cluster interactions were considered negligible and the samples were directly comparable to one another in terms of Ru properties.

Table 5-3: Ru At% and Ru surface coverages for ARXPS samples (see Instrumentation and Methodologies section 3.6.1.3 for details on data analysis and uncertainties). The fitting uncertainty for Ru At% is ~2%. The absolute error in Ru coverage is ~100%, while the relative uncertainty between the experiments is based on the Ru At% and is ~2%.

Deposition	Substrate	Ru At% (%)	Ru Surface Coverage (% ML)
CVD-Ru$_3$(CO)$_{12}$	HDS-RF-TiO$_2$	0.77	4.0
CS-Ru$_3$	HDS-RF-TiO$_2$	0.18	1.0

The fitting procedure for Ru clusters varied slightly between ARXPS and the previous TD-XPS measurements. The asymmetric line shape for Ru was changed to allow for accurate data fitting across the range of synchrotron XPS data. In Figure 5-12 three example spectra are shown with peak fitting for the Ru 3d/C 1s region: CVD-Ru$_3$(CO)$_{12}$ as-deposited, CS-Ru$_3$ as-deposited, and CVD-Ru$_3$(CO)$_{12}$ after heating to 723 K. These represent the peak fitting procedures used for all ARXPS measurements.
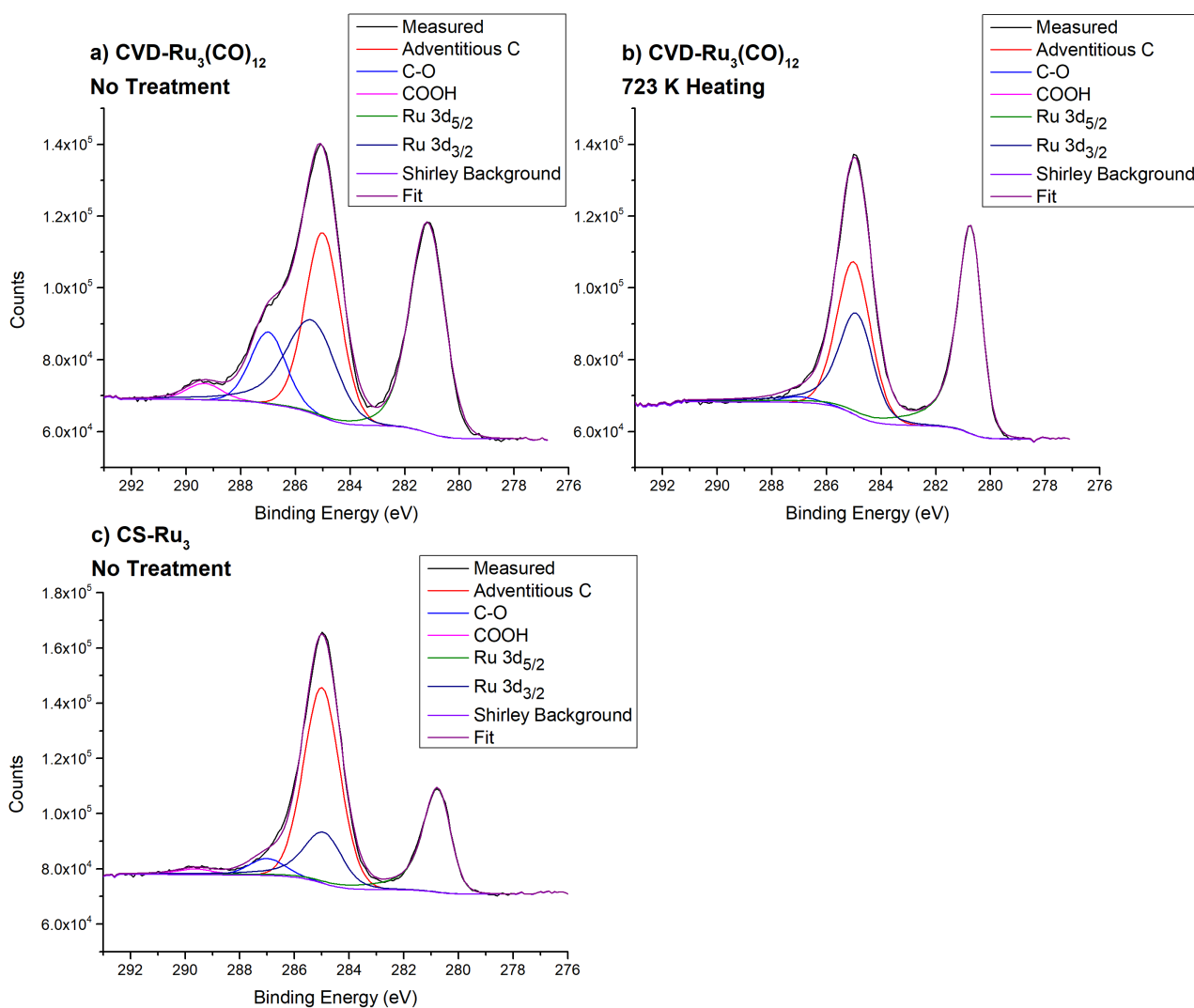
Figure 5-12: Example peak fitting of the Ru 3d/C 1s region. Measurements were at an observation angle of 0°. a) CVD-Ru₃(CO)₁₂/HDS-RF-TiO₂, no treatment. b) CVD-Ru₃(CO)₁₂/HDS-RF-TiO₂, 723 K heating. c) CS-Ru₃/HDS-RF-TiO₂, no treatment.

CVD-Ru$_3$(CO)$_{12}$/HDS-RF-TiO$_2$ and CS-Ru$_3$/HDS-RF-TiO$_2$ were both fitted with identical Ru 3d line shapes at all temperatures, except for as-deposited CVD-Ru$_3$(CO)$_{12}$/HDS-RF-TiO$_2$; this Ru 3d doublet was less asymmetrical than all other ARXPS scans. The specific line shapes were detailed in section 5.3.5.3. The increase in Ru peak asymmetry after heating was most likely related to the clusters losing their CO ligands and becoming more metallic. The slight asymmetry of the as-deposited Ru 3d peak may indicate that Ru$_3$(CO)$_{12}$ had decomposed further than other samples during the deposition as a result of the increased deposition temperature for the ARXPS sample (313 K, compared to 298 K). This discrepancy did not greatly affect the results of the ARXPS fitting procedures.

5.4.2.2 X-ray Beam Damage of Ru$_3$(CO)$_{12}$

Preliminary measurements were performed to determine the effect of the synchrotron X-ray beam on the Ru clusters. It was found that the 720 eV synchrotron X-ray beam was

desorbing CO ligands from CVD-Ru$_3$(CO)$_{12}$. To investigate this, the same cluster spot was scanned repeatedly at room temperature to determine the change in the Ru 3d/C 1s region as the total beam dosed increased. This was performed on the ARXPS CVD-Ru$_3$(CO)$_{12}$/HDS-RF-TiO$_2$ sample, using a unique scan area which did not interfere with the main ARXPS measurement. The Ru 3d$_{5/2}$ BE and CO/Ru atomic ratio were both plotted against the total X-ray beam flux, and the results are shown in Figure 5-13.
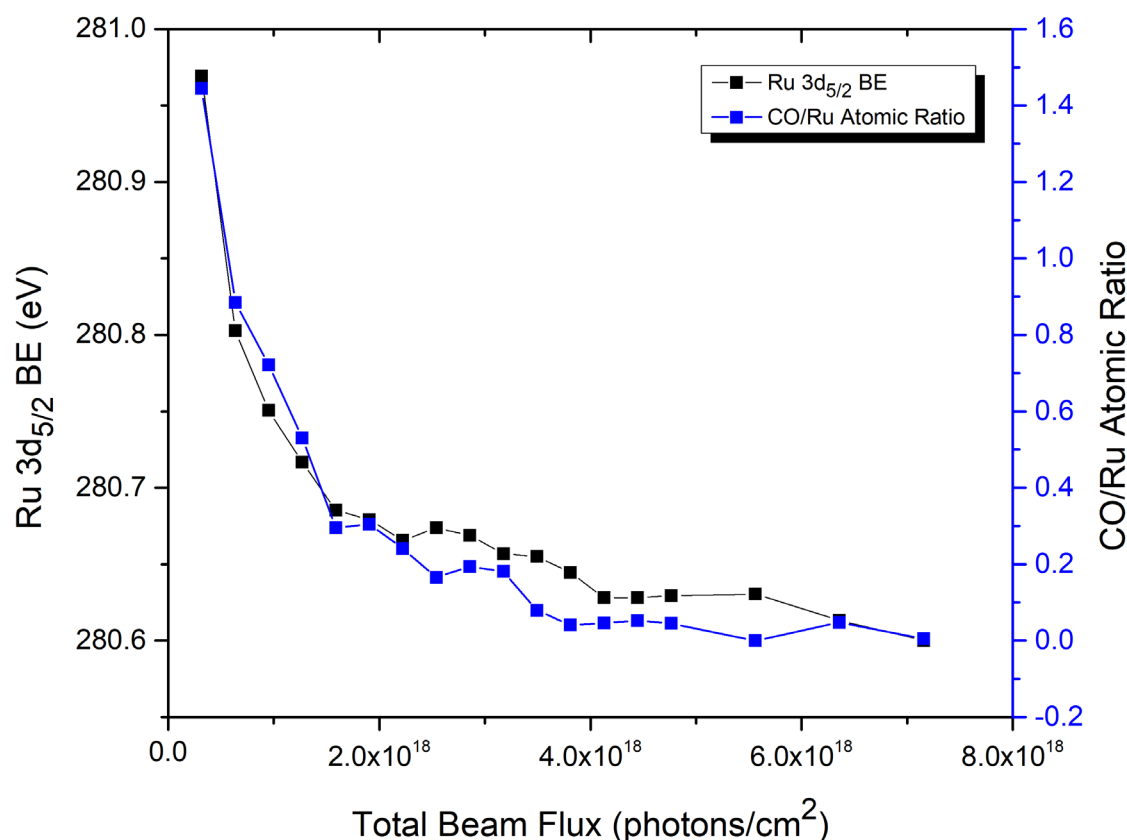
Figure 5-13: CVD-Ru$_3$(CO)$_{12}$/HDS-RF-TiO$_2$ - Beam damage vs. total beam flux of 720 eV X-ray photons. The left and right vertical axes show the Ru 3d$_{5/2}$ BE and CO/Ru atomic ratio, respectively. The uncertainty in the Ru BE is ± 0.05 eV. The fitting uncertainty in CO/Ru atomic ratio is ± 4%, while the absolute uncertainty is larger at ± 10% (see section 5.3.5.3 for discussion on uncertainties).

Figure 5-13 shows the results of XPS peak fitting for CVD-Ru$_3$(CO)$_{12}$/HDS-RF-TiO$_2$ after being left under the X-ray beam. Results for the CO/Ru atomic ratio and Ru 3d$_{5/2}$ BE are shown; the Ru 3d peak shifted towards lower BE and the CO/Ru atomic ratio decreased. Both findings align with the interpretation that the X-ray beam was stripping the CO ligands from the clusters over time. This effect was not unlike that of heating the clusters to remove the ligands, where the trend for the shape of the Ru 3d$_{5/2}$ BE (Figure 5-9a) and CO/Ru atomic ratio (Figure 5-10) was similar. The initial Ru 3d$_{5/2}$ BE of 281.0 ± 0.05 eV decreased by 0.4 eV to 280.6 eV ± 0.05 eV after a dose of 7.2 x 10^{18} photons/cm^2. For the TD-XPS

134

measurement in section 5.4.1.1, the final BE after heating to 873 K was the same, at 280.6 eV ± 0.2 eV. This indicated that the X-ray beam removed the ligands in a similar manner to the heat treatment, and the resulting chemical state of the clusters was similar.

It was detected by XPS that the Ru At% was decreased by exposing the sample to the X-ray beam (not shown in Figure 5-13). The initial Ru At% decreased by ~14% after a dose of 4×10^{18} photons/cm^2, after which the rate of loss decreased significantly. The loss of Ru 3d signal may be explained by the removal of some Ru atoms or clusters by the X-ray beam. The X-ray dose of this experiment was designed to test the surface damage and was far greater than the standard dose of ~2×10^{17} photons/cm^2 used in a standard measurement. Due to this, the level of surface damage to the Ru atoms themselves was treated as negligible for the ARXPS experiment.

Due to the findings in this section, the CVD-$Ru_3(CO)_{12}$/HDS-RF-TiO_2 sample was moved in the X-ray beam spot to a fresh, non-overlapping sample area for each ARXPS scan. This avoided accumulating beam damage which may have affected the measurements by removing CO ligands, and was discussed in the Methodology section 5.3.5.2. This was possible because the CVD-$Ru_3(CO)_{12}$ covered the entire surface evenly. The CS-Ru_3/HDS-RF-TiO_2 sample featured a single cluster spot 2 mm in diameter which was scanned repeatedly, but the extent of damage to the bare Ru clusters was deemed to be negligible for this experiment (discussed above). It must be mentioned that the CO ligand damage described in this section was not observed when performing laboratory-based XPS measurements (*e.g.* for TD-XPS). This was presumably because synchrotron radiation is typically 10^5-10^{12} times more intense than laboratory X-ray sources [414].

5.4.2.3 Main ARXPS Results and Analysis

The ARXPS results for both CVD-$Ru_3(CO)_{12}$/HDS-RF-TiO_2 and CS-Ru_3/HDS-RF-TiO_2 are shown in Figure 5-14. The results for Ru At% at each observation angle are shown first, followed by the estimated Ru depth profiles at each temperature. Finally, the differences between the measured Ru At% and those calculated by the depth profile model were plotted for each sample, angle, and temperature. ARXPS was also performed on the X-ray beam-damaged spot (see section 5.4.2.2) after a dose of 4×10^{18} photons/cm^2, to determine the effects of the X-ray beam on the Ru depth profile.
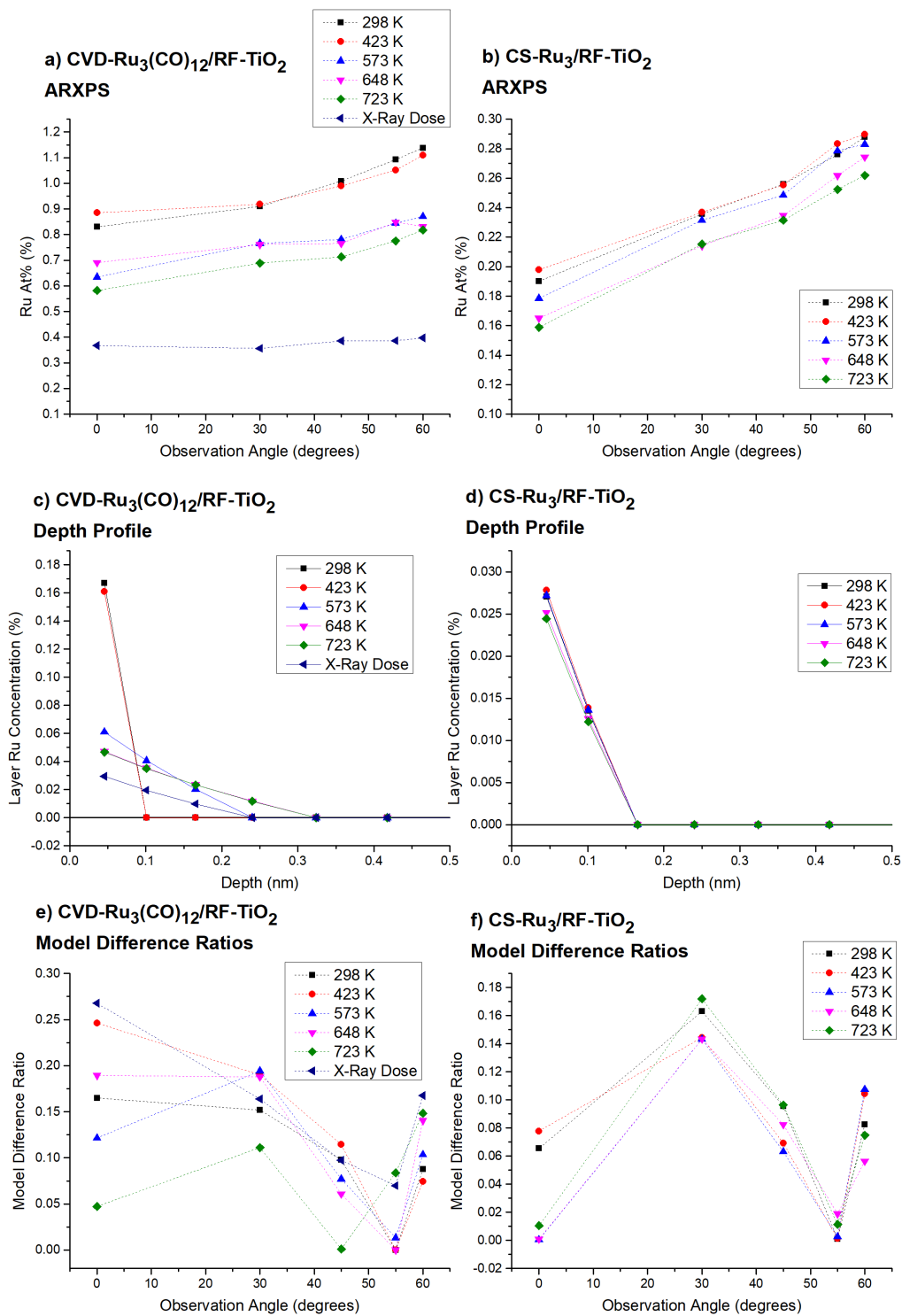
Figure 5-14: ARXPS data for CVD-Ru3(CO)12/HDS-RF-TiO2 and CS-Ru3/HDS-RF-TiO2. (a) and (b) show the data for Ru At% vs. observation angle for CVD-Ru3(CO)12 and CS-Ru3, respectively. (c) and (d) show the ARXPS depth profiles for CVD-Ru3(CO)12 and CS-Ru3, respectively. These show the atomic concentration of Ru per layer for arbitrarily defined layers of the sample, as determined by the ARXPS model (see section 5.3.5.4). (e) and (f) plot the Model Difference Ratio at each observation angle and temperature (described in section 5.3.5.4). The uncertainty in Ru At% is ± 2%, while the uncertainty in the atomic ratio per layer is ± 20% (see section 5.3.5 for discussion on uncertainties).

Figure 5-14c shows that the depth profile of CVD-Ru$_3$(CO)$_{12}$ clusters on the surface changed between 423 K and 573 K. Between 298 K and 423 K all Ru was present on the top surface layer, defined in the calculation as the top 0.046 nm. At 573 K the depth profile changed, and clusters either penetrated into deeper layers of the substrate or were covered by a titania overlayer. The penetration extended deeper again at 648 K to a maximum penetration depth of 0.24 nm ± 0.03 nm. The depth profile shows that at 723 K there was approximately 60% Ru with an overlayer, and 40% present on the surface layer. The X-ray beam-damaged spot featured a similar depth profile to the 573 K heat-treated ARXPS measurement. This indicated the cluster damage due to the X-ray beam also resulted in an overlayer forming above the clusters. However, because the X-ray beam also resulted in the loss of Ru surface atoms, the treatment of clusters with X-ray dosing is not recommended as an Ru$_3$(CO)$_{12}$ de-ligation method for experiments.

Figure 5-14d shows the depth profiles for CS-Ru$_3$/HDS-RF-TiO$_2$, which were more consistent with temperature than CVD-Ru$_3$(CO)$_{12}$/HDS-RF-TiO$_2$. The main change was a small reduction in the total amount of Ru visible in XPS as the temperature increased. Unlike CVD-Ru$_3$(CO)$_{12}$ sub-surface Ru was present at 298 K (room temperature). However, the penetration was also less pronounced; the maximum penetration depth was approximately 0.1 nm ± 0.03 nm. The ratio of surface to sub-surface Ru was consistent for all temperatures; there was ~66% surface and ~34% subsurface Ru$_3$.

The results discussed regarding Figure 5-14c and Figure 5-14d align with results presented in Chapter 4, where CO-TPD results showed that CVD-Ru$_3$(CO)$_{12}$/HDS-RF-TiO$_2$ had no Ru-CO binding sites remaining after a heating procedure to 800 K, while CS-Ru$_3$/HDS-RF-TiO$_2$ did not have Ru-CO binding sites as-deposited which was interpreted as a lack of Ru on the surface layer. This was an inconsistency between the ARXPS and CO-TPD data; ARXPS indicated some clusters were still present on the topmost layer for both samples after penetration had occurred, while CO-TPD indicated that no Ru was left on the surface. This inconsistency was most likely due to inherent flaws in the ARXPS depth profile method for this type of sample, which were discussed below in section 5.4.5.2.

Figure 5-14e-f shows the "Model Difference Ratios" plotted against observation angle at each temperature. A description of how this is calculated is given in section 5.3.5.4, and these values represent the error between the measured At% and the value from the ARXPS model, on a scale from 0 to 1. The ratios varied per measurement between a ratio of 0 and 0.3. The greatest Model Difference Ratio for CVD-Ru$_3$(CO)$_{12}$/HDS-RF-TiO$_2$ was for the X-

ray dosed measurement at 0°, and for CS-Ru$_3$/HDS-RF-TiO$_2$ it was the 723 K measurement at 30°. The maximum Model Difference Ratio of 0.3 implied there may have been differences between the modelled depth profile and the true depth profile of the sample. The Model Difference Ratios were consistently higher for particular observation angles; this may imply that the roughness of the sputtered RF-TiO$_2$ was an issue for the ARXPS, or that the samples were non-monotonic. Thus, the depth profiles alone were not considered quantitative representations of the Ru surface concentration per layer. However, ARXPS was used as an indication that CVD-Ru$_3$(CO)$_{12}$ clusters travelled deeper into the HDS-RF-TiO$_2$ as a response to heating, while the CS-Ru$_3$ depth profile did not change due to heating and started with clusters covered by substrate material. The TD-LEIS measurements discussed below provided more depth information (see section 5.4.4), and the results from ARXPS and LEIS were compared and analysed in section 5.4.5.

5.4.3 LEIS Preliminary Testing

Preliminary testing was performed prior to the main LEIS measurements. The He$^+$ beam size on the sample was estimated for each system, and spectra from blank RF-TiO$_2$ and a metallic Ru reference sample were measured. The Ru sputter rate was estimated using a measurement of the TD-LEIS CS-Ru$_3$/SiO$_2$ sample.

5.4.3.1 He$^+$ Ion Beam Area

The He$^+$ ion beam area for each UHV system was estimated so that the total ion dosage per area could be determined quantitatively for each LEIS measurement. This was important for comparing measurements between the different LEIS instruments, and for estimating the extent of surface damage by the ion beam. On the University of Utah LEIS instrument the sample was moved horizontally through the He$^+$ beam while ion current was measured. On this UHV system the substrate was spot welded to wires which held it in place such that there was no backing plate, and any detected ion current could be attributed to the He$^+$ beam impacting the sample. Figure 5-15 shows the results of this measurement, which allowed for determination of the beam radius by finding the locations where the beam first overlapped with the sample (*i.e.* an increase in ion current noted) and where the entire beam was on the sample (*i.e.* maximum ion current reached). These are shown by vertical black lines, indicating the radius of the He$^+$ beam was 5 mm. The true beam shape was unknown, so to calculate the area its shape was assumed to be circular, where $A = \pi.r^2$. Based on this, the total beam area was determined to be 79 mm^2.
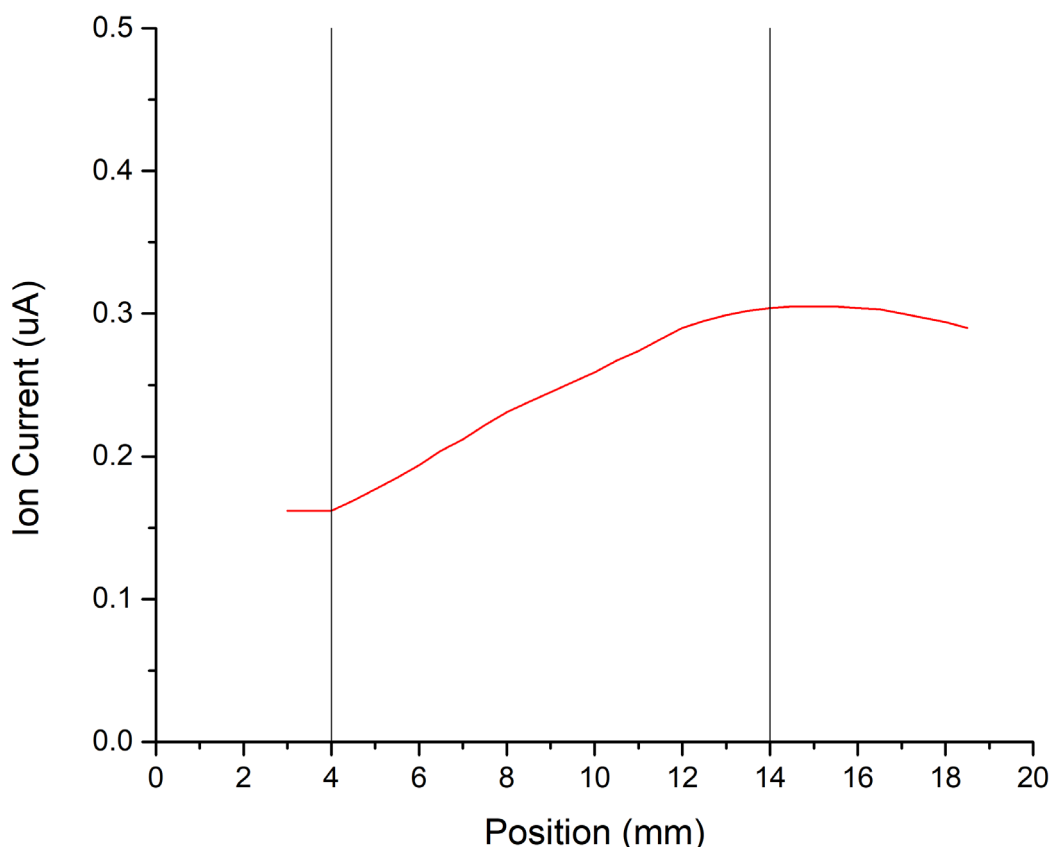
Figure 5-15: Sample position vs. He⁺ ion current measured on the University of Utah LEIS instrument. The positions are marked when the ion beam first reached the sample (4 mm) and when the entire ion beam was on the sample (14 mm). The difference indicates the diameter was 10 mm, and radius was 5 mm.

At Flinders University the samples were mounted on a conductive Mo backing plate, and the method above could not be used to determine the beam area because the ion current could also be measured through the sample plate. As an alternative, to determine the He⁺ beam area an SiO_2 substrate was sputtered using a very large dose of 1 keV He⁺ (0.188 µA for 16 hours) to induce visible surface damage, and an optical microscope was used to image the beam-damaged spot (Figure 5-16a). The damaged area was calculated using the program ImageJ. The pixels of the microscope image were calibrated to the scale bar, and the beam area was determined by creating a 2D shape which followed the edge of the damaged area. This is shown by the yellow outline in Figure 5-16b. The relationship between the extent of SiO_2 surface damage and the sample discolouring was not known, and the yellow outline thus represents an estimation of the diameter for the full width half maximum (FWHM) of the dose. The beam area was measured to be 12.06 mm² ± 0.15 mm² (see section 5.3.6 for further details on the ImageJ calculations).
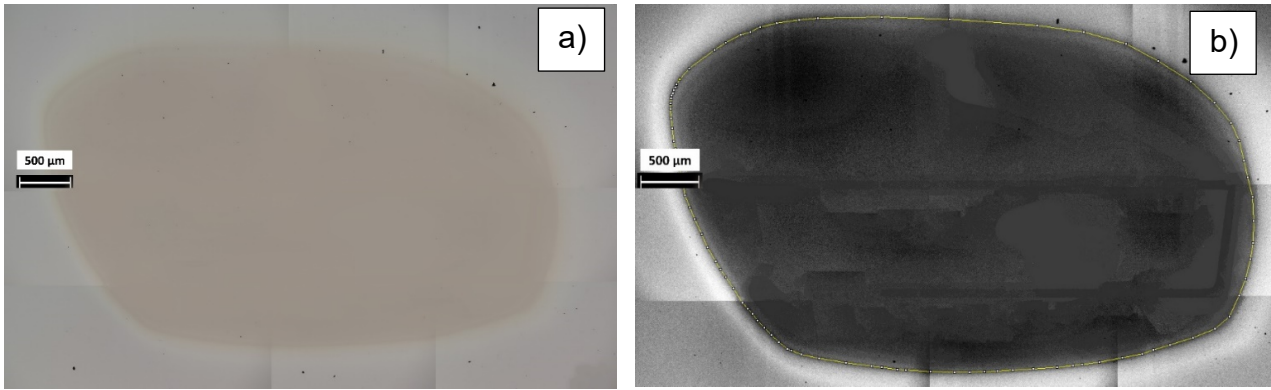
Figure 5-16: a) Optical microscope image of SiO₂ damaged by 1 keV He⁺ using the Flinders University ion gun. The discoloured oval is a damaged area of the substrate and represents the area of He⁺ beam-damage. Multiple individual microscope images were combined to measure the full spot. b) ImageJ processed version of the image used to calculate the beam damaged area. The yellow outline shows the area being measured.

5.4.3.2 LEIS of Blank Reference Materials

A blank RF-TiO₂ substrate and metallic Ru reference sample were measured with LEIS and the results are shown in Figure 5-17. From these reference measurements, it was found that the LEIS surface peak locations for the key elements of interest were E/E_0 = 0.85 for Ru, 0.73 for Ti, and 0.41 for O. These measurements were performed at Flinders University, but the peaks also occurred at the same locations on the University of Utah instrument.
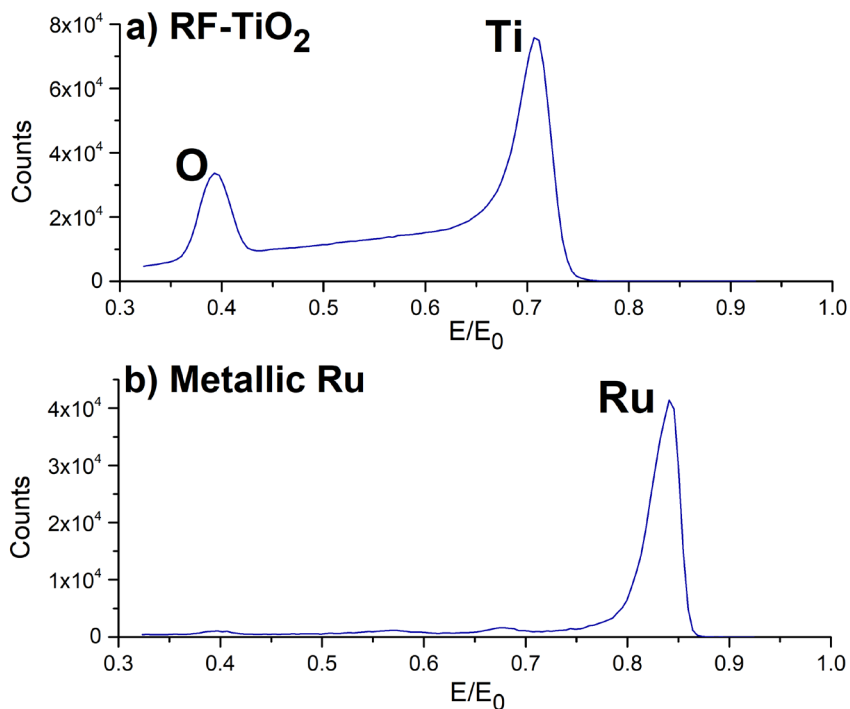
Figure 5-17: Reference LEIS measurements. a) RF-TiO₂, after heating to 723 K. b) Metallic Ru, after heating to 1073 K and sputter cleaning with 3 keV Ar⁺. Some contaminants were present in low concentrations in the metallic Ru, which are visible as 3 smaller peaks a higher E/E_0.

5.4.3.3 Determination of Ru Sputter Rate

To determine the sputter rate of Ru by the He$^+$ beam in these measurements, and thus estimate the surface damage, a LEIS measurement was performed on 800 K heat-treated CS-Ru$_3$/SiO$_2$. This was the same sample used for TD-LEIS in section 5.4.4.2 below, and was performed after the main TD-LEIS so as to not affect the results. Repeated LEIS measurements were performed on a single cluster spot to determine how the dose affected the sample. The measured LEIS spectra (not shown) were comparable in features and shape to the CS-Ru$_3$/SiO$_2$ LEIS shown in the TD-LEIS measurement in Figure 5-19a below. Figure 5-18a shows the integrated ratios of Ru/(Si+O) vs. He$^+$ ion dose. There was no noticeable decrease until ~1 x 10^{15} ions/cm^2, after which the Ru peak size began to decrease. The lack of initial change in peak size was likely due to the presence of some carbonaceous contamination atop the Ru clusters which was sputtered off by the He$^+$ beam, thus exposing the Ru.
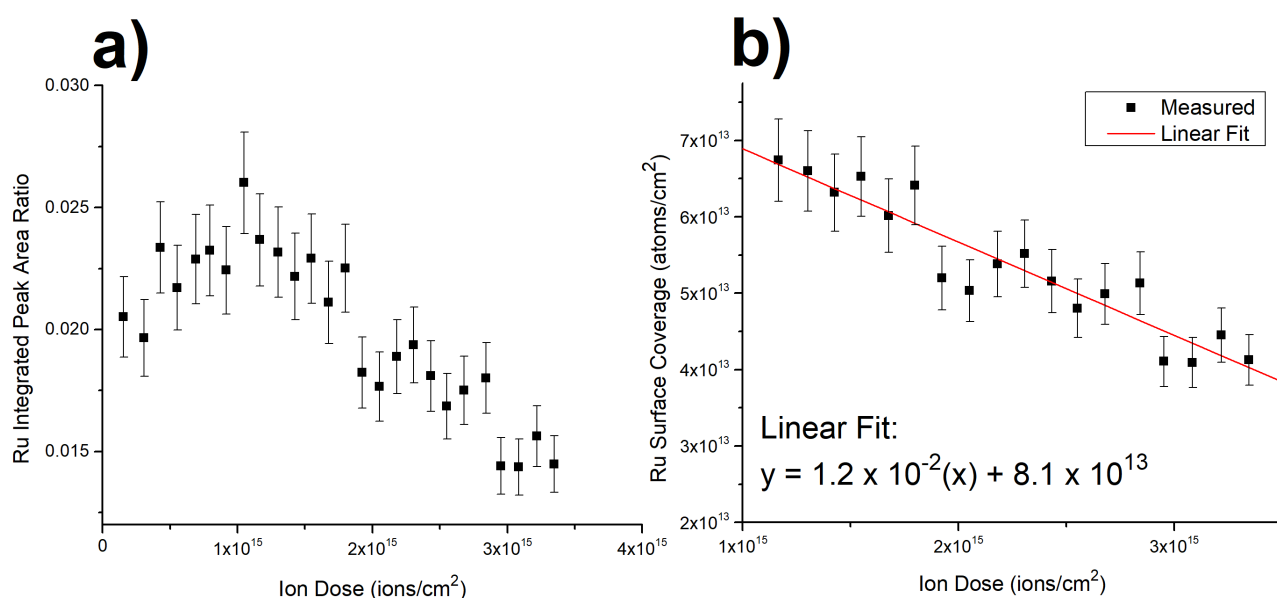
Figure 5-18: Series LEIS measurement of CS-Ru$_3$/SiO$_2$ after heating to 800 K. This was performed to determine the Ru sputter rate. a) Ru integrated peak ratios vs. cumulative ion dose. b) Calibrated graph of Ru surface coverage vs. cumulative ion dose. (b) was truncated to data points > 1 x 10^{15} ions/cm^2 (discussed in text), and a linear fitting was produced and shown in the figure inset. Uncertainties in Ru peak ratios are ~8% (see section 5.3.7.3).

Figure 5-18b shows the same LEIS measurement as Figure 5-18a. The data was truncated to data points >1 x 10^{15} ions/cm^2 where Ru sputtering was occurring, and the integrated Ru peak area ratio was calibrated to determine the number of Ru atoms per area, which was plotted on the vertical axis. The calibration was based on the fact that 1.5 x 10^{14} Ru atoms/cm^2 were initially deposited by the CS. However, this measurement was performed

after the main TD-LEIS measurement (shown in Figure 5-19), and the TD-LEIS showed that after heating to 800 K, the Ru peak area ratio and therefore number of surface atoms had decreased to 0.43 times the initial value due to agglomeration (see section 5.4.4.2 below for more details). This meant that 0.43 times the initial, as-deposited surface concentration was present for the sputter rate measurement. The integrated peak area ratio was calibrated linearly based on this known starting value to determine the surface concentration at each sputter dose. In LEIS there may be changes in the surface peak due to structure changes as well as concentration changes [309, 328], but for the purpose of surface damage estimation this was neglected and it was reasonably assumed that the cluster structure did not drastically change with agglomeration.

The linear fitting for Ru surface coverage vs. ion dose produced in Figure 5-18b had a slope of -1.2×10^{-2} atoms/ion, and an offset of 8.1×10^{13} atoms/cm^2. The offset was related to the initial surface concentration of Ru atoms. The negative slope gave the sputter rate for Ru atoms by 1 keV He$^+$, where an average of 1.2×10^{-2} Ru atoms were removed by each He$^+$. This sputter rate was used in calculations of the surface Ru damage for each TD-LEIS measurement, which are shown in Table 5-4 (see section 5.3.7.4 for an example calculation).

5.4.4 LEIS Results

TD-LEIS measurements were performed on CS-Ru$_3$/SiO$_2$, CVD-Ru$_3$(CO)$_{12}$/HDS-RF-TiO$_2$, and CS-Ru$_3$ on RF-TiO$_2$ with 3 different sputtering doses. Further LEIS measurements were also performed to assist with the interpretation of the CS-Ru$_3$/RF-TiO$_2$ results.

5.4.4.1 Ru Surface Coverage and Ion Dosage for TD-LEIS Samples

XPS was performed on each of the TD-LEIS samples after the TD-LEIS measurements were completed, in order to estimate Ru surface coverage. These XPS results are given in Table 5-4. The ratio of total carbon atoms to Ru atoms was calculated and provides a measure of the level of contamination on each sample. In addition, the total ion dose for each measurement is shown, along with the estimated sputter percentage of Ru which was used as a measurement for the level of Ru cluster surface damage due to LEIS. Between all TD-LEIS samples, the percentage of Ru sputtered from the surface during a measurement was an average of 2.9%, and a maximum of 6.8%. These values were cumulative over the TD-LEIS measurements at all temperatures, and this level of surface damage was small enough that He$^+$ beam damage was neglected as a justification for any changes to Ru peaks in TD-LEIS spectra.

Table 5-4: Ru At %, Ru surface coverage, C/Ru ratio, total He$^+$ dose, and total sputtered Ru for all TD-LEIS samples. Measurements were after TD-LEIS, and the samples were heated to 800 K (CS-Ru$_3$ depositions on RF-TiO$_2$) or 900 K (CVD-Ru$_3$(CO)$_{12}$/HDS-RF-TiO$_2$ and CS-Ru$_3$/SiO$_2$). An example calculation for estimation of the sputtered Ru is given in section 5.3.7.4. The CVD-Ru$_3$(CO)$_{12}$ values in the table are averages from two identical depositions and measurements, referred to as TD-LEIS A and TD-LEIS B. The fitting uncertainties for Ru At% and C/Ru atomic ratios are ~4%. The absolute error in Ru surface coverage is ~100%, while the relative uncertainty between the experiments is based on the Ru At% and is ~4%. Uncertainties and errors for XPS were discussed in discussed in section 3.6.1.3.

Deposition	Substrate	Ru At% (%)	Ru Surface Coverage (% ML)	C/Ru Atomic Ratio	Total Ion Dose (ions/cm^2)	Total Ru Sputtered (%)
CS-Ru$_3$	SiO$_2$	0.5	3.3	5.4	1.2 x 10^{15}	1.3
CVD-Ru$_3$(CO)$_{12}$	HDS-RF-TiO$_2$	1.5	10.7	1.5	6.0 x 10^{15}	6.8
CS-Ru$_3$	NS-RF-TiO$_2$	0.4	2.6	12.4	1.8 x 10^{15}	2.1
CS-Ru$_3$	LDS-RF-TiO$_2$	0.3	2.3	13.9	1.9 x 10^{15}	2.1
CS-Ru$_3$	HDS-RF-TiO$_2$	0.3	2.2	8.4	1.8 x 10^{15}	2.0

5.4.4.2 TD-LEIS of CS-Ru$_3$/SiO$_2$

A TD-LEIS measurement was performed on CS-Ru$_3$/SiO$_2$. The lowest and highest temperature spectra are shown in Figure 5-19a, with peaks labelled for Ru, Si, and O. The spectra were integrated, and the peak ratio of Ru/(Si+O) was determined at each temperature, shown in Figure 5-19b.
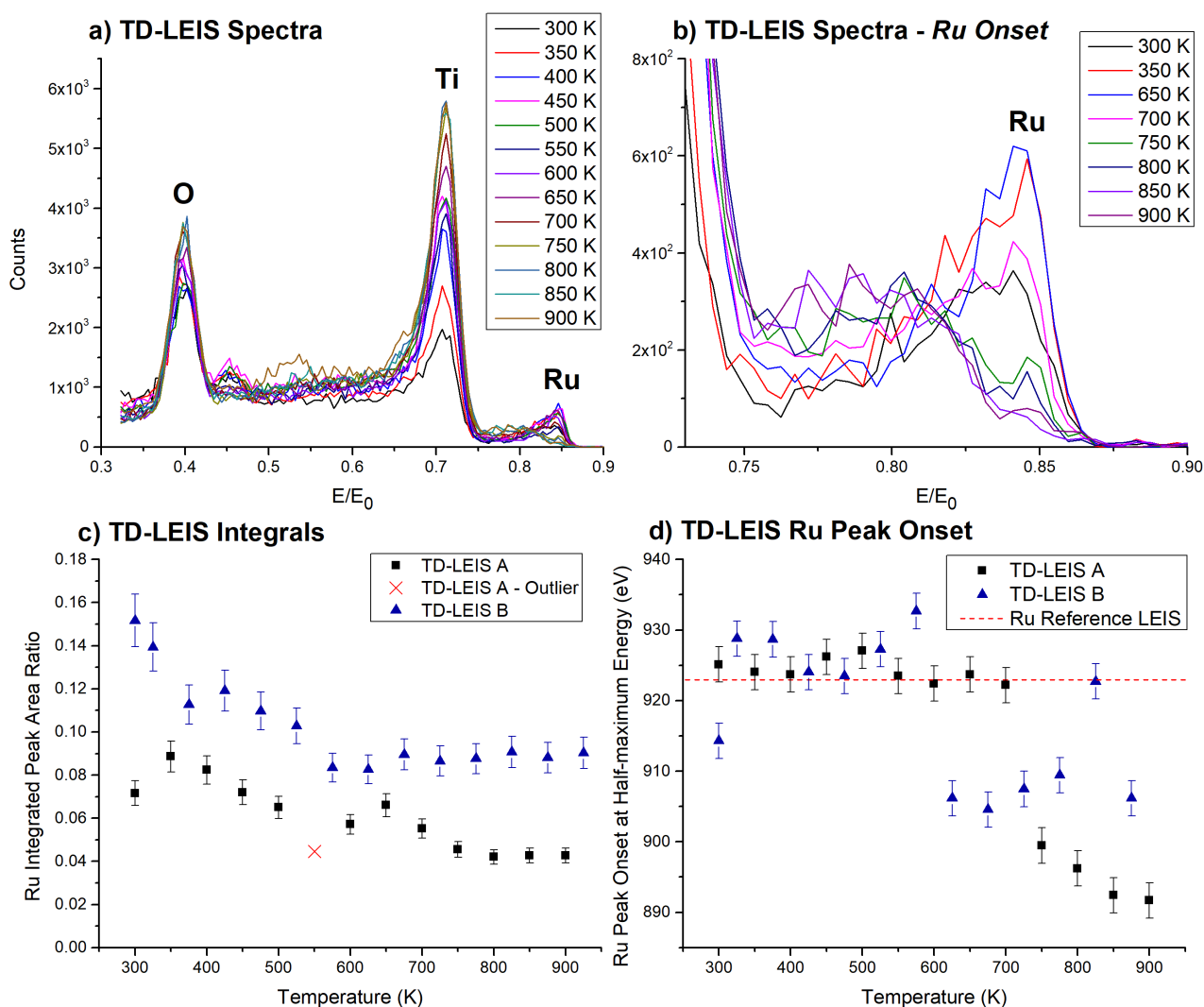
a) TD-LEIS Spectra
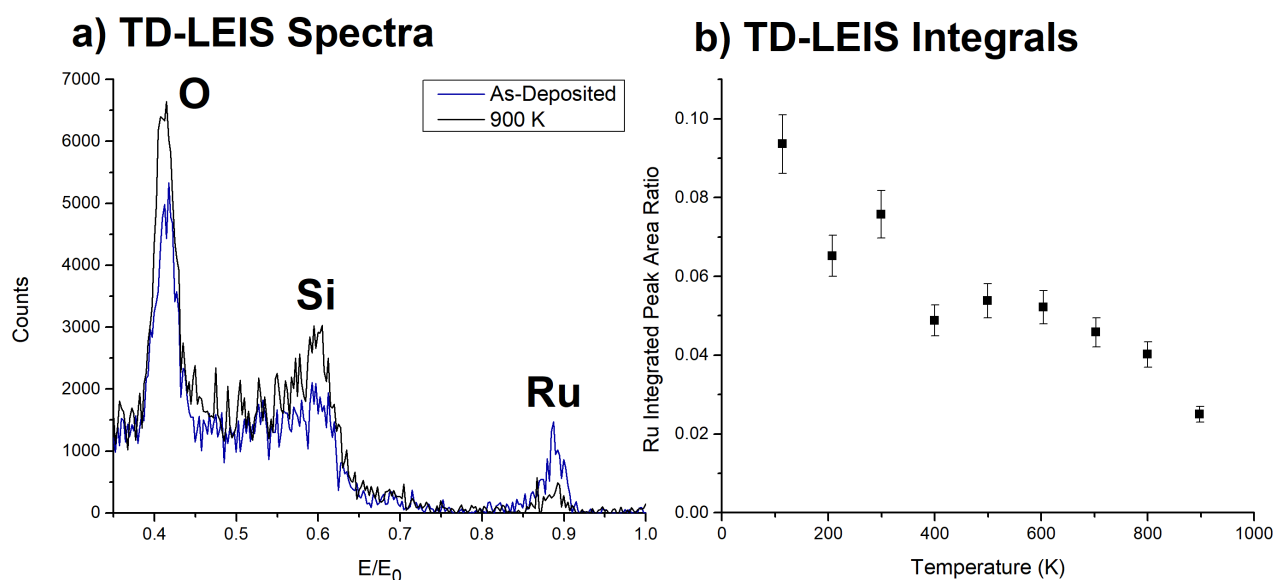
b) TD-LEIS Integrals

Figure 5-19: TD-LEIS of CS-Ru₃/SiO₂. a) LEIS spectra for initial and final temperature measurements. b) integrated Ru/(Si+O) peak ratio vs. temperature. Uncertainties in the Ru peak area ratios are ~8% (see section 5.3.7.3).

In Figure 5-19a the total count rate of the LEIS spectrum increased when heated to 900 K. This was indicative of surface contaminants such as adventitious carbon being removed. Figure 5-19b showed a decrease in the relative amount of Ru in the LEIS-accessible layer as the temperature of the sample was increased. The downward trend with temperature continued until 900 K where the LEIS peak ratio was 0.43 times the initial value. Due to the surface-sensitivity of LEIS, this indicated the amount of Ru in the topmost layer (*i.e.* not covered by other species) had decreased. This was most likely due to cluster agglomeration, where the number of surface Ru atoms in the system had reduced due to Ru forming multilayer structures. This was supported by a previous study by Kane *et al.*, where it was shown for Pd_n clusters that as cluster size increased, the change from single to multilayer clusters attenuated the LEIS signal [315]. The agglomeration of Ru clusters on SiO_2 when heated to 800 K was also supported by results in Chapter 4, as previously discussed.

5.4.4.3 TD-LEIS of CVD-Ru₃(CO)₁₂/HDS- RF-TiO₂

The full TD-LEIS measurement of $CVD-Ru_3(CO)_{12}/HDS-RF-TiO_2$ was performed 2 times on separate samples, including the substrate preparation, cluster deposition, and measurement. This was to confirm the reliability of the results, and these were named TD-LEIS A and TD-LEIS B. Figure 5-20 shows the measured TD-LEIS results for one of these measurements (TD-LEIS A), and the analysed data for both measurements.

Figure 5-20: TD-LEIS of CVD-Ru₃(CO)₁₂/HDS-RF-TiO₂. Separate depositions and TD-LEIS measurements were performed on 2 samples. (a) and (b) show spectra from TD-LEIS A, while (c) and (d) show collated data from both TD-LEIS measurements. a) LEIS spectra at all measured temperatures. b) Selected temperatures zoomed in to the Ru peak region. c) Integrated Ru/(Ti+O) peak ratios vs. temperature. The data point marked with a cross has a lower ratio than expected because the sample was left in the vacuum chamber for longer after heating due to an equipment issue, which allowed some adventitious carbon to adsorb atop the clusters. This data point is plotted for completion but is treated as an outlier. Uncertainties in Ru integrated peak ratios are ~8% (see section 5.3.7.3 for discussion on uncertainties). d) Half-maximum peak onset for Ru vs. temperature, in terms of backscattered He⁺ energy in eV. The black dashed line at 923 eV represents the Ru half-maximum onset for a metallic Ru reference sample. The error bars are ± 2.5 eV.

Figure 5-20a shows LEIS at all temperatures measured for CVD-Ru₃(CO)₁₂/HDS-RF-TiO₂. The overall signal strength increased with increasing temperature, which was indicative of surface contamination being sputtered. Figure 5-20b displays the Ru peak region. The onset slope of the Ru peak (on the right) decreased at 650-700 K, and decreased further as the temperature was increased to 850 K. The shape then remained constant when heated to 900 K. Starting at 650-700 K, the counts at ~0.79 E/E₀ increased and the peak location of

Ru was shifted to lower E/E_0 values. The peak shifting was indicative of the clusters being covered by an overlayer. For LEIS measurements, if there is material covering the species of interest the peak shifts to lower E/E_0. This is because the He^+ projectiles lose energy penetrating through the upper layer before and after backscattering [328, 403]. In Chapter 4 it was proposed that CVD-$Ru_3(CO)_{12}$/HDS-RF-TiO_2 may be encapsulated by the HDS-RF-TiO_2 substrate when heated, based on the loss of all Ru-CO binding sites after heating the sample to 723 K. This result aligns with the finding in TD-LEIS, and together presents a strong argument that the clusters were encapsulated by the substrate.

In Figure 5-20c the integrated Ru peak ratios are shown vs. temperature, where the integration included both the high and low energy regions of the Ru peak (for surface and sub-surface species). The relative Ru LEIS peak size decreased with increasing temperature; this decrease was most likely related to the encapsulation of the clusters, possibly combined with an amount of Ru sputtering by the He^+ beam. Comparing the two LEIS measurements, the results were similar. TD-LEIS B had a higher Ru/(Ti+O) ratio than TD-LEIS A at all temperatures, however both depositions were performed identically, and the difference in Ru peak ratios was because TD-LEIS B featured a higher background count rate. No background correction was performed for the peak integration, which comparatively made the Ru peaks larger.

Figure 18d shows the onset half-maximum energy determined from the high E/E_0 side of the Ru peaks in each TD-LEIS spectrum. This is the energy where the Ru peak reached half its maximum height. For TD-LEIS A, the onset half-maximum energy was at approximately the metallic Ru value (indicated by the black dotted line) until 750 K, where the onset half-maximum energy shifted to a lower energy. After 750 K the peak energy decreased slightly with heating to 900 K. For TD-LEIS B, the shift to a lower Ru onset half-maximum energy occurred slightly earlier at 575 K, and there did not appear to be a further decrease with heating. These differences may be due to thermocouple calibration differences between the measurements (this can be affected by the spot weld joint between the sample and thermocouple). The large shift in onset half-maximum energy which occurred in both spectra corresponded to the complete loss of the surface peak and was treated as an indicator of the clusters being covered by a substrate overlayer. The average temperature for this to occur was 660 K ± 120 K. In TD-LEIS B the as-deposited (298 K) measurement had a lower onset half-maximum energy than expected, likely due to the presence of some hydrocarbon contaminants. Additionally, the 825 K measurement appears to be an outlier, being present at a higher energy than expected.

From the results in Figure 18d the depth of the titania layer covering the clusters was calculated. A similar method was used in a study by Belsey *et al.*, where Au nanoparticles were covered with an organic layer and the shifting of the LEIS onset half-maximum energy for the Au peak compared to a clean Au reference was used to determine the overlayer thickness, based on the stopping power of the organic layer [403]. For each TD-LEIS measurement the onset half-maximum energies were averaged before and after the onset half-maximum energy of encapsulation, and the shift was calculated to determine the loss of He^+ energy due to the stopping power of the overlayer, ΔE (this did not include the backscattering energy loss). Disregarding the mentioned outliers, ΔE was determined to be 29.9 eV ± 5.3 eV and 19.7 eV ± 5.2 eV for TD-LEIS A and B respectively, where the average was 24.8 eV ± 5.3 eV.

ΔE was divided by the stopping power of the overlayer to give the total length of titania which the He^+ projectiles travelled through, L. This relationship is shown in Equation 5-1.

$$L = \frac{\Delta E}{Stopping\ Power} \qquad \text{5-1}$$

Because the projectiles travelled into and out of the titania overlayer, L was equal to the sum of the incoming length H, and outgoing length D. The beam impact angle was 45° and the angle to the detector was 90°; D thus represented the titania overlayer depth. The relationship between D and L was determined using right-angle trigonometry, so that the titania depth could be determined. The calculations in Equations 5-2 to 5-4 below determined the relationship between D and L, and an expression for D was found by substituting in Equation 5-1.

$$\cos(45°) = \frac{D}{H} \qquad \text{5-2}$$

$$L = D + H = D(1 + \frac{1}{\sin(45°)}) \qquad \text{5-3}$$

$$D = 0.4142\ L = \frac{0.4142 * \Delta E}{Stopping\ Power} \qquad \text{5-4}$$

SRIM was used to calculate the stopping power of He^+ ions in TiO_2; 29.74 eV/nm ± 2.97 eV/nm (see section 5.3.7.3 for details). Incorporating the average ΔE and stopping power into Equation 5-4, it was determined that D = 0.35 nm ± 0.08 nm. This represented the average overlayer depth, and this result was analysed further and compared to the depth

information gained from ARXPS in section 5.4.5.

5.4.4.4 LEIS of CS-Ru$_3$/RF-TiO$_2$

TD-LEIS was performed on CS-Ru$_3$ with 3 different substrate preparation methods: NS-, LDS-, and HDS-RF-TiO$_2$, and the results are shown in Figure 5-21. The Ru peak was not clearly visible in the LEIS spectra, which is discussed below.
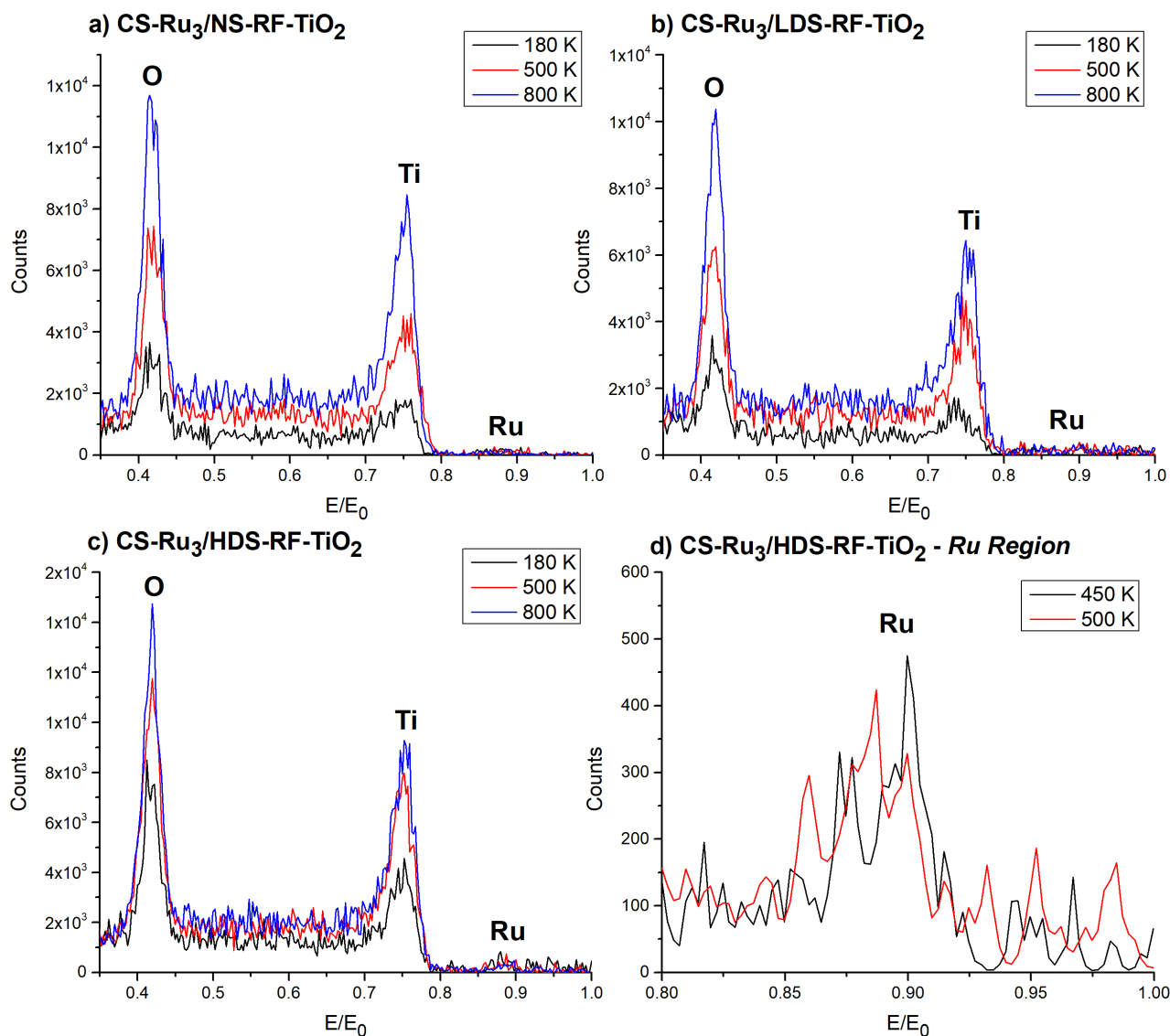
Figure 5-21: TD-LEIS of CS-Ru$_3$ on NS-, LDS-, and HDS-RF-TiO$_2$. Scanned at 14 temperatures between 180 K and 800 K. Selected temperature spectra are shown. a) CS-Ru$_3$/NS-RF-TiO$_2$. b) CS-Ru$_3$/LDS-RF-TiO$_2$. c) CS-Ru$_3$/HDS-RF-TiO$_2$. d) 450 K and 500 K spectra for CS-Ru$_3$/HDS-RF-TiO$_2$, zoomed in to the Ru peak region.

In each of Figure 5-21a-c the total count rate increased after heating which was indicative of surface contaminants being removed. Figure 5-21a and Figure 5-21b both showed no clear Ru peak. The measurement in Figure 5-21a was repeated with a separate sample to check the reliability, and the results were identical. Figure 5-21c featured a small Ru peak

at intermediate temperatures, from 400 K to 700 K. These peaks were smaller than expected, for example, when compared to the TD-LEIS of CS-Ru_3/SiO_2 in Figure 5-19a. The Ru peak was much larger when supported on SiO_2, but this was not due to the Ru surface coverage which was comparable between the samples (see Table 5-4). The fact that CS-Ru_3 peaks were generally not visible in LEIS on the RF-TiO_2 substrates was different to the behaviour of CVD-$Ru_3(CO)_{12}$/HDS-RF-TiO_2 (Figure 5-20a), where the clusters were covered by the substrate but the Ru peak was still visible in the LEIS spectrum at reduced E/E_0. From the CO-TPD results in Chapter 4 it was expected that CS-Ru_3 supported on NS-RF-TiO_2 would be on the topmost layer as-deposited, but the clusters may be encapsulated by LDS- or HDS-RF-TiO_2 as-deposited. This did not match what was seen in the TD-LEIS data; no CS-Ru_3 clusters were visible on any RF-TiO_2 substrate as-deposited. However, because an Ru peak was still visible for CVD-$Ru_3(CO)_{12}$/HDS-RF-TiO_2 after encapsulation, this was not likely to be the mechanism for the lack of visible peaks for CS-Ru_3.

It is most likely that the level of carbon contamination present on the samples was affecting the results. In Table 5-4, the C/Ru atomic ratio was 12.4, 13.9, and 8.4 for the NS-, LDS-, and HDS-RF-TiO_2 respectively. These were based on XPS measurements performed after heating to 800 K for TD-LEIS, and thus represent the level of contamination still present after heat-treatment. CS-Ru_3/HDS-RF-TiO_2 had the lowest C/Ru ratio, and the most visible Ru peaks of the CS-Ru_3/RF-TiO_2 samples (from 400 K to 700 K). Additionally, Ru was most easily visible in the LEIS for CS-Ru_3/SiO_2, where the same amount of Ru was deposited, and the C/Ru ratio was 5.4. Because the CS-Ru_3 samples with lower C/Ru ratios had larger peaks, this points towards an interpretation that the Ru cluster peaks were being affected by carbonaceous contamination on the surface which attenuated the He^+ beam before it reached the Ru material. In order to support this interpretation, two additional series LEIS measurements were performed to determine the effects of the He^+ ion dose on the resulting spectra. This was performed for two separate CS-Ru_3/NS-RF-TiO_2 samples: as-deposited, and after heating to 800 K. The results for these measurements are shown in Figure 5-22.
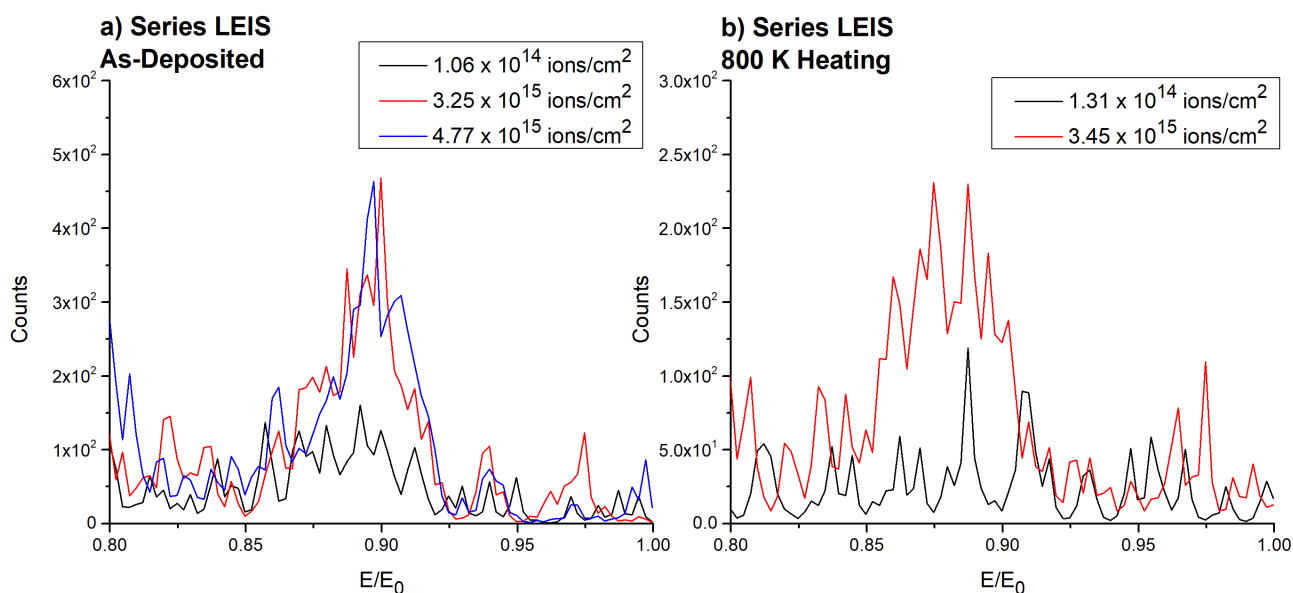
Figure 5-22: Series LEIS measurements, zoomed into the Ru peak region. a) CS-Ru$_3$/NS-RF-TiO$_2$, as-deposited. b) CS-Ru$_3$/NS-RF-TiO$_2$, after heating to 800 K. Cumulative doses for the presented scans are given in the legends. Separate samples were used in (a) and (b).

In Figure 5-22a the Ru region had no peak in the earlier measurements (see the lowest dose scan), but after a dose of 3.25 x 10^{15} ions/cm^2 a small Ru peak is apparent. The Ru peak size did not increase significantly after further sputtering. This indicated that the LEIS He$^+$ beam had sputtered off a covering layer which was blocking the He$^+$ from reaching the Ru. In Figure 5-22b an Ru peak also became visible after a similar dosage of 3.45 x 10^{15} ions/cm^2. This once again indicated that the He$^+$ blocking occurred similarly whether the sample had been heated to 800 K or not. Because a small Ru peak was made visible after sputtering the samples with 1 keV He$^+$, the Ru must have still been close to the surface layer. This conclusion supports the interpretation that carbonaceous contamination was attenuating the LEIS signal and obscuring the Ru peaks. As a note, in Chapter 4 it was argued that CS-Ru$_3$ was oxidised by heating to 800 K on NS-RF-TiO$_2$; thus, for the post-heating measurement in Figure 5-22b the covering species blocking the He$^+$ beam may be a combination of carbon contamination and oxides on the clusters. Due to the contamination, the CS-Ru$_3$/RF-TiO$_2$ TD-LEIS measurements could not be used to provide depth information about the clusters. This kind of LEIS signal attenuation by contamination has been seen in previous studies; an example by Brongersma [327] showed that an untreated Au sample which was exposed to atmosphere featured so much adsorbed hydrocarbons that no Au surface peak was present, even when XPS showed that the sample was high-purity with only minor carbon contamination.

The TD-LEIS measurements of CS-Ru$_3$ on RF-TiO$_2$ could not be repeated with a new RF-

TiO$_2$ wafer featuring less contamination; because the collaborative overseas trip was time constrained, with only a limited time was available for experiments at The University of Utah. However, if the experiments were to be repeated using a wafer with less contamination, there is an expectation that a Ru peak would likely be visible in LEIS. As an alternative, the clusters may be easier to measure in LEIS on a different type of TiO$_2$ substrate such as TiO$_2$(110), which would feature a purer structure with less carbon contamination and a flatter surface. Lastly, if a higher Ru surface coverage was used it may have been easier to identify the Ru peaks in LEIS.

5.4.5 Depth Information from ARXPS and LEIS

Both ARXPS and LEIS showed that for CVD-Ru$_3$(CO)$_{12}$/HDS-RF-TiO$_2$, the clusters were covered by a substrate overlayer due to heat treatment of the sample. Figure 5-23 shows a diagram of an Ru cluster with a substrate overlayer, which showing that the overlayer depth is the distance between the top of the surface and top of the Ru clusters. ARXPS further showed that CS-Ru$_3$/HDS-RF-TiO$_2$ was covered by an overlayer as-deposited, and the depth of penetration did not change by additional heating. In this section the number of titania overlayers in each case was estimated, and the surface depth information gained from ARXPS and LEIS was compared and discussed.
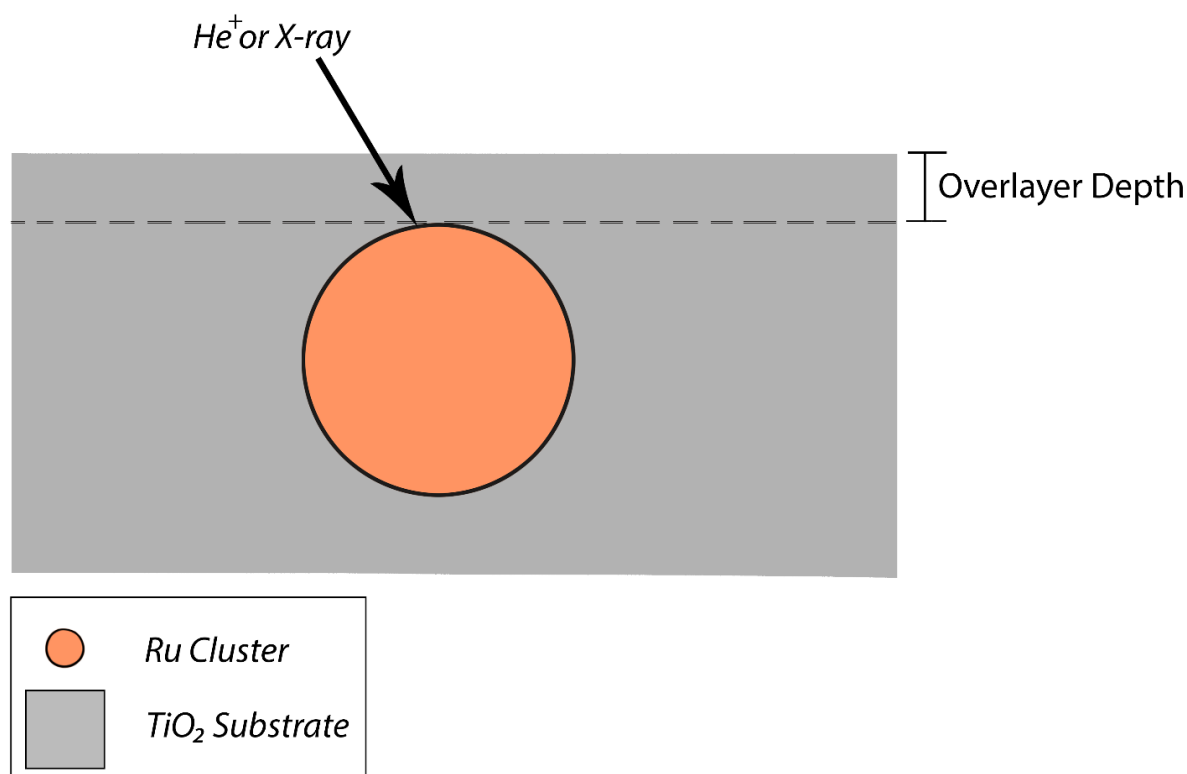
Figure 5-23: Diagram showing the overlayer depth of an Ru cluster which has been covered by a substrate overlayer. He$^+$ or X-rays must travel through this overlayer before reaching the Ru in TD-LEIS and ARXPS measurements, respectively.

5.4.5.1 Number of Titania Overlayers

Based on the estimated penetration depth of Ru into the titania substrate for each sample, the number of titania overlayers atop the clusters was estimated in units of monolayers, or ML. An assumption was made that the thickness of a ML of RF-TiO$_2$ could be estimated by the apical Ti-O bond length of the rutile TiO$_2$ crystal. This has been measured to be 1.98 Å ± 0.0009 Å [415], which is in agreement with a separate study using DFT calculations [416]. For each sample, the estimated penetration depth was divided by the ML thickness to determine the number of titania overlayers atop the clusters, which is given in Equation 5-5.

$$Titania\ Layers\ (ML) = \frac{D}{(Ti - O\ Bond\ Length)} \qquad 5\text{-}5$$

The number of titania overlayers was determined based on the LEIS and ARXPS results for D, in cases where the penetration depth could be estimated. The results of this are summarised in Table 5-5. The number of overlayers represent averages, and the number of overlayers atop a particular cluster may have varied across the sample surface. For ARXPS results, the depth profiles showed some Ru present on the surfaces even when overlayers were detected; for these measurements, the maximum penetration depth was used in the calculations. The reliability of these results was discussed and compared in section 5.4.5.2 below.

Table 5-5: Estimated number of titania monolayers atop Ru clusters, based on TD-LEIS and ARXPS results. Results are for the samples post-heat treatment. Numbers of overlayers represent averages which may have varied across each sample surface.

Deposition	Substrate	Technique	Ru Depth (nm)	Number of Overlayers (ML)
CVD-Ru$_3$(CO)$_{12}$	HDS-RF-TiO$_2$	LEIS	0.35 ± 0.08	1.74 ± 0.41
CVD-Ru$_3$(CO)$_{12}$	HDS-RF-TiO$_2$	ARXPS	0.24 ± 0.03	1.21 ± 0.15
CS-Ru$_3$	HDS-RF-TiO$_2$	ARXPS	0.10 ± 0.03	0.51 ± 0.15

Table 5-5 shows that CVD-Ru$_3$(CO)$_{12}$/HDS-RF-TiO$_2$ was covered by 1.21 ML ± 0.15 ML titania according to ARXPS, but 1.74 ML ± 0.41 ML according to LEIS. The results were between 1 and 2 ML for both cases, and it is likely that there were typically 1 or 2 ML of titania covering the Ru clusters in both cases, which may not have been consistent for all areas of the samples at all temperatures. The CS-Ru$_3$/HDS-RF-TiO$_2$ depth profile was only determined using ARXPS, and a maximum penetration of 0.51 ML ± 0.15 ML was determined. The calculated value being <1 ML implies that not all of the clusters were

covered, however from Chapter 4 the results suggested that the clusters were most likely completely encapsulated as-deposited in a measurement of the same system (based on the lack of Ru-CO sites). This inconsistency was most likely due to the accuracy of the ARXPS measurements, which is discussed below.

5.4.5.2 Comparing ARXPS and LEIS Results

Both ARXPS and LEIS were successfully used to determine depth information for CVD-$Ru_3(CO)_{12}$/HDS-RF-TiO_2. A key difference between the ARXPS and LEIS results was the extent to which Ru was covered by the titania substrate; in the ARXPS results, the depth profile showed ~40% of the Ru was not covered by the substrate, while LEIS showed that there was no Ru left in the surface layer after heat treatment. ARXPS also showed that ~66% of Ru was present on the surface layer for CS-Ru_3/HDS-RF-TiO_2, which contradicted results from Chapter 4 showing there was most likely no clusters on the surface layer as-deposited. Thus, a question presents itself as to which technique is more reliable for this system.

One of the advantages of LEIS is its extreme surface sensitivity [309]. Thus, for CVD-$Ru_3(CO)_{12}$/HDS-RF-TiO_2 the lack of an Ru surface peak in LEIS after heat-treatment reliably indicated that no Ru was remaining in the surface layer. LEIS has been used in similar ways previously [403]. Conversely, ARXPS is known to be non-reliable for surfaces which do not have a monotonic concentration depth profile, and do not have smooth depth profiles [400]. The fact that the Ru clusters were close to the surface when encapsulated meant the Ru concentration depth profile increased then decreased with depth, and the depth profile was thus non-monotonic. Also, RF-TiO_2 had a rough surface due to its nanoparticulate structure [357], which further complicated the ARXPS results because the measured XPS intensity may have been affected by the XPS observation angle as well as the surface roughness [400]. No such change in observation angle is required for LEIS. Additionally, the fact that a model and calculation was needed to determine depth information with ARXPS is a disadvantage compared to LEIS.

Due to the reasons listed above, the LEIS results were interpreted as being more reliable than ARXPS, and only the Ru depth information from LEIS was treated as quantitatively accurate. Because the LEIS was most likely more reliable, the ARXPS depth profiles shown in Figure 5-14c-d were deemed to not be completely accurate in shape, and the presence of surface clusters in the depth profiles after encapsulation was most likely a product of the model calculation procedure. Because of this, the ARXPS depth profiles were treated as

qualitative only. While the shapes of the ARXPS depth profiles most likely did not represent the true depth profiles, the qualitative evidence was sufficiently reliable such that for CVD-$Ru_3(CO)_{12}$/HDS-RF-TiO_2 the clusters were on the surface as-deposited but covered after heating, while for CS-Ru_3/HDS-RF-TiO_2 clusters were covered from room temperature. This interpretation aligns with the CO-TPD results in Chapter 4 as discussed earlier, providing further evidence for these qualitative results.

5.4.6 Cluster Encapsulation

5.4.6.1 Encapsulation by Substrate

In Chapter 4, CO-TPD and XPS data provided evidence that Ru-CO binding sites were being blocked for Ru_3 on sputtered RF-TiO_2 substrates, and it was argued that this may be due to encapsulation. The results in this chapter provide strong evidence for this encapsulation reaction. Importantly, CVD-$Ru_3(CO)_{12}$ was directly shown to be covered by HDS-RF-TiO_2 substrate material as a result of heat treatment using TD-LEIS. This was the first direct measurement of the migration of Ru clusters below the surface layer of HDS-RF-TiO_2; the interpretations in Chapter 4 were based on changes in the Ru-CO binding sites available on the surface, rather than measuring the presence of Ru on the surface layer. The ARXPS results suggested that CS-Ru_3/HDS-RF-TiO_2 was covered by substrate material as-deposited, which also matched CO-TPD results in Chapter 4 which indicated that no Ru-CO binding sites were available for this system as-deposited. TD-LEIS results indicated cluster encapsulation did not occur for CS-Ru_3/SiO_2, and instead the Ru_3 clusters agglomerated on the surface. Diagrams summarising the results regarding encapsulation for these three sample types before and after heat treatment are shown in Figure 5-24.
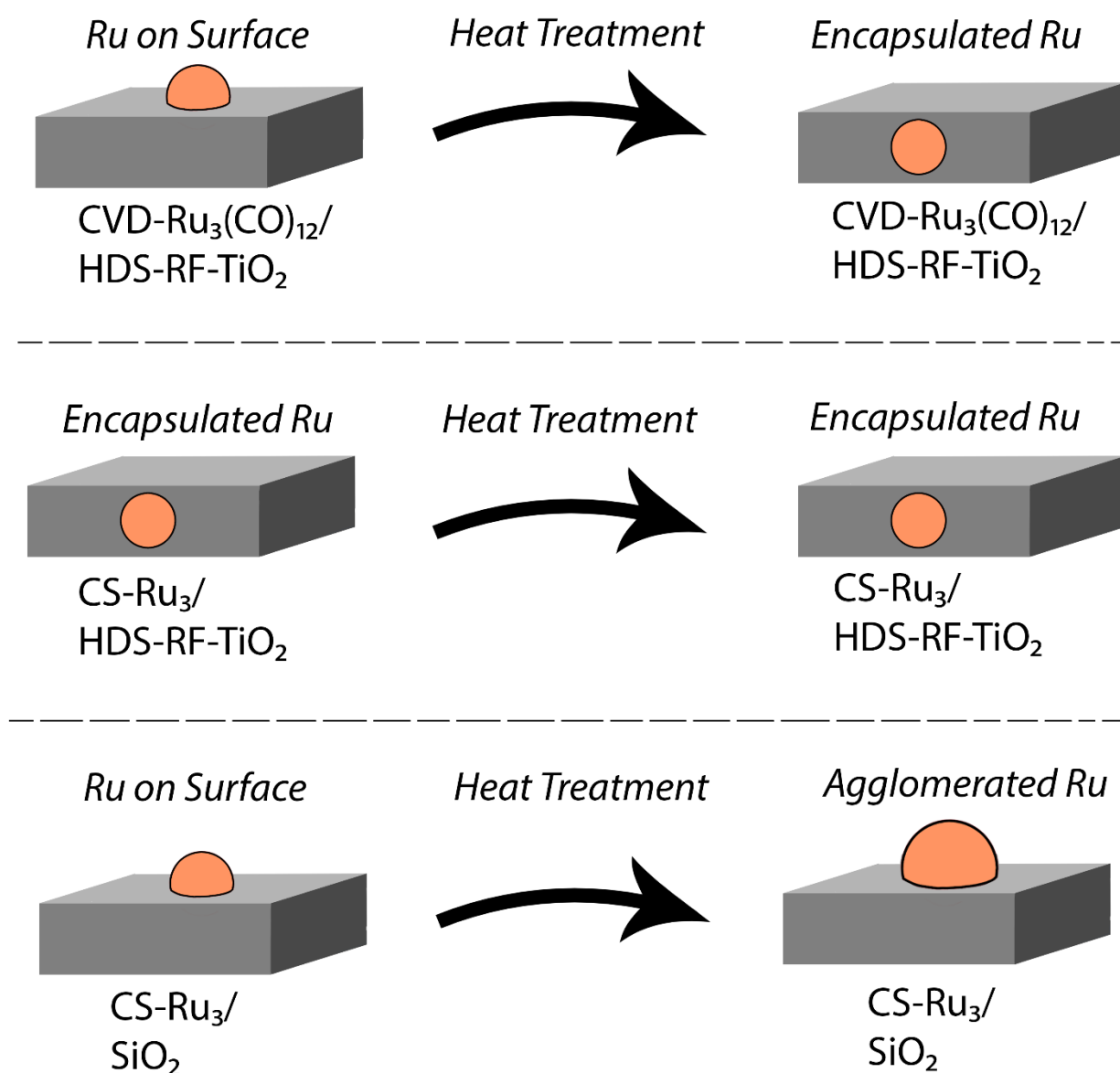
Figure 5-24: Summary of results regarding cluster encapsulation for CVD-Ru₃(CO)₁₂/ HDS-RF-TiO₂ (top), CS-Ru₃/HDS-RF-TiO₂ (middle), and CS-Ru₃/SiO₂ (bottom). Each sample is shown before and after heat treatment (see individual results sections for heat treatment temperatures).

The penetration of Ru clusters into the substrate for CVD-Ru₃(CO)₁₂/HDS-RF-TiO₂ was quantitatively measured to be 0.35 nm, ± 0.08 nm. This reported encapsulation depth was comparable to previously reported results in a study by Fu *et al.* [203], where 3 samples of Pd nanoparticles supported on TiO_2(110) were analysed, and using the shift in the RBS high energy edges of Pd compared to uncovered particles it was estimated that the samples had TiO_x overlayers with thicknesses of 0.13 nm, 0.14 nm, and 0.27 nm. These were of a comparable overlayer depth to the measurements in this study, and the fact that very few MLs of titania were covering the clusters was the same in both studies.

The encapsulation of bare, as-deposited Ru clusters was not expected when compared to other examples of cluster encapsulation in the literature. For example, Ovari *et al.* [308] used LEIS to show that Rh clusters were present on a TiO_2(110) surface layer until 700 K, however after heating to 900 K the clusters were encapsulated. Similarly, in another example for Pd clusters on TiO_2(110) the encapsulation started at ~553 K and reached a maximum at ~773 K [185]. In the Pd cluster study, the authors suggested that the activation of defect mobility due to heating was required for encapsulation to occur. Because no heating was required for the encapsulation of Ru, this implied the reaction mechanism was most likely different in the case of Ru clusters on sputtered RF-TiO_2.

The possible mechanisms behind cluster encapsulation by RF-TiO_2 were previously discussed in section 4.4.3.3 of Chapter 4, where several possible mechanisms were put forward which accounted for the cluster encapsulation at room temperature. These included: 1) a possible increased RF-TiO_2 mobility at low temperatures when it was sputtered, and 2) pre-deposition sputtering creating small, oxygen deficient pores for the clusters to enter and pin to [186]. Both of these interpretations, however, had inconsistencies; RF-TiO_2 mobility is typically only shown at elevated temperatures [185, 204, 394], and based on the availability of Ru-CO binding sites on the surface in Chapter 4, if there were indeed pores causing the lack of surface Ru clusters there must have also been a mechanism for the pores to close at without heating, because no Ru-CO sites were available to CO when dosed under UHV. Information in this chapter did not provide further evidence to elucidate the true encapsulation mechanism.

The results in this chapter did not provide information about the structure of the Ru clusters underneath the overlayers, and it was not clear whether the clusters were encapsulated as bare Ru_3, agglomerated particles, or decomposed Ru atoms. The agglomeration of Ru clusters on SiO_2 did not result in a significant shift in the Ru 3d XPS peak, and thus in this study TD-XPS could not be used as a measurement for agglomeration as is the case for some other metal clusters such as Au, where peak shifting relationships between cluster size and XPS core BE have been shown [73, 98, 102, 287, 288]. Furthermore, the ARXPS and LEIS depth profiling were not able to provide information on the size of the clusters. It is possible that the structure of the clusters could be measured using a scanning transmission electron microscope (STEM) if the sample was sliced with a focused ion beam, but this may also change the sample due to the method causing local heating.

To the best knowledge of the author, this type of titania encapsulation of Ru clusters has not

been previously reported in the literature. In fact, there is a previous measurement of $Ru_3(CO)_{12}$ supported on $TiO_2(110)$ where the surface was heat treated under UHV and encapsulation did not occur, as evidenced by the availability of Ru-CO binding sites [75]. Additionally, the encapsulation of bare CS Ru clusters as-deposited was unique from other cluster studies [185, 308], as previously described. The differences between this study and other literature can be attributed to the differences between the titania substrates; $TiO_2(110)$ was used in the other studies [185, 308], which did not have the same surface properties as the HDS-RF-TiO_2 used in this study. Encapsulation is typically based on the minimisation of surface energy [185, 203, 210, 213], and the nature of encapsulation varying per system of metal and substrate is well known in the literature [184, 185, 210, 417, 418].

5.4.6.2 Composition of Substrate Overlayer

TD-LEIS and ARXPS both showed that heat treatment caused cluster encapsulation for CVD-$Ru_3(CO)_{12}$/HDS-RF-TiO_2, and this allowed for monitoring the differences in surface composition due to encapsulation. The TD-XPS results for the Ti defect ratio in Figure 5-11 showed that when heat-treated the level of titania defects in the upper, XPS-accessible layers of the surface of CVD-$Ru_3(CO)_{12}$/HDS-RF-TiO_2 increased beyond the level of a blank sample. This provided evidence that an encapsulation reaction was occurring where the clusters were being covered by reduced titania; TiO_x, where x < 2. Increases in Ti defects such as this have been used previously in the literature as evidence for metal particle encapsulation by a layer of reduced titania for a range of other TiO_2-supported systems, including Pd/TiO_2 [185, 213], Pt/TiO_2 [207, 210], and Rh/TiO_2 [186, 211, 212]. However, an increase in Ti defects alone is not evidence that reduced TiO_x is atop the clusters; for example, an increase in defects may still be visible in XPS if the defects were the clusters. Based on the TD-XPS Ti defect results in addition to the prevalence of reduced titania overlayers for encapsulation in the literature, it was assumed the overlayers were reduced TiO_x. This is further discussed in Chapter 6 based on MIES results. In other studies, the reduced nature of the overlayer has also been confirmed using microscopy for systems involving larger supported particles [208, 216, 386].

5.4.6.3 De-ligation and Encapsulation for CVD-$Ru_3(CO)_{12}$

For CVD-$Ru_3(CO)_{12}$/HDS-RF-TiO_2, both the de-ligation of CO and encapsulation of the clusters occurred due to heating. This naturally presents a question about how the ligand removal is related to encapsulation, and whether there is a temperature range in which bare CVD-deposited clusters could exist on the surface. In the TD-XPS results, Ru 3d BE and CO/Ru atomic ratios indicated the majority of CO ligands were removed by heating to 423

K, but there may have still been ~1 or a few ligands attached until higher temperatures such as 700 K to 800 K [74, 75]. In the synchrotron ARXPS depth profile (Figure 5-14c), the clusters were all on the surface layer at 423 K, but encapsulation began upon heating to 523 K and reached the full depth at 648 K. TD-LEIS similarly showed encapsulation was completed (*i.e.* no Ru in the surface layer) at 660 K ± 120 K. Because ARXPS showed encapsulation starts at ~523 K, it is concluded that the majority of ligands need to be removed for encapsulation, but complete ligand removal is not required. Therefore, there is not an existing temperature range where fully bare Ru clusters can exist on the surface layer without encapsulation. This outcome must be kept in mind when considering catalytic applications, because it is often it is desired to remove the ligands to expose bare clusters for catalysis [3, 5, 74, 75].

5.4.6.4 Application for Catalysis

For catalytic applications, encapsulation of supported metal catalysts by the substrate material is generally not desirable because the catalytic properties can be effected by either the change in properties of the metal, or the steric hindrance of reactant molecules being blocked from the metal catalyst [185, 186, 213]. However, in some cases overlayers have been found to be of benefit to small metal clusters. As was mentioned in the Introduction of this chapter, Negishi *et al.* [4] have produced photocatalytic Au_{25}-loaded $BaLa_4Ti_4O_{15}$, where the clusters were covered by a chromium oxide overlayer. This system had a dual benefit for catalysis of decreasing the rate of the O_2 photoreduction back-reaction, as well as decreasing the level of UV irradiation-induced cluster agglomeration which occurred for Au_n clusters [4, 146]. Using HRTEM they showed the clusters were ~1 nm in diameter and the Cd_2O_3 overlayer was 0.8-0.9 nm thick [4].

In light of the study by Negishi *et al.* [4], the effect of the reduced titania overlayer on the catalytic and photocatalytic activity of the Ru clusters in this study needs to be tested explicitly for reactions such as catalytic CO hydrogenation and photocatalytic water splitting to determine its viability. There is potential for the overlayer to increase the stability of the clusters without suppressing the catalytic reaction. The estimated overlayer depth in the study by Negishi [4] was ~3 times thicker than the 0.35 nm ± 0.08 nm overlayer depth for Ru in this study, but the clusters were used for efficient photocatalysis, indicating this overlayer depth is not so large so as to suppress all reactions. Given the catalytic potential for supported Ru clusters [43-47, 49-51, 53, 54], these encapsulated Ru clusters are a strong candidate for studies on encapsulated catalysts. Furthermore, in a future study the catalytic and/or photocatalytic activity of supported Ru clusters could be compared between

ligated clusters (below ~423 K) and the de-ligated, encapsulated clusters (complete encapsulation occurs at ~648-660 K). Such a course of work is warranted as a study has been conducted showing the catalytic activity of partially ligated clusters, where the presence of ligands increased the reaction selectivity [236].

5.5 Conclusions

Ru$_3$ clusters were deposited by both solution-based and CVD depositions of Ru$_3$(CO)$_{12}$, as well as CS depositions of bare Ru$_3$ onto SiO$_2$ and a variety of different forms of TiO$_2$ substrates. TD-LEIS results supported CO-TPD evidence from Chapter 4 that CS Ru clusters were agglomerated due to heat treatment when supported on SiO$_2$. TD-XPS showed that the oxidation state of Ru on TiO$_2$ varied for as-deposited clusters depending on the deposition method and type of TiO$_2$ substrate (RF-TiO$_2$ or TiO$_2$(110)), but after heat treating to 723-873 K the oxidation state for Ru became identical, within experimental accuracy, for all the analysed TiO$_2$ systems. The result indicates that the specific deposition process is not of importance to the oxidation state if the clusters are to be heated.

TD-LEIS results provided a direct measurement for the encapsulation of CVD-deposited Ru$_3$ by a layer of substrate material when supported on HDS-RF-TiO$_2$, showing that no Ru was left on the topmost layer after heat treatment to 660 K ± 120 K. The overlayer thickness was measured by TD-LEIS to be 0.35 nm ± 0.08 nm for CVD-Ru$_3$(CO)$_{12}$/HDS-RF-TiO$_2$, equivalent to an average of 1.74 ML ± 0.41 ML of titania. ARXPS showed encapsulation starting between 423-573 K, reaching a maximum by 648 K. Combined with TD-XPS results this suggests that the majority of the CO ligands need to be removed for encapsulation, but complete de-ligation is not required. ARXPS provided evidence that bare CS-Ru$_3$ on HDS-RF-TiO$_2$ was encapsulated as-deposited. The evidence for cluster encapsulation explains the mechanism behind the complete Ru-CO binding site blocking for Ru$_3$ on sputter-treated RF-TiO$_2$ found using CO-TPD in Chapter 4. Cluster encapsulation may provide an advantage for catalysis or photocatalysis based on recent studies [4].

Information about the valence electronic DOS of the supported clusters, and how the clusters affect the DOS of the RF-TiO$_2$ substrates is not known and this would be crucial for photocatalysis applications. In Chapter 6, MIES and UPS were used together to determine how the surface electronic DOS was modified by the deposition of Ru$_3$ clusters. MIES measured the topmost layer only while UPS averaged over the top several layers, making the combination of techniques a perfect candidate for studying the system of clusters and overlayers.

Chapter 6   Valence spectroscopy of size-selected Ru$_3$ and Pt$_3$ clusters supported on RF-deposited TiO$_2$

6.1 Abstract

In this study, 3-atom Ru$_3$ and Pt$_3$ clusters were deposited onto radio frequency (RF)-sputter deposited TiO$_2$ (RF-TiO$_2$). RF-TiO$_2$ surfaces were treated with Ar$^+$ ion sputtering prior to cluster depositions. Ru$_3$ was deposited using Ru$_3$(CO)$_{12}$ by solution submersion as well as chemical vapor deposition, while Pt$_3$ was deposited under ultra-high vacuum using a cluster source. The valence electronic density of states (DOS) of the deposited clusters were analysed after sample heat treatment using ultraviolet photoelectron spectroscopy (UPS) and metastable impact electron spectroscopy (MIES), where UPS measures the top several layers while MIES measured only the top atomic layer. Further details on the surface coverage and surface properties of the clusters were provided by XPS. The work is motivated by the potential use for titania-supported small Pt and Ru clusters as catalysts and cocatalysts.

UPS and MIES difference spectra were determined due to the deposition of Ru$_3$ and Pt$_3$ clusters onto titania. UPS showed that supported Ru$_3$ clusters have metallic properties while supported Pt$_3$ clusters have non-metallic properties. MIES measurements provided evidence that Ru$_3$ was encapsulated by a reduced titania layer with a bonding structure such as Ru-Ti-O atop the clusters. This measurement highlighted the benefit of performing both MIES and UPS experiments together, where MIES measured the titania atop the clusters and UPS measured the clusters themselves. The results showed the deposition method does not have a significant effect on the cluster DOS for Ru$_3$, indicating the CO ligand-removal by heating most likely has a greater effect on the final cluster-substrate interaction that the initial cluster deposition. For Pt$_3$ clusters the UPS and MIES results provided evidence that Pt was available on the topmost layer, and encapsulation did not occur. The reason for encapsulation of Ru$_3$, but not Pt$_3$, points to the fact that there may be an energetic benefit for Ru encapsulation in terms of the minimisation of surface energy.

6.2 Introduction

The concept of metal clusters, and their uses, was introduced in the Literature Review (Chapter 2), as well as the Introduction sections of Chapter 4 and Chapter 5. In brief, metal clusters are generally defined as groups of metal atoms with sizes less than ~300 atoms [11, 14-18]. They often possess unique electronic and catalytic and/or photocatalytic properties, where the addition or subtraction of a single atom to a small cluster can influence whether it functions as a catalyst [56]. For this reason, experiments often focus on a single cluster size. The type of supporting material used can further influence the catalytic properties of the supported clusters [177, 194-196]. For transition metal clusters supported on metal oxide surfaces such as titania (TiO_2), the clusters can in some cases undergo a strong metal-support interaction (SMSI). The SMSI can involve oxidisation or charge transfer [185, 201, 202], as well as encapsulation by the substrate itself, typically after high temperature reduction [184-186, 198, 199, 207-215]. The occurrence of the SMSI depends on factors such as the particular metal adsorbate/substrate combination [184, 185, 210, 417, 418], adsorbate particle size [39], and surface pre-treatment such as sputtering [185, 186]. Importantly, two different transition metals will therefore not necessarily have the same interaction when supported on the same type of substrate.

TiO_2 is a photocatalytically active substrate [204] and is a common choice as a substrate material for catalysis and photocatalysis, and for the deposition of clusters [6, 26, 38, 60, 66, 74, 75, 103, 184-190]. In typical surface science experiments, the rutile TiO_2(110) single crystal is the most commonly used form of TiO_2, but in this study RF-sputter deposited TiO_2 (RF-TiO_2) was used as the substrate. It is a nanoparticulate form of TiO_2 made by RF-sputtering a ceramic TiO_2 wafer under UHV onto a substrate, in the present case Si(100). This process produces a dense, uniform, stoichiometry-controlled layer of TiO_2 more cheaply and readily than the TiO_2(110) single crystal [357]. Furthermore, the substrates were treated with Ar^+ ion sputtering prior to the deposition of clusters. This has been shown, in some cases, to stabilise clusters against agglomeration by anchoring them to defect sites [5, 222], and in other studies has it been shown to promote the SMSI and encapsulation of metal adsorbates [185, 186]. In studies where encapsulation is reported due to SMSI with TiO_2, the overlayer of titania is typically reported to be a reduced form of titania [185, 186, 207, 208, 210-213, 216, 386].

Small metal clusters supported on photocatalytic substrates such as TiO_2 can act as cocatalysts, increasing the efficiency of photochemical reactions [4, 10, 419]. Cocatalysts are used with semiconductors to suppress the recombination of charge carriers and

accelerate reaction kinetics [420-422]. A common, well-studied photocatalytic reaction is water splitting, which has been considered as a method to produce hydrogen fuel in a sustainable way [423, 424]. Both small Ru and Pt adsorbates have been used as co-catalysts for photochemical reactions [28, 419, 425-430]. There is a push for cocatalysts towards smaller sizes including small clusters and the single atom limit, as only surface atoms are involved as active sites allowing for an increase in catalytic efficiency per material for small particle sizes [431]. Pt often has high performance as a cocatalyst for TiO_2 and other substrates due to its large work function and capability of efficient electron migration [432, 433], but its practical applications are limited by the high cost of Pt. Ru is a cheaper cocatalyst material, although typically has less satisfactory results as a cocatalyst [422, 434]. Efficient Ru/TiO_2 photocatalysts have been produced; by way of example a study prepared isolated Ru atoms on multi-edged TiO_2 sphere catalysts, which had a hydrogen evolution rate of 7.2 $mmol.g^{-1}.hour^{-1}$, higher than that of typical Pt-based cocatalyst systems [419]. Aside from use as a cocatalyst, Ru clusters have otherwise been shown to be among the most active catalysts for industry and environment-relevant reactions such as CO and CO_2 hydrogenation [43-47, 49-51, 53, 54].

The concept of valence electronic density of states (DOS) and its measurement was previously introduced in section 2.2.2. Metal clusters typically feature discrete electron energy levels similar to molecules, rather than energy bands which would be expected of a bulk counterpart [13]. The catalytic and photocatalytic abilities of a cluster (or other surface adsorbates) are related to their electronic properties, and thus their valence electronic DOS [17, 57, 435]. Because of this, the measurement of the DOS for small metal clusters supported on semiconductors provides vital experimental evidence that enables the understanding of photocatalytic reactions at cluster surfaces.

Two techniques which can be used to measure the valence DOS of a surface are UPS and MIES; the use of these techniques for measuring small, supported clusters was discussed in the Literature Review, section 2.7.1. UPS uses ultraviolet light to probe surface electrons, while MIES uses metastable helium atoms (He*). In a MIES procedure He* does not penetrate into the surface, and only interacts at a distance of 2-4 angstroms [298]. Thus MIES provides sensitivity to only the topmost layer of the surface of a sample, while UPS offers an information depth of approximately 2-3 nm [284]. When used in tandem these techniques give more complete information on the DOS of the surface. As an example of the benefit of combining UPS and MIES, a previous study by Chamber *et al.* [436] used UPS/MIES to analyse the valence structure of double-walled carbon nanotubes, and it was

shown that UPS measures the DOS across the whole nanotube while MIES only measured the DOS of the outer nanotube layer, which is responsible for the attachment of functional groups. Previous studies using MIES on supported metal clusters are limited. Several MIES studies by Andersson *et al.* [3, 5, 104] have been performed on small, TiO_2-supported Au clusters, where the surface sensitivity of MIES was utilised measuring clusters on the topmost layer. To the best knowledge of the author, there are no previous studies which have used MIES on supported Ru or Pt clusters, however some UPS experiments have been performed for small, size-selected Pt_n clusters on various substrates [57, 437].

Two of the main ways to deposit clusters onto substrates is through the preparation of bare clusters under ultra-high vacuum (UHV) using a cluster source (CS), or through depositing ligand-stabilised clusters such as $Ru_3(CO)_{12}$ using chemical vapor deposition (CVD) [74, 75, 135-137] or a solution deposition (SD) involving submersion of the substrate into a cluster solution [332]. These techniques were introduced in detail in the Literature Review, section 2.4. Each method has different advantages with respect to experimental and industrial applications, which are discussed in section 2.4 and the Introduction of Chapter 5. When depositing ligand-stabilised clutters, extra post-deposition surface treatments such as heating are needed to remove the ligands to enable contact between the cluster core and the surface. In Chapter 5, SD and CVD-$Ru_3(CO)_{12}$ were compared as-deposited using temperature-dependent XPS (TD-XPS), and the estimated average stoichiometric ratios were $Ru_3(CO)_{6.3}$ and $Ru_3(CO)_{3.0}$ respectively; this showed for both deposition methods some ligands were lost, and CVD results in a larger fraction of ligand loss. However, after heat-treatment the BEs converged and both cluster types were shown to have similar oxidation states. Very few other studies have previously compared the cluster properties of identically sized clusters resulting from different deposition methods [74].

In the present work we use UPS and MIES to measure the valence DOS of small, supported Ru_3 and Pt_3 clusters deposited onto Ar^+ ion sputter-treated RF-TiO_2. Ru_3 was deposited *in situ* using $Ru_3(CO)_{12}$ (both SD and CVD depositions were performed), while Pt_3 was deposited under UHV using a size-selected laser vaporisation (LaVa) CS. XPS provided additional information about the cluster surface coverage and chemical properties for each sample. The main aims of the work were to determine the DOS of the RF-TiO_2-supported Ru_3 and Pt_3 clusters and determine how the unique cluster-surface interactions of the two transition metal clusters with the RF-TiO_2 substrates differed. Such DOS measurements are challenging in cases such as this when low cluster surface coverages are used to avoid agglomeration. Thus, for each cluster type multiple samples were measured with varied

cluster loadings; this was done to determine the effect of the cluster depositions on the surface DOS with suitable reliability. The work is motivated by the potential use for small Pt and Ru clusters as cocatalysts when supported on titania; because the electronic and catalytic properties of supported clusters are related [57], these experimental measurements will help with the designing of future efficient catalysts and cocatalysts.

6.3 Methodology

6.3.1 Substrates

The substrates for all cluster depositions were RF-sputter deposited TiO_2 onto Si(100) wafers (shortened to RF-TiO_2). See section 3.1 in the Instrumentation and Methodologies for information on preparation of RF-TiO_2. For all cluster-deposited samples, RF-TiO_2 was treated prior to cluster deposition or UPS/MIES measurements by heating to 723 K for 10 minutes and sputtering with 6 x 10^{14} Ar^+ ions/cm^2, to remove surface contamination and induce surface defects. This is the same as the treatment of the substrate dubbed "HDS-RF-TiO_2" in Chapter 4 and Chapter 5, however this longer name is not used in this chapter because the same treatment was used for all samples.

6.3.2 Instrumentation

MIES, UPS, and XPS analysis were performed on the Flinders University UHV system. Solution-based and CVD cluster depositions were performed *in situ* with the spectroscopy measurements, while CS depositions (and the corresponding substrate treatment) were performed *ex situ* on the University of Utah system. With regards to Ar^+ ion sputtering, Flinders University experiments used 3 keV impact energy while the University of Utah experiments used 2 keV. The effects of this have been discussed previously (section 3.4) and was deemed to not be of critical importance for this experiment.

6.3.3 Cluster Depositions

6.3.3.1 Solution Submersion

The solution submersion procedure (also referred to as a solution-based deposition) is described in the Instrumentation and Methodologies section 3.5.2. $Ru_3(CO)_{12}$ was necessarily deposited *ex situ* (as this method cannot be used *in situ*). Clusters which were solution-deposited (SD) are referred to with a prefix of "SD" in this chapter. For the deposition series, six samples and a blank were prepared. The solution was $Ru_3(CO)_{12}$ in dichloromethane. Concentrations were varied from 0.002 mM to 0.2 mM to produce a range in surface coverages of clusters on the substrates. Prior to removing each substrate from UHV to perform the solution-based deposition, RF-TiO_2 samples were heated under UHV to 723 K for 10 minutes, then Ar^+ ion sputtered with 6 x 10^{14} ions/cm^2. Solution submersion coated the whole surface with an approximately even layer of clusters.

6.3.3.2 Chemical Vapor Deposition

CVD of $Ru_3(CO)_{12}$ was performed *in situ* at Flinders University, with a series of 5 loaded samples and a blank. The CVD procedure followed the method described in the

Instrumentation and Methodologies section 3.5.1. Deposition times were varied from 1 minute to 90 minutes to produce a variation in cluster loading for the samples. The deposited clusters covered the entire sample areas in an approximately even manner.

6.3.3.3 Cluster Source

CS depositions were performed *ex situ* (in a different UHV system to UPS/MIES) by a LaVa CS. The instrument details and standard deposition procedure are given in the Instrumentation and Methodologies, section 3.5.3. A retarding potential was used for ~1 eV/atom deposition energy to prevent fragmentation [157]. Cluster spots were 2 mm in diameter. For CS-deposited Pt_3 samples, 7 individual circular Pt_3 cluster spots were deposited per sample without overlapping to increase the analysis area for UPS and MIES. In addition to a blank, 2 Pt_3 sampled were prepared, with cluster spot coverages of nominally 3×10^{13} atoms/cm^2 and 4.5×10^{13} atoms/cm^2, respectively (based on the measured neutralisation current during depositions). These values only include the cluster-deposited areas, not the blank substrate area in between. While the full sample area was analysed with UPS, MIES, and XPS, the cluster-covered area ratio of the analysis area was approximately 0.22. Regarding CS-deposited Ru_3, several different deposition series were performed using various cluster coverages but UPS and MIES could not be used to separate a DOS component due to the cluster depositions. This is discussed in section 6.4.3.5.

6.3.4 Samples and Procedures

For each UPS/MIES series there is one changing variable (*i.e.* surface sputtering or cluster surface coverage), which helps to separate the UPS and MIES signal due to the substrate and the changing factor. Table 6-1 shows a list of the 5 UPS/MIES series measured, and the variable surface treatment which was changed for each. Each UPS/MIES series was given a shortened name, which are shown in the table.

Table 6-1: List of UPS/MIES series, with series names and variables changed in the series.

UPS/MIES Series Name	Cluster Deposition	Series Variable
Defect-TiO$_2$	None	Substrate Ar$^+$ sputter dosage
SD-Ru$_3$	SD - Ru$_3$(CO)$_{12}$	Cluster coverage
CVD-Ru$_3$	CVD - Ru$_3$(CO)$_{12}$	Cluster coverage
CS-Pt$_3$	CS - Pt$_3$	Cluster coverage

When performing measurements, UPS and MIES were first performed together (see below) followed by XPS. For Defect-TiO_2, a single RF-TiO_2 substrate was measured repeatedly as increasing Ar^+ ions were applied to the sample, with a maximum of 3.6×10^{15} ions/cm^2. For the cluster-deposited UPS/MIES series, each series featured one blank and multiple unique cluster-deposited samples. UPS, MIES, and XPS were first performed on the samples with clusters as-deposited. Samples were then heated for 10 minutes before re-analysing with UPS, MIES, and XPS. Lower temperatures such as 423 K were trialled for UPS/MIES measurements, but it was found that the temperature needed to be increased to 723 K for Ru_3 samples and 573 K for Pt_3 samples to achieve suitable inter-sample spectrum consistency to determine UPS and MIES difference spectra. The MIES and UPS results shown are after heating to these temperatures. At the lower temperatures, the inter-sample variation precluded the determination of difference spectra which was presumably due to the removal of hydrocarbon contamination (and also CO ligands for ligated Ru_3 clusters).

For each cluster UPS/MIES series, multiple samples were measured. The lowest number was a blank and two cluster-loaded samples (for CS-Pt_3), while the highest was a blank and 6 loaded samples (SD-Ru_3). Thus, the repeatability of the UPS and MIES measurements is built into the measurement procedure. The shape of the resultant UPS and MIES spectra is the important factor, and this was shown to be reproducible in these experiments. In addition to the cluster UPS/MIES series, a blank titania series was measured with a varying Ar^+ ion dosage (Defect-TiO_2).

A metallic Ru reference sample was also measured with UPS/MIES, which was from a single sample and was not related to a UPS/MIES series. The Ru reference sample was taken from a 99.9% pure metallic Ru sample cut to 1 cm x 1 cm to accommodate the sample mounting plate. The sample was heat treated by heating to 1073 K for 10 minutes and sputtering with 3 keV Ar^+ ions for 1 hour to remove the surface Ru oxide layer and any hydrocarbon contamination, which was confirmed by XPS.

6.3.5 XPS

The experimental and data analysis procedures for XPS measurements are given in section 3.6.1. All XPS were performed using the Flinders University XPS instrument with a Mg kα X-ray anode. For analysing XPS spectra the binding energy (BE) scale was calibrated to adventitious C 1s = 285.0 eV. Details on the XPS peak fitting procedure, including extensive details on fitting the Ru 3d/C 1s region, are given in section 3.6.1.3. Regarding Pt_3 clusters, the Pt 4f region was scanned and fitted with 3 peaks, relating to the Pt 4f doublet as well as

an energy loss (E loss) peak in the same region which was also present for the blank substrate. The fitting procedure for the blank was used as a template for the peak location and full width half maximum (FWHM) of the E loss peak when fitting the Pt 4f region for clusters. Surface coverages of clusters were calculated according to the method in section 3.6.1.3, and represent the coverage of Ru or Pt atoms on the surface in units of percentage of a monolayer (% ML). For Pt_3 measurements a scaling factor based on the ratio of the analysed surface covered by clusters (discussed above) was used when calculating surface coverages. Details about errors and uncertainties in the XPS measurements are given in section 3.6.1.3. The uncertainty in BE positions are ± 0.1 eV. This is lower than the value of 0.2 eV given in section 3.6.1.3, and is because in this study the BEs reported represent an average based on repeats of the same type of cluster sample, and it was determined for the samples measured the weighted average standard deviation for the cluster peak location (for Ru 3d and Pt 4f) was ± 0.1 eV.

6.3.6 UPS and MIES

The experimental, data analysis, and error analysis procedures for UPS and MIES measurements are given in section 3.6.2. UPS and MIES spectra were measured under UHV simultaneously. In the measured spectra for titania substrates, 0 eV BE corresponds to the Fermi level of the titania. For each UPS/MIES measurement a series of samples were prepared and analysed, where for each series there is a changing surface treatment such as cluster surface coverage. These are hereafter referred to as a UPS/MIES series. For each UPS/MIES series, "difference spectra" are determined for UPS and MIES which are related to the change in DOS due to the to the deposition of metal clusters or surface treatment. Once difference spectra were determined, for each series linear combinations of the blank titania spectrum and difference spectrum were fitted to the measured spectra to determine substrate and deposition-related weighting factors for the measured spectra; these were normalised to determine weighting factor ratios so that the sum of weighting factors were unity, *i.e.* A(C) + B(C) = 1. For CS-Pt_3 the ratio of cluster-covered substrate in the Pt_3 analysis area (discussed above) was factored into the reported weighting factors by dividing the Pt_3 cluster weighting factors by 0.22 and adjusting the titania ratio accordingly to normalise the results.
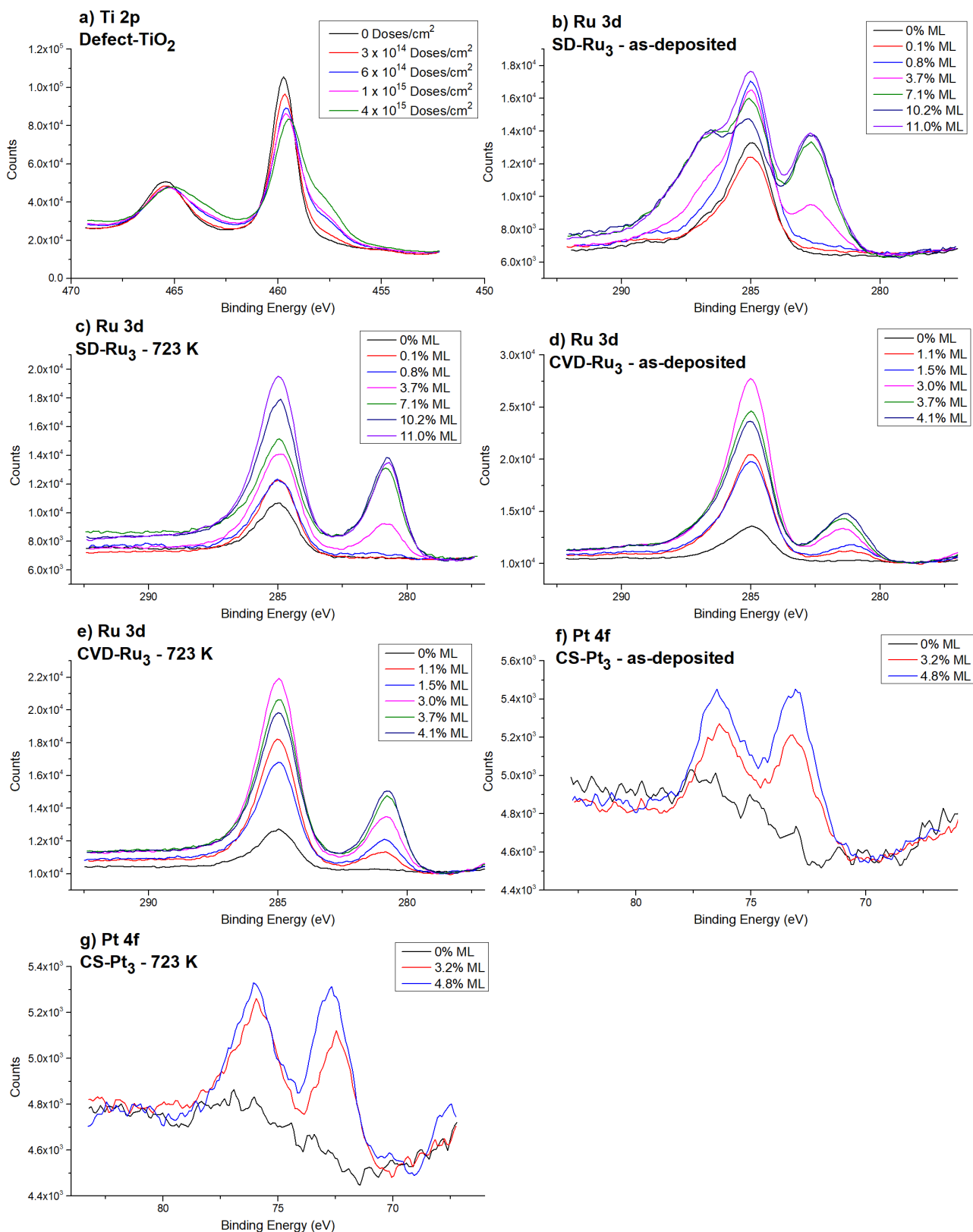
6.4 Results

The companion XPS results for all UPS/MIES series are collated in section 6.4.1. UPS/MIES results are shown in individual sub-sections of section 6.4.2 for each sample.

6.4.1 XPS

6.4.1.1 XPS Spectra

The XPS spectra were measured for the same set of samples which were measured using UPS/MIES. This allows for the measurement of the sample composition, which cannot be done with UPS and MIES alone. For Ru_3 the results are very similar to the XPS results presented in Chapter 4 and Chapter 5, which confirms that while the samples are not identical, the UPS/MIES samples are directly comparable in terms of composition to those in the previous chapters. Conversely, Pt_3 XPS results are presented in this chapter for the first time, and thus XPS is used to confirm the deposition of Pt, measure the sample compositions, and determine oxidation properties for the clusters.

Figure 6-1 shows relevant overlayed XPS spectra for the different UPS/MIES series. For all samples, the Ru 3d/C 1s region, Ti 2p region, and O 1s region were scanned, and for Pt_3 samples the Pt 4f region was also scanned. For Defect-TiO_2, the Ti 2p region is shown to highlight the increasing peak size of Ti^{3+} with increasing ion sputter dosage as the lower BE shoulder of the main Ti $2p^{3/2}$ peak increases in size. For Ru_3 and Pt_3 cluster samples, the Ru 3d/C 1s region and Pt 4f region are shown, respectively. Each cluster type has a range of surface coverages within each UPS/MIES series, which is reflected in the changes in Ru 3d and Pt 4f peak sizes seen in Figure 6-1. To achieve this, for SD-Ru_3 the solution concentration was varied while for CVD-Ru_3 and CS-Pt_3 the deposition time was varied (see section 5.3.3 for details). The spectra in Figure 6-1 were fitted for analysis to determine core BE locations for Ru_3 and Pt_3 clusters, as well as the cluster surface coverages for each sample. Examples of the peak fitting procedures used in the Ti 2p, Ru 3d, and Pt 4f regions are shown in Figure 6-2. Important features of the peak fitting results are described.

Figure 6-1: XPS results - spectra from the same UPS/MIES series are overlayed for comparison. a) Ti 2p region, Defect-TiO₂. b) Ru 3d region, SD-Ru₃ as-deposited. c) Same samples as (b) after 723 K heat-treatment. d) Ru 3d region, CVD-Ru₃ as-deposited. e) Same sampled as (d) after 723 K heat-treatment. f) Pt 4f region, CS-Pt₃ at room temperature. g) Same samples as (f) after 573 K heat-treatment.
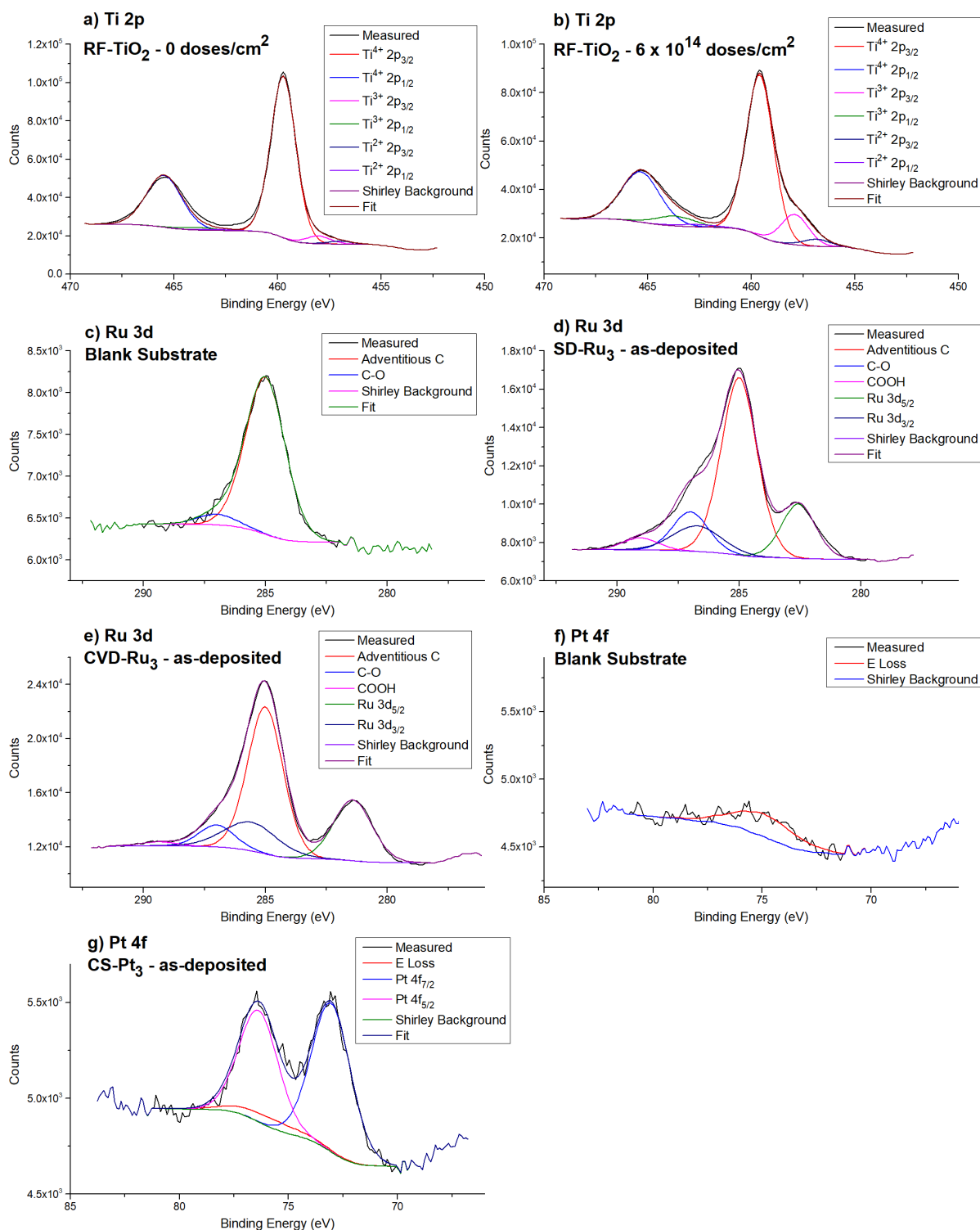
Figure 6-2: a) Ti 2p peak fitting for RF-TiO$_2$, heated to 723 K with no Ar$^+$ sputtering. **b)** Ti 2p peak fitting for RF-TiO$_2$ after 6 x 10^{14} Ar$^+$ ions/cm^2. **c)** Ru 3d/C 1s peak fitting for RF-TiO$_2$ after heating to 723 K and 6 x 10^{14} Ar$^+$ ions/cm^2 (this shows the Ru 3d/C 1s region with no Ru clusters present). **d)** Ru 3d/C 1s peak fitting, SD-Ru$_3$ as-deposited - from 0.1 mM sample at room temperature. **e)** Ru 3d/C 1s peak fitting, CVD-Ru$_3$ - from 30 min CVD deposition room temperature. **f)** Pt 4f region fitting, 0% ML loading at room temperature (this shows the Pt 4f region with no clusters). **g)** Pt 4f region fitting, highest surface coverage CS-Pt$_3$ sample at room temperature.

6.4.1.2 XPS Analysis

Figure 6-2 a and b show the Ti 2p region for $RF\text{-}TiO_2$ before and after sputtering with 6 x 10^{14} Ar^+ ions/cm², respectively. The titania regions have been fit with three doublets relating to Ti^{4+}, Ti^{3+}, and Ti^{2+}. Ti^{4+} was located at 459.6 eV ± 0.1 eV, and Ti^{3+} and Ti^{2+} were shifted from this by -1.7 eV ± 0.1 eV and -2.7 eV ± 0.1 eV, respectively. Ti^{4+} is related to stoichiometric titania, while Ti^{3+} and Ti^{2+} relate to defects in the structure. As described in Chapter 4, section 4.4.2.2, the Ti 2p region has a changing background. This causes a discrepancy where the fitted spectra have a signal lower than the measured spectra between the peaks of the Ti 2p doublet. It was also noted that a Ti^{2+} doublet is also present for non-sputtered $RF\text{-}TiO_2$; the presence of this doublet is also likely a result of fitting the peaks on a changing background. The ratios of Ti^{3+} and Ti^{2+} peaks to the total summed Ti peak signals, Ti^{Defect}/Ti^{Total}, are used as a measurement for the level of defects in the titania and are referred to as the Ti defect ratio. From the XPS peak analysis, the sputter dosage used to prepare cluster-loaded samples (6 x 10^{14} Ar^+ ions/cm²) resulted in 24% ± 15% surface defects (Ti^{Defect}/Ti^{Total}) in the $RF\text{-}TiO_2$ substrate. The level of surface defects was calculated in this manner for each sputter dosage in the Defect-TiO_2 UPS/MIES series, for comparison to the UPS/MIES weighting factors of blank $RF\text{-}TiO_2$ and sputtered $RF\text{-}TiO_2$ (see Figure 6-4g in section 6.4.3.1). The ~15% uncertainty was estimated and is discussed in section 3.6.1.3.

Figure 6-2c-e show the Ru 3d/C 1s region for blank $RF\text{-}TiO_2$ and 2 Ru_3 cluster-loaded samples. Three peaks are needed to fit for carbon, which are related to surface contamination and attributed to adventitious carbon (285.0 ± 0.1 eV), C-O (287.0 eV ± 0.1 eV), and C=O (289.4 eV ± 0.1 eV) [370]. For Ru 3d peaks, one asymmetrical doublet peak was used per spectrum according to the method in section 3.6.1.3. This doublet shifts to lower BEs when heated due to the loss of ligands (see previous analysis in section 4.4.2.3 for more details).

Figure 6-2f-g show the Pt 4f region for blank $RF\text{-}TiO_2$ and Pt_3-loaded $RF\text{-}TiO_2$, respectively. An E loss peak was present at ~75 eV on both the blank and Pt_3-loaded samples. For Figure 6-2g three peaks were used to fit the Pt 4f region; in addition to the E loss peak there was a Pt $4f_{7/2}$ and $4f_{5/2}$ doublet associated with Pt_3. The Pt peaks were fit with symmetrical peak shapes. Th XPS fitting procedure is discussed in section 6.3.5.

The results of the XPS peak fitting procedures are summarised in Table 6-2 and Table 6-3. These show the atomic concentration (At%) and calculated cluster surface coverages for

each of the UPS/MIES samples (Table 6-2), and the average core BEs for the metal clusters (Table 6-3). At% was determined for as-deposited cluster samples at room temperature and represents the atomic concentration of Ru or Pt atoms detectable by XPS. The surface coverage of clusters was calculated in units of % ML (see section 3.6.1.3 for details). The BEs presented are averages of the BE found for each UPS/MIES series for each sample type. This process assumes that in the range of surface coverages used the BE will not be affected by loading; this was assumed to be reasonable as the surface coverages were all a small fraction of a monolayer, which minimised cluster-cluster interactions. The number of samples analysed per UPS/MIES series was not consistent; each series had a blank, while for cluster-loaded samples SD-Ru$_3$ had 6, CVD-Ru$_3$ had 5, and CS-Pt$_3$ had 2. Ideally a higher number of repeat samples would have been desirable for the CS-Pt$_3$ series to be consistent with the other series, but this was somewhat less repeatable due to the nature of preparing the clusters in a different UHV system at The University of Utah. However, in this case 3 samples, including a blank, was found to be sufficient for determining the DOS due to the addition of Pt$_3$ clusters using UPS and MIES.

Table 6-2: XPS results for all samples, including the At% and surface coverages for clusters. Fitting uncertainties in Ru and Pt XPS peaks give an At% uncertainty of ± 4%. The absolute error in the surface coverage is ~100%, while the relative uncertainty when comparing samples is based only on the Ru and Pt At% and is also ± 4%.

UPS/MIES Series	Sample	Cluster At%	Surface Coverage (% ML)
SD-Ru$_3$	SD-Blank	0.00	0.0
	SD-Ru$_3$-1	0.02	0.1
	SD-Ru$_3$-2	0.11	0.8
	SD-Ru$_3$-3	0.51	3.7
	SD-Ru$_3$-4	0.98	7.1
	SD-Ru$_3$-5	1.42	10.2
	SD-Ru$_3$-6	1.52	11.0
CVD-Ru$_3$	CVD-Blank	0.00	0.0
	CVD-Ru$_3$-1	0.15	1.1
	CVD-Ru$_3$-2	0.20	1.5
	CVD-Ru$_3$-3	0.41	3.0
	CVD-Ru$_3$-4	0.51	3.7
	CVD-Ru$_3$-5	0.57	4.1
CS-Pt$_3$	CS-Blank	0.00	0.0
	CS-Pt-1	0.10	3.2
	CS-Pt-2	0.15	4.8

Table 6-3: XPS core electron BEs for Ru 3d$_{5/2}$ and Pt 4f$_{7/2}$. XPS was measured as-deposited and after heat-treatment (723 K for Ru$_3$ and 573 K for Pt$_3$). The BE shift is the difference in BE due to the heating procedure. The uncertainty in BE is ± 0.1 eV.

UPS/MIES Series	Peak	Initial BE (eV)	Heat-Treated BE (eV)	BE Shift (eV)
SD-Ru$_3$	Ru 3d$_{5/2}$	282.6	280.7	-1.9
CVD-Ru$_3$	Ru 3d$_{5/2}$	281.4	280.8	-0.6
CS-Pt$_3$	Pt 4f$_{7/2}$	73.0	72.5	-0.5

Table 6-3 shows that the SD-Ru$_3$ clusters have a higher BE than CVD deposited before heat treatment, but after heat treatment both types of Ru$_3$ cluster samples shifted lower in BE to 280.7 eV ± 0.1 eV and 280.8 eV ± 0.1 eV, respectively. These BEs are aligned with earlier results reported for the TD-XPS of SD and CVD deposited Ru$_3$(CO)$_{12}$ onto RF-TiO$_2$ in Chapter 5. Further discussion on the peak shifting due to heating can be found in section 5.4.1.4 of that chapter. The reported BE after heating is higher than bulk Ru, which was

previously determined to have a BE of 279.7 eV ± 0.2 eV (see Chapter 4, section 4.4.2.1). The BE shifting of -1.9 ± 0.1 eV for SD-Ru_3, and -0.6 eV ± 0.1 eV for CVD-Ru_3, are predominantly due to the removal of CO ligands from the clusters [74, 75]. The BE shift is larger for the SD and CVD because some ligands are lost in the CVD deposition; this partial de-ligation has also been previously shown by Zhao *et al.* [75], and was seen on an RF-TiO_2 substrate as per the TD-XPS results of Chapter 5.

Table 6-3 shows that the Pt $4f_{7/2}$ peak for CS-Pt_3 was present at 73.0 eV ± 0.1 eV at room temperature and shifted -0.5 eV to 72.5 eV ± 0.1 eV after heating to 573 K. These values are higher than the typically reported bulk Pt $4f_{7/2}$ BE, 71.2 eV [367, 438], and are outside the range of typically reported bulk Pt BEs; 70.9 to 71.3 eV [439]. This higher BE is not related to fully oxidised Pt clusters, because the BE is lower than that of PtO, which is reported with an average of ~74.0 eV [439]. The Pt $4f_{7/2}$ BE for small Pt clusters being greater than that of bulk Pt aligns with previous studies [9, 57, 60, 289, 292, 315, 352]. The greater BE may be due to a final state effect related to the small cluster size, because there is a trend for increasing core level BE with decreasing cluster size, due to less final state stabilisation by screening and charge delocalisation [60, 292, 317]. The reported BE here is somewhat higher than has been reported in previous XPS studies of the similarly-sized Pt_3/TiO_2(110), 71.9 eV [352], and Pt_2/SiO_2, 71.8 eV [9]. The surface coverages used were 5-10%, which are similar to this study, so differences in cluster-cluster interactions do not account for the BE differences between the studies. Thus, the higher Pt 4f BE for CS-Pt_3 in this study may be related to a unique cluster-surface interaction of Pt_3 on RF-TiO_2. The -0.5 eV ± 0.1 eV BE shift after heating is discussed more in section 6.5.2.

6.4.2 UPS/MIES: Metallic Reference Material

A UPS/MIES measurement was performed on a sample of bulk, metallic Ru, and is shown in Figure 6-3. This was not a measurement series like other UPS/MIES measurements in this study, but a single reference measurement for comparison purposes. The Ru sample was heated and sputtered to remove any hydrocarbons and oxide layer on the sample.
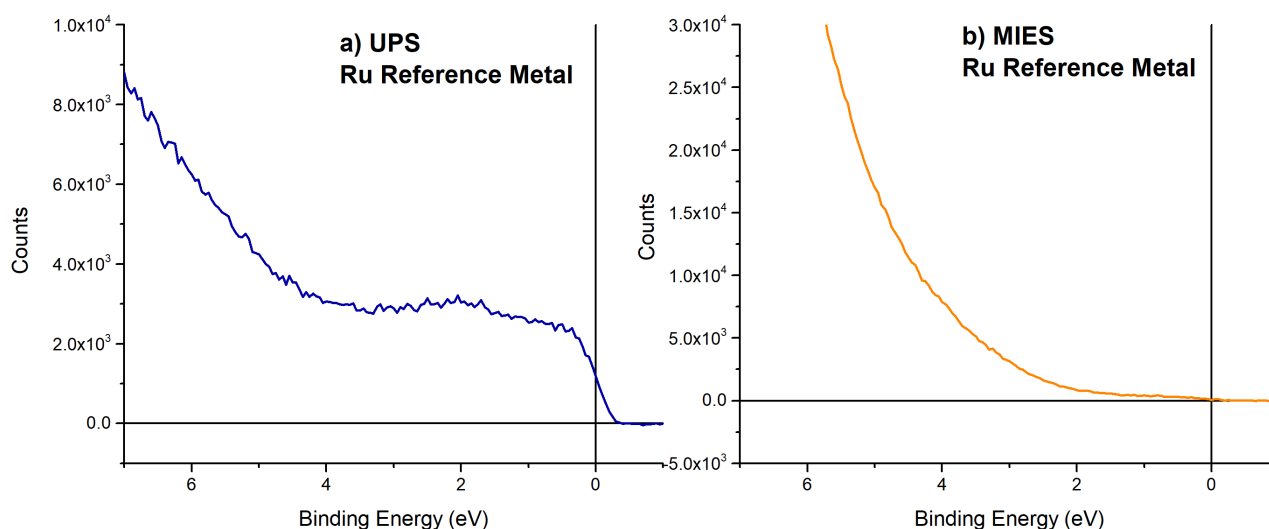
Figure 6-3: Reference valence electron spectra for bulk, metallic Ru. a) UPS results, b) MIES results.

The UPS spectrum for metallic Ru (Figure 6-3a) shows an onset at the Fermi level, which is expected for a bulk metallic sample [61, 437, 440-442], and features present at 0.3 eV and 2.0 eV. The MIES spectrum (Figure 6-3b) has no such distinct features, and features a broad, increasing background. This is because the MIES spectrum was the result of Auger neutralisation (AN) and resonance ionisation (RI), which is typical for metallic samples. This type of He* de-excitation results in a spectrum which is broadened and smeared compared to the true valence DOS [298]. See section 3.6.2 for more details on the MIES technique. Note that the BE axis of Figure 6-3b strictly does not show the true BE with regards to the DOS due to the mentioned broadening, but the BE axis is retained for consistency.

A bulk, high purity metallic Pt reference material was not available for analysis with UPS and MIES in this study. A reference UPS measurement of the Pt(111) surface is available in a study by Crowell *et al*. [443], where the onset of the spectrum was at the fermi level as per the Ru UPS reference above, and there were 3 distinct d-band peaks between 0 and 6 eV. No previous Pt reference measurement using MIES has been published, but it is expected the spectrum would look similar to the Ru MIES spectrum above, because the metallic nature of the surface would promote AN+RI de-excitation.

6.4.3 UPS/MIES Series

6.4.3.1 Defect-TiO$_2$

The Defect-TiO$_2$ UPS/MIES series was performed on a single RF-TiO$_2$ sample, by performing consecutive Ar$^+$ doses while measuring UPS and MIES spectra after each dose. This was used to determine how the Ar$^+$-induced defects effect the UPS and MIES spectra

of the RF-TiO$_2$ surface. These are used as reference measurements aiding in the interpretation of the UPS and MIES spectra related to the depositions of metal clusters in the Discussions section. Figure 6-4 shows all measured UPS and MIES data for Defect-TiO$_2$, as well as the difference spectra and the weighting factors of the difference spectra. The difference spectra were multiplied by a scaling factor for ease of comparison to the substrate spectra.
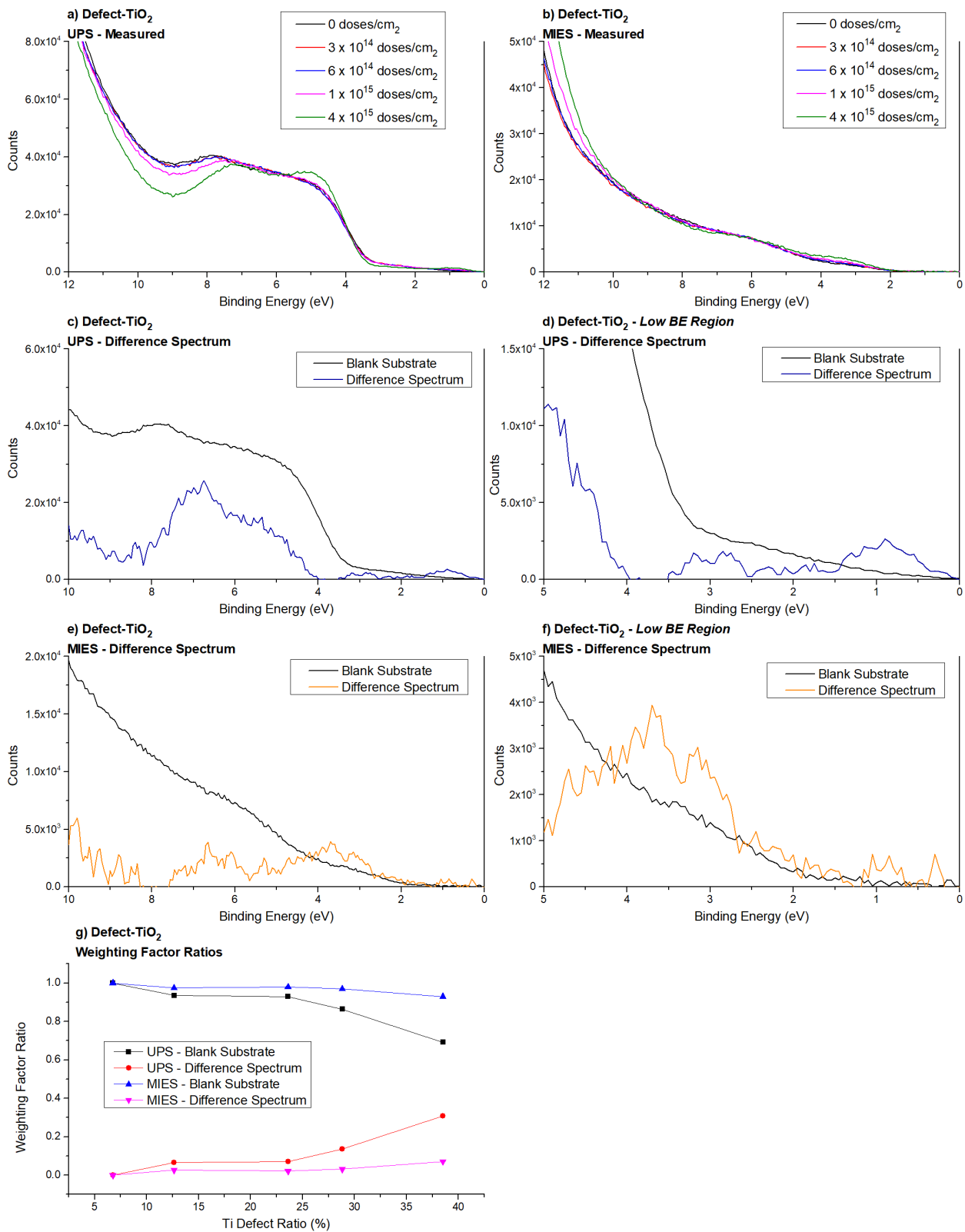
Figure 6-4: UPS/MIES results for Defect-TiO₂. a) Measured UP spectra. b) Measured MIE spectra. c) UPS Defect-TiO₂ difference spectrum, and the blank substrate. D) Spectra from (c), zoomed into the low-BE region. e) MIES Defect-TiO₂ difference spectrum due to surface defects, and the blank substrate. f) Spectra from (e), zoomed into the low-BE region. g) UPS/MIES weighting factors for the Defect-TiO₂ difference spectrum and blank substrate, as a function of Ti defect ratio. The uncertainty in the weighting factor ratios is ± 0.05, and the uncertainty in Ti defect ratio is ± 15%.

The shape of the Defect-TiO$_2$ spectra for UPS and MIES in Figure 6-4a-d changed as the sputter dose was increased, with the most dramatic change being for the 3.6 x 10^{15} ions/cm^2 spectrum. The main features are the same for all UPS spectra (Figure 6-4a), and before sputtering are present at 0.8 eV, 5.0 eV and 8.0 eV. The 0.8 eV feature in the band gap is most prominent after higher sputter doses; this peak is related to Ti^{3+} defects [60, 204]. The other peaks are related mostly to O 2p levels and are part of the titania valence band, which here spans from ~3 to 9 eV. After 3.6 x 10^{15} ions/cm^2 the 8.0 eV BE peak had shifted lower by 0.8 eV. It has been previously reported that this peak is from O 2p states in the oxygen plan of the titania [444, 445], and it is possible that the defects cause the shifting of this peak. The MIES spectra (Figure 6-4b) features broader features at 3.2 eV and 6.0 eV, which appear to be shifted versions of the two higher energy UPS features. Due to the surface sensitivity of MIES, these are likely modified O 2p states due to the surface defects. No Ti^{3+} feature at ~0.8 eV is seen in MIES, most likely because AN is favoured at the associated orbitals [298].

The weighting factors for the Defect-TiO$_2$ spectra in UPS and MIES increase approximately linearly with Ti^{Defect}/Ti^{Total} as shown in Figure 6-4g. This provides evidence that the determined UPS/MIES difference spectra for Defect-TiO$_2$ are related to the Ar$^+$ sputter treatment, and thus most likely represent the UPS/MIES signal from substrate defects. The main features seen in the Defect-TiO$_2$ UPS difference spectrum (Figure 6-4c) are peaks at 0.8, 3.0, 5.0, 6.8 eV. As the 0.8 eV peak is related to titania defects, it is unsurprising this peak appears in the difference spectrum. The other peaks are most likely related to oxygen states. The shape of the UPS difference spectrum for titania surface defects matches previous experiments which have been performed on amorphous Ti^{3+}-doped TiO$_2$ nanoparticles [446]. For the MIES difference spectrum there are peaks present at 3.5 and 6.6 eV (the ~0.8 eV defect state is missing in MEIS as described above).

6.4.3.2 SD-Ru$_3$

The SD-Ru$_3$ UPS/MIES series was performed using a range of a solution concentrations to control the surface coverage of Ru. Samples were heated to 723 K prior to analysis with UPS/MIES. Figure 6-5 shows all UPS and MIES data for SD-Ru$_3$, as well as the difference spectra and the weighting factors ratios.
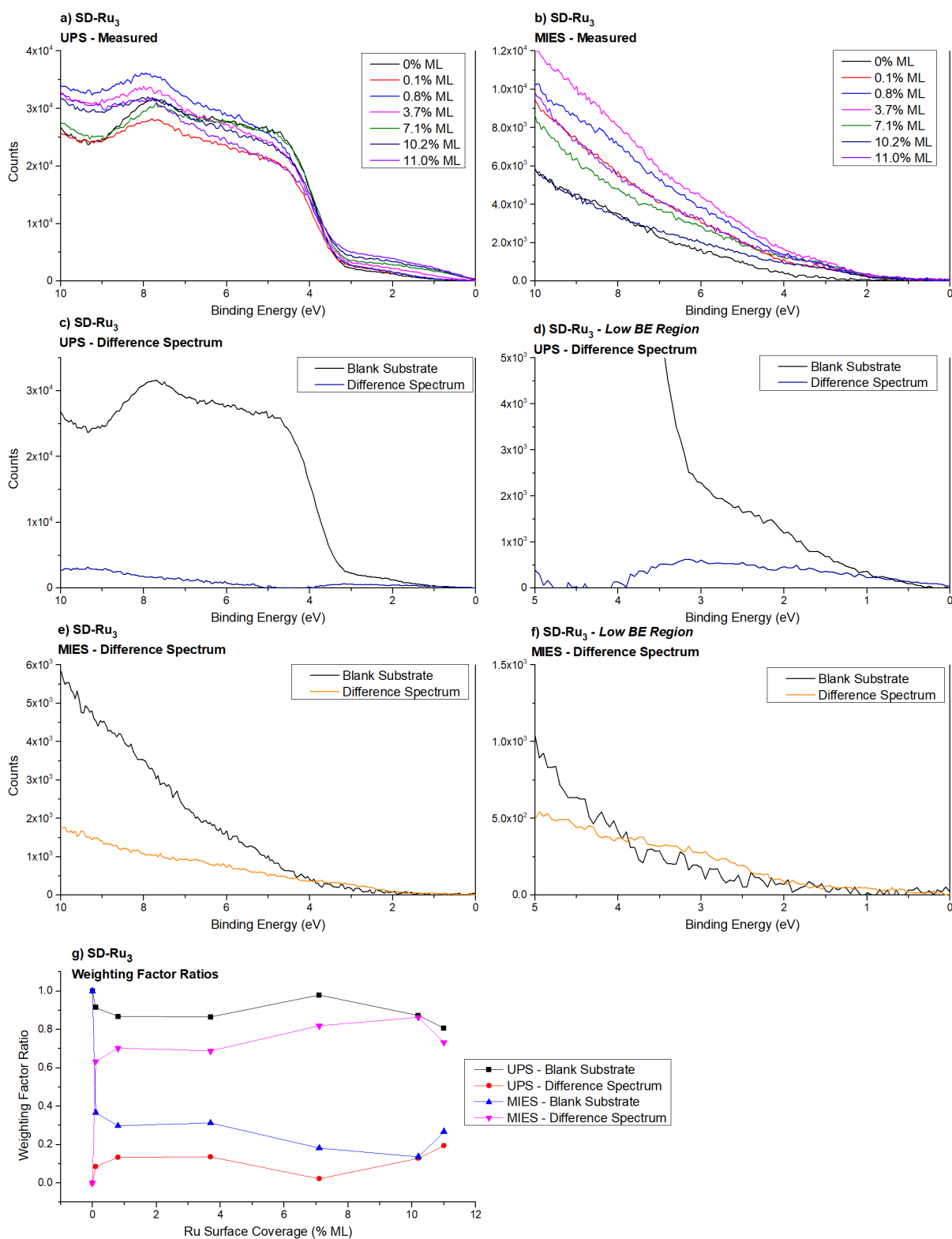
Figure 6-5 UPS/MIES results for the SD-Ru₃ UPS/MIES series. a) Measured UPS spectra. b) Measured MIES spectra. c) UPS of SD-Ru₃ difference spectrum and blank substrate. d) Spectra from (c), zoomed into low-BE region. e) MIES of SD-Ru₃ difference spectrum and blank substrate. f) Spectra from (e), zoomed into low-BE region. g) UPS/MIES weighting factor ratios for the SD-Ru₃ difference spectrum and blank substrate, as a function of Ru surface coverage. The uncertainty in the weighting factor ratios is ± 0.05. The absolute error in the surface coverage is ~100% while the relative uncertainty is based on the Ru At% and is only ± 4% (discussed in section 3.6.1.3).

When compared to the RF-TiO$_2$ blank sample, the cluster depositions made visible differences to the measured UPS and MIES spectra shown in Figure 6-5a-b. The main feature for the SD-Ru$_3$ UPS difference spectrum (Figure 6-5c) is an asymmetrical energy band from 0 eV to 4.0 eV, with a peak located at 3.1 eV. For MIES (Figure 6-5e), the SD-Ru$_3$ difference spectrum has a feature at approximately 3.3 eV, but the peak is weak and somewhat obscured by the secondary electron background.

The SD-Ru$_3$ UPS and MIES weighting factors increase approximately with Ru surface coverage (Figure 6-5g), providing evidence that the calculated SD-Ru$_3$ difference spectra are related to the cluster depositions. The weighting factor for UPS increases with Ru surface coverage as expected, except for the 7.1% ML sample which was lower than the trend and appears to be an outlier. The MIES weighting factor for SD-Ru$_3$ increased from 0 to 0.63 for the lowest surface concentration compared to the blank, and then appears to increase with surface concentration. The large initial increase is most likely due to the high surface sensitivity of MIES, where the surface layer is being changed more dramatically than for UPS due to the presence of the clusters.

6.4.3.3 CVD-Ru$_3$

A UPS/MIES series, shortened to CVD-Ru$_3$, was performed on CVD-deposited Ru$_3$ on RF-TiO$_2$ using a range of a deposition times. Samples were heated to 723 K prior to analysis with UPS/MIES. Figure 6-6 shows all UPS and MIES data for CVD-Ru$_3$, as well as the difference spectra and the weighting factors ratios.
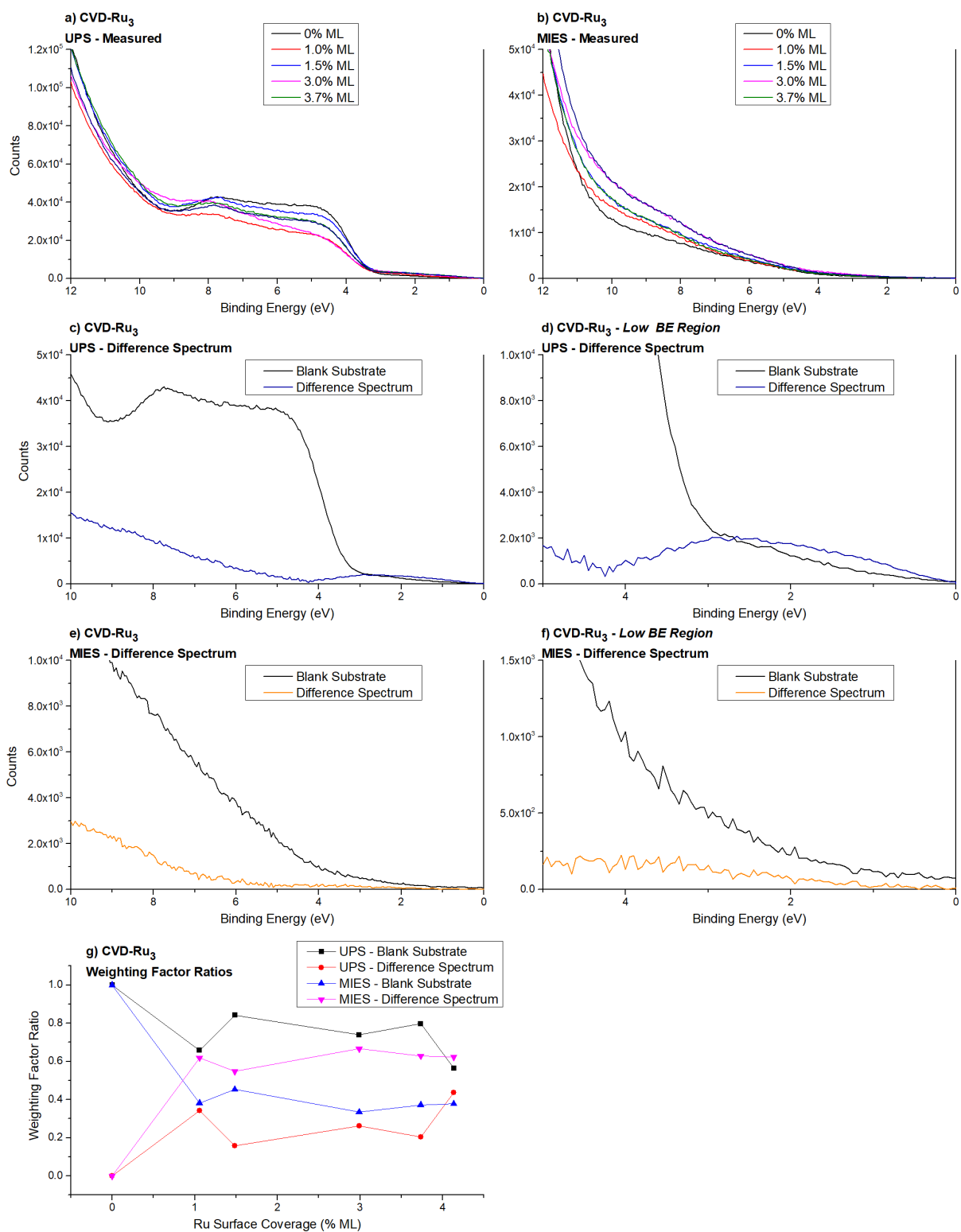
Figure 6-6: UPS/MIES results for the CVD-Ru₃ UPS/MIES series. a) Measured UPS spectra. b) Measured MIES spectra. c) UPS spectra of the CVD-Ru₃ difference spectrum and blank substrate. d) Spectra from (c), zoomed into the low-BE region. e) MIES spectra of the CVD-Ru₃ difference spectrum and blank substrate. g) Spectra from (e), zoomed into the low-BE region. g) UPS/MIES weighting factor ratios for the CVD-Ru₃ difference spectrum and blank substrate, as a function of Ru surface coverage. The uncertainty in the weighting factor ratios is ± 0.05. The absolute error in the surface coverage is ~100% while the relative uncertainty is based on the Ru At% and is ± 4%.

The CVD-Ru$_3$ depositions made a visible difference to the measured UPS and MIES spectra (see Figure 6-6a-b). The main feature for the CVD-Ru$_3$ UPS difference spectrum (Figure 6-6c) is an asymmetrical energy band from 0 eV to 4.1 eV, with a peak at 2.7 eV. For MIES (Figure 6-6e), the CVD-Ru$_3$ difference spectrum has a feature at approximately 3.6 eV. The UPS and MIES difference spectra are very similar between SD-Ru$_3$ and CVD-Ru$_3$; this will be disused in section 6.5.1.

The weighting factor ratios for the UPS CVD-Ru$_3$ difference spectrum increase approximately linearly with Ru surface coverage, as expected. The 1.1% ML measurement sample (1 minute CVD deposition) appears to be an outlier with a higher than expected weighting factor. The MIES weighting factor ratios for the CVD-Ru$_3$ difference spectrum increased from 0 to 0.62 for the lowest surface concentration compared to the blank, and then approximately linearly increases with surface concentration at increasing concentrations, similar to what was seen for the MIES of SD-Ru$_3$ (Figure 6-5g). The increase in weighting factors is sufficient evidence that the determined UPS and MIES spectra for CVD-Ru$_3$ are related to the CVD depositions.

6.4.3.4 CS-Pt$_3$

The CS-Pt$_3$ UPS/MIES series was performed using a range of Pt surface loadings. CS-Pt$_3$ samples were not deposited *in situ*, and samples were heated to 573 K prior to UPS/MIES measurements to remove any surface hydrocarbons that can interfere with surface-sensitive MIES measurements. Figure 6-7 shows all measured UPS and MIES data for CS-Pt$_3$, as well as the difference spectra and weighting factor ratios.
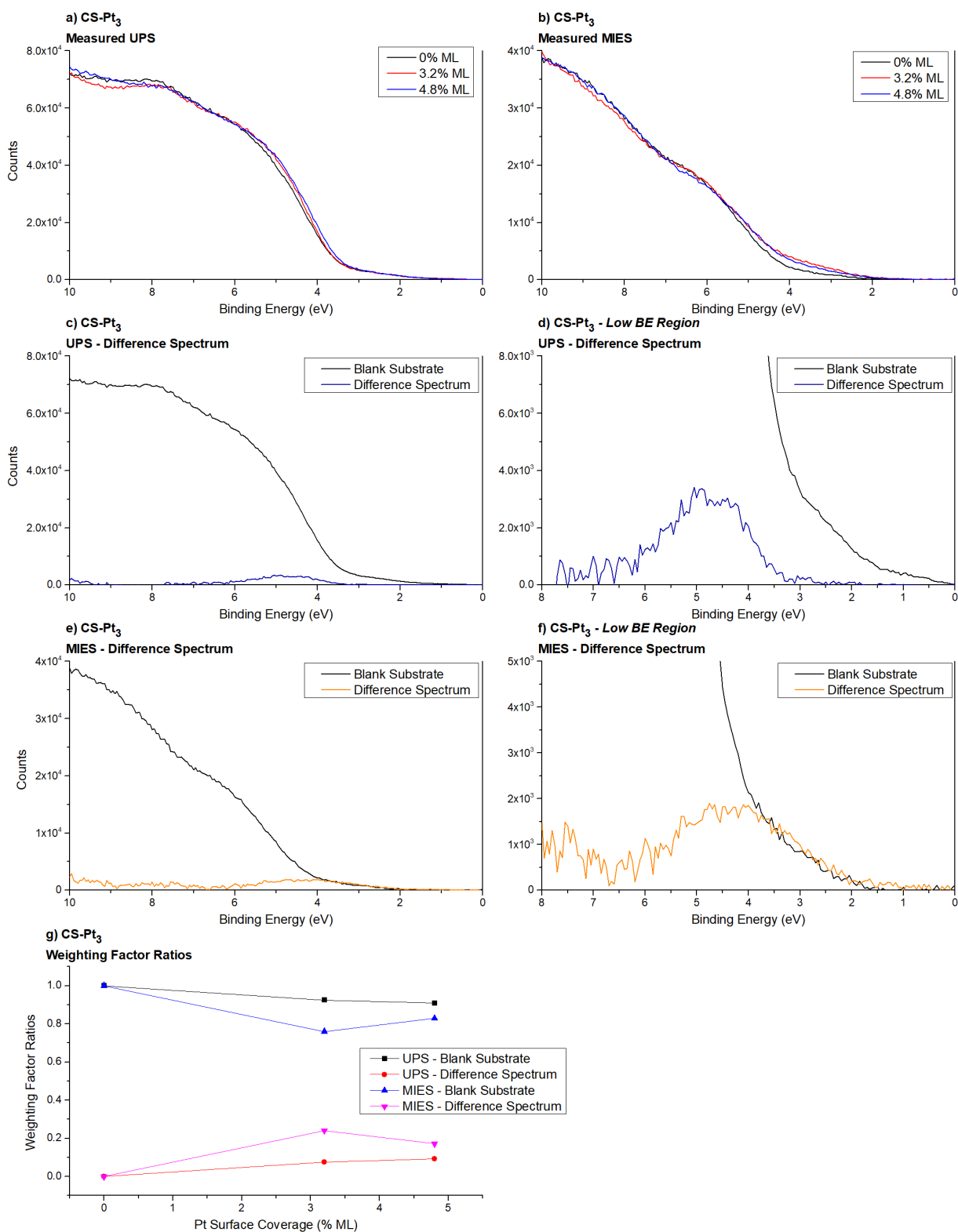
Figure 6-7: UPS/MIES results for the CS-Pt₃ UPS/MIES series. a) Measured UPS spectra. b) Measured MIES spectra. c) UPS of the CS-Pt₃ difference spectrum and blank substrate. d) Spectra from (c), zoomed into the low-BE region. e) MIES of the CS-Pt₃ difference spectrum and the blank substrate. f) Spectra from (e), zoomed into the low-BE region. g) UPS/MIES weighting factor ratios for the CS-Pt₃ difference spectrum and blank substrate, and as a function of Pt surface coverage. The uncertainty in the weighting factor ratios is ± 0.05. The absolute error in the surface coverage is ~100% while the relative uncertainty is based on the Pt At% and is ± 4%.

The CS-Pt$_3$ cluster depositions had a visible effect on the measured UPS and MIES seen in Figure 6-7a-b, when compared to the blank substrate. The main feature of the CS-Pt$_3$ UPS difference spectrum in Figure 6-7c is a d-band peak spanning from 3.3 eV to 6.3 eV, with a peak location at 4.7 eV. There does not appear to be any other peaks in the spectrum, and there is no signal below or above this peak (besides a signal at higher BEs related to the ejection of secondary electrons). In the MIES difference spectrum (Figure 6-7e) there is a single peak spanning 2.0 eV to 6.7 eV, with a maximum at 4.3 eV. The peak is similar to that of UPS but shifted by -0.4 eV and broadened (discussed further in section 6.5.2). The CS-Pt$_3$ UPS/MIES weighting factors in Figure 6-7g increase with Pt surface coverage, which provides evidence the CS-Pt$_3$ spectrum is related to the deposition of Pt$_3$ clusters. The MIES weighting factor ratio for CS-Pt$_3$ increases from the blank (0% loading) to the 3.2% ML sample, but then decreases slightly for the 4.8% ML sample; this is deemed acceptable within the ± 0.05 uncertainty for the weighting factor ratios.

6.4.3.5 CS-Ru$_3$

Several attempts were made to determine UPS/MIES difference spectra due to CS-Ru$_3$ on RF-TiO$_2$. Due to equipment limitations, the experiment could not be performed *in situ* (see Methodology). 4 separate experiments were performed featuring a range of cluster surface loadings, but the Ru$_3$ cluster difference spectra could not be determined. Measurements were attempted after heating samples to both 473 K and 723 K. In some experiments there was too much inter-sample difference in valence structure, and in one case the substrates were more consistent but the cluster-loaded UPS/MIES spectra were identical to the blank substrate spectra, meaning the difference between loaded and unloaded samples could not be seen within the given resolution.
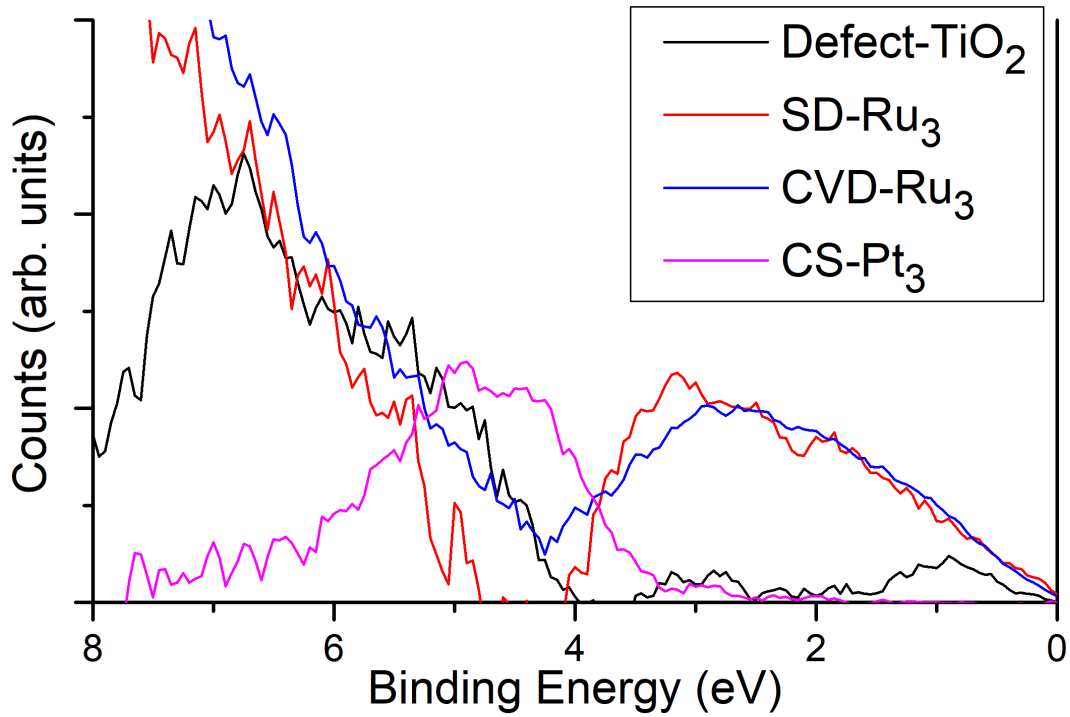
In Chapter 4 it was shown that CS-Ru$_3$ has no available Ru-CO states when deposited on sputtered RF-TiO$_2$; this means there were most likely no Ru$_3$ clusters present on the topmost layer. This accounts for the lack of visible Ru in MIES (due to the surface sensitivity) but does not account for the lack of UPS difference spectra. Considering difference spectra could be determined earlier in the Results for both SD-Ru$_3$ and CVD-Ru$_3$, it is possible the exposure of CS-Ru$_3$ clusters to atmosphere caused an interaction which obscured or changed the DOS of the clusters. This did not appear to be the case for CS-Pt$_3$ (above), which was also analysed *ex situ* in the same way, which is possibly because Pt is known to be particularly chemically inert [447]. If the experiment were to be repeated as part of some future work, depositing the clusters *in situ* may therefore resolve the potential issue of the Ru$_3$ clusters interacting with atmosphere. However, this would involve the modification of

the UHV system used such that both a CS and UPS/MIES are available in the same instrument.

6.4.4 UPS/MIES Difference Spectra Comparison

The UPS/MIES difference spectra for RF-TiO_2 defects, SD-Ru_3, CVD-Ru_3, and CS-Pt_3 were overlayed on one set of axes each for UPS and MIES, shown in Figure 6-8. The difference spectrum for each UPS/MIES series was multiplied by a linear scaling factor for ease of comparison between the results (due to differing count rates), which means the absolute intensities of the spectra cannot be directly compared. Regarding the cluster difference spectra, it was noted that there was a possibility for the cluster deposition to change the DOS of the TiO_2 substrate, due to charge transfer, bond formation, or changes in the work function [448-450]. In this study the clusters had a low surface coverage, where the highest coverage was ~11.0 % ML (see Table 6-2), and thus it was not expected that large changes in the substrate DOS would be detected in the difference spectra for UPS. However, due to its surface sensitivity, changes in the substrate DOS may be more noticeable with MIES spectra.
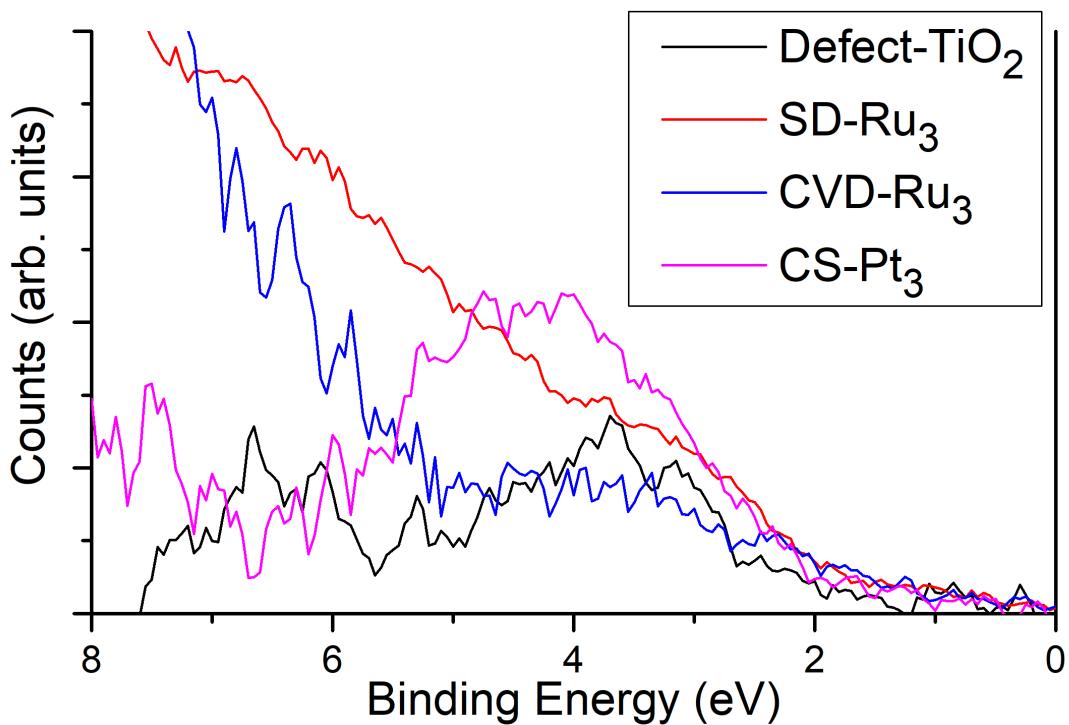
Figure 6-8: Overlayed UPS (a) and MIES (b) spectra for SD-Ru₃, CVD-Ru₃, and CS-Pt₃, and Defect-TiO₂ substrate.

6.5 Discussions

6.5.1 Ru$_3$ Analysis

The Ru$_3$ clusters from both SD-Ru$_3$ and CVD-Ru$_3$ have very similar UPS and MIES spectra to each another. The UPS spectra (Figure 6-8a) have the same features and are almost identical. For MIES (Figure 6-8b), the SD-Ru$_3$ and CVD-Ru$_3$ spectra are very similar but a key difference is that the SD-Ru$_3$ signal has a larger contribution from the secondary electron background. Within the accuracy of the measurement it can be assumed the difference spectra for SD-Ru$_3$ and CVD-Ru$_3$ are identical in UPS and MIES. The XPS results in Table 6-3 showed that for these two samples the Ru 3d BE of SD-Ru$_3$ was 1.2 eV higher as-deposited, but after heating the BE was the same within the ± 0.1 eV resolution. This provides evidence that between SD and CVD depositions the method of depositing Ru$_3$ onto RF-TiO$_2$ does not have a large effect on the DOS of the clusters after heating to 723 K. The heating procedure involves complete or near-complete ligand removal (see previous analysis in section 5.4.1, Chapter 5), which suggests that the ligand-removal step has the greatest effect on the final cluster-substrate interactions, and not the deposition step. As such, the deposition method could be chosen on a per case basis, based on the intended application without concerns for differences in cluster properties after removing ligands. That is, SD depositions have a greater ability to scale up for industrial purposes [66, 72, 99, 104] and can deposit onto the inside surfaces of porous substrates such as mesoporous silica [76, 77], while CVD can be performed *in situ* for fundamental studies [74, 75].

For the metallic Ru reference MIES (see Figure 6-3b) there were no distinct MIES features. However, for the MIES difference spectra (Figure 6-8b), the SD-Ru$_3$ and CVD-Ru$_3$ spectra both look very similar to the Defect-TiO$_2$ spectrum. All three spectra feature a peak in the 3.0 to 3.5 eV region. For the Defect-TiO$_2$ difference spectrum this was assigned to defect-modified O 2p sites (see section 6.4.3.1 above). The similarity between this and the Ru$_3$ difference spectra suggests that the SD-Ru$_3$ and CVD-Ru$_3$ MIES difference spectra are in fact related to an increase in titania defect-related O 2p sites compared to the blank substrate, as a result of the deposition of Ru$_3$ clusters. This suggests that reduced titania has encapsulated the Ru$_3$. This is consistent based on previously reported data in Chapter 5; TD-LEIS results showed that after heating the substrate to an average of 660 K ± 120 K, Ru$_3$ clusters deposited by CVD were encapsulated by a layer of substrate material, ~0.35 nm ± 0.08 nm in thickness. The reduced nature of the titania overlayer agrees with previously reported XPS and microscopy studies on metal encapsulation by titania [185, 186, 207, 208, 210-213, 216, 386]. The SD-Ru$_3$ and CVD-Ru$_3$ MIES spectra provide a direct measurement

of the reduced titania covering the clusters. Because the MIES spectra for SD-Ru$_3$ and CVD-Ru$_3$ feature O 2p sites, this suggests a bonding structure such as Ru-Ti-O at the topmost layer, where the O 2p sites are available for probing by He* but Ru is not.

Conversely, for the UPS difference spectra (Figure 6-8a) the Defect-TiO$_2$ spectrum was unique, and not similar to SD-Ru$_3$ or CVD-Ru$_3$. The Defect-TiO$_2$ UPS features a much narrower energy band than Ru$_3$, just above the Fermi level. This provides evidence that the UPS difference spectra determined for SD-Ru$_3$ or CVD-Ru$_3$ represent the valence DOS due to the deposited Ru$_3$ clusters, and do not represent surface titania defects as was the case for the MIES results. The extra analysis depth of UPS over MIES allowed for the detection of the encapsulated Ru$_3$ clusters, given the probing depth of UPS is 2-3 nm [284], larger than the overlayer thickness of ~0.35 nm ± 0.08 nm. Any effects from the substrate-cluster interaction on the cluster and/or substrate DOS may also be included in these difference spectra, which is discussed in further detail below. These results highlight the benefits of combining MIES and UPS experiments; MIES measured the DOS due to the uppermost layer, assigned to defected titania O 2p states, while UPS measured the DOS due to the covered Ru$_3$ clusters. To the best knowledge of the author this is the first explicit measurement of the valence structure of an encapsulating layer covering clusters using a surface-sensitive technique such as MIES.

6.5.2 Pt$_3$ Analysis

Table 6-3 shows that there was a -0.5 eV ± 0.1 eV shift in the Pt 4f BE for the clusters after heating to 523 K. XPS was also measured at 423 K for Pt$_3$ and the -0.5 eV ± 0.1 eV shift also occurred at this temperature, with no further shifting between 423 K and 573 K (results not shown). Because the Pt$_3$ clusters were deposited *ex situ* and exposed to atmosphere before analysis, it is likely the -0.5 eV ± 0.1 eV peak shift upon heating was related to the removal of contamination from the surface of the clusters, which was affecting the core electron distribution. It is also possible that the peak shift was related to some amount of cluster agglomeration, because previous studies on size-selected, small Pt clusters on oxide substrates have shown depositing larger clusters decreased the BE towards the bulk Pt value [9, 352]. However, if cluster agglomeration occurred for Pt, it must have been minimal because the BE of Pt 4f$_{7/2}$ at 523 K was 72.5 eV ± 0.1 eV, above the range of typical bulk Pt BEs. Additionally, the sputter-induced defects on the surface are likely to pin the Pt$_3$ clusters and minimise the agglomeration; this has been shown previously for Au clusters on titania [5, 222].

The shape of the CS-Pt$_3$ difference spectra are unique compared to all other UPS/MIES spectra in Figure 6-8. Furthermore, UPS and MIES spectra are very similar to each other; the only difference is an effect of peak broadening towards the Fermi level in MIES, with a -0.4 eV shift of the overall peak location. The similarity between UPS and MIES spectra shows that He* de-excitation in MIES was predominantly by the Auger de-excitation (AD) mechanism [298]. Furthermore, this provides evidence that the Pt$_3$ clusters were present on the topmost layer after heating to 573 K, because the difference spectra determined for the topmost layer (MIES) and top several layers (UPS) were very similar, unlike for the Ru$_3$ UPS and MIES difference spectra. The presence of Pt on the topmost layer is most likely a benefit for photocatalysis, because photocatalytic reactions typically occur at active sites on the topmost surface layer [431].

The CS-Pt$_3$ MIES onset is at a similar location to the Defect-TiO$_2$ MIES onset. Thus, the peak broadening towards the Fermi level for the CS-Pt$_3$ MIES may be due to a contribution of titania surface defects to the CS-Pt$_3$ MIES spectrum. The broadening may additionally be contributed to by the interaction of He* with the surface, and the fact that during AD de-excitation electron density is sampled 2 to 4 angstroms above the outer-most surface layer, which can affect the measured DOS [298].

Several previous studies have been performed analysing the DOS of small, size-selected Pt$_n$ clusters using UPS [57, 437], but this is the first study performed using RF-TiO$_2$ as a substrate. Comparisons between this study and previous studies are therefore important to determine how the substrate effects the DOS. Note that there are not previous studies such as this for size-selected Ru clusters in the same size range, so the Ru$_3$ DOS cannot be compared to previous literature in this way.

The UPS/MIES difference spectra for Pt$_3$ are comparable to the UPS difference spectrum determined in a study by Eberhardt *et al.* [437] for CS-deposited, size-selected Pt$_3$/SiO$_2$; this study found two peaks present at ~4.9 eV and ~8.5 eV, with an overall onset at ~2.0 eV. The 4.9 eV peak appears to be the same feature as the 4.7 eV peak in the UPS for CS-Pt$_3$. The second, higher BE feature was not present in this study, which may be due to differences between the cluster-surface interaction in the studies, or due to the effect of variations in secondary electron contributions on the difference spectra. Interestingly, in a different study by Roberts *et al.* [57] the onset energy of the d-band for small, size-selected Pt$_n$ clusters (n = 1, 2, 4, 7, 10, 14, 18) supported on Al$_2$O$_3$ (~10% ML coverage) was found to be between 0.3 (n ≥ 9) and 0.7 eV (n = 2) [57]. Compared to an onset of ~3.3 eV for the

Pt_3 UPS difference spectrum in this study (Figure 6-8), and ~2.0 eV for Pt_3/SiO_2 [437], this was much closer to the Fermi level. The difference in DOS onset between this study and those with Pt_n supported on SiO_2 and Al_2O_3 is likely due to the unique cluster-surface interactions of Pt with the different oxide substrates. The higher onset for Pt_3 supported on RF-TiO_2 than either Pt_3/SiO_2 or Pt_n/Al_2O_3 may be partially due to the Ar^+ ion sputtering treatment prior to cluster depositions influencing the cluster DOS [3]. This has been shown with UPS and XPS measurements for larger, 3D Pt nucleates on TiO_2(110) [417, 451]. It would be beneficial to perform future DFT calculations to determine the DOS of Pt_3 clusters supported on sputter-treated RF-TiO_2 for comparison to the results of this study.

The cluster shapes may also be influenced by the defects, thus also influencing the DOS. DFT studies on cluster shape have shown Pt_n clusters (n = 1 - 4) on stoichiometric TiO_2(110) have atomic structures similar to the gas-phase minimum-energy structures, but have distorted atomic structures when on reduced titania with oxygen vacancies [452]. The XPS and UPS/MIES results in this chapter do not provide evidence about the shape of the Pt clusters. Previous experimental evidence for Pt_n/TiO_2(110) [352, 453] and DFT studies for non-supported Pt_n [454] both suggested that Pt_3 clusters have planar structures, however as mentioned due to the presence of surface defects the cluster structures in this study may be distorted.

6.5.3 Cluster Metallicity

The blank metallic Ru reference UPS in Figure 6-3a features an onset at the Fermi level. For both SD-Ru_3 and CVD-Ru_3 the UPS DOS onset is also at the Fermi level (Figure 6-8a). This onset indicates the clusters have metallic states [61, 437, 440-442]. This is interesting because metal clusters are generally known for their molecule-like discrete electron levels and lack of typical metallic properties [13]. In Chapter 4 the Ru 3d BEs showed that Ru_3 clusters deposited using either a CS or CVD are both partially oxidised after heating to 800 K on RF-TiO_2, although the exact stoichiometry was not known. Note that in the current chapter the presence of the CO ligands on the clusters obscures the oxidation-related BE shift after heating (see section 6.4.1.2). Evidence from TD-LEIS in Chapter 5 further showed that Ru_3 clusters deposited by CVD were encapsulated by sputtered RF-TiO_2 after heating to 660 K ± 120 K. The oxidation and encapsulation of the Ru_3 clusters are both evidence of the SMSI, and it is possible this is resulting in the metallisation of the Ru_3 clusters on RF-TiO_2.

Conversely, for CS-Pt_3 the DOS onset was at 3.3 eV for UPS and 2 eV for MIES. Considering
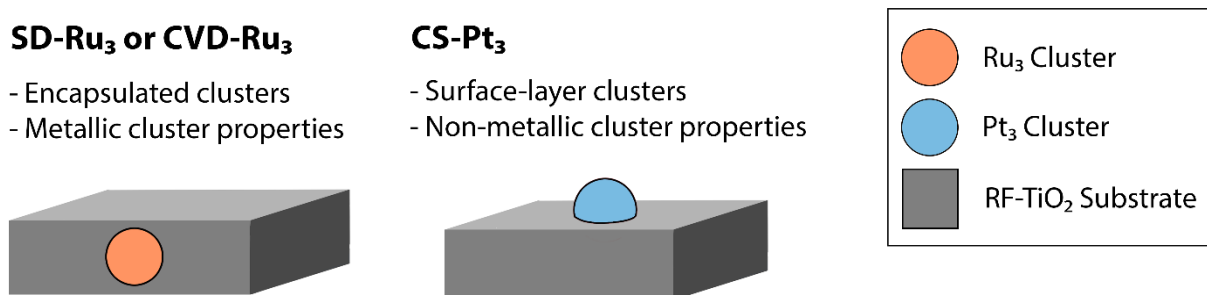
the top region of the Pt$_3$ DOS is not close in energy to the Fermi level and does not exhibit the modified step function characteristic of a metallic Fermi level, this suggests that the supported Pt$_3$ clusters have non-metallic properties (unlike the Ru$_3$ clusters) [437, 440-442]. Such a conclusion is supported by previously reported Pt$_n$ cluster UPS results [57, 437], and is in contrast to bulk forms of Pt such as Pt(111) where the UP onset is present at the Fermi level [443]. The non-metallic properties of the Pt$_3$ clusters are further supported by the Pt 4f XPS results in section 6.4.1.2, which featured symmetrical Pt doublet peak shapes, contrasting bulk Pt where the 4f doublet typically has asymmetrical peak shapes [352]. A previous study by Isomura et $al.$ [352] has similarly shown symmetrical Pt 4f peak shapes for small, mass-selected Pt$_n$ clusters. Lastly, further evidence Pt$_3$ is non-metallic comes from MIES and UPS; the spectra look very similar for CS-Pt$_3$, suggesting AD de-excitation in MIES related to a non-metal [298].

This notion of small, non-metallic Pt$_n$ clusters has been previously supported in the literature. In the previous mentioned studies of Pt$_n$ clusters on SiO$_2$ [437] and Al$_2$O$_3$ [57] the Pt UPS spectra had band gaps similar to that of CS-Pt$_3$ seen in this study. A size-dependent UPS study of Pt$_n$ (n = 1-15) on Ag(111) showed that small Pt clusters featured an onset which shifts closer to the Fermi level as cluster size increases [455], showing that there is a trend towards the Fermi level as the clusters become more bulk-like. A DFT study of Pt$_n$ (n = 1-4) on TiO$_2$(110) also supports this idea, calculating that no metallisation of the clusters had occurred [452].

6.5.4 Cluster Encapsulation

As discussed above, SD-Ru$_3$ and CVD-Ru$_3$ deposited onto sputtered RF-TiO$_2$ were encapsulated by a layer of reduced titania after heating. Previous literature on the encapsulation of Ru by TiO$_2$ has been discussed in detail in Chapter 5, section 5.4.6. However, CS-Pt$_3$ was not encapsulated, evidenced by the availability of Pt$_3$ clusters on the topmost layer to He* in MIES. This suggests that the SMSI is occurring for Ru$_3$ clusters, but not for Pt$_3$ clusters on sputtered RF-TiO$_2$. Figure 6-9 shows diagrams summarising these encapsulation results for both Ru$_3$ and Pt$_3$ on sputtered RF-TiO$_2$. Previous studies in the literature which have shown Pt adsorbates being encapsulated by TiO$_2$(110) after heating are typically for larger Pt nanoparticles (not small clusters) and/or much higher surface coverages than those used in this study [39, 207, 208]. In a study by Wu et $al.$, it was evidenced using TPD that supported Pt clusters on TiO$_2$(110) were not encapsulated, while larger supported nanoparticles were encapsulated and underwent the SMSI (this study was not on atomically size-selected clusters, but the results are still comparable) [39]. This study

puts forward the idea that the encapsulation of Pt adsorbates by titania is promoted by larger Pt particle sizes, which is supported by the results in this chapter which show Pt_3 clusters are not encapsulated. This is further supported by a study on ultrafine Pt nanoparticles (~1 nm) on TiO_2 powder, which were not encapsulated after to heating at 723 K under UHV [456]. Considering there are previous studies which show that sputtering can promote encapsulation on titania [185, 186], this suggests the Pt_3 clusters are quite stable to encapsulation on RF-TiO_2.

SD-Ru$_3$ or CVD-Ru$_3$

- Encapsulated clusters
- Metallic cluster properties

CS-Pt$_3$

- Surface-layer clusters
- Non-metallic cluster properties

Ru$_3$ Cluster

Pt$_3$ Cluster

RF-TiO$_2$ Substrate

Figure 6-9: Summary of the results regarding encapsulation and metallicity for SD-Ru$_3$, CVD-Ru$_3$ and CS-Pt$_3$ clusters supported on sputtered RF-TiO$_2$ substrates. These images represent the surfaces after 723 K heat treatment. Only one image is shown for Ru$_3$ clusters because the same results were found for both cluster types.

The mechanism for the encapsulation of Ru_3 (but not Pt_3) on RF-TiO_2 substrates is most likely related to the minimisation of surface energy in each of the systems [185, 203, 210, 213]. The surface free energy for Ru (~2.7 $J.m^{-2}$) is higher than that of Pt (~2.2 $J.m^{-2}$), which is consistent with the logic used herein as Pt will be favoured to remain on the surface [457]. Experimental evidence for this has been shown by Galhenage *et al*. [326], where bimetallic Pt-Ru clusters were grown on HOPG surfaces by vapor deposition. In this study, approximately even coverages of Pt and Ru were deposited and after heating to 403 K the surface composition increased to 98–99% Pt, indicating that Pt has the higher surface affinity [326].

In Chapter 4 it was shown that CS-Ru_3 clusters were encapsulated by sputtered RF-TiO_2 even without heating the substrate, but this does not occur when the surface is not Ar^+ ion sputtered prior to depositing clusters. Thus, it must be considered that the surface defects play a key role in the encapsulation process. In light of this, another possible mechanism for encapsulation may be that the Ru_3 clusters dissociate on the surface due to the interaction with the defect-rich, reduced titania. This is possible because Ru-Ru has a lower bond dissociation energy than Pt-Pt; 193.0 ± 19.3 kJ/mol for Ru-Ru [458] compared to 307 ± 2 kJ/mol for Pt-Pt [392, 459]. If the Ru_3 clusters were dissociated this may promote

encapsulation because less TiO_2 must be displaced by encapsulating a single atom. Additionally, single atoms are typically more mobile on surfaces than small clusters, which would further promote encapsulation. The increased mobility of single atoms at room temperature has been shown for isolated Ag, Cu, and Pd atoms on oxide supports [70]. It is difficult to provide evidence for or against this mechanism because the structure of the small clusters underneath a reduced titania covering layer would need to be determined. Thus, to provide stronger evidence for or against this, DFT studies of Ru_3 on reduced titania will be needed to compare to experimental results.

6.6 Conclusions

In this study UPS and MIES were performed on samples after heat treatment, and difference spectra were determined due to the deposition of Ru_3 (SD and CVD depositions) and Pt_3 (CS depositions) onto Ar^+ ion sputter-treated RF-TiO_2. Further details on the surface coverage and properties of the clusters was provided by XPS. Comparing SD-Ru_3 to CVD-Ru_3, it was determined based on the similarity of the UPS/MIES results that the method of depositing $Ru_3(CO)_{12}$ onto the surfaces does not have a significant effect on the DOS of the Ru_3 clusters after heating. Thus, it is likely that that the heating-based CO ligand-removal has a greater effect on the final cluster-substrate interaction that the initial deposition step.

Based on their UPS/MIES difference spectra, Ru_3 clusters were found to have metallic properties while Pt_3 clusters had non-metallic properties. For Ru_3 clusters, the UPS measured the clusters while the MIES spectrum was in fact a measurement of defected titania atop of the clusters, due to encapsulation by the substrate. Conversely, for Pt_3 clusters the UPS and MIES spectra were very similar, which provides evidence that Pt_3 clusters were present on the topmost surface layer after heating to 523 K, which is most likely a benefit for catalysis. The fact that Ru_3 was encapsulated but Pt_3 was not is possibly due to an energetic benefit for Ru encapsulation, related to the minimisation of surface energy. However, such a possibility does not exclude other, more complicated mechanisms related to the induced surface defects on the substrate.

Chapter 7   Investigations into $H_4Ru_4(CO)_{12}$ supported on RF-deposited TiO_2

7.1 Abstract

Size-selected 4-atom Ru_4 clusters were deposited onto radio frequency (RF)-sputter deposited TiO_2 (RF-TiO_2). RF-TiO_2 surfaces were treated by Ar^+ ion sputtering prior to cluster depositions, and Ru_4 was deposited by chemical vapor deposition of $H_4Ru_4(CO)_{12}$. This work compares results to previous studies which used $Ru_3(CO)_{12}$ and is motivated by the potential use of titania-supported Ru clusters as cocatalysts for reactions such as photocatalytic water splitting. Supported Ru_4 samples were prepared for analysis using temperature-dependent XPS (TD-XPS), temperature programmed desorption (TPD), and ultraviolet photoelectron spectroscopy (UPS). The CO-TPD results indicated that after heating to 723 K all Ru-CO binding sites on the surface layer were blocked, caused by the encapsulation of clusters by substrate material. UPS provided evidence that the encapsulated clusters have metallic properties. Comparing to previous studies on $Ru_3(CO)_{12}$, TD-XPS shows that $H_4Ru_4(CO)_{12}$ begins to lose CO at a slightly lower temperature. However, after heat treatment the valence electronic structures of both cluster types are similar, suggesting that encapsulated Ru_4 has the same potential catalytic benefits as Ru_3.

7.2 Introduction

In this chapter, studies from the previous chapters on ligated Ru clusters are expanded upon by using a larger cluster size, namely $H_4Ru_4(CO)_{12}$. Most concepts which are relevant to this study have been introduced in previous chapters, including the dependence of cluster properties on; size, the effect of the supporting material on clusters, the strong metal-support interaction (SMSI), chemical vapor deposition (CVD), and the applications of supported clusters in catalysis and photocatalysis. Therefore, in this introduction only the most relevant concepts will be re-summarised. In addition, other studies on size-dependent cluster effects, and in particular $H_4Ru_4(CO)_{12}$, are discussed.

Small, size-selected metal clusters often possess unique electronic and catalytic properties which are highly dependent on cluster size [11, 14-18, 57, 292, 315, 460-462]. A specific range of cluster sizes may result in lower energy reaction pathways or altered reactivity for catalysis. Due to their size-sensitivity, the addition or subtraction of just one atom to a small cluster can influence whether the cluster functions as a catalyst [56]. By way of example, Sanchez *et al.* [56] showed for the catalytic oxidation of CO, gold Au_8 clusters catalysed the reaction effectively, but clusters with 7 or less atoms ceased to be catalytically active. This dependence of catalytic activity on cluster size also extends to other supported clusters [57, 154, 229, 314, 398]. Furthermore, the catalytic activity of the clusters is related to the cluster density of states (DOS) [17, 435]. It is therefore important, for catalytic purposes, to measure the size-effects on the DOS of supported clusters. This is because the DOS has been experimentally shown to depend on cluster size for clusters deposited using a size-selected cluster source (CS); including Pd_n/TiO_2 [6, 60, 292], Au_n/MgO [177], Pt_n/SiO_2 [9], Pt_n/Al_2O_3 [57], and Pt, Pd, and Ni clusters on Ag single crystals [463]. However, there are relatively fewer studies focussing on substrate-supported, ligand protected clusters [3, 5, 464].

A common way to deposit metal clusters onto substrates is by depositing ligand-stabilised clusters using CVD (described in section 2.4.1.2) [74, 75, 135-137]. Metal carbonyls including $Ru_3(CO)_{12}$ and $H_4Ru_4(CO)_{12}$ are the most common class of clusters deposited using this method [75, 138-143]. $H_4Ru_4(CO)_{12}$ features supporting H ligands bridging the metal-metal bonds, while the metal-metal bonding in $Ru_3(CO)_{12}$ is unsupported [105]. There are only a few studies previously performed on supported $H_4Ru_4(CO)_{12}$ [250] compared to those using $Ru_3(CO)_{12}$. A number of $H_4Ru_4(CO)_{12}$ catalysis studies have been performed [91, 93, 105, 250, 465, 466] but the clusters were not TiO_2-supported and the electronic structure of the clusters was not measured. These studies showed the homogeneous catalytic abilities of $H_4Ru_4(CO)_{12}$ and $H_4Ru_4(CO)_{12}$-based catalysts for the; hydrogenation of

ethylene [91, 93], hydrogenation and isomerisation of cyclic dienes [465], and hydrogenation of pentynes [466]. In addition, solid-gas catalysis was shown by $H_4Ru_4(CO)_{12}$/glass reacting with 1,4-cyclohexadiene, or hex-3-yne and dihydrogen to produce monoenes [105]. In a rare study on metal oxide-supported $H_4Ru_4(CO)_{12}$, Pierantozzi *et al.* [250] showed that $H_4Ru_4(CO)_{12}$ supported on Al_2O_3 and MgO had significant oxygenate yields from the catalytic reaction of CO + H_2.

To the best knowledge of the author there are no previous size-dependent, experimental studies of small, metal-oxide supported Ru clusters. Previous DFT calculations have shown the importance of the supporting substrate, arguing that the adsorption behaviour of Ru_n (n = 1 − 4) onto Al_2O_3 effected cluster electronic structures, and was dependent on both the cluster size and metal-oxide surface structure [467, 468]. While this study was for bare clusters on Al_2O_3, similar differences in cluster adsorption may be expected for clusters of differing sizes deposited by CVD onto RF-TiO_2.

The present study was designed to investigate the effect of a small change in Ru cluster size on the resulting properties when the clusters were supported on Ar^+ ion sputter-treated RF-TiO_2. The surface properties of CVD-deposited Ru_4/RF-TiO_2, were measured using temperature-dependent XPS (TD-XPS), TPD, and UPS. The main aim of the work was to compare the properties of supported Ru_4 to previously reported results for supported Ru_3 (Chapter 4 to Chapter 6), because it is not yet known whether the encapsulation depends on cluster size. The Ar^+ ion sputter treatment of the substrate is consistent with the previous studies herein, and was shown to cause encapsulation of Ru_3 clusters by titania (Chapter 4). The work is motivated by the potential use for small Ru clusters supported on TiO_2 in efficient catalytic and/or photocatalytic reactions, in addition to the strong dependence of cluster properties on size [11, 14-18, 57, 292, 315, 460-462]. Understanding how the Ru cluster size effects its DOS and stability to heating is vital for the full comprehension of catalysis involving small Ru clusters.

7.3 Methodology

7.3.1 Substrates

Substrates were RF-sputter deposited TiO_2 on Si(100) wafers (shortened to RF-TiO_2). See section 3.1 in the Instrumentation and Methodologies for complete details on the preparation of RF-TiO_2. Substrates were treated prior to cluster depositions by heating to 723 K for 10 minutes, and 3 keV Ar^+ ion sputtering with 6×10^{14} ions/cm^2 to remove surface contamination and induce surface defects. This is the same procedure as for the treatment of "high-defect sputtered RF-TiO_2" (HDS-RF-TiO_2) in Chapter 4 and Chapter 5, however this longer nomenclature is not needed or used in this chapter as only one substrate type was utilised.

7.3.2 Instrumentation

Two separate ultra-high vacuum (UHV) systems were used. Sample treatment, cluster depositions, XPS, UPS, and MIES were performed on the Flinders University system, while TPD was performed on the University of Utah system. These systems are described in detail in section 3.3.

7.3.3 CVD

CVD of $H_4Ru_4(CO)_{12}$ was performed *in situ* at Flinders University. The CVD procedure was described in the Instrumentation and Methodologies section 3.5.1. Deposition times were varied from 30 minutes to 90 minutes to produce a variation in cluster loading for the UPS samples. Separate samples were prepared for TD-XPS and CO-TPD, by depositing clusters for 60 minutes. The deposited clusters covered the entire sample areas in an approximately even manner. A notable difference in the CVD procedure of $H_4Ru_4(CO)_{12}$ compared to the CVD of $Ru_3(CO)_{12}$ in earlier chapters is that the clusters and substrate were heated to 353 K during deposition to increase the deposition speed, due to the lower vapor pressure of the clusters.

7.3.4 Samples and Procedures

In this chapter nomenclature of samples of CVD-deposited $H_4Ru_4(CO)_{12}$ on sputtered RF-TiO_2 will be shortened to "Ru_4/RF-TiO_2". 5 separate Ru_4/RF-TiO_2 samples were prepared, as well as 1 blank substrate. XPS was measured for all samples immediately following CVD to determine the Ru surface coverage (detailed below). For TD-XPS and CO-TPD there were unique samples per measurement, and for UPS/MIES there were 3 Ru_4/RF-TiO_2 samples and 1 blank substrate. XPS, TD-XPS, UPS, and MIES were performed *in situ.* The CO-TPD sample was removed from vacuum after CVD and XPS and was moved to the University of Utah system for analysis.

7.3.5 XPS and TD-XPS

The instrumentation, measurement procedures, and data analysis procedures for XPS measurements are detailed in section 3.6.1. XPS was performed using the Flinders University XPS instrument with a Mg kα X-ray anode. For analysing XPS spectra the binding energy (BE) scale was calibrated to adventitious C 1s = 285.0 eV. Details on the XPS peak fitting procedure, including extensive details on fitting the Ru 3d/C 1s region, are given in section 3.6.1.3. For $H_4Ru_4(CO)_{12}$ the peak fitting procedure of the Ru 3d XPS region as well as the method for calculating the Ru surface coverage was the same as for CVD-deposited $Ru_3(CO)_{12}$ in earlier chapters. Details about the TD-XPS procedure are given in section 3.6.1.4. For TD-XPS of Ru_4/RF-TIO$_2$, 8 temperatures were measured from 298 K to 827 K. Details about errors and uncertainties in the XPS measurements are given in section 3.6.1.3. The uncertainty in BEs when comparing between samples is ± 0.2 eV, uncertainty in BEs shifted due to sample treatment is ± 0.1 eV, uncertainty in Ru At% is ± 4%, and uncertainty in CO At% is ± 9%. The absolute error in Ru surface coverages is estimated to be ~100%, while the relative uncertainty is based on the Ru At% and is ± 4%.

7.3.6 CO-TPD

Details on the CO-TPD instrumentation and measurement procedures are provided in section 3.6.3. CO-TPD measurements were performed *ex situ*; clusters were deposited in the Flinders University UHV system and then transferred for analysis in the University of Utah UHV system. The CO-TPD process was performed with the same procedure as was used for the CO-TPD of CVD-deposited $Ru_3(CO)_{12}$ in Chapter 4. For the 1st cycle the heating was ramped to 723 K, while for the 2nd and 3rd cycles the heating was ramped to 800 K. As discussed in section 3.6.3.2, ^{13}CO was dosed for the 2nd and 3rd TPD cycles, but on the 1st cycle ^{13}CO was not dosed and only the desorption of the ^{12}CO ligands from $H_4Ru_4(CO)_{12}$ was detected. This was because the CO binding sites of the clusters are saturated by the ligands prior to heat treatment. During the 1st cycle the mass-28 TPD channel (for ^{12}CO ligands) was saturated by the signal, exceeding the maximum detectable limit during measurement, and causing ^{12}CO to overflow into the mass-29 channel. The same situation also occurred for CVD-deposited $Ru_3(CO)_{12}$ in Chapter 4, and this was corrected for in the data analysis (discussed in section 3.6.3.3).

7.3.7 UPS and MIES

Details of the UPS and MIES instrumentation, measurement procedures, and data analysis are provided in section 3.6.2. The measurements and data analysis were performed with the same procedure as for CVD $Ru_3(CO)_{12}$ on RF-TiO$_2$ in Chapter 6. A series of 1 blank

substrate sample and 3 Ru$_4$-loaded samples was analysed with UPS and MIES. The Ru$_4$/TiO$_2$ samples were heated to 723 K for 10 minutes before analysis. Chapter 5 and Chapter 6 showed that heating to this temperature resulted in cluster encapsulation by the substrate material, for Ru$_3$ clusters on sputter-treated RF-TiO$_2$. This serves to remove the ligands as well as any adventitious carbon contamination resulting from the CVD procedure.

For this chapter only UPS results are presented and not MIES results. Based on the series of UPS and MIES measurements, an "Ru$_4$ difference spectrum" was determined for the UPS spectra but this could not be determined for MIES (discussed further in section 7.4.5). The difference spectrum is a calculated spectrum related to the contribution of the Ru$_4$ depositions to the measured valence spectra of the substrate. Weighting factors for the Ru$_4$ difference spectrum and blank substrate spectrum were determined for each sample. The uncertainty in weighting factors is estimated to be ± 0.05. Conclusions will be drawn from the weighting factors based on the trend rather than specific values. For this measurement, the 3 individual cluster-loaded samples needed consistent valence spectrum features to determine a viable Ru$_4$ difference spectrum. Thus, the repeatability of the UPS measurements is built into the measurement procedure.

7.4 Results

Throughout this chapter, results for CVD-deposited $Ru_3(CO)_{12}$ on sputtered RF-TiO$_2$ are referred to from Chapter 4 to Chapter 6 for comparative purposes. These samples will be referred to as "Ru$_3$/TiO$_2$" for naming consistency within this chapter, and the results are shown in dotted lines in relevant figures.

7.4.1 Ru Surface Coverage

XPS was measured for each sample to determine the relative atomic % (At%) of Ru on the surfaces. At% was measured after heating to 723 K for all samples, except for the CO-TPD sample which was measured before heating. All spectra were peak fitted and Ru surface coverages were determined using the same procedures described in section 3.6.1.3, and results are shown in Table 7-1. The range of Ru surface coverages for UPS was 2.1% ML to 5.6% ML, where the variation in coverage assists with the UPS data analysis. The Ru surface coverage was similar between the TD-XPS sample (3.1%) and CO-TPD sample (2.9%), which helps when comparing the results between samples. Additionally, having only a small fraction of a surface monolayer covered helps reduce the probability of cluster agglomeration, which can interfere with size-selected cluster properties.

Table 7-1: XPS results for Ru surface concentrations. Ru surface coverages were calculated based on At% (see section 3.6.1.3 for details). The uncertainty in Ru At% is ± 4%. The absolute error in the Ru surface coverage is estimated to be ~100%, while the relative uncertainty is based on the Ru At% and is ± 4%. Errors and uncertainties are discussed in section 3.6.1.3.

Measurement	Sample	XPS At%	Ru Surface Coverage (% ML)
TD-XPS	Ru$_4$/RF-TiO$_2$	0.43	3.1
CO-TPD	Ru$_4$/RF-TiO$_2$	0.40	2.9
UPS (1)	Blank RF-TiO$_2$	0.00	0.0
UPS (2)	Ru$_4$/RF-TiO$_2$	0.29	2.1
UPS (3)	Ru$_4$/RF-TiO$_2$	0.30	2.2
UPS (4)	Ru$_4$/RF-TiO$_2$	0.77	5.6

7.4.2 TD-XPS Results

For TD-XPS, Ru$_4$/TiO$_2$ was measured with XPS at 8 temperatures from 298 K to 873 K. Ru 3d/C 1s, Ti 2p, and O 1s regions were measured. Three examples of Ru 3d/C 1s peak fitting results are given in Figure 7-1. Figure 7-1a shows an example fitting at 298 K (room temperature), where the sample has not been heated and excess ligands have not been

removed. For this sample, the Ru doublet peak shapes are symmetrical. Figure 7-1b shows an example fitting after heating to 323 K; temperatures between 323 K and 373 K (lightly heated) are in a transition range of temperatures, where Ru 3d fitting requires one symmetrical doublet and one asymmetrical doublet. Figure 7-1c shows an example fitting after heating to 723 K; at 423 K and above the Ru doublet has asymmetrical line shapes (see section 3.6.1.3 for line shape details). The Ti 2p and O 1s regions were fitted according to the procedure described in 3.6.1.3 but are not shown in this results section because they were only used for determining the At% of Ru.
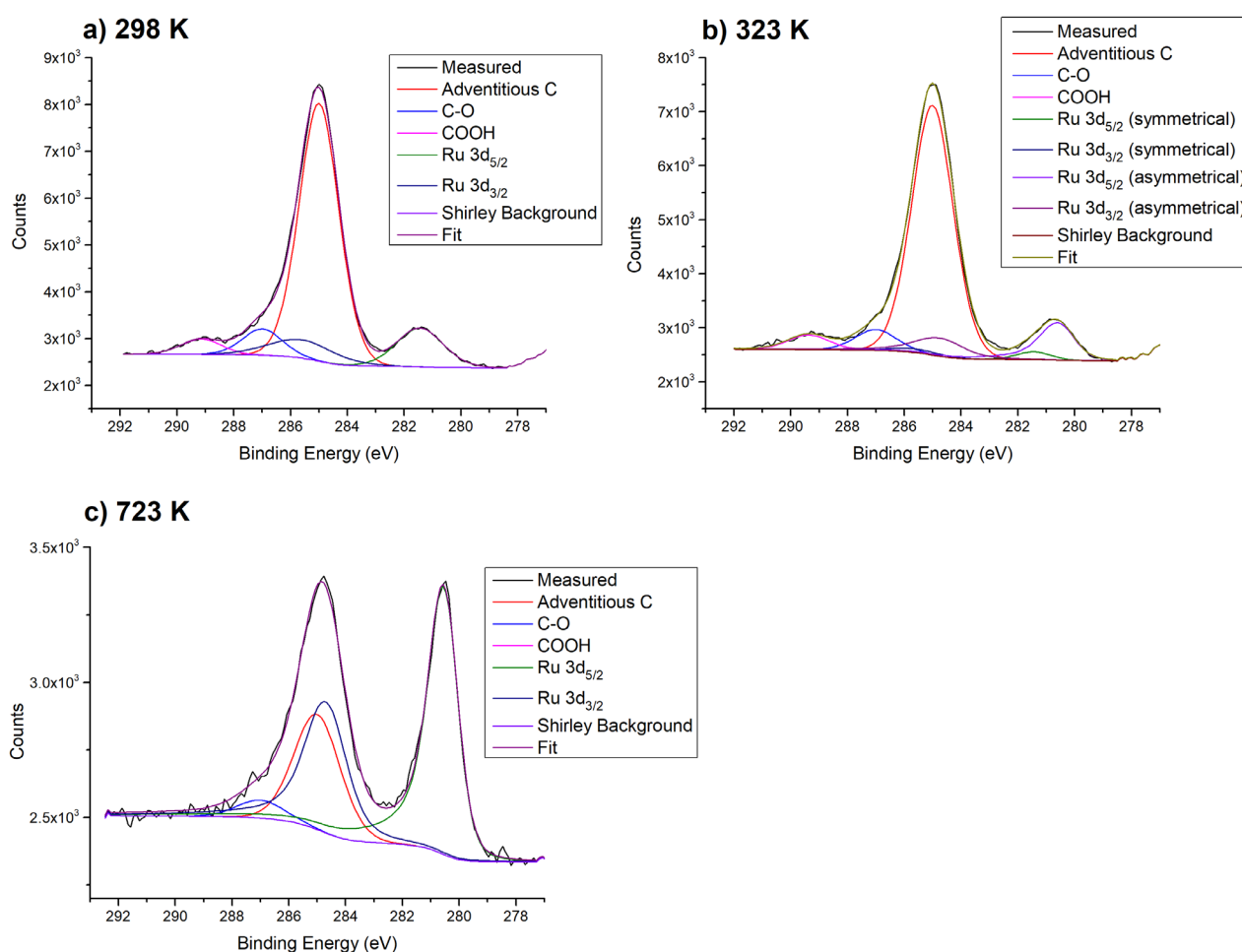
Figure 7-1: Peak fitting results from the TD-XPS of Ru4/RF-TiO2. 3 difference temperatures are shown as examples. A) 298 K – symmetrical Ru doublet. B) 323 K – 1 symmetrical Ru doublet and 1 asymmetrical Ru doublet (transition temperature). C) 723 K – asymmetrical Ru doublet.

The Ru 3d BE can give information about the chemical state of the clusters, and the CO/Ru atomic ratio can be used as a measure of the extent of cluster de-ligation. Note that the H bridging ligands cannot be detected using XPS. The analysed TD-XPS results for Ru $3d_{5/2}$ BE and CO/Ru atomic ratio are shown in Figure 7-2, where they are compared to Ru3/RF-TiO2 results from Chapter 5 (dotted lines). A baseline CO signal was removed before

determining CO/Ru atomic ratios.
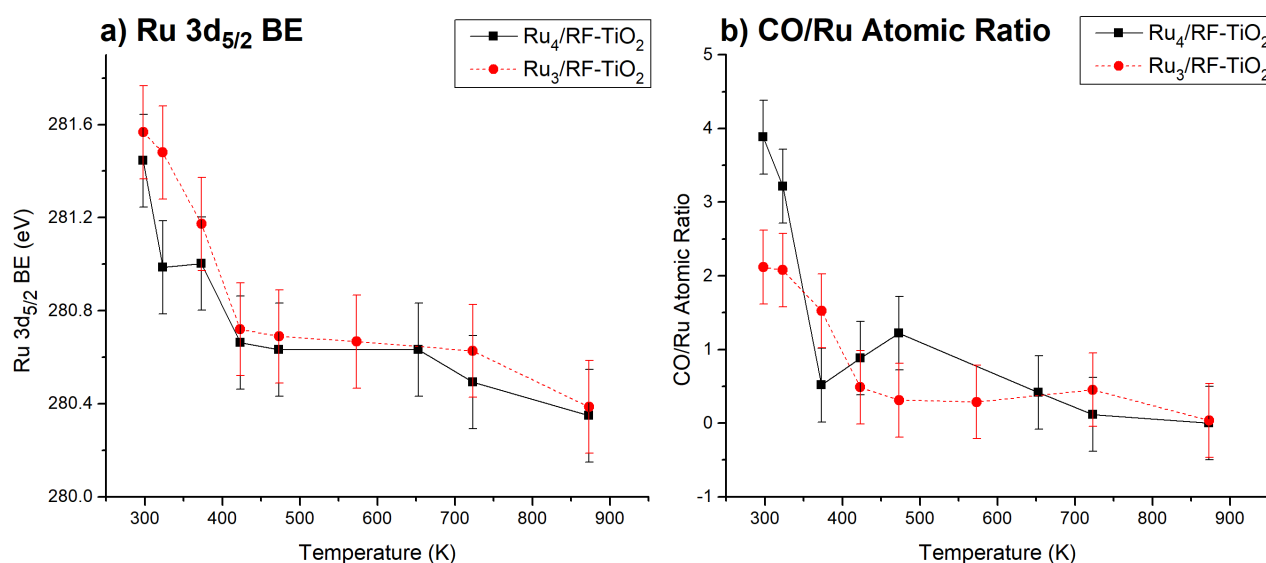
Figure 7-2: TD-XPS results for Ru4/RF-TiO2. Ru3/RF-TiO2 results from Chapter 5 are shown in dotted lines for comparison. a) Ru 3d5/2 BE. For transition states with both symmetrical and asymmetrical Ru doublets, the average BE is used. Error bars represent the ± 0.2 eV uncertainty in Ru 3d5/2 BE when comparing different samples but note that the uncertainty is lower at ± 0.1 eV when comparing temperature-induced BE shifting for the same sample. b) CO/Ru atomic ratio vs. temperature. The absolute uncertainty in CO/Ru is estimated to be ± 0.5.

Figure 7-2a shows that the Ru $3d_{5/2}$ BE for Ru4/RF-TiO2 decreases upon heating, starting at 281.4 eV ± 0.2 eV (as-deposited) and ending at 280.3 ± 0.2 eV (after heating to 873 K). This decrease in BE is related to the removal of the ligands from the Ru cluster core [75]. There is a sharp decrease, followed by an "elbow point" at 423 K, after which the decrease is less steep. The BE trend for Ru3/RF-TiO2 follows the same shape. However, the BE decreases more dramatically during the first heating step to 323 K for Ru4/RF-TiO2 than for Ru3/RF-TiO2. It is also noted that Ru4/RF-TiO2 entered the transition temperature range at 323 K, while for Ru3 this occurred at 373 K. This suggests the ligands were being removed at a lower temperature (323 K) for Ru4, however the CO/Ru atomic ratio does not have a strong decrease until 373 K (Figure 7-2b). This may suggest the initial decrease in BE for Ru4 is related to the loss of H bridging ligands. At 423 K and above, there is a difference in BE of <0.2 eV between the Ru4/RF-TiO2 and Ru3/RF-TiO2, indicating there was no detectable difference between the samples within the resolution of the XPS instrument. The as-deposited Ru $3d_{5/2}$ BE for Ru4/RF-TiO2 was 0.2 eV lower than Ru3/RF-TiO2, which provides some evidence that the Ru4/RF-TiO2 has a lower number of ligands per Ru atom when deposited by CVD, but it must be noted that this is on the edge of the ± 0.2 eV resolution of the instrument.

The CO/Ru atomic ratio for Ru$_4$/RF-TiO$_2$ in Figure 7-2b decreases as the temperature increases, then evens off at an "elbow point" before decreasing to approximately 0 at ~873 K. The Ru$_3$/RF-TiO$_2$ spectrum shares a similar trend, but the CO/Ru atomic ratio decreases to the elbow point at a higher temperature; 373 K for Ru$_4$/RF-TiO$_2$ and 423 K for Ru$_3$/RF-TiO$_2$. This suggests that the lowest energy Ru-CO binding sites are easier to desorb for H$_4$Ru$_4$(CO)$_{12}$ than for Ru$_3$(CO)$_{12}$. The CO/Ru atomic ratio for Ru$_4$/RF-TiO$_2$ at room temperature (298 K) is 3.9 ± ~0.5, while for Ru$_3$/RF-TiO$_2$ it is 2.1 ± ~0.5. This difference is greater than the ~0.5 absolute error. If no ligands were lost in the deposition processes, Ru$_3$/RF-TiO$_2$ would hypothetically have a CO/Ru atomic ratio of 4, while Ru$_4$/RF-TiO$_2$ would have a ratio of 3. Therefore, the result for Ru$_4$/RF-TiO$_2$ is unreasonably high and greater than the maximum ratio. This result points towards a level of CO contamination occurring during the CVD deposition of Ru$_4$, possibly due to the heating process promoting the desorption of contaminants from the sample holder and other chamber components. Due to this, further commentary cannot be made on the CO/Ru atomic ratio of Ru$_4$/RF-TiO$_2$ prior to heating.

7.4.3 CO-TPD Results

Figure 7-3 shows the CO-TPD results. The data for the 1st CO-TPD cycle was measuring only the desorbing ^{12}CO ligands present on the clusters. For the 2nd and 3rd TPD cycles, ^{13}CO was dosed onto the sample at 180 K prior to the CO-TPD temperature ramping, and it is these isotopically-tagged ligands which were detected. The 1st cycle of CO-TPD for Ru$_3$/RF-TiO$_2$ from Chapter 4 is shown for comparison.
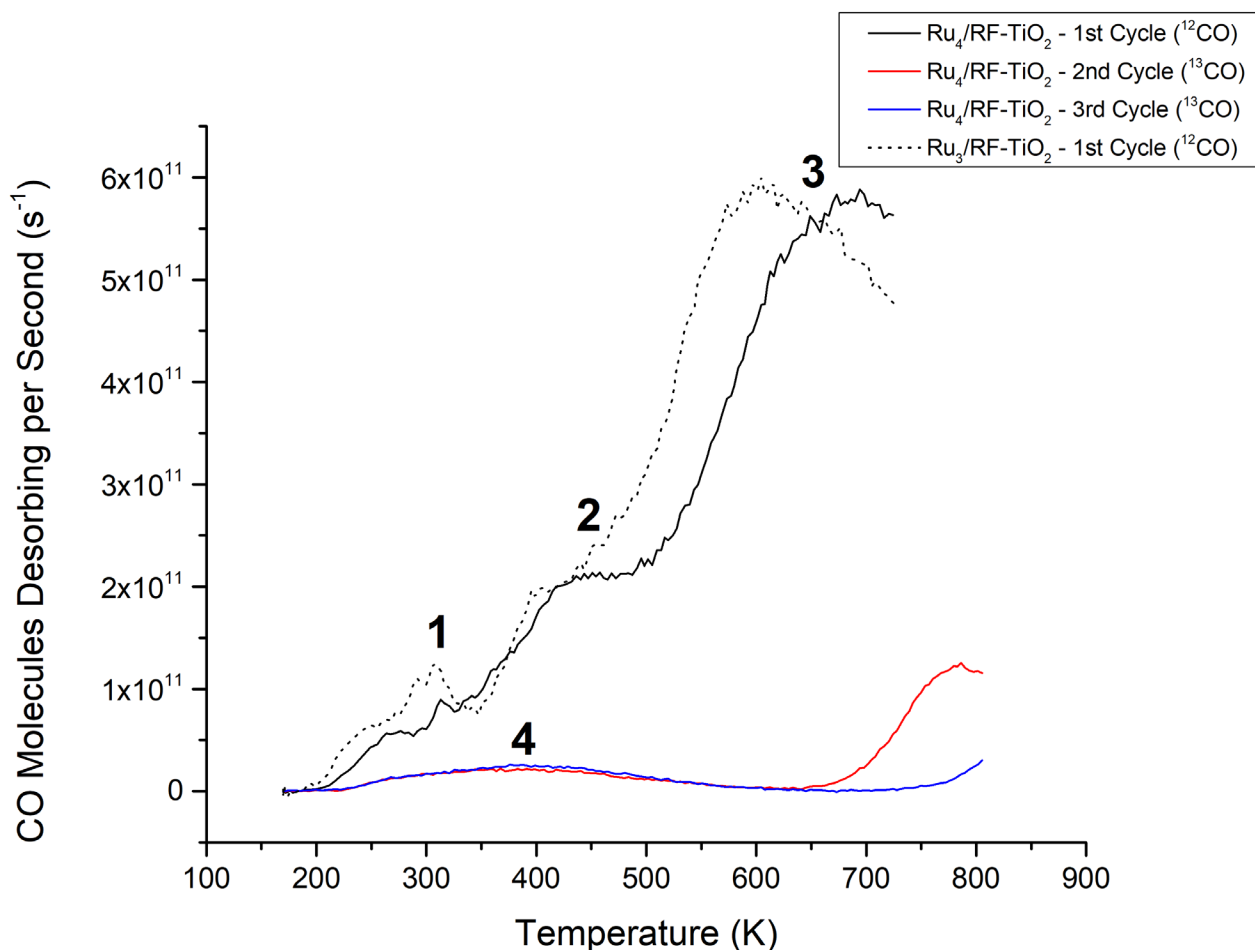
Figure 7-3: CO-TPD results for Ru4/RF-TiO2. 3 CO-TPD cycles were performed. ^{12}CO was measured the 1st cycle and ^{13}CO was measured on the 2nd and 3rd cycles (see section 7.3.6 for details). Peaks were identified at 300 K (1), 410 K (2), and 690 K (3) for the 1st cycle, and a broad desorption feature (4) was identified for the 2nd and 3rd cycles. The 1st cycle CO-TPD results for Ru3/RF-TiO2 are shown for comparison as a dotted line (data from Chapter 4).

In Figure 7-3, the 1st cycle CO-TPD spectrum of Ru4/RF-TiO2 has a low-temperature peak at 300 K, medium-temperature peak at 410 K, and high-temperature peak at 690 K. The 2nd and 3rd heating cycles show vastly different spectra to the 1st, where none of the original Ru-CO sites are remaining and there is a broad, featureless CO desorption trace. The 2nd cycle has a feature at ~780 K which is most likely related to the removal of some ligands which were not removed in the 1st cycle, due to the flash-heating nature of the CO-TPD measurements where temperatures are ramped at 3 K/s. Because no Ru-CO sites are present in the 2nd or 3rd cycles, this indicates that there are no Ru-CO sites available on the surface of Ru4/RF-TiO2 after heating to 723 K (1st cycle). This result where Ru-CO sites are blocked due to heating also occurred for the 2nd and 3rd cycles of Ru3/RF-TiO2 (not shown in Figure 7-3, refer to Chapter 4).

Comparing the CO desorption of the 1st CO-TPD cycle for Ru4/RF-TiO2 and Ru3/RF-TiO2

indicated that the spectra were very similar. There is a low-temperature desorption peak at 300 K for both cluster sizes, and the high-temperature peak is similar but present at 690 K for Ru_4 instead of 620 K for Ru_3. One difference is that the medium-temperature peak; for Ru_3/RF-TiO$_2$ may be present in this location but the feature is difficult to distinguish from the high temperature peak. In Chapter 4, this was interpreted as part of the onset of the high temperature peak, rather than a feature in its own right. However, for Ru_4/RF-TiO$_2$ a 410 K feature is prominent, and more clearly defined as a peak. This is discussed further in section 7.5.1.

7.4.4 UPS Results

For UPS, 3 unique Ru_4/RF-TiO$_2$ samples and 1 blank RF-TiO$_2$ sample were prepared. As per Table 7-1, the samples were loaded with 0, 2.1, 2.2, and 5.6% ML of Ru_4 clusters. The blank sample underwent the same treatment procedure as the cluster-deposited samples, except no clusters were added to the deposition vial. This process helped with consistency in the valence electron spectra. UPS measurements were performed after heating the Ru_4/RF-TiO$_2$ samples to 723 K for 10 minutes. This allowed for a direct comparison between the Ru_4/RF-TiO$_2$ results and the results for Ru_3/RF-TiO$_2$ in Chapter 6. At this temperature, the CO/Ru atomic ratio was ~0.1 (see TD-XPS results, Figure 7-2b), indicating all (or almost all) of the ligands were removed from $H_4Ru_4(CO)_{12}$. Figure 7-4 shows the measured UPS spectra, Ru_4 difference spectrum, and UPS weighting factors. Results for Ru_3/RF-TiO$_2$ from Chapter 6 are included as dotted lines for comparison.
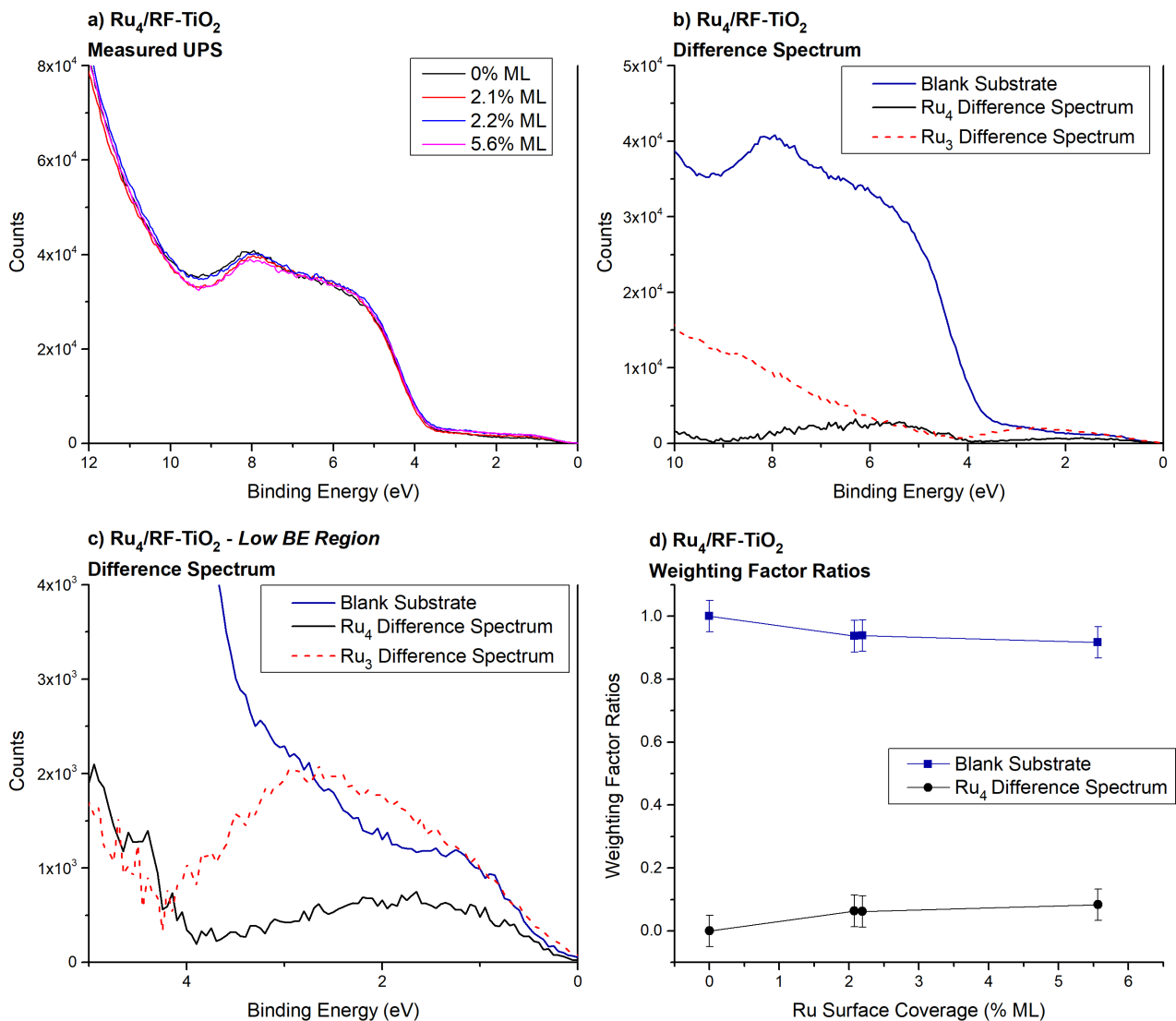
Figure 7-4: UPS results for the Ru4/RF-TiO2 deposition series. a) Measured UPS spectra. b) Ru4 difference spectrum compared to blank RF-TiO2 spectrum. The Ru3 difference spectrum from Ru3/RF-TiO2 is shown as a dotted line for comparison (data from Chapter 6). c) UPS data from (b), zoomed in to the low BE region. d) UPS weighting factor ratios for the Ru4 difference spectrum and blank substrate spectrum, plotted against Ru surface coverage. The uncertainty in the weighting factor ratios is ± 0.05.

The measured UPS spectra in Figure 7-4a are dominated by the RF-TiO2 substrate signal, but distinct changes can be observed between the blank and cluster-loaded samples due to the modification of the substrates by the Ru4 depositions. Figure 7-4b and Figure 7-4c show the Ru4 difference spectrum, which features an energy band starting at 0 eV and ending at ~3.9 eV. There is also a broad feature from 4.0 to 9.0 eV, which is most likely due to secondary electron contributions. Figure 7-4d shows that the weighting factor ratio of the Ru4 difference spectrum increases with Ru surface coverage, which provides evidence that the determined Ru4 difference spectrum is related to the deposition of Ru4 clusters.

The low BE energy band of the Ru_4 difference spectrum has a slightly different shape than Ru_3. The peak is at 1.8 eV for Ru_4 and 2.7 eV for Ru_3, and the energy band is slightly narrower for Ru_4 at ~3.9 eV wide compared to ~4.2 eV for Ru_3. Although the difference in peak position may appear significant, it seems most likely related to a slight change in band shape rather than a true shifted feature. The main differences between Ru_4 and Ru_3 difference spectra are in the higher BE region >6 eV, which is less reliable due to secondary electron effects. The differences between the 2 difference spectra are small, and possibly related to the accuracy inherent in determining the cluster difference spectra from a series of measured spectra which are dominated by the substrate signal.

7.4.5 MIES Results

In this study, UPS and MIES measurements were performed simultaneously. This was possible due to a 2000 Hz chopper in the path of a He* source and UV light (detailed in section 3.6.2.2). However, a MIES difference spectrum could not be determined for Ru_4, and thus the results are not shown. This was due to inter-sample differences in the MIES spectra where some samples had extra features not present on others. This is likely due to some degree of surface contamination being present, which appears strongly in MIES due to its sensitivity to only the topmost layer. In Chapter 6, a MIES Ru_3 difference spectrum was determined, where the success was due to better MIES spectrum consistency for Ru_3.

7.5 Discussions

7.5.1 Ru-CO Binding Sites

In the TD-XPS results (Figure 7-2), Ru_4/RF-TiO_2 is shown to have a large shift in both BE and CO/Ru ratio at lower temperatures than Ru_3/RF-TiO_2. Furthermore, Ru_4/RF-TiO_2 entered the transition temperature range where both symmetrical and asymmetrical peak doublets are needed for peak fitting at 323 K, while for Ru_3 this occurred at 373 K. This points towards $H_4Ru_4(CO)_{12}$ beginning de-ligation at a lower temperature, which may be due to the nature of the clusters or due to $H_4Ru_4(CO)_{12}$ being decomposed by heating to 353 K during the deposition. This implies that for the CO-TPD the low-temperature onset for CO desorption should be at a lower temperature for Ru_4/RF-TiO_2, but this not seen in the spectrum (Figure 7-3). This discrepancy may be due to the continuous temperature ramping of CO-TPD, compared to TD-XPS where distinct measurements were performed after heating for 10 minutes at each temperature. Due to this, the TD-XPS results are taken as being reliable in this case.

The 1st cycle CO-TPD spectra for Ru_4/RF-TiO_2 and Ru_3/RF-TiO_2 (Figure 7-3) are very similar, which implies that the Ru-CO binding sites are similar for both $H_4Ru_4(CO)_{12}$ and $Ru_3(CO)_{12}$ when supported on RF-TiO_2. However, some notable differences are that for Ru_4/RF-TiO_2 the medium-temperature peak is significantly more prominent, and the high-temperature peak has been shifted to a higher temperature by 70 K. This shifting indicates that the bonding for the high-temperature site is more stable for Ru_4, as more energy is required for desorption. In Chapter 4, section 4.4.3.1 it was argued that the low temperature feature in the 1st CO-TPD cycle for Ru_3 at was most likely from on-top binding positions (with μ_1 and/or μ_2 bond structures) while the high temperature feature was from μ_2 cluster-substrate bridging sites. Similar peak assigning can be applied to the 1st cycle CO-TPD for Ru_4/RF-TiO_2, where there are 300 K, 410 K, and 690 K peaks. Based on the previous arguments (see section 4.4.3.1) the 690 K peak was assigned to μ_2 cluster-substrate bridging sites. The medium temperature peak was significantly less prominent for Ru_3 and was not assigned. Considering the similarity in desorption temperature, both the 300 K and 410 K peaks for Ru_4 are assigned to on-top CO binding positions, where it is a possibility that the 300 K peak is related to μ_1 bonding and the 410 K peak is related to μ_2 bonding, where μ_2 requires more energy for bond dissociation [128]. This is proposed as the most likely bonding structure for the three binding sites, and a diagram showing examples of each of the binding sites is shown in Figure 7-5.
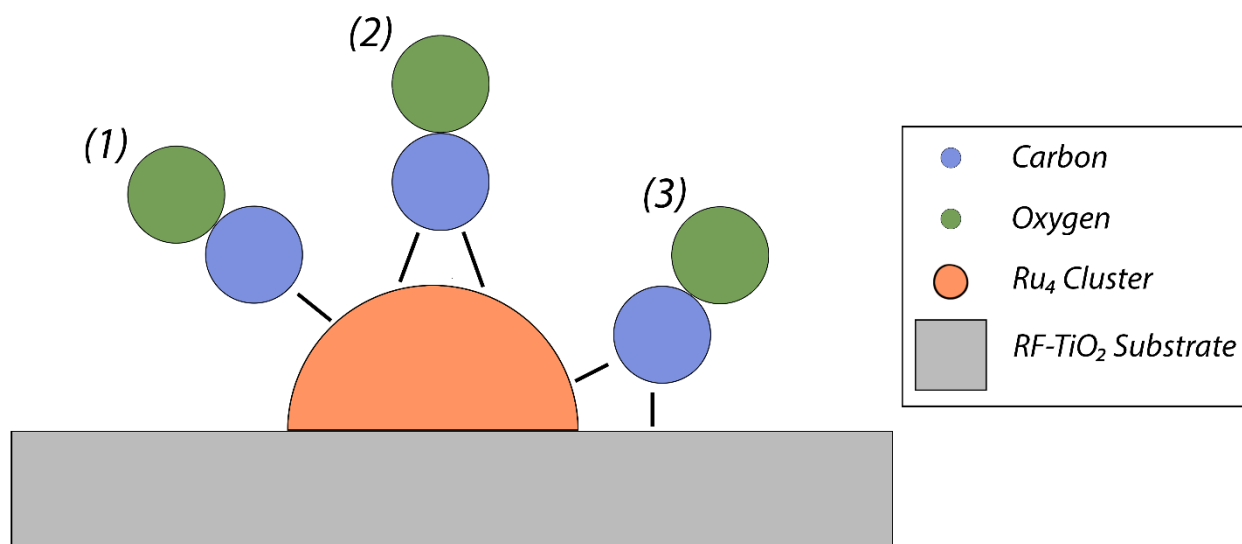
Figure 7-5: Diagram showing the most likely binding site candidates associated with the 3 desorption peaks seen in the CO-TPD spectrum of Ru$_4$/RF-TiO$_2$. (1) is an on-top position with μ$_1$ bonding, assigned to the 300 K peak. (2) is an on-top position with μ$_2$ bonding, assigned to the 410 K peak. (3) is a μ$_2$ cluster-substrate bridging site, assigned to the 690 K peak.

7.5.2 Cluster-Surface Interaction

The fact that all Ru-CO binding sites were blocked for Ru$_4$/RF-TiO$_2$ after the 1st CO-TPD heating cycle (Figure 7-3) points towards heat treatment causing the covering of clusters by substrate material, thereby blocking Ru-CO binding from occurring. These CO-TPD results match what occurred for Ru$_3$/RF-TiO$_2$ in Chapter 4; similarly, in that study all Ru-CO sites were lost after the 1st heating cycle. Chapter 5 provided further evidence to support the conclusion that substrate material was covering the Ru$_3$ clusters after heating. These conclusions were assisted by LEIS and AR-XPS measurements which were not available for Ru$_4$. However, the similarity of the TD-XPS, CO-TPD, and UPS results between the samples suggests the heating-induced encapsulation also occurred for Ru$_4$/RF-TiO$_2$. Figure 7-6 shows a diagram of the cluster and surface before and after heat treatment, where heat treatment results in the encapsulation of the clusters. Chapter 6 showed the titania overlayer was a reduced form of titania, which matches previously reported findings for the encapsulation reaction of metal adsorbates atop TiO$_2$ [185, 186, 207, 208, 210-213, 216, 386].

Ru on Surface *Heat Treatment* *Encapsulated Ru*

Ru$_4$/RF-TiO$_2$ Ru$_4$/RF-TiO$_2$
Ligated clusters
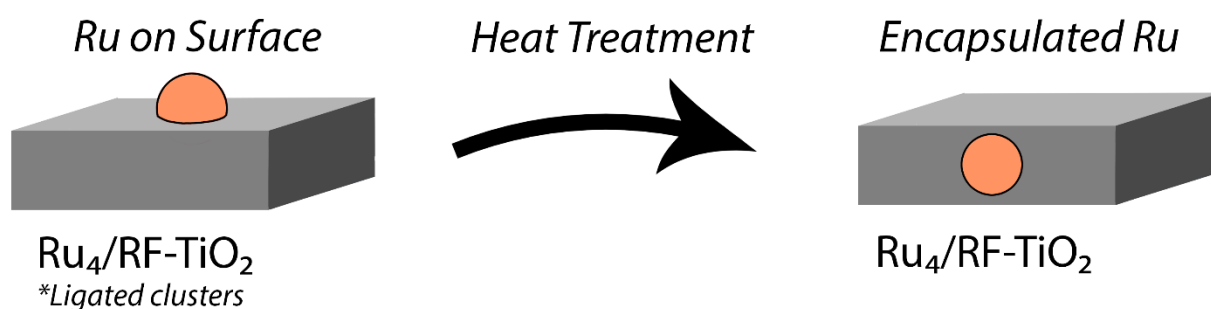
Figure 7-6: Diagram showing the results regarding the encapsulation of Ru$_4$/RF-TiO$_2$, before and after heat treatment to 723 K.

The UPS difference spectra for Ru$_4$ and Ru$_3$ are very similar, with only a slightly different shape in the low BE band (Figure 7-4c). In both cases the UPS onset is at 0 eV, providing evidence the supported Ru$_4$ and Ru$_3$ clusters have metallic states [61, 437, 440-442]. This is interesting because metal clusters are generally known for their molecule-like discrete electron levels and lack of metallic properties [13]. In Chapter 6, it was shown RF-TiO$_2$-supported Pt$_3$ clusters had non-metallic characteristics, while Ru$_3$ was metallic. This suggests the occurrence of metallic states is most likely related to the SMSI between Ru$_4$ and RF-TiO$_2$.

In Chapter 5 it was shown that heating causes a partial oxidation of the Ru$_3$ clusters (by XPS comparison to a size-selected, CS-deposited Ru$_3$ sample). However, this is not visible in the Ru$_4$/RF-TiO$_2$ TD-XPS results (Figure 7-2a) because the BE shifting with heat treatment was dominated by the effects of CO ligand removal. However, the similarity of the BEs after heating to 873 K (Figure 7-2a) implies Ru$_4$ clusters are oxidised in the same way. These results do not show whether the clusters remain as bare 4-atom clusters, agglomerate, or break apart after heating to remove the ligands.

7.5.3 Properties of Ru$_4$ Compared to Ru$_3$

The TD-XPS, CO-TPD, and UPS results were very similar between Ru$_4$/RF-TiO$_2$ and Ru$_3$/RF-TiO$_2$. The main difference between the cluster types was the onset temperature for CO de-ligation, which was slightly lower for Ru$_4$. However, after heating the similarity of the low BE region in UPS provides evidence that the effect of the CVD of Ru$_4$ on the valence electron structure of RF-TiO$_2$ is very similar to that of Ru$_3$. This suggests that the encapsulation reaction is the dominating factor in determining the properties of the clusters after heating. It may also be the case that the cluster size difference of Ru$_4$ compared to Ru$_3$ was too small to detect a noticeable difference with the techniques used. It is possible that

the difference may have been more noticeable in the UPS and other results for a larger change in cluster size. However, the change in DOS of supported clusters with cluster size is difficult to predict due to both the discrete energy levels of clusters in vacuum, as well as the possible effect of the SMSI for clusters on metal-oxide supports [185, 201, 202].

There are not any previously published studies on titania-supported $H_4Ru_4(CO)_{12}$ to compare the results to. Comparisons between similar titania-supported $Ru_3(CO)_{12}$ results and previous literature can be found in the earlier chapters (sections 4.4.3, 5.4.6, 6.5). DFT calculations of Ru_4 clusters on RF-TiO_2 substrates would be ideal for the discussion on the DOS, but to the best knowledge of the author there are no such published results. Outside of Ru clusters, Krishnan *et al.* [3] have comparably reported only a small difference in UPS measurements for similarly-sized TiO_2-supported Au_9 and Au_{13} clusters (deposited by solution submersion with diphenylphosphino-protected clusters and heated to remove ligands), where Au_{13} was shifted closer to the Fermi level by only ~0.1 eV. However, in that study the clusters were not metallised on the substrate like Ru_4 was in this study, so these results are not directly comparable. Other experimental studies on CS-deposited, size-selected clusters have shown a trend for the cluster DOS to extend towards the Fermi level as cluster size increases, becoming more bulk-like for $Pd_n/TiO_2(110)$ [60], $Pt_n/Ag(110)$ [455], $Pd_n/Ag(110)$ [455]. This phenomenon does not hold for the case of Ru_3 and Ru_4 on RF-TiO_2, most likely due to the metallisation and encapsulation of the clusters.

Considering the properties of Ru_4/RF-TiO_2 and Ru_3/RF-TiO_2 were found to be very similar after heating suggests that clusters deposited onto sputter-treated RF-TiO_2 using $H_4Ru_4(CO)_{12}$ have the same potential uses as $Ru_3(CO)_{12}$. Notably, Ru clusters are particularly active catalysts for industry and environment-relevant reactions such as CO and CO_2 hydrogenation [43-47, 49-51, 53, 54]. It is a possibility the reduction in CO adsorption capacity due to cluster encapsulation may reduce the capacity for CO hydrogenation [185, 186, 213]. Alternatively, there have been cases showing an electronic structure which is suitable for photocatalysis without direct reactant-cluster contact [4, 397, 398], where cluster encapsulation can include additional benefits such as an increase in resistance to cluster agglomeration [4, 397], increase in photocatalytic reaction selectivity [398], and an increase in photocatalytic activity by hindering back reactions [4]. As such, measurements are necessary to determine the photocatalytic abilities of the Ru_4/RF-TiO_2.

7.6 Conclusions

Ru_4 was deposited onto Ar^+ ion sputter-treated $RF-TiO_2$ substrates by the CVD of $H_4Ru_4(CO)_{12}$. Separate samples were prepared for analysis with TD-XPS, CO-TPD, and UPS. The results indicated that after heating to 723 K for the 1st CO-TPD cycle, all Ru-CO sites were lost due to the encapsulation of the Ru_4 clusters by the $RF-TiO_2$ substrate. UPS showed that after heating to 723 K Ru_4 clusters have metallic properties, unlike what is generally expected for non-supported metal clusters. These results are very similar to previously reported (Chapter 4 to Chapter 6) results for CVD-deposited $Ru_3(CO)_{12}$ on $RF-TiO_2$ ($Ru_3/RF-TiO_2$). One notable difference between the clusters is that Ru_4 appears to desorb CO at a lower temperature than Ru_3 based on TD-XPS results. After heating to 723 K, UPS shows that the valence electronic structures of the supported clusters are very similar. The similarity after heating suggests that Ru_4 has the same potential catalytic benefits as Ru_3, including use in the photocatalytic water splitting reaction. Studying the temperature stability and valence electronic structure of supported clusters works towards the goal of using such catalytic systems for technical or industrial applications.

Chapter 8   Concluding Remarks

There is a trend in catalysis research for catalytic materials to be decreased in size towards the single-atom limit, where the active catalyst is present in only the topmost layer [40-42]. Metal clusters form part of this trend and are a rapidly growing area of interest [2-11] with the main motivation of cluster research being their potential use in catalysis and photocatalysis [4, 10, 56]. Recent cluster research has focussed on aspects such as cluster morphology, size, surface interaction, mobility, catalytic and photocatalytic properties, and electronic properties, as well as how these different aspects affect one another [20-39]. The DOS for some supported clusters have been previously measured using UPS and/or MIES [3, 5, 6, 57, 60, 73, 102, 292, 315], but exhaustive DOS measurements have not been performed for many types of supported clusters including small Ru clusters.

The significant original contribution to knowledge in this thesis is the measurements and analysis of the surface properties and electronic structures of surface-supported Ru_3 clusters on RF-sputter deposited titania (RF-TiO_2) substrates, as well as comparisons to other systems. Small Ru clusters were chosen as they display promise for catalysis, being efficient catalysts for the hydrogenation of CO and CO_2 [43-55]. RF-TiO_2 substrates were chosen as a cost-effective, more industry-applicable alternative to the TiO_2(110) single crystal which is typically used in studies on titania-supported clusters.

The focus of this thesis was on experimental measurements of the Ru_3 temperature stability, electronic DOS, oxidation properties, and details about the cluster-surface interaction when supported on RF-TiO_2. An additional goal was to compare the results using different deposition methods, as no previous studies comparing clusters of the same size deposited using different methods had been undertaken. To do this Ru_3 was deposited by; solution submersion of $Ru_3(CO)_{12}$, CVD of $Ru_3(CO)_{12}$, and cluster source (CS) deposition of bare Ru_3. To extend the study, results for Pt_3 clusters and Ru_4 clusters were compared to Ru_3 in Chapter 6 and Chapter 7, respectively.

8.1 Summary of Conclusions

In Chapter 4 and Chapter 5 evidence was established showing that Ru_3 clusters are encapsulated when supported on sputter-treated RF-TiO_2. It was firstly shown, using CO-TPD, that after heat-treatment of Ru_3 on non-sputtered RF-TiO_2, the main Ru-CO binding site was blocked while other Ru-CO sites remained. However, sputter-treated RF-TiO_2 resulted in the complete blocking of all Ru-CO sites for CS-deposited Ru_3 with no heat-

treatment required. For CVD-deposited $Ru_3(CO)_{12}$ heat-treatment was required before sites were blocked, presumably due to the loss of the protecting CO ligands. The mechanism for complete blocking of Ru-CO sites could not be initially determined in Chapter 4. This influenced the studies undertaken in Chapter 5, where ARXPS and LEIS results supported the interpretation that the loss of Ru-CO sites was due to cluster encapsulation. TD-LEIS results showed $Ru_3(CO)_{12}$ on sputter-treated $RF\text{-}TiO_2$ was encapsulated by a 0.35 nm ± 0.08 nm titania overlayer after heating, which is a thin enough overlayer for potential catalytic reactions to take place. In Chapter 6 MIES was used to measure the overlayer encapsulating the Ru_3, and provided evidence that the overlayer was composed of reduced titania with a bonding structure such as Ru-Ti-O. This aligns with previous studies of metal adsorbates encapsulated by titania [185, 186, 207, 208, 210-213, 216, 386]. For Pt_3 on sputter-treated $RF\text{-}TiO_2$, UPS and MIES conversely provided evidence Pt was present on the top-most layer and was not encapsulated. The most likely reason for the difference in cluster-surface interaction between Ru_3 and Pt_3 was an energetic benefit for Ru encapsulation related to the minimisation of surface energy.

It was shown with XPS in Chapter 4 and Chapter 5 that heating Ru_3 clusters on $RF\text{-}TiO_2$ results in partially oxidised Ru clusters, which occurs on both sputter-treated and non-sputtered $RF\text{-}TiO_2$. Furthermore, the initial Ru 3d BE of the Ru_3 clusters differed depending on the deposition method (solution, CVD, or CS), but heating to 723-873 K negated this difference and the BEs became identical, within experimental accuracy, suggesting that the oxidation state of the clusters was the same after heat treatment. The similarity of electronic properties was supported by UPS and MIES results in Chapter 6, showing that the electronic DOSs for solution-deposited Ru_3 and CVD-deposited Ru_3 on sputter-treated $RF\text{-}TiO_2$ were very similar after heat-treatment. This suggests that if the Ru_3 clusters are to be heated, the specific type of deposition method used would not be an important consideration for the production of catalytic materials.

A notable achievement in Chapter 6 was the measurement of the valence electronic DOS for both Ru_3 and Pt_3 supported on sputter-treated $RF\text{-}TiO_2$. Based on experimental measurements of supported clusters, valence spectra were determined for UPS and MIES which were associated with the cluster depositions (and not contributions from the blank substrate). These showed that after heat treatment Ru_3 has metallic properties and Pt_3 has non-metallic properties. The metallic properties of Ru_3 may be related to the encapsulation and or/ oxidation of the clusters. Measurements of the DOS for small clusters such as this are vital for comparison to DFT measurements, the understanding of catalytic reactions, and

the design of efficient catalytic materials.

To test the effects of changing the Ru_3 cluster size by one atom to Ru_4, Chapter 7 involved various complementary measurements of CVD-deposited Ru_4 ($H_4Ru_4(CO)_{12}$) on sputter-treated RF-TiO_2. The results were similar to those reported for CVD-deposited $Ru_3(CO)_{12}$ in earlier chapters. The main difference, based on TD-XPS, was that Ru_4 begins desorbing ligands at a slightly lower temperature than Ru_3, likely related to the loss of H bridging ligands. It was shown that Ru_4 is encapsulated when heat-treated and has an electronic DOS with very similar features to Ru_3. This suggests that the catalytic potentials of Ru_3 and Ru_4 are most likely similar when supported on sputter-treated RF-TiO_2.

8.2 Potential for Future Research

Throughout this study much was learnt about Ru clusters, especially regarding the encapsulation of Ru_n by RF-TiO_2. However, one important question which was not resolved was: what is the structure of the Ru_n clusters after being encapsulated by sputter-treated RF-TiO_2? It is not clear whether the clusters remain as size-selected clusters beneath the overlayer, or whether they are agglomerated or dissociated. To remedy this, a future experiment should be devised to determine the structure of the clusters. For example, the Ru_n clusters could be analysed using scanning transmission electron microscopy (STEM), which would help with identifying the size of the clusters after encapsulation. However, the Ru_n/RF-TiO_2 system would be problematic using STEM, because this requires the sample to be thin enough for electrons to pass through [334, 337, 338], and RF-TiO_2 is present as a layer atop on a thick, bulk-scale SiO_2 wafer. An alternative methodology to solve this issue would be to deposit Ru_n onto titania nanoparticles, such as P25, as nanoparticles can be measured using STEM. For the deposition of clusters onto titania nanoparticles, solution submersion is often used by suspending the substrate nanoparticles in a solution of the clusters and stirring [10, 73, 100, 102, 103, 132-134]. This experimental work would be an ideal continuation of the work performed in this thesis, and the understanding of Ru cluster size after encapsulation would be beneficial due to the often size-dependent nature of metal cluster catalysis. It would have to be noted, however, that measurements on titania nanoparticles would not be directly comparable to those on RF-TiO_2 because a difference in the cluster-surface interaction may be observed.

A second avenue for future research opened by the work presented herein is the photocatalytic measurements of RF-TiO_2-supported Ru_n clusters. Such a course of study would be warranted as the encapsulation of Ru_3 and Ru_4 clusters by sputter-treated RF-

TiO$_2$ may provide an advantage for photocatalysis applications. A previous study on Au$_n$-loaded BaLa$_4$Ti$_4$O$_{15}$ showed than when encapsulated by a chromium oxide overlayer, Au$_n$ was stabilised against agglomeration and received a photocatalytic benefit for water splitting by decreasing the back-reaction rate, even when thicker overlayers were present than those of Ru$_3$/RF-TiO$_2$ in this study [4, 146]. The water splitting reaction has notably received great attention in photocatalysis research as it is a potential source of H$_2$, and a potential green fuel source [4, 10, 34, 36, 146, 271]. Thus, the encapsulation of Ru$_n$ by RF-TiO$_2$ opens a pathway for photocatalytic water splitting measurements of the Ru$_n$/RF-TiO$_2$ systems. With a well-designed reaction vessel, reactions such as photocatalytic water splitting as well as the catalytic hydrogenation of CO could be tested for potential benefits using encapsulated Ru clusters. While instrumentation for such measurements was not available at Flinders University, it is hoped these studies will inspire further research on the materials.

In this thesis it was demonstrated that UPS and MIES could be used collectively to measure the DOS for an encapsulated cluster and overlayer, respectively. By extension this leads to an idea that the unique surface sensitivity of MIES would work well in tandem with catalysis measurements to probe individual reaction steps. For such an experiment a gas molecule such as H$_2$O could be introduced onto supported clusters, and UPS and MIES measurements would be performed before and after dosing. Since MIES only measures atoms on the top-most layer it could be used to probe how the electronic DOS of an adsorbed molecule changes due to its adsorption to clusters. This type of measurement could be performed with Ru$_3$/RF-TiO$_2$, or any other cluster/substrate combination showing catalytic or photocatalytic potential. While other surface-sensitive measurements of gaseous molecules adsorbed to metal clusters have been performed, such as ion scattering showing the molecule attachment [154, 331, 469], to the best knowledge of the author measurements have not been performed measuring the DOS of the top layer only. This may provide an experimental path for probing individual steps in catalytic reactions, which could further the understanding of catalysis by small metal clusters and in turn allow for the production of more efficient, cheaper catalysts for use in industrial and environmental settings.

Chapter 9   References

[1] M. Wilson, K. Kannangara, G. Smith, M. Simmons, B. Raguse, Nanotechnology: basic science and emerging technologies, CRC press, Boca Raton, Florida, 2002.

[2] S.J. Carroll, S.G. Hall, R.E. Palmer, R. Smith, Energetic Impact of Size- Selected Metal Cluster Ions on Graphite, Phys. Rev. Lett. 81 (1998) 3715-3718.

[3] G. Krishnan, N. Eom, R.M. Kirk, V.B. Golovko, G.F. Metha, G.G. Andersson, Investigation of Phosphine Ligand Protected Au13 Clusters on Defect Rich Titania, J. Phys. Chem. C 123 (2019) 6642−6649.

[4] W. Kurashige, R. Kumazawa, D. Ishii, R. Hayashi, Y. Niihori, S. Hossain, L.V. Nair, T. Takayama, A. Iwase, S. Yamazoe, T. Tsukuda, A. Kudo, Y. Negishi, Au25-Loaded BaLa4Ti4O15 Water-Splitting Photocatalyst with Enhanced Activity and Durability Produced Using New Chromium Oxide Shell Formation Method, J. Phys. Chem. C 122 (2018) 13669-13681.

[5] G. Krishnan, H.S. Al Qahtani, J. Li, Y. Yin, N. Eom, V.B. Golovko, G.F. Metha, G.G. Andersson, Investigation of Ligand-Stabilized Gold Clusters on Defect-Rich Titania, J. Phys. Chem. C 121 (2017) 28007-28016.

[6] A.C. Reber, S.N. Khanna, F.S. Roberts, S.L. Anderson, Effect of O2 and CO Exposure on the Photoelectron Spectroscopy of Size-Selected Pd n Clusters Supported on TiO2 (110), J. Phys. Chem. C 120 (2016) 2126-2138.

[7] R. Passalacqua, S. Parathoner, G. Centi, A. Halder, E.C. Tyo, B. Yang, S. Seifert, S. Vajda, Electrochemical behaviour of naked sub-nanometre sized copper clusters and effect of CO2, Catal. Sci. Technol. 6 (2016) 6977-6985.

[8] Z. Luo, A. Castleman Jr, S.N. Khanna, Reactivity of metal clusters, Chem. Rev. 116 (2016) 14456-14492.

[9] Y. Dai, T.J. Gorey, S.L. Anderson, S. Lee, S. Lee, S. Seifert, R.E. Winans, Inherent size effects on XANES of nanometer metal clusters: size-selected platinum clusters on silica, J. Phys. Chem. C 121 (2017) 361-374.

[10] Y. Negishi, Y. Matsuura, R. Tomizawa, W. Kurashige, Y. Niihori, T. Takayama, A. Iwase, A. Kudo, Controlled Loading of Small Au n Clusters (n= 10–39) onto BaLa4Ti4O15 Photocatalysts: Toward an Understanding of Size Effect of Cocatalyst on Water-Splitting Photocatalytic Activity, J. Phys. Chem. C 119 (2015) 11224-11232.

[11] C.P. Joshi, M.S. Bootharaju, O.M. Bakr, Tuning properties in silver clusters, J. Phys. Chem. Lett. 6 (2015) 3023-3035.

[12] A. Dollinger, C.H. Strobel, H. Bleuel, A. Marsteller, G. Gantefoer, D.H. Fairbrother, X. Tang, K.H. Bowen, Y.D. Kim, Growth modes of thin films of ligand- free metal clusters, J. Appl. Phys. 117 (2015) 195302.

[13] H. Li, L. Li, Y. Li, The electronic structure and geometric structure of nanoclusters as catalytic active sites, Nanotechnol. Rev. 2 (2013) 515-528.

[14] D. Lee, R.L. Donkers, G. Wang, A.S. Harper, R.W. Murray, Electrochemistry and optical absorbance and luminescence of molecule-like Au38 nanoparticles, J. Am. Chem. Soc. 126 (2004) 6193-6199.

[15] J. Jung, H. Kim, Y.-K. Han, Can an electron-shell closing model explain the structure and stability of ligand-stabilized metal clusters?, J. Am. Chem. Soc. 133 (2011) 6090-6095.

[16] G. Ramakrishna, O. Varnavski, J. Kim, D. Lee, T. Goodson, Quantum-sized gold clusters as efficient two-photon absorbers, J. Am. Chem. Soc. 130 (2008) 5032-5033.

[17] M. Valden, X. Lai, D.W. Goodman, Onset of catalytic activity of gold clusters on titania with the appearance of nonmetallic properties, Science 281 (1998) 1647-1650.

[18] C. Xu, X. Lai, G. Zajac, D. Goodman, Scanning tunneling microscopy studies of the TiO2 (110) surface: structure and the nucleation growth of Pd, Phys. Rev. B 56 (1997) 13464.

[19] N. Ortiz, S.E. Skrabalak, On the Dual Roles of Ligands in the Synthesis of Colloidal Metal Nanostructures, Langmuir 30 (2014) 6649-6659.

[20] G.E. Johnson, R. Colby, J. Laskin, Soft landing of bare nanoparticles with controlled size, composition, and morphology, Nanoscale 7 (2015) 3491-3503.

[21] R. Nielsen, S. Murphy, C. Strebel, M. Johansson, I. Chorkendorff, J. Nielsen, The morphology of mass selected ruthenium nanoparticles from a magnetron- sputter gas-aggregation source, J. Nanopart. Res. 12 (2010) 1249-1262.

[22] A.A. Herzing, C.J. Kiely, A.F. Carley, P. Landon, G.J. Hutchings, Identification of active gold nanoclusters on iron oxide supports for CO oxidation, Science 321 (2008) 1331.

[23] M. Chen, D. Goodman, The structure of catalytically active gold on titania, Science 306 (2004) 252-255.

[24] M. Mason, L. Gerenser, S.-T. Lee, Electronic structure of catalytic metal clusters studied by X-ray photoemission spectroscopy, Phys. Rev. Lett. 39 (1977) 288.

[25] C.-C. Hou, H.-F. Wang, C. Li, Q. Xu, From metal–organic frameworks to single/dual-atom and cluster metal catalysts for energy applications, Energy Environ. Sci. 13 (2020) 1658-1693.

[26] F.X. Xiao, S.F. Hung, J. Miao, H.Y. Wang, H. Yang, B. Liu, Metal-Cluster-Decorated TiO2 Nanotube Arrays: A Composite Heterostructure toward Versatile Photocatalytic and Photoelectrochemical Applications, Small 11 (2015) 554-567.

[27] J. Li, W. Wang, W. Chen, Q. Gong, J. Luo, R. Lin, H. Xin, H. Zhang, D. Wang, Q. Peng, Sub-nm ruthenium cluster as an efficient and robust catalyst for decomposition and synthesis of ammonia: Break the "size shackles", Nano Res. 11 (2018) 4774-4785.

[28] J. Xu, T. Liu, J. Li, B. Li, Y. Liu, B. Zhang, D. Xiong, I. Amorim, W. Li, L. Liu, Boosting the hydrogen evolution performance of ruthenium clusters through synergistic coupling with cobalt phosphide, Energy Environ. Sci. 11 (2018) 1819-1827.

[29] X.-C. Hu, X.-P. Fu, W.-W. Wang, X. Wang, K. Wu, R. Si, C. Ma, C.-J. Jia, C.-H. Yan, Ceria-supported ruthenium clusters transforming from isolated single atoms for hydrogen production via decomposition of ammonia, Appl. Catal. B 268 (2020) 118424.

[30] K. Miura, F. Kimata, R. Watanabe, C. Fukuhara, Theoretical study of the oxygen adsorption energy for the supported Pt cluster, focused on the electronic metal-support interaction, Surf. Sci. 704 (2021) 121747.

[31] S. Vajda, M.G. White, Catalysis applications of size-selected cluster deposition, ACS Catal. 5 (2015) 7152-7176.

[32] C. Cui, Z. Luo, J. Yao, Enhanced catalysis of Pt3 clusters supported on graphene for N–H bond dissociation, CCS Chemistry (2019) 215-225.

[33] C. Dong, Y. Li, D. Cheng, M. Zhang, J. Liu, Y.-G. Wang, D. Xiao, D. Ma, Supported Metal Clusters: Fabrication and Application in Heterogeneous Catalysis, ACS Catal. 10 (2020) 11011-11045.

[34] S. Sultan, J.N. Tiwari, A.N. Singh, S. Zhumagali, M. Ha, C.W. Myung, P. Thangavel, K.S. Kim, Single atoms and clusters based nanomaterials for hydrogen evolution, oxygen evolution reactions, and full water splitting, Adv. Energy Mater. 9 (2019) 1900624.

[35] D. Wang, Z.-P. Liu, W.-M. Yang, Revealing the size effect of platinum cocatalyst for photocatalytic hydrogen evolution on TiO2 support: a DFT study, ACS Catal. 8 (2018) 7270-7278.

[36] Q. Wu, S. Xiong, P. Shen, S. Zhao, Y. Li, D. Su, A. Orlov, Exceptional activity of sub-nm Pt clusters on CdS for photocatalytic hydrogen production: a combined experimental and first-principles study, Catal. Sci. Technol. 5 (2015) 2059-2064.

[37] C. Witt, J.M. Dieterich, B. Hartke, Cluster structures influenced by interaction with a surface, Phys. Chem. Chem. Phys. 20 (2018) 15661-15670.

[38] K. Katsiev, G. Harrison, Y. Al-Salik, G. Thornton, H. Idriss, Gold Cluster Coverage Effect on H2 Production over Rutile TiO2 (110), ACS Catal. 9 (2019) 8294-8305.

[39] Z. Wu, Y. Li, W. Huang, Size-Dependent Pt-TiO2 Strong Metal-Support Interaction, J. Phys. Chem. Lett. (2020).

[40] X.-F. Yang, A. Wang, B. Qiao, J. Li, J. Liu, T. Zhang, Single-atom catalysts: a new frontier in heterogeneous catalysis, Acc. Chem. Res. 46 (2013) 1740-1748.

[41] J.M. Thomas, Tens of thousands of atoms replaced by one, Nature 525 (2015) 325.

[42] H. Wei, X. Liu, A. Wang, L. Zhang, B. Qiao, X. Yang, Y. Huang, S. Miao, J. Liu, T. Zhang, FeO x-supported platinum single-atom and pseudo-single-atom catalysts for chemoselective hydrogenation of functionalized nitroarenes, Nat. Commun. 5 (2014) 5634.

[43] C. Moreno-Castilla, M.A. Salas-Peregrín, F.J. López-Garzón, Hydrogenation of carbon oxides by Ru/activated carbon catalysts obtained from Ru3(CO)12: effect of pretreatment on their dispersion, composition and activity, J. Mol. Catal. A: Chem. 95 (1995) 223-233.

[44] G.D. Weatherbee, C.H. Bartholomew, Hydrogenation of CO2 on group VIII metals: IV. Specific activities and selectivities of silica-supported Co, Fe, and Ru, J. Catal. 87 (1984) 352-362.

[45] K. Asakura, Y. Iwasawa, Surface structure and catalysis for CO hydrogenation of the supported Ru species derived from the Ru3(CO)12 inorganic oxides, J. Chem. Soc., Faraday Trans. 86 (1990)

2657-2662.

[46] F. Solymosi, A. Erdöhelyi, M. Kocsis, Methanation of CO2 on supported Ru catalysts, J. Chem. Soc., Faraday Trans. 1 77 (1981) 1003-1012.

[47] W.R. Hastings, C.J. Cameron, M.J. Thomas, M.C. Baird, Carbon monoxide and carbon dioxide hydrogenation catalyzed by supported ruthenium carbonyl clusters. A novel procedure for encapsulating triruthenium dodecacarbonyl within the pores of Na-Y zeolite, Inorg. Chem. 27 (1988) 3024-3028.

[48] D.L. King, A Fischer-Tropsch study of supported ruthenium catalysts, J. Catal. 51 (1978) 386-397.

[49] C.S. Kellner, A.T. Bell, Effects of dispersion on the activity and selectivity of alumina-supported ruthenium catalysts for carbon monoxide hydrogenation, J. Catal. 75 (1982) 251-261.

[50] R.D. Gonzalez, H. Miura, Methanation and Fischer-Tropsch studies on potassium-promoted silica-supported Ru catalysts, J. Catal. 77 (1982) 338-347.

[51] E. Kikuchi, H. Nomura, M. Matsumoto, Y. Morita, Fischer-tropsch synthesis of hydrocarbons on V2O3-supported ruthenium catalysts, Appl. Catal. 7 (1983) 1-9.

[52] K. Fujimoto, T. Nobusawa, T. Fukushima, H.-o. Tominaga, Activity and selectivity regulation of synthesis gas reaction over supported ruthenium catalysts, Bull. Chem. Soc. Jpn. 58 (1985) 3164-3171.

[53] P. Panagiotopoulou, Hydrogenation of CO2 over supported noble metal catalysts, Appl. Catal. A 542 (2017) 63-70.

[54] R. Mutschler, E. Moioli, A. Züttel, Modelling the CO2 hydrogenation reaction over Co, Ni and Ru/Al2O3, J. Catal. 375 (2019) 193-201.

[55] J.M.G. Carballo, J. Yang, A. Holmen, S. García-Rodríguez, S. Rojas, M. Ojeda, J.L.G. Fierro, Catalytic effects of ruthenium particle size on the Fischer–Tropsch Synthesis, J. Catal. 284 (2011) 102-108.

[56] A. Sanchez, S. Abbet, U. Heiz, W.D. Schneider, H. Hakkinen, R.N. Barnett, U. Landman, When gold is not noble: nanoscale gold catalysts, J. Phys. Chem. A 103 (1999) 9573.

[57] F.S. Roberts, M.D. Kane, E.T. Baxter, S.L. Anderson, Oxygen activation and CO oxidation over size-selected Pt n/alumina/Re (0001) model catalysts: correlations with valence electronic structure, physical structure, and binding sites, Phys. Chem. Chem. Phys. 16 (2014) 26443-26457.

[58] H. Häkkinen, S. Abbet, A. Sanchez, U. Heiz, U. Landman, Structural, electronic, and impurity-doping effects in nanoscale chemistry: supported gold nanoclusters, Angew. Chem. Int. Ed. 42 (2003) 1297-1300.

[59] M. Kuno, Introductory nanoscience: Physical and chemical concepts, 1 ed., Garland Science, New York, 2011.

[60] F.S. Roberts, S.L. Anderson, A.C. Reber, S.N. Khanna, Initial and Final State Effects in the Ultraviolet and X-ray Photoelectron Spectroscopy (UPS and XPS) of Size-Selected Pd n Clusters Supported on TiO2 (110), J. Phys. Chem. C 119 (2015) 6033-6046.

[61] C. Mead, W. Spitzer, Fermi level position at semiconductor surfaces, Phys. Rev. Lett. 10 (1963) 471.

[62] M.I. Bruce, B.K. Nicholson, Cluster chemistry: XXIII. Mono-, di-and tri-auration of H4Ru4 (CO) 12 with [{Au (PPh3)} 3O][BF4]: X-ray crystal structure of HRu4Au3 (CO) 12 (PPh3) 3, J. Organomet. Chem. 252 (1983) 243-255.

[63] Z.W. Wang, O. Toikkanen, B.M. Quinn, R.E. Palmer, Real-Space Observation of Prolate Monolayer-Protected Au38 Clusters Using Aberration-Corrected Scanning Transmission Electron Microscopy, Small 7 (2011) 1542-1545.

[64] S. Van Aert, K.J. Batenburg, M.D. Rossell, R. Erni, G. Van Tendeloo, Three-dimensional atomic imaging of crystalline nanoparticles, Nature 470 (2011) 374.

[65] B. Yoon, H. Häkkinen, U. Landman, A.S. Wörz, J.-M. Antonietti, S. Abbet, K. Judai, U. Heiz, Charging effects on bonding and catalyzed oxidation of CO on Au8 clusters on MgO, Science 307 (2005) 403-407.

[66] H.S. Al Qahtani, K. Kimoto, T. Bennett, J.F. Alvino, G.G. Andersson, G.F. Metha, V.B. Golovko, T. Sasaki, T. Nakayama, Atomically resolved structure of ligand-protected Au9 clusters on TiO2 nanosheets using aberration-corrected STEM, J. Chem. Phys. 144 (2016) 114703.

[67] Y. Fukamori, M. König, B. Yoon, B. Wang, F. Esch, U. Heiz, U. Landman, Fundamental Insight into the Substrate-Dependent Ripening of Monodisperse Clusters, ChemCatChem 5 (2013) 3330-3341.

[68] J. Ramsden, Nanotechnology: an introduction, 1 ed., William Andrew, Oxford, UK, 2011.

[69] C. Campbell, J. Sellers, Anchored metal nanoparticles: Effects of support and size on their energy, sintering resistance and reactivity, Faraday Discuss. 162 (2013) 9-30.

[70] C.T. Campbell, The energetics of supported metal nanoparticles: relationships to sintering rates and catalytic activity, Acc. Chem. Res. 46 (2013) 1712-1719.

[71] B. Wortmann, K. Mende, S. Duffe, N. Grönhagen, B. Von Issendorff, H. Hövel, Ultraviolet photoelectron spectroscopy of supported mass selected silver clusters, Phys. Status Solidi B 247 (2010) 1116-1121.

[72] H.S. Al Qahtani, R. Higuchi, T. Sasaki, J.F. Alvino, G.F. Metha, V.B. Golovko, R. Adnan, G.G. Andersson, T. Nakayama, Grouping and aggregation of ligand protected Au9 clusters on TiO2 nanosheets, RSC Adv. 6 (2016) 110765-110774.

[73] D.P. Anderson, J.F. Alvino, A. Gentleman, H.A. Qahtani, L. Thomsen, M.I.J. Polson, G.F. Metha, V.B. Golovko, G.G. Andersson, Chemically-synthesised, atomically-precise gold clusters deposited and activated on titania, Phys. Chem. Chem. Phys. 15 (2013) 3917.

[74] D. Meier, G. Rizzi, G. Granozzi, X. Lai, D. Goodman, Ru3(CO)12 adsorption and decomposition on TiO2, Langmuir 18 (2002) 698-705.

[75] X. Zhao, J. Hrbek, J.A. Rodriguez, The decomposition and chemistry of Ru3(CO)12 on TiO2 (110) studied with X-ray photoelectron spectroscopy and temperature programmed desorption, Surf. Sci. 575 (2005) 115-124.

[76] Y. Liu, H. Tsunoyama, T. Akita, T. Tsukuda, Preparation of~ 1 nm gold clusters confined within mesoporous silica and microwave-assisted catalytic application for alcohol oxidation, J. Phys. Chem. C 113 (2009) 13457-13461.

[77] W. Zhou, J.M. Thomas, D.S. Shephard, B.F. Johnson, D. Ozkaya, T. Maschmeyer, R.G. Bell, Q. Ge, Ordering of ruthenium cluster carbonyls in mesoporous silica, Science 280 (1998) 705-708.

[78] B. Gates, Supported metal clusters: synthesis, structure, and catalysis, Chem. Rev. 95 (1995) 511-522.

[79] B. Gates, Supported metal cluster catalysts, J. Mol. Catal. A: Chem. 163 (2000) 55-65.

[80] D. Chandra, M. Garner, K. Lau, Vapor pressures of osmium, rhodium, and ruthenium carbonyls, J. Phase. Equilib. 20 (1999) 565-572.

[81] S. Saha, B. Captain, Synthesis and Structural Characterization of Ruthenium Carbonyl Cluster Complexes Containing Platinum with a Bulky N-Heterocyclic Carbene Ligand, Inorg. Chem. 53 (2014) 1210-1216.

[82] F. Hoffmann, Y. Hoo, T. Cai, M. White, J. Hrbek, Infrared study of triruthenium dodecacarbonyl interactions with gold, Surf. Sci. 606 (2012) 1906-1913.

[83] E. Baerends, P. Ros, The electronic structure of transition metal carbonyl complexes: A comparison of Hartree-Fock-Slater calculations with UV photoelectron spectra and IR and Raman data, Mol. Phys. 30 (1975) 1735-1747.

[84] Y. Zhu, H. Qian, B.A. Drake, R. Jin, Atomically Precise Au25(SR)18 Nanoparticles as Catalysts for the Selective Hydrogenation of α, β-Unsaturated Ketones and Aldehydes, Angew. Chem. 122 (2010) 1317-1320.

[85] X. Nie, H. Qian, Q. Ge, H. Xu, R. Jin, CO oxidation catalyzed by oxide-supported Au25 (SR) 18 nanoclusters and identification of perimeter sites as active centers, ACS Nano 6 (2012) 6014-6022.

[86] R. Jin, Quantum sized, thiolate-protected gold nanoclusters, Nanoscale 2 (2010) 343-362.

[87] H. Qian, M. Zhu, Z. Wu, R. Jin, Quantum Sized Gold Nanoclusters with Atomic Precision, Acc. Chem. Res. 45 (2012) 1470-1479.

[88] S. Li, X.-S. Du, B. Li, J.-Y. Wang, G.-P. Li, G.-G. Gao, S.-Q. Zang, Atom-precise modification of silver (I) thiolate cluster by shell ligand substitution: a new approach to generation of cluster functionality and chirality, J. Am. Chem. Soc. 140 (2018) 594-597.

[89] B. Li, R.W. Huang, J.H. Qin, S.Q. Zang, G.G. Gao, H.W. Hou, T.C. Mak, Thermochromic Luminescent Nest-Like Silver Thiolate Cluster, Chem.: Eur. J 20 (2014) 12416-12420.

[90] C.J. Murphy, CdS nanoclusters stabilized by thiolate ligands: A mini-review, J. Cluster Sci. 7 (1996) 341-350.

[91] Y. Doi, K. Koshizuka, T. Keii, Metal cluster catalysis. Kinetics and mechanism of the catalytic hydrogenation of ethylene by the ruthenium cluster complex H4Ru4(CO)12, Inorg. Chem. 21 (1982) 2732-2736.

[92] K.E. Inkrott, S.G. Shore, Stepwise deprotonation of H4Ru4(CO)12: high-yield synthesis and carbon-13 NMR spectra of H3Ru4(CO)12(-) and H2Ru4(CO)12(2-), Inorg. Chem. 18 (1979) 2817-

2821.

[93] Y. Doi, S. Tamura, K. Koshizuka, Metal cluster photo catalysis: photoinduced hydrogenation of ethylene by the tetraruthenium cluster complex H4Ru4 (CO) 12, J. Mol. Catal. 19 (1983) 213-222.

[94] R. Belford, M. Bruce, M. Cairns, M. Green, H.P. Taylor, P. Woodward, The crystal structure of C12H16Ru4(CO)10: an open Ru4 cluster containing a novel three-carbon bridging group, J. Chem. Soc. D (1970) 1159-1159.

[95] J.F. Corrigan, M. Dinardo, S. Doherty, A.J. Carty, Chemistry on the rhomboidal Ru 4 faces of the clusters RU 4 (CO) 13 (μ-PR 2) 2: Novel small molecule, ligand, and skeletal transformations, J. Cluster Sci. 3 (1992) 313-332.

[96] R.D. Adams, J.E. Babin, M. Tasi, Cluster synthesis. 17. Synthesis and structural characterizations of Ru5 (CO) 15 (. mu. 4-S), Ru6 (CO) 18 (. mu. 4-S), and Ru7 (CO) 21 (. mu. 4-S), Organometallics 7 (1988) 503-513.

[97] M.I. Bruce, J.G. Matisons, B.K. Nicholson, Cluster Chemistry: XVII. Radical ion-initiated synthesis of ruthenium cluster carbonyls containing tertiary phosphines, phosphites, arsines, SbPh3, or isocyanides, J. Organomet. Chem. 247 (1983) 321-343.

[98] C.C. Chusuei, X. Lai, K. Davis, E. Bowers, J.P. Fackler, D. Goodman, A nanoscale model catalyst preparation: Solution deposition of phosphine-stabilized gold clusters onto a planar TiO2 (110) support, Langmuir 17 (2001) 4113-4117.

[99] T. Choudhary, C. Sivadinarayana, C.C. Chusuei, A. Datye, J. Fackler Jr, D. Goodman, CO oxidation on supported nano-Au catalysts synthesized from a [Au6(PPh3)6](BF4)2 complex, J. Catal. 207 (2002) 247-255.

[100] L.D. Menard, F. Xu, R.G. Nuzzo, J.C. Yang, Preparation of TiO2-supported Au nanoparticle catalysts from a Au13 cluster precursor: ligand removal using ozone exposure versus a rapid thermal treatment, J. Catal. 243 (2006) 64-73.

[101] J. Chen, Q.-F. Zhang, T.A. Bonaccorso, P.G. Williard, L.-S. Wang, Controlling gold nanoclusters by diphospine ligands, J. Am. Chem. Soc. 136 (2013) 92-95.

[102] D.P. Anderson, R.H. Adnan, J.F. Alvino, O. Shipper, B. Donoeva, J.-Y. Ruzicka, H.A. Qahtani, H.H. Harris, B. Cowie, J.B. Aitken, V.B. Golovko, G.F. Metha, G.G. Andersson, Chemically synthesised atomically precise gold clusters deposited and activated on titania. Part II, Phys. Chem. Chem. Phys. 15 (2013) 14806.

[103] J.-Y. Ruzicka, F. Abu Bakar, C. Hoeck, R. Adnan, C. McNicoll, T. Kemmitt, B.C. Cowie, G.F. Metha, G.G. Andersson, V.B. Golovko, Toward Control of Gold Cluster Aggregation on TiO2 via Surface Treatments, J. Phys. Chem. C 119 (2015) 24465-24474.

[104] G.G. Andersson, V.B. Golovko, J.F. Alvino, T. Bennett, O. Wrede, S.M. Mejia, H.S. Al Qahtani, R. Adnan, N. Gunby, D.P. Anderson, Phosphine-stabilised Au9 clusters interacting with titania and silica surfaces: The first evidence for the density of states signature of the support-immobilised cluster, J. Chem. Phys. 141 (2014) 014702.

[105] D. Campagnola, M. Castiglioni, W. Dastrù, S. Deabate, R. Giordano, P.J. King, E. Sappa, Solid–gas reactions of metal carbonyl clusters. Hydrogenation of 1, 4-cyclohexadiene and hex-3-yne in the presence of H4Ru4(CO)12, Ru3(CO)12 or Ru3(CO)3(μ-CO)(μ3-CO)(μ3-‖-C2Ph2)(η-C5H5)2, Inorg. Chim. Acta 262 (1997) 157-165.

[106] J.-i. Nishigaki, K. Koyasu, T. Tsukuda, Chemically modified gold superatoms and superatomic molecules, Chem. Rec. 14 (2014) 897-909.

[107] S. Hayashi, R. Ishida, S. Hasegawa, S. Yamazoe, T. Tsukuda, Doping a Single Palladium Atom into Gold Superatoms Stabilized by PVP: Emergence of Hydrogenation Catalysis, Top. Catal. 61 (2018) 136-141.

[108] K. Hirata, R. Tomihara, K. Kim, K. Koyasu, T. Tsukuda, Characterization of chemically modified gold and silver clusters in gas phase, Phys. Chem. Chem. Phys. (2019).

[109] S. Takano, S. Hasegawa, M. Suyama, T. Tsukuda, Hydride Doping of Chemically Modified Gold-Based Superatoms, Acc. Chem. Res. 51 (2018) 3074-3083.

[110] R. Tomihara, K. Hirata, H. Yamamoto, S. Takano, K. Koyasu, T. Tsukuda, Collision-Induced Dissociation of Undecagold Clusters Protected by Mixed Ligands [Au11(PPh3)8X2]+(X=Cl, C≡CPh), ACS Omega 3 (2018) 6237-6242.

[111] D. Bergeron, P. Roach, A. Castleman, N. Jones, S. Khanna, Al cluster superatoms as halogens in polyhalides and as alkaline earths in iodide salts, Science 307 (2005) 231-235.

[112] B. Kiran, P. Jena, X. Li, A. Grubisic, S.T. Stokes, G. Ganteför, K.H. Bowen, R. Burgert, H. Schnöckel, Magic rule for Al n H m magic clusters, Phys. Rev. Lett. 98 (2007) 256802.

[113] M. Walter, J. Akola, O. Lopez-Acevedo, P.D. Jadzinsky, G. Calero, C.J. Ackerson, R.L. Whetten, H. Grönbeck, H. Häkkinen, A unified view of ligand-protected gold clusters as superatom complexes, Proc. Natl. Acad. Sci. U.S.A. 105 (2008) 9157-9162.

[114] A. Castleman Jr, S. Khanna, Clusters, superatoms, and building blocks of new materials, J. Phys. Chem. C 113 (2009) 2664-2675.

[115] Y.-K. Han, J. Jung, Does the "superatom" exist in halogenated aluminum clusters?, J. Am. Chem. Soc. 130 (2008) 2-3.

[116] Z.-G. Zhang, H.-G. Xu, Y. Feng, W. Zheng, Communications: Investigation of the superatomic character of Al13 via its interaction with sulfur atoms, J. Chem. Phys. 132 (2010) 161103.

[117] J.R. Reimers, Y. Wang, B.O. Cankurtaran, M.J. Ford, Chemical analysis of the superatom model for sulfur-stabilized gold nanoparticles, J. Am. Chem. Soc. 132 (2010) 8378-8384.

[118] C. Zeng, H. Qian, T. Li, G. Li, N.L. Rosi, B. Yoon, R.N. Barnett, R.L. Whetten, U. Landman, R. Jin, Total structure and electronic properties of the gold nanocrystal Au36(SR)24, Angew. Chem. Int. Ed. 51 (2012) 13114-13118.

[119] J.-i. Nishigaki, R. Tsunoyama, H. Tsunoyama, N. Ichikuni, S. Yamazoe, Y. Negishi, M. Ito, T. Matsuo, K. Tamao, T. Tsukuda, A new binding motif of sterically demanding thiolates on a gold cluster, J. Am. Chem. Soc. 134 (2012) 14295-14297.

[120] C. Zeng, Y. Chen, G. Li, R. Jin, Synthesis of a Au44(SR)28 nanocluster: Structure prediction and evolution from Au28(SR)20, Au36(SR)24 to Au44(SR)28, Chem. Commun. 50 (2014) 55-57.

[121] R. Tsunoyama, H. Tsunoyama, P. Pannopard, J. Limtrakul, T. Tsukuda, MALDI mass analysis of 11 kDa gold clusters protected by octadecanethiolate ligands, J. Phys. Chem. C 114 (2010) 16004-16009.

[122] P.R. Nimmala, B. Yoon, R.L. Whetten, U. Landman, A. Dass, Au67(SR)35 nanomolecules: characteristic size-specific optical, electrochemical, structural properties and first-principles theoretical analysis, J. Phys. Chem. A 117 (2013) 504-517.

[123] Y. Negishi, C. Sakamoto, T. Ohyama, T. Tsukuda, Synthesis and the Origin of the Stability of Thiolate-Protected Au130 and Au187 Clusters, J. Phys. Chem. Lett. 3 (2012) 1624-1628.

[124] A. Tlahuice-Flores, U. Santiago, D. Bahena, E. Vinogradova, C.V. Conroy, T. Ahuja, S.B. Bach, A. Ponce, G. Wang, M. José-Yacamán, Structure of the thiolated Au130 cluster, J. Phys. Chem. A 117 (2013) 10470-10476.

[125] O. Lopez-Acevedo, J. Akola, R.L. Whetten, H. Gronbeck, H. Häkkinen, Structure and bonding in the ubiquitous icosahedral metallic gold cluster Au144(SR)60, J. Phys. Chem. C 113 (2009) 5035-5038.

[126] D. Bahena, N. Bhattarai, U. Santiago, A. Tlahuice, A. Ponce, S.B. Bach, B. Yoon, R.L. Whetten, U. Landman, M. Jose-Yacaman, STEM electron diffraction and high-resolution images used in the determination of the crystal structure of the Au144(SR)60 cluster, J. Phys. Chem. Lett. 4 (2013) 975-981.

[127] F.A. Cotton, C. Kraihanzel, Vibrational spectra and bonding in metal carbonyls. I. infrared spectra of phosphine-substituted group VI carbonyls in the CO stretching region, J. Am. Chem. Soc. 84 (1962) 4432-4438.

[128] R. White, T. Bennett, V. Golovko, G.G. Andersson, G.F. Metha, A Systematic Density Functional Theory Study of the Complete De–ligation of Ru3(CO)12, ChemistrySelect 1 (2016) 1163-1167.

[129] Y. Negishi, W. Kurashige, U. Kamimura, Isolation and structural characterization of an octaneselenolate-protected Au25 cluster, Langmuir 27 (2011) 12289-12292.

[130] W. Kurashige, M. Yamaguchi, K. Nobusada, Y. Negishi, Ligand-induced stability of gold nanoclusters: thiolate versus selenolate, J. Phys. Chem. Lett. 3 (2012) 2649-2652.

[131] W. Kurashige, S. Yamazoe, K. Kanehira, T. Tsukuda, Y. Negishi, Selenolate-protected Au38 nanoclusters: Isolation and structural characterization, J. Phys. Chem. Lett. 4 (2013) 3181-3185.

[132] S.D. Jackson, R.B. Moyes, P.B. Wells, R. Whyman, Chemisorption and catalysis by metal clusters. Hydrogenation of carbon monoxide and carbon dioxide catalysed by supported Ruthenium clusters derived from Ru3(CO)12 and from H4Ru4(CO)12, J. Chem. Soc., Faraday Trans. 1 83 (1987) 905-911.

[133] T. Mizushima, K. Tohji, Y. Udagawa, An extended x-ray absorption fine structure study on the morphology change of ruthenium catalyst by carbon monoxide adsorption, J. Am. Chem. Soc. 110 (1988) 4459-4460.

[134] T. Mizushima, K. Tohji, Y. Udagawa, A. Ueno, An EXAFS and IR study of the CO adsorption-

induced morphology change in ruthenium catalysts, J. Am. Chem. Soc. 112 (1990) 7887-7893.

[135] T. Cai, Z. Song, Z. Chang, G. Liu, J. Rodriguez, J. Hrbek, Ru nanoclusters prepared by Ru3(CO)12 deposition on Au (111), Surf. Sci. 538 (2003) 76-88.

[136] G.A. Rizzi, A. Magrin, G. Granozzi, Substitutional Ti(1-x)RuxO2 surface alloys obtained from the decomposition of Ru3(CO)12 on TiO2 (110), Phys. Chem. Chem. Phys. 1 (1999) 709-711.

[137] F. Yang, S. Kundu, A.B. Vidal, J. Graciani, P.J. Ramírez, S.D. Senanayake, D. Stacchiola, J. Evans, P. Liu, J.F. Sanz, Determining the Behavior of RuOx Nanoparticles in Mixed-Metal Oxides: Structural and Catalytic Properties of RuO2/TiO2 (110) Surfaces, Angew. Chem. Int. Ed. 50 (2011) 10198-10202.

[138] P. Serp, P. Kalck, R. Feurer, Chemical vapor deposition methods for the controlled preparation of supported catalytic materials, Chem. Rev. 102 (2002) 3085-3128.

[139] J.A. Rodriguez, J. Dvorak, T. Jirsak, J. Hrbek, Formation of Mo and MoSx nanoparticles on Au (111) from Mo(CO)6 and S2 precursors: electronic and chemical properties, Surf. Sci. 490 (2001) 315-326.

[140] R. Psaro, S. Recchia, Supported metals derived from organometallics, Catal. Today 41 (1998) 139-147.

[141] M. Xu, F. Zaera, Mechanistic studies of the thermal decomposition of metal carbonyls on Ni (100) surfaces in connection with chemical vapor deposition processes, Journal of Vacuum Science & Technology A: Vacuum, Surfaces, and Films 14 (1996) 415-424.

[142] A.C. Papageorgiou, K. Diller, S. Fischer, F. Allegretti, F. Klappenberger, S.C. Oh, O.z. Sağlam, J. Reichert, A. Wiengarten, K. Seufert, In Vacuo Porphyrin Metalation on Ag(111) via Chemical Vapor Deposition of Ru3(CO)12: Mechanistic Insights, J. Phys. Chem. C 120 (2016) 8751-8758.

[143] E. Mohimi, Z.V. Zhang, S. Liu, J.L. Mallek, G.S. Girolami, J.R. Abelson, Area selective CVD of metallic films from molybdenum, iron, and ruthenium carbonyl precursors: Use of ammonia to inhibit nucleation on oxide surfaces, J. Vac. Sci. Technol. A 36 (2018) 041507.

[144] A.I. Kozlov, A.P. Kozlova, H. Liu, Y. Iwasawa, A new approach to active supported Au catalysts, Appl. Catal. A 182 (1999) 9-28.

[145] Z. Wu, D.-e. Jiang, A.K. Mann, D.R. Mullins, Z.-A. Qiao, L.F. Allard, C. Zeng, R. Jin, S.H. Overbury, Thiolate ligands as a double-edged sword for CO oxidation on CeO2 supported Au25(SCH2CH2Ph)18 nanoclusters, J. Am. Chem. Soc. 136 (2014) 6111-6122.

[146] Y. Negishi, M. Mizuno, M. Hirayama, M. Omatoi, T. Takayama, A. Iwase, A. Kudo, Enhanced photocatalytic water splitting by BaLa4Ti4O15 loaded with~ 1 nm gold nanoclusters using glutathione-protected Au25 clusters, Nanoscale 5 (2013) 7188-7192.

[147] Y. Liu, H. Tsunoyama, T. Akita, T. Tsukuda, Efficient and selective epoxidation of styrene with TBHP catalyzed by Au25 clusters on hydroxyapatite, Chem. Commun. 46 (2010) 550-552.

[148] H. Haberland, Mall, M., Moseler, M., Qiang, Y., Reiners, T., and Thurner, Y., Filling of micron-sized contact holes with copper by energetic cluster impact, J. Vac. Sci. Technol. A 12 (1994) 2925-2930.

[149] Z. Luo, W.H. Woodward, J.C. Smith, A. Castleman Jr, Growth kinetics of Al clusters in the gas phase produced by a magnetron-sputtering source, Int. J. Mass Spectrom. 309 (2012) 176-181.

[150] T. Guo, C. Jin, R. Smalley, Doping bucky: formation and properties of boron-doped buckminsterfullerene, J. Phys. Chem. 95 (1991) 4948-4950.

[151] R.F. Curl, R.E. Smalley, Probing C60, Science 242 (1988) 1017-1022.

[152] S. Maruyama, L.R. Anderson, R.E. Smalley, Direct injection supersonic cluster beam source for FT-ICR studies of clusters, Rev. Sci. Instrum. 61 (1990) 3686-3693.

[153] C. Kerpal, D.J. Harding, J.T. Lyon, G. Meijer, A. Fielicke, N2 activation by neutral ruthenium clusters, J. Phys. Chem. C 117 (2013) 12153-12158.

[154] S. Lee, C. Fan, T. Wu, S.L. Anderson, CO oxidation on Au n/TiO2 catalysts produced by size-selected cluster deposition, J. Am. Chem. Soc. 126 (2004) 5682-5683.

[155] H. Siekmann, C. Lüder, J. Faehrmann, H. Lutz, K. Meiwes-Broer, The pulsed arc cluster ion source (PACIS), Z. Phys. D : At., mol. clusters 20 (1991) 417-420.

[156] J.B. Fenn, M. Mann, C.K. Meng, S.F. Wong, C.M. Whitehouse, Electrospray ionization for mass spectrometry of large biomolecules, Science 246 (1989) 64-71.

[157] V.N. Popok, I. Barke, E.E.B. Campbell, K.-H. Meiwes-Broer, Cluster–surface interaction: From soft landing to implantation, Surf. Sci. Rep. 66 (2011) 347-377.

[158] H. Haberland, Karrais, M., Mall, M., and Thurner, Y., Thin films from energetic cluster impact: A feasibility study, J. Vac. Sci. Technol. A 10 (1992) 3266-3271.

[159] R.M. Nielsen, S. Murphy, C. Strebel, M. Johansson, J.H. Nielsen, I. Chorkendorff, A comparative STM study of Ru nanoparticles deposited on HOPG by mass- selected gas aggregation versus thermal evaporation, Surf. Sci. 603 (2009) 3420-3430.

[160] R. Smalley, Laser studies of metal cluster beams, Laser Chem. 2 (1983) 167-184.

[161] C. Pettiette, S. Yang, M. Craycraft, J. Conceicao, R. Laaksonen, O. Cheshnovsky, R. Smalley, Ultraviolet photoelectron spectroscopy of copper clusters, J. Chem. Phys. 88 (1988) 5377-5382.

[162] S. Nonose, Y. Sone, K. Onodera, S. Sudo, K. Kaya, Structure and reactivity of bimetallic cobalt-vanadium (ConVm) clusters, J. Phys. Chem. 94 (1990) 2744-2746.

[163] J. Rousset, A. Cadrot, F. Cadete Santos Aires, A. Renouprez, P. Mélinon, A. Perez, M. Pellarin, J. Vialle, M. Broyer, Study of bimetallic Pd–Pt clusters in both free and supported phases, J. Chem. Phys. 102 (1995) 8574-8585.

[164] R. Wagner, W. Vann, A. Castleman Jr, A technique for efficiently generating bimetallic clusters, Rev. Sci. Instrum. 68 (1997) 3010-3013.

[165] W. Bouwen, P. Thoen, F. Vanhoutte, S. Bouckaert, F. Despa, H. Weidele, R.E. Silverans, P. Lievens, Production of bimetallic clusters by a dual-target dual-laser vaporization source, Rev. Sci. Instrum. 71 (2000) 54-58.

[166] O. Cheshnovsky, K. Taylor, J. Conceicao, R. Smalley, Ultraviolet photoelectron spectra of mass-selected copper clusters: Evolution of the 3d band, Phys. Rev. Lett. 64 (1990) 1785.

[167] S. Murphy, R.M. Nielsen, C. Strebel, M. Johansson, J.H. Nielsen, Catalytic oxidation of graphite by mass- selected ruthenium nanoparticles, Carbon 49 (2011) 376-385.

[168] R.P. Sear, Nucleation: theory and applications to protein solutions and colloidal suspensions, J. Phys. Condens. Matter 19 (2007) 033101.

[169] O. Polonskyi, P. Solař, O. Kylián, M. Drábik, A. Artemenko, J. Kousal, J. Hanuš, J. Pešička, I. Matolínová, E. Kolíbalová, Nanocomposite metal/plasma polymer films prepared by means of gas aggregation cluster source, Thin Solid Films 520 (2012) 4155-4162.

[170] I. Shyjumon, M. Gopinadhan, C.A. Helm, B.M. Smirnov, R. Hippler, Deposition of titanium/titanium oxide clusters produced by magnetron sputtering, Thin Solid Films 500 (2006) 41-51.

[171] S. Pratontep, S. Carroll, C. Xirouchaki, M. Streun, R. Palmer, Size-selected cluster beam source based on radio frequency magnetron plasma sputtering and gas condensation, Rev. Sci. Instrum. 76 (2005) 045103.

[172] F. Di Fonzo, A. Gidwani, M. Fan, D. Neumann, D. Iordanoglou, J. Heberlein, P. McMurry, S. Girshick, N. Tymiak, W. Gerberich, Focused nanoparticle-beam deposition of patterned microstructures, Appl. Phys. Lett. 77 (2000) 910-912.

[173] P.M. Dinh, P.G. Reinhard, E. Suraud, Dynamics of clusters and molecules in contact with an environment, Phys. Rep. 485 (2010) 43-107.

[174] H. Yasumatsu, T. Kondow, Reactive scattering of clusters and cluster ions from solid surfaces, Rep. Prog. Phys. 66 (2003) 1783.

[175] S. Carroll, P. Weibel, B. Von Issendorff, L. Kuipers, R. Palmer, The impact of size-selected Ag clusters on graphite: an STM study, J. Phys. Condens. Matter 8 (1996) L617.

[176] S. Carroll, S. Pratontep, M. Streun, R. Palmer, S. Hobday, R. Smith, Pinning of size-selected Ag clusters on graphite surfaces, J. Chem. Phys. 113 (2000) 7723-7727.

[177] U. Heiz, E. Bullock, Fundamental aspects of catalysis on supported metal clusters, J. Mater. Chem. 14 (2004) 564-577.

[178] J.-D. Grunwaldt, A. Baiker, Gold/titania interfaces and their role in carbon monoxide oxidation, J. Phys. Chem. B 103 (1999) 1002-1012.

[179] S. Bagheri, N. Muhd Julkapli, S. Bee Abd Hamid, Titanium dioxide as a catalyst support in heterogeneous catalysis, Sci. World J. 2014 (2014) 727496.

[180] A. Ruiz Puigdollers, P. Schlexer, S. Tosoni, G. Pacchioni, Increasing oxide reducibility: the role of metal/oxide interfaces in the formation of oxygen vacancies, ACS Catal. 7 (2017) 6493-6513.

[181] G. Pacchioni, H. Freund, Electron transfer at oxide surfaces. The MgO paradigm: from defects to ultrathin films, Chem. Rev. 113 (2013) 4035-4072.

[182] R. Baker, Catalytic gasification of graphite by bimetallic particles, J. Catal. 62 (1980) 221-230.

[183] E. Unger, G.S. Duesberg, M. Liebau, A.P. Graham, R. Seidel, F. Kreupl, W. Hoenlein, Decoration of multi- walled carbon nanotubes with noble- and transition-metal clusters and formation of CNT–CNT networks, Appl. Phys. A 77 (2003) 735-738.

[184] R. Bennett, C. Pang, N. Perkins, R. Smith, P. Morrall, R. Kvon, M. Bowker, Surface structures

in the SMSI state; Pd on (1×2) reconstructed TiO2 (110), J. Phys. Chem. B 106 (2002) 4688-4696.

[185] Q. Fu, T. Wagner, S. Olliges, H.-D. Carstanjen, Metal–oxide interfacial reactions: Encapsulation of Pd on TiO2 (110), J. Phys. Chem. B 109 (2005) 944-951.

[186] A. Berkó, I. Ulrych, K. Prince, Encapsulation of Rh nanoparticles supported on TiO2 (110)-(1×1) surface: XPS and STM studies, J. Phys. Chem. B 102 (1998) 3379-3386.

[187] I.X. Green, W. Tang, M. Neurock, J.T. Yates, Spectroscopic observation of dual catalytic sites during oxidation of CO on a Au/TiO2 catalyst, Science 333 (2011) 736-739.

[188] H.S. Al Qahtani, G.F. Metha, R.B. Walsh, V.B. Golovko, G.G. Andersson, T. Nakayama, Aggregation behavior of ligand-protected Au9 clusters on sputtered atomic layer deposition TiO2, J. Phys. Chem. C 121 (2017) 10781-10789.

[189] K. Nakata, S. Sugawara, W. Kurashige, Y. Negishi, M. Nagata, S. Uchida, C. Terashima, T. Kondo, M. Yuasa, A. Fujishima, Cosensitization Properties of Glutathione-Protected Au25 Cluster on Ruthenium Dye-Sensitized TiO2 Photoelectrode, Int. J. Photoenergy 2013 (2013) 456583.

[190] P. López-Caballero, A.W. Hauser, M.a. Pilar de Lara-Castells, Exploring the Catalytic Properties of Unsupported and TiO2-Supported Cu5 Clusters: CO2 Decomposition to CO and CO2 Photoactivation, J. Phys. Chem. C 123 (2019) 23064-23074.

[191] V. Jeyalakshmi, R. Mahalakshmy, K. Krishnamurthy, B. Viswanathan, Titania based catalysts for photoreduction of carbon dioxide: Role of modifiers, Indian J. Chem., Sect. A: Inorg., Bio-inorg., Phys., Theor. Anal. Chem. 51A (2012) 1263-1283.

[192] M. Turner, V.B. Golovko, O.P. Vaughan, P. Abdulkin, A. Berenguer-Murcia, M.S. Tikhov, B.F. Johnson, R.M. Lambert, Selective oxidation with dioxygen by gold nanoparticle catalysts derived from 55-atom clusters, Nature 454 (2008) 981.

[193] K. Suttiponparnit, J. Jiang, M. Sahu, S. Suvachittanont, T. Charinpanitkul, P. Biswas, Role of surface area, primary particle size, and crystal phase on titanium dioxide nanoparticle dispersion properties, Nanoscale Res. Lett. 6 (2011) 27.

[194] H.-J. Freund, G. Pacchioni, Oxide ultra-thin films on metals: new materials for the design of supported metal catalysts, Chem. Soc. Rev. 37 (2008) 2224-2242.

[195] G. Pacchioni, L. Giordano, M. Baistrocchi, Charging of metal atoms on ultrathin MgO/Mo (100) films, Phys. Rev. Lett. 94 (2005) 226104.

[196] D. Ricci, A. Bongiorno, G. Pacchioni, U. Landman, Bonding trends and dimensionality crossover of gold nanoclusters on metal-supported MgO thin films, Phys. Rev. Lett. 97 (2006) 036106.

[197] M. Sterrer, T. Risse, M. Heyde, H.-P. Rust, H.-J. Freund, Crossover from three-dimensional to two-dimensional geometries of Au nanostructures on thin MgO (001) films: A confirmation of theoretical predictions, Phys. Rev. Lett. 98 (2007) 206103.

[198] S. Tauster, S. Fung, R. Baker, J. Horsley, Strong interactions in supported-metal catalysts, Science 211 (1981) 1121-1125.

[199] G.L. Haller, D.E. Resasco, Metal–support interaction: Group VIII metals and reducible oxides, Advances in catalysis, Elsevier1989, pp. 173-235.

[200] C.-J. Pan, M.-C. Tsai, W.-N. Su, J. Rick, N.G. Akalework, A.K. Agegnehu, S.-Y. Cheng, B.-J. Hwang, Tuning/exploiting strong metal-support interaction (SMSI) in heterogeneous catalysis, Journal of the Taiwan Institute of Chemical Engineers 74 (2017) 154-186.

[201] C. Vayenas, S. Brosda, C. Pliangos, The double-layer approach to promotion, electrocatalysis, electrochemical promotion, and metal–support interactions, J. Catal. 216 (2003) 487-504.

[202] T. Ioannides, X.E. Verykios, Charge transfer in metal catalysts supported on doped TiO2: a theoretical approach based on metal–semiconductor contact theory, J. Catal. 161 (1996) 560-569.

[203] Q. Fu, T. Wagner, Metal/oxide interfacial reactions: Oxidation of metals on SrTiO3 (100) and TiO2 (110), J. Phys. Chem. B 109 (2005) 11697-11705.

[204] U. Diebold, The surface science of titanium dioxide, Surf. Sci. Rep. 48 (2003) 53-229.

[205] U. Diebold, J.-M. Pan, T.E. Madey, Ultrathin metal film growth on TiO2 (110): an overview, Surf. Sci. 331 (1995) 845-854.

[206] C.T. Campbell, Ultrathin metal films and particles on oxide surfaces: structural, electronic and chemisorptive properties, Surf. Sci. Rep. 27 (1997) 1-111.

[207] F. Pesty, H.-P. Steinrück, T.E. Madey, Thermal stability of Pt films on TiO2 (110): evidence for encapsulation, Surf. Sci. 339 (1995) 83-95.

[208] O. Dulub, W. Hebenstreit, U. Diebold, Imaging cluster surfaces with atomic resolution: the strong metal-support interaction state of Pt supported on TiO 2 (110), Phys. Rev. Lett. 84 (2000)

3646.

[209] R. Bennett, P. Stone, M. Bowker, Pd nanoparticle enhanced re-oxidation of non-stoichiometric TiO2: STM imaging of spillover and a new form of SMSI, Catal. Lett. 59 (1999) 99-105.

[210] Y. Gao, Y. Liang, S. Chambers, Thermal stability and the role of oxygen vacancy defects in strong metal support interaction—Pt on Nb-doped TiO2 (100), Surf. Sci. 365 (1996) 638-648.

[211] H.R. Sadeghi, V.E. Henrich, Electronic interactions in the rhodium/TiO2 system, J. Catal. 109 (1988) 1-11.

[212] H.R. Sadeghi, V.E. Henrich, Rh on TiO2: Model catalyst studies of the strong metal-support interaction, Applications of Surface Science 19 (1984) 330-340.

[213] S. Labich, E. Taglauer, H. Knözinger, Metal–support interactions on rhodium model catalysts, Top. Catal. 14 (2000) 153-161.

[214] D. Mullins, K. Zhang, Metal–support interactions between Pt and thin film cerium oxide, Surf. Sci. 513 (2002) 163-173.

[215] S. Tauster, S. Fung, R.L. Garten, Strong metal-support interactions. Group 8 noble metals supported on titanium dioxide, J. Am. Chem. Soc. 100 (1978) 170-175.

[216] S. Bernal, F. Botana, J. Calvino, C. López, J. Pérez-Omil, J. Rodríguez-Izquierdo, High-resolution electron microscopy investigation of metal–support interactions in Rh/TiO 2, J. Chem. Soc., Faraday Trans. 92 (1996) 2799-2809.

[217] S. Bernal, J. Calvino, M. Cauqui, J. Gatica, C.L. Cartes, J.P. Omil, J. Pintado, Some contributions of electron microscopy to the characterisation of the strong metal–support interaction effect, Catal. Today 77 (2003) 385-406.

[218] M. Aizawa, S. Lee, S.L. Anderson, Sintering, oxidation, and chemical properties of size-selected nickel clusters on TiO2 (110), J. Chem. Phys. 117 (2002) 5001-5011.

[219] P. Reyes, M. Aguirre, I. Melián-Cabrera, M.L. Granados, J. Fierro, Interfacial properties of an Ir/TiO2 system and their relevance in crotonaldehyde hydrogenation, J. Catal. 208 (2002) 229-237.

[220] R. Gubó, C.M. Yim, M. Allan, C.L. Pang, A. Berkó, G. Thornton, Variation of SMSI with the Au: Pd Ratio of Bimetallic Nanoparticles on TiO2 (110), Top. Catal. 61 (2018) 308-317.

[221] H. Jensen, A. Soloviev, Z. Li, E.G. Søgaard, XPS and FTIR investigation of the surface properties of different prepared titania nano-powders, Appl. Surf. Sci. 246 (2005) 239-249.

[222] E. Wahlström, N. Lopez, R. Schaub, P. Thostrup, A. Rønnau, C. Africh, E. Lægsgaard, J. Nørskov, F. Besenbacher, Bonding of Gold Nanoclusters to Oxygen Vacancies on Rutile TiO2 (110), Phys. Rev. Lett. 90 (2003) 026101.

[223] F. Claeyssens, S. Pratontep, C. Xirouchaki, R. Palmer, Immobilization of large size-selected silver clusters on graphite, Nanotechnology 17 (2006) 805.

[224] D. Matthey, J. Wang, S. Wendt, J. Matthiesen, R. Schaub, E. Lægsgaard, B. Hammer, F. Besenbacher, Enhanced bonding of gold nanoparticles on oxidized TiO2 (110), Science 315 (2007) 1692-1696.

[225] S. Carroll, K. Seeger, R. Palmer, Trapping of size-selected Ag clusters at surface steps, Appl. Phys. Lett. 72 (1998) 305-307.

[226] B. Prevel, L. Bardotti, S. Fanget, A. Hannour, P. Melinon, A. Perez, J. Gierak, G. Faini, E. Bourhis, D. Mailly, Gold nanoparticle arrays on graphite surfaces, Appl. Surf. Sci. 226 (2004) 173-177.

[227] Y. Lei, F. Mehmood, S. Lee, J. Greeley, B. Lee, S. Seifert, R.E. Winans, J.W. Elam, R.J. Meyer, P.C. Redfern, Increased silver activity for direct propylene epoxidation via subnanometer size effects, Science 328 (2010) 224-228.

[228] J.A. Rodríguez, S. Ma, P. Liu, J. Hrbek, J. Evans, M. Perez, Activity of CeOx and TiOx nanoparticles grown on Au (111) in the water-gas shift reaction, Science 318 (2007) 1757-1760.

[229] U. Heiz, A. Sanchez, S. Abbet, W.-D. Schneider, The reactivity of gold and platinum metals in their cluster phase, Eur. Phys. J. D 9 (1999) 35-39.

[230] V. Borman, M. Pushkin, V. Tronin, V. Troyan, Evolution of the electronic properties of transition metal nanoclusters on graphite surface, J. Exp. Theor. Phys. 110 (2010) 1005-1025.

[231] M. Haruta, N. Yamada, T. Kobayashi, S. Iijima, Gold catalysts prepared by coprecipitation for low-temperature oxidation of hydrogen and of carbon monoxide, J. Catal. 115 (1989) 301-309.

[232] X.-N. Li, Z. Yuan, S.-G. He, CO oxidation promoted by gold atoms supported on titanium oxide cluster anions, J. Am. Chem. Soc. 136 (2014) 3617-3623.

[233] T.A. Nijhuis, T. Visser, B.M. Weckhuysen, Mechanistic study into the direct epoxidation of propene over gold/titania catalysts, J. Phys. Chem. B 109 (2005) 19309-19319.

[234] A. Sinha, S. Seelan, S. Tsubota, M. Haruta, Catalysis by gold nanoparticles: epoxidation of propene, Top. Catal. 29 (2004) 95-102.

[235] R.H. Adnan, G.G. Andersson, M.I. Polson, G.F. Metha, V.B. Golovko, Factors influencing the catalytic oxidation of benzyl alcohol using supported phosphine-capped gold nanoparticles, Catal. Sci. Technol. 5 (2015) 1323-1333.

[236] T. Yoskamtorn, S. Yamazoe, R. Takahata, J.-i. Nishigaki, A. Thivasasith, J. Limtrakul, T. Tsukuda, Thiolate-mediated selectivity control in aerobic alcohol oxidation by porous carbon-supported Au25 clusters, ACS Catal. 4 (2014) 3696-3700.

[237] H. Tsunoyama, H. Sakurai, N. Ichikuni, Y. Negishi, T. Tsukuda, Colloidal gold nanoparticles as catalyst for carbon− carbon bond formation: application to aerobic homocoupling of phenylboronic acid in water, Langmuir 20 (2004) 11293-11296.

[238] T.C. Boorman, I. Larrosa, Gold-mediated C–H bond functionalisation, Chem. Soc. Rev. 40 (2011) 1910-1925.

[239] L. McEwan, M. Julius, S. Roberts, J.C. Fletcher, A review of the use of gold catalysts in selective hydrogenation reactions, Gold Bull. 43 (2010) 298-306.

[240] G. Bond, Mechanisms of the gold-catalysed water-gas shift, Gold Bull. 42 (2009) 337-342.

[241] G. Zhang, Y. Peng, L. Cui, L. Zhang, Gold-Catalyzed Homogeneous Oxidative Cross-Coupling Reactions, Angew. Chem. Int. Ed. 48 (2009) 3112-3115.

[242] U. Heiz, A. Sanchez, S. Abbet, W.-D. Schneider, Tuning the oxidation of carbon monoxide using nanoassembled model catalysts, Chem. Phys. 262 (2000) 189-200.

[243] A. Eichler, J. Hafner, Molecular precursors in the dissociative adsorption of O2 on Pt (111), Phys. Rev. Lett. 79 (1997) 4481.

[244] A. Eichler, J. Hafner, Reaction channels for the catalytic oxidation of CO on Pt (111), Phys. Rev. B 59 (1999) 5960.

[245] S. Tosoni, G. Pacchioni, Oxide-Supported Gold Clusters and Nanoparticles in Catalysis: A Computational Chemistry Perspective, ChemCatChem 11 (2019) 73-89.

[246] S. Yamazoe, K. Koyasu, T. Tsukuda, Nonscalable oxidation catalysis of gold clusters, Acc. Chem. Res. 47 (2013) 816-824.

[247] Y. Liu, H. Tsunoyama, T. Akita, S. Xie, T. Tsukuda, Aerobic oxidation of cyclohexane catalyzed by size-controlled Au clusters on hydroxyapatite: size effect in the sub-2 nm regime, ACS Catal. 1 (2010) 2-6.

[248] R.N. Barnett, U. Landman, Born-Oppenheimer molecular-dynamics simulations of finite systems: Structure and dynamics of (H2O)2, Phys. Rev. B 48 (1993) 2081.

[249] R.B. Moyes, P.B. Wells, S.D. Jackson, R. Whyman, Chemisorption and catalysis by metal clusters. Hydrogenation of ethene and hydrogenolysis of ethane catalysed by supported ruthenium clusters derived from Ru3(CO)12 and from H4Ru4(CO)12, J. Chem. Soc., Faraday Trans. 1 82 (1986) 2719-2727.

[250] R. Pierantozzi, E.G. Valagene, A.F. Nordquist, P.N. Dyer, Support and cluster effects on synthesis gas conversion with supported ruthenium clusters, J. Mol. Catal. 21 (1983) 189-202.

[251] J.G. Shen, M. Ichikawa, Intrazeolite Anchoring of Co, Ru, and [Ru−Co] Carbonyl Clusters: Synthesis, Characterization, and Their Catalysis for CO Hydrogenation, J. Phys. Chem. B 102 (1998) 5602-5613.

[252] Z. Song, T. Cai, J. Grey, J. Rodriguez, J. Hrbek, Structure and Reactivity of Ru Nanoparticles Supported on Modified Graphite Surfaces: A Study of the Model Catalysts for Ammonia Synthesis, J. Am. Chem. Soc. 126 (2004) 8576-8584.

[253] O. Hernandez, S. Isenberg, V. Steinmetz, G.L. Glish, P. Maitre, Probing mobility-selected saccharide isomers: selective ion–molecule reactions and wavelength-specific IR activation, J. Phys. Chem. A 119 (2015) 6057-6064.

[254] J. Oomens, B.G. Sartakov, G. Meijer, G. Von Helden, Gas-phase infrared multiple photon dissociation spectroscopy of mass-selected molecular ions, Int. J. Mass Spectrom. 254 (2006) 1-19.

[255] I. Savić, D. Gerlich, O. Asvany, P. Jusko, S. Schlemmer, Controlled synthesis and analysis of He–H+ 3 in a 3.7 K ion trap, Mol. Phys. 113 (2015) 2320-2332.

[256] S. Daly, M. Krstić, A. Giuliani, R. Antoine, L. Nahon, A. Zavras, G.N. Khairallah, V. Bonačić-Koutecký, P. Dugourd, A. Richard, Gas-phase VUV photoionisation and photofragmentation of the silver deuteride nanocluster [Ag10D8L6]2+(L=bis(diphenylphosphino)methane). A joint experimental and theoretical study, Phys. Chem. Chem. Phys. 17 (2015) 25772-25777.

[257] S.M. Lang, A. Frank, T.M. Bernhardt, Activation and Catalytic Dehydrogenation of Methane on

Small Pd x+ and Pd x O+ Clusters, J. Phys. Chem. C 117 (2013) 9791-9800.

[258] N.D. Loewen, T.V. Neelakantan, L.A. Berben, Renewable formate from C–H bond formation with CO2: Using iron carbonyl clusters as electrocatalysts, Acc. Chem. Res. 50 (2017) 2362-2370.

[259] A. Taheri, E.J. Thompson, J.C. Fettinger, L.A. Berben, An iron electrocatalyst for selective reduction of CO2 to formate in water: Including thermochemical insights, ACS Catal. 5 (2015) 7140-7151.

[260] M.D. Rail, L.A. Berben, Directing the reactivity of [HFe4N(CO)12]− toward H+ or CO2 reduction by understanding the electrocatalytic mechanism, J. Am. Chem. Soc. 133 (2011) 18577-18579.

[261] N.D. Loewen, E.J. Thompson, M. Kagan, C.L. Banales, T.W. Myers, J.C. Fettinger, L.A. Berben, A pendant proton shuttle on [Fe4N(CO)12]− alters product selectivity in formate vs. H 2 production via the hydride [H–Fe4N(CO)12]−, Chem. Sci. 7 (2016) 2728-2735.

[262] K. Matsubara, T. Iura, T. Maki, H. Nagashima, A triruthenium carbonyl cluster bearing a bridging acenaphthylene ligand: An efficient catalyst for reduction of esters, carboxylic acids, and amides by trialkylsilanes, J. Org. Chem. 67 (2002) 4985-4988.

[263] M. Igarashi, R. Mizuno, T. Fuchikami, Ruthenium complex catalyzed hydrosilylation of esters: a facile transformation of esters to alkyl silyl acetals and aldehydes, Tetrahedron Lett. 42 (2001) 2149-2151.

[264] M. Igarashi, T. Fuchikami, Transition-metal complex-catalyzed reduction of amides with hydrosilanes: a facile transformation of amides to amines, Tetrahedron Lett. 42 (2001) 1945-1947.

[265] S.R. Drake, Electrochemical studies on iron, ruthenium and osmium carbonyl clusters, Polyhedron 9 (1990) 455-474.

[266] M.A. Fox, M.T. Dulay, Heterogeneous photocatalysis, Chem. Rev. 93 (1993) 341-357.

[267] B. Ohtani, Photocatalysis A to Z—What we know and what we do not know in a scientific sense, J. Photochem. Photobiol. C 11 (2010) 157-178.

[268] M.R. Hoffmann, S.T. Martin, W. Choi, D.W. Bahnemann, Environmental applications of semiconductor photocatalysis, Chem. Rev. 95 (1995) 69-96.

[269] Q. Guo, C. Zhou, Z. Ma, X. Yang, Fundamentals of TiO2 Photocatalysis: Concepts, Mechanisms, and Challenges, Adv. Mater. (2019) 1901997.

[270] M. Ni, M.K. Leung, D.Y. Leung, K. Sumathy, A review and recent developments in photocatalytic water-splitting using TiO2 for hydrogen production, Renew. Sust, Energg. Rev. 11 (2007) 401-425.

[271] G. Colón, Towards the hydrogen production by photocatalysis, Appl. Catal. A 518 (2016) 48-59.

[272] E. Yesodharan, M. Grätzel, Photodecomposition of Liquid Water with TiO2-Supported Noble Metal Clusters, Helv. Chim. Acta 66 (1983) 2145-2153.

[273] N. Sakai, T. Tatsuma, Photovoltaic Properties of Glutathione-Protected Gold Clusters Adsorbed on TiO2 Electrodes, Adv. Mater. 22 (2010) 3185-3188.

[274] J. Lee, H.S. Shim, M. Lee, J.K. Song, D. Lee, Size-controlled electron transfer and photocatalytic activity of ZnO–Au nanoparticle composites, J. Phys. Chem. Lett. 2 (2011) 2840-2845.

[275] Y.-S. Chen, P.V. Kamat, Glutathione-capped gold nanoclusters as photosensitizers. Visible light-induced hydrogen generation in neutral water, J. Am. Chem. Soc. 136 (2014) 6075-6082.

[276] A. Iwase, H. Kato, A. Kudo, Nanosized Au particles as an efficient cocatalyst for photocatalytic overall water splitting, Catal. Lett. 108 (2006) 7-10.

[277] A. Iwase, H. Kato, A. Kudo, The effect of Au cocatalyst loaded on La-doped NaTaO3 on photocatalytic water splitting and O2 photoreduction, Appl. Catal. B 136 (2013) 89-93.

[278] N. Sakamoto, H. Ohtsuka, T. Ikeda, K. Maeda, D. Lu, M. Kanehara, K. Teramura, T. Teranishi, K. Domen, Highly dispersed noble-metal/chromia (core/shell) nanoparticles as efficient hydrogen evolution promoters for photocatalytic overall water splitting under visible light, Nanoscale 1 (2009) 106-109.

[279] K. Maeda, N. Sakamoto, T. Ikeda, H. Ohtsuka, A. Xiong, D. Lu, M. Kanehara, T. Teranishi, K. Domen, Preparation of Core–Shell-Structured Nanoparticles (with a Noble-Metal or Metal Oxide Core and a Chromia Shell) and Their Application in Water Splitting by Means of Visible Light, Chem.: Eur. J 16 (2010) 7750-7759.

[280] K. Maeda, K. Teramura, D. Lu, N. Saito, Y. Inoue, K. Domen, Noble-metal/Cr2O3 core/shell nanoparticles as a cocatalyst for photocatalytic overall water splitting, Angew. Chem. Int. Ed. 45 (2006) 7806-7809.

[281] M. Yoshida, K. Takanabe, K. Maeda, A. Ishikawa, J. Kubota, Y. Sakata, Y. Ikezawa, K. Domen,

Role and function of noble-metal/Cr-layer core/shell structure cocatalysts for photocatalytic overall water splitting studied by model electrodes, J. Phys. Chem. C 113 (2009) 10151-10157.

[282] K. Maeda, K. Domen, New non-oxide photocatalysts designed for overall water splitting under visible light, J. Phys. Chem. C 111 (2007) 7851-7861.

[283] M. Guittet, J. Crocombette, M. Gautier-Soyer, Bonding and XPS chemical shifts in ZrSiO 4 versus SiO 2 and ZrO 2: Charge transfer and electrostatic effects, Phys. Rev. B 63 (2001) 125117.

[284] M. Seah, W. Dench, Quantitative electron spectroscopy of surfaces: a standard data base for electron inelastic mean free paths in solids, Surf. Interface Anal. 1 (1979) 2-11.

[285] M. Seah, A review of the analysis of surfaces and thin films by AES and XPS, Vacuum 34 (1984) 463-478.

[286] M. Seah, The quantitative analysis of surfaces by XPS: a review, Surf. Interface Anal. 2 (1980) 222-239.

[287] Y. Kitsudo, A. Iwamoto, H. Matsumoto, K. Mitsuhara, T. Nishimura, M. Takizawa, T. Akita, Y. Maeda, Y. Kido, Final state effect for Au 4f line from gold-nano-particles grown on oxides and HOPG supports, Surf. Sci. 603 (2009) 2108-2114.

[288] D.-C. Lim, C.-C. Hwang, G. Ganteför, Y.D. Kim, Model catalysts of supported Au nanoparticles and mass-selected clusters, Phys. Chem. Chem. Phys. 12 (2010) 15172-15180.

[289] W.E. Kaden, C. Büchner, L. Lichtenstein, S. Stuckenholz, F. Ringleb, M. Heyde, M. Sterrer, H.-J. Freund, L. Giordano, G. Pacchioni, Understanding surface core-level shifts using the Auger parameter: a study of Pd atoms adsorbed on ultrathin SiO2 films, Phys. Rev. B 89 (2014) 115436.

[290] G. Hohlneicher, H. Pulm, H.-J. Freund, On the separation of initial and final state effects in photoelectron spectroscopy using an extension of the Auger-parameter concept, J. Electron. Spectrosc. Relat. Phenom. 37 (1985) 209-224.

[291] J. Tao, J. Pan, C. Huan, Z. Zhang, J. Chai, S. Wang, Origin of XPS binding energy shifts in Ni clusters and atoms on rutile TiO2 surfaces, Surf. Sci. 602 (2008) 2769-2773.

[292] W.E. Kaden, T. Wu, W.A. Kunkel, S.L. Anderson, Electronic structure controls reactivity of size-selected Pd clusters adsorbed on TiO2 surfaces, Science 326 (2009) 826-829.

[293] J. Rowe, H. Ibach, Surface and bulk contributions to ultraviolet photoemission spectra of silicon, Phys. Rev. Lett. 32 (1974) 421.

[294] M. Helander, M. Greiner, Z. Wang, Z. Lu, Pitfalls in measuring work function using photoelectron spectroscopy, Appl. Surf. Sci. 256 (2010) 2602-2605.

[295] R.W. Joyner, Electron spectroscopy applied to the study of reactivity at metal surfaces—A review, Surf. Sci. 63 (1977) 291-314.

[296] U. Lammers, G. Borstel, Electronic and atomic structure of copper clusters, Phys. Rev. B 49 (1994) 17360.

[297] Y. Harada, S. Masuda, H. Ozaki, Electron spectroscopy using metastable atoms as probes for solid surfaces, Chem. Rev. 97 (1997) 1897-1952.

[298] H. Morgner, The characterization of liquid and solid surfaces with metastable helium atoms, Adv. At. Mol. Opt. Phys. 42 (2000) 387-488.

[299] J.E. Penner-Hahn, X-ray absorption spectroscopy in coordination chemistry, Coord. Chem. Rev. 190 (1999) 1101-1123.

[300] L. Que, Physical methods in bioinorganic chemistry: spectroscopy and magnetism, Sterling Publishing Company, New York, 2000.

[301] F. De Groot, High-resolution X-ray emission and X-ray absorption spectroscopy, Chem. Rev. 101 (2001) 1779-1808.

[302] T. Mizushima, K. Tohji, Y. Udagawa, A. Ueno, EXAFS study of the carbon monoxide adsorption-induced morphology change in ruthenium clusters supported on alumina, J. Phys. Chem. 94 (1990) 4980-4985.

[303] T. Mizushima, K. Tohji, Y. Udagawa, An EXAFS study on the morphology change of Ru catalyst by CO adsorption, Physica B 158 (1989) 195-197.

[304] v.t.H.F.J. Blik, J.B.A.D. van Zon, D.C. Koningsberger, R. Prins, EXAFS determination of the change in the structure of rhodium in highly dispersed Rh/gamma-Al2O3 catalysts after Co and/or H2 adsorption at different temperatures, J. Mol. Catal. 25 (1984) 379-396.

[305] v.t.H.F.J. Blik, J.B.A.D. van Zon, T. Huizinga, J.C. Vis, D.C. Koningsberger, R. Prins, Structure of rhodium in an ultradispersed Rh/Al2O3 catalyst as studied by EXAFS and other techniques, J. Am. Chem. Soc. 107 (1985) 3139-3147.

[306] R. Toyoshima, H. Kondoh, In-situ observations of catalytic surface reactions with soft x-rays

under working conditions, J. Phys. Condens. Matter 27 (2015) 083003.

[307] Y. Nagai, K. Dohmae, Y. Ikeda, N. Takagi, T. Tanabe, N. Hara, G. Guilera, S. Pascarelli, M.A. Newton, O. Kuno, In Situ Redispersion of Platinum Autoexhaust Catalysts: An On-Line Approach to Increasing Catalyst Lifetimes?, Angew. Chem. Int. Ed. 47 (2008) 9303-9306.

[308] L. Óvári, J. Kiss, Growth of Rh nanoclusters on TiO2 (110): XPS and LEIS studies, Appl. Surf. Sci. 252 (2006) 8624-8629.

[309] G. Li, B. Zandkarimi, A.C. Cass, T.J. Gorey, B.J. Allen, A.N. Alexandrova, S.L. Anderson, Sn-modification of Pt7/alumina model catalysts: Suppression of carbon deposition and enhanced thermal stability, J. Chem. Phys. 152 (2020) 024702.

[310] T.J. Gorey, Y. Dai, S.L. Anderson, S. Lee, S. Lee, S. Seifert, R.E. Winans, Selective growth of Al2O3 on size-selected platinum clusters by atomic layer deposition, Surf. Sci. 691 (2020) 121485.

[311] B. Zandkarimi, T.J. Gorey, G. Li, J. Munarriz, S.L. Anderson, A.N. Alexandrova, Alloying with Sn Suppresses Sintering of Size-Selected Sub-Nano Pt Clusters on SiO2 with and without Adsorbates, Chem. Mater. 32 (2020) 8595–8605.

[312] T.J. Gorey, B. Zandkarimi, G. Li, E.T. Baxter, A.N. Alexandrova, S.L. Anderson, Preparation of Size and Composition-Controlled PtnSnx/SiO2 (n= 2, 4, 24) Bimetallic Model Catalysts Using Atomic Layer Deposition, J. Phys. Chem. C 123 (2019) 16194-16209.

[313] E.T. Baxter, M.-A. Ha, A.C. Cass, H. Zhai, A.N. Alexandrova, S.L. Anderson, Diborane Interactions with Pt7/Alumina: Preparation of Size-Controlled Borated Pt Model Catalysts, J. Phys. Chem. C 122 (2018) 1631-1644.

[314] E.T. Baxter, M.-A. Ha, A.C. Cass, A.N. Alexandrova, S.L. Anderson, Ethylene dehydrogenation on Pt4, 7, 8 clusters on Al2O3: Strong cluster size dependence linked to preferred catalyst morphologies, ACS Catal. 7 (2017) 3322-3335.

[315] M.D. Kane, F.S. Roberts, S.L. Anderson, Mass-selected supported cluster catalysts: Size effects on CO oxidation activity, electronic structure, and thermal stability of Pdn/alumina (n≤ 30) model catalysts, Int. J. Mass Spectrom. Ion Processes 370 (2014) 1-15.

[316] L. Ovári, L. Bugyi, Z. Majzik, A. Berkó, J. Kiss, Surface Structure and Composition of Au−Rh Bimetallic Nanoclusters on TiO2 (110): A LEIS and STM Study, J. Phys. Chem. C 112 (2008) 18011-18016.

[317] C.C. Chusuei, X. Lai, K. Luo, D. Goodman, Modeling heterogeneous catalysts: metal clusters on planar oxide supports, Top. Catal. 14 (2000) 71-83.

[318] S.L. Tait, L.T. Ngo, Q. Yu, S.C. Fain Jr, C.T. Campbell, Growth and sintering of Pd clusters on α-Al2O3 (0001), J. Chem. Phys. 122 (2005) 064712.

[319] S. Lee, C. Fan, T.P. Wu, S. Anderson, Agglomeration, sputtering, and carbon monoxide adsorption behavior for Au/Al2O3 prepared by Au-n(+) deposition on Al2O3/NiAl(110), J. Phys. Chem. B 109 (2005) 11340-11347.

[320] J. Kiss, L. Óvári, A. Oszkó, G. Pótári, M. Tóth, K. Baán, A. Erdóhelyi, Structure and reactivity of Au–Rh bimetallic clusters on titanate nanowires, nanotubes and TiO2 (110), Catal. Today 181 (2012) 163-170.

[321] S.A. Tenney, W. He, J.S. Ratliff, D.R. Mullins, D.A. Chen, Characterization of Pt–Au and Ni–Au Clusters on TiO2 (110), Top. Catal. 54 (2011) 42-55.

[322] S.A. Tenney, W. He, C.C. Roberts, J.S. Ratliff, S.I. Shah, G.S. Shafai, V. Turkowski, T.S. Rahman, D.A. Chen, CO-induced diffusion of Ni atoms to the surface of Ni–Au clusters on TiO2 (110), J. Phys. Chem. C 115 (2011) 11112-11123.

[323] L. Óvári, A. Berkó, N. Balázs, Z. Majzik, J. Kiss, Formation of Rh−Au Core−Shell Nanoparticles on TiO2 (110) Surface Studied by STM and LEIS, Langmuir 26 (2010) 2167-2175.

[324] Z.-j. Wang, F. Yang, S. Axnanda, C.-j. Liu, D.W. Goodman, Preparation and characterization of Co–Rh bimetallic model catalysts: From thin films to dispersed clusters, Appl. Catal. A 391 (2011) 342-349.

[325] Y. Niu, P. Schlexer, B. Sebok, I. Chorkendorff, G. Pacchioni, R.E. Palmer, Reduced sintering of mass-selected Au clusters on SiO2 by alloying with Ti: an aberration-corrected STEM and computational study, Nanoscale 10 (2018) 2363-2370.

[326] R.P. Galhenage, K. Xie, W. Diao, J.M.M. Tengco, G.S. Seuser, J.R. Monnier, D.A. Chen, Platinum–ruthenium bimetallic clusters on graphite: a comparison of vapor deposition and electroless deposition methods, Phys. Chem. Chem. Phys. 17 (2015) 28354-28363.

[327] H.H. Brongersma, Low-energy ion scattering, Characterization of Materials (2012) 1-23.

[328] H.H. Brongersma, M. Draxler, M. De Ridder, P. Bauer, Surface composition analysis by low-

energy ion scattering, Surf. Sci. Rep. 62 (2007) 63-109.

[329] J.L. Falconer, J.A. Schwarz, Temperature-programmed desorption and reaction: applications to supported catalysts, Catalysis Reviews Science Engineering 25 (1983) 141-227.

[330] W.E. Kaden, W.A. Kunkel, F.S. Roberts, M. Kane, S.L. Anderson, CO adsorption and desorption on size-selected Pdn/TiO2 (110) model catalysts: Size dependence of binding sites and energies, and support-mediated adsorption, J. Chem. Phys. 136 (2012) 204705.

[331] W.E. Kaden, W.A. Kunkel, S.L. Anderson, Cluster size effects on sintering, CO adsorption, and implantation in Ir/SiO2, J. Chem. Phys. 131 (2009) 114701.

[332] K. Asakura, K.-K. Bando, Y. Iwasawa, Structure and behaviour of Ru3(CO)12 supported on inorganic oxide surfaces, studied by EXAFS, infrared spectroscopy and temperature-programmed decomposition, J. Chem. Soc., Faraday Trans. 86 (1990) 2645-2655.

[333] A. Kulkarni, R.J. Lobo-Lapidus, B.C. Gates, Metal clusters on supports: synthesis, structure, reactivity, and catalytic properties, Chem. Commun. 46 (2010) 5997-6015.

[334] J.I. Goldstein, D.E. Newbury, J.R. Michael, N.W. Ritchie, J.H.J. Scott, D.C. Joy, Scanning electron microscopy and X-ray microanalysis, Springer, New York, 2017.

[335] P.E. Batson, Motion of gold atoms on carbon in the aberration-corrected STEM, Microsc. Microanal. 14 (2008) 89-97.

[336] Z. Li, N. Young, M. Di Vece, S. Palomba, R. Palmer, A. Bleloch, B. Curley, R. Johnston, J. Jiang, J. Yuan, Three-dimensional atomic-scale structure of size-selected gold nanoclusters, Nature 451 (2008) 46.

[337] D.B. Williams, C.B. Carter, The transmission electron microscope, Transmission electron microscopy, Springer, New York, 1996, pp. 3-17.

[338] D.A. Muller, Structure and bonding at the atomic scale by scanning transmission electron microscopy, Nat. Mater. 8 (2009) 263.

[339] L.D. Menard, S.-P. Gao, H. Xu, R.D. Twesten, A.S. Harper, Y. Song, G. Wang, A.D. Douglas, J.C. Yang, A.I. Frenkel, Sub-nanometer Au monolayer-protected clusters exhibiting molecule-like electronic behavior: quantitative high-angle annular dark-field scanning transmission electron microscopy and electrochemical characterization of clusters with precise atomic stoichiometry, J. Phys. Chem. B 110 (2006) 12874-12883.

[340] J. Liu, Advanced electron microscopy characterization of nanostructured heterogeneous catalysts, Microsc. Microanal. 10 (2004) 55-76.

[341] P.D. Nellist, S.J. Pennycook, The principles and interpretation of annular dark-field Z-contrast imaging, Adv. Imag. Elect. Phys. 113 (2000) 147-203.

[342] A. Singhal, J. Yang, J. Gibson, STEM-based mass spectroscopy of supported Re clusters, Ultramicroscopy 67 (1997) 191-206.

[343] J.C. Yang, S. Bradley, J.M. Gibson, The oblate morphology of supported PtRu5 on carbon black, Mater. Charact. 51 (2003) 101-107.

[344] R. Blonder, E. Joselevich, S.R. Cohen, Atomic force microscopy: opening the teaching laboratory to the nanoworld, J. Chem. Educ. 87 (2010) 1290-1293.

[345] I. Lopez-Salido, D.C. Lim, Y.D. Kim, Ag nanoparticles on highly ordered pyrolytic graphite (HOPG) surfaces studied using STM and XPS, Surf. Sci. 588 (2005) 6-18.

[346] J. Pethica, W. Oliver, Tip surface interactions in STM and AFM, Phys. Scr. 1987 (1987) 61.

[347] P. Hapala, G. Kichin, C. Wagner, F.S. Tautz, R. Temirov, P. Jelínek, Mechanism of high-resolution STM/AFM imaging with functionalized tips, Phys. Rev. B 90 (2014) 085421.

[348] J. Tersoff, D. Hamann, Theory and application for the scanning tunneling microscope, Phys. Rev. Lett. 50 (1983) 1998.

[349] G. Binnig, H. Rohrer, C. Gerber, E. Weibel, Surface studies by scanning tunneling microscopy, Phys. Rev. Lett. 49 (1982) 57.

[350] P. Rodríguez-Zamora, F. Yin, R. Palmer, Enhanced immobilization of gold nanoclusters on graphite, J. Phys. Chem. A 118 (2014) 8182-8187.

[351] H. Al Qahtani, Characterisation of Au9–Nanoclusters Deposited on Titania Surfaces Using Spectroscopic and Microscopic Techniques, Flinders University, Adelaide, 2016.

[352] N. Isomura, X. Wu, H. Hirata, Y. Watanabe, Cluster size dependence of Pt core-level shifts for mass-selected Pt clusters on TiO2 (110) surfaces, J. Vac. Sci. Technol. A 28 (2010) 1141-1144.

[353] Y. Watanabe, X. Wu, H. Hirata, N. Isomura, Size-dependent catalytic activity and geometries of size-selected Pt clusters on TiO 2 (110) surfaces, Catal. Sci. Technol. 1 (2011) 1490-1495.

[354] T. Worren, K.H. Hansen, E. Lægsgaard, F. Besenbacher, I. Stensgaard, Copper clusters on

Al2O3/NiAl (1 1 0) studied with STM, Surf. Sci. 477 (2001) 8-16.

[355] A. Piednoir, E. Perrot, S. Granjeaud, A. Humbert, C. Chapon, C. Henry, Atomic resolution on small three-dimensional metal clusters by STM, Surf. Sci. 391 (1997) 19-26.

[356] X. Lin, N. Nilius, H.-J. Freund, M. Walter, P. Frondelius, K. Honkala, H. Häkkinen, Quantum well states in two-dimensional gold clusters on MgO thin films, Phys. Rev. Lett. 102 (2009) 206801.

[357] I. Hadjoub, T. Touam, A. Chelouche, M. Atoui, J. Solard, M. Chakaroun, A. Fischer, A. Boudrioua, L.-H. Peng, Post-deposition annealing effect on RF-sputtered TiO2 thin-film properties for photonic applications, Appl. Phys. A 122 (2016) 78.

[358] J. Daughtry, A. Alotabi, L. Howard-Fabretto, G.G. Andersson, Composition and Properties of RF-Sputter Deposited Titanium Dioxide Thin Films, Nanoscale Advances 3 (2020) 1077-1086.

[359] A. Haseeb, M. Hasan, H.H. Masjuki, Structural and mechanical properties of nanostructured TiO2 thin films deposited by RF sputtering, Surf. Coat. Technol. 205 (2010) 338-344.

[360] Q. Ye, P. Liu, Z. Tang, L. Zhai, Hydrophilic properties of nano-TiO2 thin films deposited by RF magnetron sputtering, Vacuum 81 (2007) 627-631.

[361] C.R. Eady, P.F. Jackson, B.F. Johnson, J. Lewis, M.C. Malatesta, M. Mcpartlin, W.J. Nelson, Improved syntheses of the hexanuclear clusters [Ru6(CO)18]2–, [HRu6-(CO)18]–, and H2Ru6(CO)18. The X-ray analysis of [HRu6(CO)18]–, a polynuclear carbonyl containing an interstitial hydrogen ligand, J. Chem. Soc., Dalton Trans. (1980) 383-392.

[362] M. Bruce, C. Jensen, N. Jones, Polynuclear ruthenium complexes, Inorg. Synth., John Wiley & Sons, Inc.2007, pp. 259-263.

[363] M. Aizawa, S. Lee, S.L. Anderson, Deposition dynamics and chemical properties of size-selected Ir clusters on TiO2, Surf. Sci. 542 (2003) 253-275.

[364] S.L. Anderson, Personal Communication of Technical Diagram, 2020.

[365] A. Einstein, Concerning an heuristic point of view toward the emission and transformation of light, Annalen der Physik 17 (1905) 132-148.

[366] S. Harmer, Personal Communication of Technical Diagram, 2016.

[367] J. Chastain, Handbook of X-ray photoelectron spectroscopy, Perkin-Elmer Corporation, Minnesota, USA, 1992, pp. 221.

[368] E. Spiller, Soft X-ray optics, SPIE Optical Engineering Press Bellingham, WA1994.

[369] J. Castle, A. Salvi, Chemical state information from the near-peak region of the X-ray photoelectron background, J. Electron. Spectrosc. Relat. Phenom. 114 (2001) 1103-1113.

[370] E.L. Strein, D. Allred, Eliminating carbon contamination on oxidized Si surfaces using a VUV excimer lamp, Thin Solid Films 517 (2008) 1011-1015.

[371] Y.J. Kim, Y. Gao, S.A. Chambers, Core-level X-ray photoelectron spectra and X-ray photoelectron diffraction of RuO2 (110) grown by molecular beam epitaxy on TiO2 (110), Appl. Surf. Sci. 120 (1997) 250-260.

[372] D.J. Morgan, Resolving ruthenium: XPS studies of common ruthenium materials, Surf. Interface Anal. 47 (2015) 1072-1079.

[373] J. Riga, C. Tenret-Noel, J.-J. Pireaux, R. Caudano, J. Verbist, Y. Gobillon, Electronic structure of rutile oxides TiO2, RuO2 and IrO2 studied by X-ray photoelectron spectroscopy, Phys. Scr. 16 (1977) 351.

[374] F. Eschen, M. Heyerhoff, H. Morgner, J. Vogt, The concentration-depth profile at the surface of a solution of tetrabutylammonium iodide in formamide, based on angle-resolved photoelectron spectroscopy, J. Phys. Condens. Matter 7 (1995) 1961.

[375] L. Sutton, Tables of interatomic distances and configuration in molecules and ions, Chemical Society1965.

[376] G. Fuentes, E. Elizalde, F. Yubero, J. Sanz, Electron inelastic mean free path for Ti, TiC, TiN and TiO2 as determined by quantitative reflection electron energy-loss spectroscopy, Surf. Interface Anal. 33 (2002) 230-237.

[377] V.L. Moruzzi, J.F. Janak, A.R. Williams, Calculated electronic properties of metals, Pergamon2013.

[378] H.D. Hagstrum, Excited-Atom Deexcitation Spectroscopy using Incident Ions, Phys. Rev. Lett. 43 (1979) 1050.

[379] B. Heinz, H. Morgner, A metastable induced electron spectroscopy study of graphite: The k-vector dependence of the ionization probability, Surf. Sci. 405 (1998) 104-111.

[380] R. Cvetanović, Y. Amenomiya, A temperature programmed desorption technique for investigation of practical catalysts, Catalysis Reviews 6 (1972) 21-48.

[381] J. Sasaki, N. Peterson, K. Hoshino, Tracer impurity diffusion in single-crystal rutile (TiO2−x), J. Phys. Chem. Solids 46 (1985) 1267-1283.

[382] M. Li, W. Hebenstreit, U. Diebold, A.M. Tyryshkin, M.K. Bowman, G.G. Dunham, M.A. Henderson, The influence of the bulk reduction state on the surface structure and morphology of rutile TiO2 (110) single crystals, J. Phys. Chem. B 104 (2000) 4944-4950.

[383] T. Sekiya, T. Yagisawa, N. Kamiya, D. Das Mulmi, S. Kurita, Y. Murakami, T. Kodaira, Defects in anatase TiO2 single crystal controlled by heat treatments, J. Phys. Soc. Jpn. 73 (2004) 703-710.

[384] V.E. Henrich, G. Dresselhaus, H. Zeiger, Observation of Two-Dimensional Phases Associated with Defect States on the Surface of TiO2, Phys. Rev. Lett. 36 (1976) 1335.

[385] P. Lindan, N. Harrison, M. Gillan, J. White, First-principles spin-polarized calculations on the reduced and reconstructed TiO2 (110) surface, Phys. Rev. B 55 (1997) 15919.

[386] T. Komaya, A.T. Bell, Z. Wengsieh, R. Gronsky, F. Engelke, T.S. King, M. Pruski, The influence of metal-support interactions on the accurate determination of Ru dispersion for Ru/TiO2, J. Catal. 149 (1994) 142-148.

[387] T. Ueckert, R. Lamber, N. Jaeger, U. Schubert, Strong metal support interactions in a Ni/SiO2 catalyst prepared via sol-gel synthesis, Applied Catalysis A: General 155 (1997) 75-85.

[388] Y. Zhang, J.R. Evans, S. Yang, Corrected values for boiling points and enthalpies of vaporization of elements in handbooks, Journal of Chemical Engineering Data 56 (2011) 328-337.

[389] L. Mezey, J. Giber, The surface free energies of solid chemical elements: calculation from internal free enthalpies of atomization, Jpn. J. Appl. Phys. 21 (1982) 1569.

[390] Y.D. Kim, S. Schwegmann, A.P. Seitsonen, H. Over, Epitaxial growth of RuO2 (100) on Ru (1010): Surface structure and other properties, J. Phys. Chem. B 105 (2001) 2205-2211.

[391] A. Navrotsky, C. Ma, K. Lilova, N. Birkner, Nanophase transition metal oxides show large thermodynamically driven shifts in oxidation-reduction equilibria, Science 330 (2010) 199-201.

[392] D.R. Lide, CRC handbook of chemistry and physics: a ready-reference book of chemical and physical data, CRC press1995.

[393] L. Wang, T. Maxisch, G. Ceder, Oxidation energies of transition metal oxides within the GGA+ U framework, Phys. Rev. B 73 (2006) 195107.

[394] E. Hebenstreit, W. Hebenstreit, H. Geisler, C. Ventrice Jr, P. Sprunger, U. Diebold, Bulk-defect dependent adsorption on a metal oxide surface: S/TiO2 (110), Surf. Sci. 486 (2001) L467-L474.

[395] A. Howard, C. Mitchell, D. Morris, R. Egdell, S. Parker, The surface structure of TiO2 (210) studied by atomically resolved STM and atomistic simulation, Surf. Sci. 448 (2000) 131-141.

[396] T. Sham, T. Ohta, T. Yokoyama, Y. Kitajima, M. Funabashi, N. Kosugi, H. Kuroda, Ru L edge x-ray absorption studies of the electronic structure of Ru3(CO)12 adsorption and the formation of Ru–Cu bimetallics on Cu (111), J. Chem. Phys. 88 (1988) 475-477.

[397] H. Feng, J. Lu, P.C. Stair, J.W. Elam, Alumina over-coating on Pd nanoparticle catalysts by atomic layer deposition: enhanced stability and reactivity, Catal. Lett. 141 (2011) 512-517.

[398] S. Vajda, M.J. Pellin, J.P. Greeley, C.L. Marshall, L.A. Curtiss, G.A. Ballentine, J.W. Elam, S. Catillon-Mucherie, P.C. Redfern, F. Mehmood, Subnanometre platinum clusters as highly active and selective catalysts for the oxidative dehydrogenation of propane, Nat. Mater. 8 (2009) 213-216.

[399] P.J. Cumpson, Angle-resolved XPS depth-profiling strategies, Appl. Surf. Sci. 144 (1999) 16-20.

[400] C. Wang, G.G. Andersson, Measuring concentration depth profiles at liquid surfaces: Comparing angle resolved X-ray photoelectron spectroscopy and neutral impact collision scattering spectroscopy, Surf. Sci. 605 (2011) 889-897.

[401] H.H. Brongersma, T. Grehl, P.A. van Hal, N.C. Kuijpers, S.G. Mathijssen, E.R. Schofield, R.A. Smith, H.R. ter Veen, High-sensitivity and high-resolution low-energy ion scattering, Vacuum 84 (2010) 1005-1007.

[402] A. Rafati, R. ter Veen, D.G. Castner, Low-energy ion scattering: Determining overlayer thickness for functionalized gold nanoparticles, Surf. Interface Anal. 45 (2013) 1737-1741.

[403] N. Belsey, D. Cant, C. Minelli, J. Araujo, B. Bock, P. Bruener, D. Castner, G. Ceccone, J. Counsell, P. Dietrich, Versailles Project on Advanced Materials and Standards Interlaboratory Study on Measuring the Thickness and Chemistry of Nanoparticle Coatings Using XPS and LEIS, J. Phys. Chem. C 120 (2016) 24070-24079.

[404] M. Li, W. Hebenstreit, U. Diebold, Morphology change of oxygen-restructured TiO2 (110) surfaces by UHV annealing: Formation of a low-temperature (1×2) structure, Phys. Rev. B 61 (2000) 4926.

[405] O. Baschenko, A. Nesmeev, The effect of elastic photoelectron scattering on depth-profiling by angular resolved X-ray photoelectron spectroscopy, J. Electron. Spectrosc. Relat. Phenom. 57 (1991) 33-46.

[406] B.A. Chambers, Personal Communication of Technical Diagram, 2021.

[407] G. Bertuccio, D. Maiocchi, Electron-hole pair generation energy in gallium arsenide by x and γ photons, J. Appl. Phys. 92 (2002) 1248-1255.

[408] J.W. Rabalais, Principles and applications of ion scattering spectrometry: surface chemical and structural analysis, Wiley New York2003.

[409] S. Mikhailov, L. Van den Oetelaar, H. Brongersma, Strong matrix effect in low-energy He+ ion scattering from carbon, Nucl. Instrum. Methods Phys. Res., B 93 (1994) 210-214.

[410] J.F. Ziegler, M.D. Ziegler, J.P. Biersack, SRIM–The stopping and range of ions in matter (2010), Nucl. Instrum. Methods Phys. Res., B 268 (2010) 1818-1823.

[411] W.H. Bragg, R. Kleeman, XXXIX. On the α particles of radium, and their loss of range in passing through various atoms and molecules, Lond. Edinb. Dubl. Phil. Mag. 10 (1905) 318-340.

[412] J.W. Arblaster, Crystallographic properties of ruthenium, Platinum Met. Rev. 57 (2013) 127-136.

[413] G. Lu, A. Linsebigler, J.T. Yates Jr, Ti3+ defect sites on TiO2 (110): production and chemical detection of active sites, J. Phys. Chem. 98 (1994) 11733-11738.

[414] Z. Gong, Y. Yang, The application of synchrotron X-ray techniques to the study of rechargeable batteries, J. Energy Chem. 27 (2018) 1566-1583.

[415] S. Abrahams, J. Bernstein, Rutile: normal probability plot analysis and accurate measurement of crystal structure, J. Chem. Phys. 55 (1971) 3206-3211.

[416] N. Jiang, D. Su, J. Spence, Determination of Ti coordination from pre-edge peaks in Ti K-edge XANES, Phys. Rev. B 76 (2007) 214117.

[417] K. Schierbaum, S. Fischer, M. Torquemada, J. De Segovia, E. Roman, J. Martin-Gago, The interaction of Pt with TiO2 (110) surfaces: a comparative XPS, UPS, ISS, and ESD study, Surf. Sci. 345 (1996) 261-273.

[418] M. Della Negra, N.M. Nicolaisen, Z. Li, P.J. Møller, Study of the interactions between the overlayer and the substrate in the early stages of palladium growth on TiO2 (110), Surf. Sci. 540 (2003) 117-128.

[419] H. Zhang, S. Zuo, M. Qiu, S. Wang, Y. Zhang, J. Zhang, X.W.D. Lou, Direct probing of atomically dispersed Ru species over multi-edged TiO2 for highly efficient photocatalytic hydrogen evolution, Sci. Adv. 6 (2020) eabb9823.

[420] W.-J. Ong, L.-L. Tan, Y.H. Ng, S.-T. Yong, S.-P. Chai, Graphitic carbon nitride (g-C3N4)-based photocatalysts for artificial photosynthesis and environmental remediation: are we a step closer to achieving sustainability?, Chem. Rev. 116 (2016) 7159-7329.

[421] S. Wang, B.Y. Guan, X. Wang, X.W.D. Lou, Formation of hierarchical Co9S8@ZnIn2S4 heterostructured cages as an efficient photocatalyst for hydrogen evolution, J. Am. Chem. Soc. 140 (2018) 15145-15148.

[422] G. Xu, H. Zhang, J. Wei, H.-X. Zhang, X. Wu, Y. Li, C. Li, J. Zhang, J. Ye, Integrating the g-C3N4 Nanosheet with B–H Bonding Decorated Metal–Organic Framework for CO2 Activation and Photoreduction, ACS Nano 12 (2018) 5333-5340.

[423] J. Liu, Y. Liu, N. Liu, Y. Han, X. Zhang, H. Huang, Y. Lifshitz, S.-T. Lee, J. Zhong, Z. Kang, Metal-free efficient photocatalyst for stable visible water splitting via a two-electron pathway, Science 347 (2015) 970-974.

[424] X. Li, J. Yu, M. Jaroniec, Hierarchical photocatalysts, Chem. Soc. Rev. 45 (2016) 2603-2636.

[425] Q. Hao, ZhiqiangWang, T. Wang, Z. Ren, C. Zhou, X. Yang, Role of Pt loading in the photocatalytic chemistry of methanol on rutile TiO2 (110), ACS Catal. 9 (2019) 286-294.

[426] T. Kawai, T. Sakata, Photocatalytic hydrogen production from liquid methanol and water, J. Chem. Soc., Chem. Commun. (1980) 694-695.

[427] Z. Shu, Y. Cai, J. Ji, C. Tang, S. Yu, W. Zou, L. Dong, Pt deposites on TiO2 for photocatalytic H2 evolution: Pt is not only the cocatalyst, but also the defect repair agent, Catalysts 10 (2020) 1047.

[428] E. Kowalska, H. Remita, C. Colbeau-Justin, J. Hupka, J. Belloni, Modification of titanium dioxide with platinum ions and clusters: application in photocatalysis, J. Phys. Chem. C 112 (2008) 1124-1131.

[429] W. Ouyang, M.J. Munoz-Batista, A. Kubacka, R. Luque, M. Fernández-García, Enhancing photocatalytic performance of TiO2 in H2 evolution via Ru co-catalyst deposition, Appl. Catal. B 238

(2018) 434-443.

[430] G.L. Chiarello, D. Ferri, E. Selli, Effect of the CH3OH/H2O ratio on the mechanism of the gas-phase photocatalytic reforming of methanol on noble metal-modified TiO2, J. Catal. 280 (2011) 168-177.

[431] A. Wang, J. Li, T. Zhang, Heterogeneous single-atom catalysis, Nature Reviews Chemistry 2 (2018) 65-81.

[432] T. Sreethawong, S. Yoshikawa, Comparative investigation on photocatalytic hydrogen evolution over Cu-, Pd-, and Au-loaded mesoporous TiO2 photocatalysts, Catal. Commun. 6 (2005) 661-668.

[433] X. Li, W. Bi, L. Zhang, S. Tao, W. Chu, Q. Zhang, Y. Luo, C. Wu, Y. Xie, Single-atom Pt as co-catalyst for enhanced photocatalytic H2 evolution, Adv. Mater. 28 (2016) 2427-2431.

[434] H. Zhang, W. Zhou, X.F. Lu, T. Chen, X.W. Lou, Implanting Isolated Ru Atoms into Edge-Rich Carbon Matrix for Efficient Electrocatalytic Hydrogen Evolution, Adv. Energy Mater. 10 (2020) 2000882.

[435] M. Chen, D. Goodman, Structure–activity relationships in supported Au catalysts, Catal. Today 111 (2006) 22-33.

[436] B.A. Chambers, C.J. Shearer, L. Yu, C.T. Gibson, G.G. Andersson, Measuring the density of states of the inner and outer wall of double-walled carbon nanotubes, Nanomaterials 8 (2018) 448.

[437] W. Eberhardt, P. Fayet, D. Cox, Z. Fu, A. Kaldor, R. Sherwood, D. Sondericker, Photoemission from mass-selected monodispersed Pt clusters, Phys. Rev. Lett. 64 (1990) 780.

[438] M. Peuckert, H. Bonzel, Characterization of oxidized platinum surfaces by X-ray photoelectron spectroscopy, Surf. Sci. 145 (1984) 239-259.

[439] C.N. Wagner, AV; Kraut-Vass, A; Allison, JW; Powell, CJ; Rumble, JR, Jr., NIST Standard Reference Database 20, Version 3.2 (Web Version), NIST X-ray Photoelectron Spectroscopy Database, 2002.

[440] G. Wertheim, S. DiCenzo, Cluster growth and core-electron binding energies in supported metal clusters, Phys. Rev. B 37 (1988) 844.

[441] S. DiCenzo, G. Wertheim, Photoelectron spectroscopy of supported metal clusters, Solid State Phys. 11 (1985) 203.

[442] D.J. Alberas, J. Kiss, Z.-M. Liu, J.M. White, Surface chemistry of hydrazine on Pt (111), Surf. Sci. 278 (1992) 51-61.

[443] J. Crowell, E. Garfunkel, G. Somorjai, The coadsorption of potassium and CO on the Pt (111) crystal surface: A TDS, HREELS and UPS study, Surf. Sci. 121 (1982) 303-320.

[444] S. Krischok, J. Schaefer, O. Höfft, V. Kempter, Lithium adsorption on TiO2: studies with electron spectroscopies (MIES and UPS), Surf. Interface Anal. 37 (2005) 83-89.

[445] S. Krischok, J. Günster, D. Goodman, O. Höfft, V. Kempter, MIES and UPS (HeI) studies on reduced TiO2 (110), Surf. Interface Anal. 37 (2005) 77-82.

[446] S. Pan, X. Liu, M. Guo, S. fung Yu, H. Huang, H. Fan, G. Li, Engineering the intermediate band states in amorphous Ti 3+-doped TiO 2 for hybrid dye-sensitized solar cell applications, J. Mater. Chem. A 3 (2015) 11437-11443.

[447] N.N.E. Greenwood, Alan, Chemistry of the Elements, Pergamon Press, Oxford, 1984.

[448] R. Schlaf, P. Schroeder, M. Nelson, B. Parkinson, C. Merritt, L. Crisafulli, H. Murata, Z. Kafafi, Determination of interface dipole and band bending at the Ag/tris (8-hydroxyquinolinato) gallium organic Schottky contact by ultraviolet photoemission spectroscopy, Surf. Sci. 450 (2000) 142-152.

[449] R.A. Bennett, J. Mulley, M. Newton, M. Surman, Spectroscopy of ultrathin epitaxial rutile TiO2 (110) films grown on W (100), J. Chem. Phys. 127 (2007) 084707.

[450] L. Zhang, R. Persaud, T.E. Madey, Ultrathin metal films on a metal oxide surface: Growth of Au on TiO2 (110), Phys. Rev. B 56 (1997) 10549.

[451] S. Fischer, F. Schneider, K. Schierbaum, Intrinsic defects and Pt atoms at TiO2 (110) surfaces: a valence band spectroscopy study using synchrotron radiation, Vacuum 47 (1996) 1149-1152.

[452] V. Çelik, H. Ünal, E. Mete, Ş. Ellialtıoğlu, Theoretical analysis of small Pt particles on rutile TiO2 (110) surfaces, Phys. Rev. B 82 (2010) 205113.

[453] N. Isomura, X. Wu, Y. Watanabe, Atomic-resolution imaging of size-selected platinum clusters on TiO2 (110) surfaces, J. Chem. Phys. 131 (2009) 164707.

[454] S.H. Yang, D.A. Drabold, J.B. Adams, P. Ordejón, K. Glassford, Density functional studies of small platinum clusters, J. Phys. Condens. Matter 9 (1997) L39.

[455] H.-V. Roy, P. Fayet, F. Patthey, W.-D. Schneider, B. Delley, C. Massobrio, Evolution of the

electronic and geometric structure of size-selected Pt and Pd clusters on Ag (110) observed by photoemission, Phys. Rev. B 49 (1994) 5611.

[456] M. Macino, A.J. Barnes, S.M. Althahban, R. Qu, E.K. Gibson, D.J. Morgan, S.J. Freakley, N. Dimitratos, C.J. Kiely, X. Gao, Tuning of catalytic sites in Pt/TiO2 catalysts for the chemoselective hydrogenation of 3-nitrostyrene, Nat. Catal. 2 (2019) 873-881.

[457] W. Tyson, W. Miller, Surface free energies of solid metals: Estimation from liquid surface tension measurements, Surface Science 62 (1977) 267-276.

[458] Y.-R. Luo, Comprehensive handbook of chemical bond energies, CRC press, Boca Raton, FL, 2007.

[459] S. Taylor, G.W. Lemire, Y.M. Hamrick, Z. Fu, M.D. Morse, Resonant two-photon ionization spectroscopy of jet-cooled Pt2, J. Chem. Phys. 89 (1988) 5517-5523.

[460] T. Wu, W.E. Kaden, W.A. Kunkel, S.L. Anderson, Size-dependent oxidation of Pdn (n⩽ 13) on alumina/NiAl (110): Correlation with Pd core level binding energies, Surf. Sci. 603 (2009) 2764-2770.

[461] S. Lee, L.M. Molina, M.J. López, J.A. Alonso, B. Hammer, B. Lee, S. Seifert, R.E. Winans, J.W. Elam, M.J. Pellin, Selective propene epoxidation on immobilized Au6–10 clusters: the effect of hydrogen and water on activity and selectivity, Angew. Chem. Int. Ed. 48 (2009) 1467-1471.

[462] G. Kwon, G.A. Ferguson, C.J. Heard, E.C. Tyo, C. Yin, J. DeBartolo, S.n. Seifert, R.E. Winans, A.J. Kropf, J. Greeley, Size-dependent subnanometer Pd cluster (Pd4, Pd6, and Pd17) water oxidation electrocatalysis, ACS Nano 7 (2013) 5808-5817.

[463] H.-V. Roy, J. Boschung, P. Fayet, F. Patthey, W.-D. Schneider, Photoemission study of the electronic structure of size-selected transition metal clusters deposited on Ag (110), Z. Phys. D: At., Mol. Clusters 26 (1993) 252-254.

[464] M.A. MacDonald, D.M. Chevrier, P. Zhang, H. Qian, R. Jin, The structure and bonding of Au25(SR)18 nanoclusters from EXAFS: the interplay of metallic and molecular behavior, J. Phys. Chem. C 115 (2011) 15282-15287.

[465] M. Castiglioni, R. Giordano, E. Sappa, Metal carbonyl clusters in homogeneous catalysis. Hydrogenation and isomerization of cyclic dienes in the presence of [H4Ru4(CO)12], [H2Ru4(CO)13], [H2FeRu3(CO)13] and [Fe2Ru(CO)12]. Identification of organometallic products and a discussion of their role, J. Organomet. Chem. 491 (1995) 111-120.

[466] P.M. Lausarot, G. Vaglio, M. Valle, Hydrogenation of pentynes catalyzed by substituted derivatives of H4Ru4(CO)12 with phosphorus-donor ligands, Inorg. Chim. Acta 36 (1979) 213-217.

[467] J. Yang, H. Wang, X. Zhao, Y. Li, W. Fan, Correlating the surface structure and hydration of a γ-Al2O3 support with the Ru n (n= 1–4) cluster adsorption behavior: a density functional theory study, RSC Adv. 6 (2016) 40459-40473.

[468] J. Yang, X. Zhao, S. Bu, W. Fan, Theoretical Insights into the Role of Metal–Support Interactions of an Al2O3-Supported Ru4 Cluster in CO2 Dissociation, J. Phys. Chem. C 122 (2018) 17287-17300.

[469] S. Lee, C. Fan, T. Wu, S.L. Anderson, Cluster size effects on CO oxidation activity, adsorbate affinity, and temporal behavior of model Aun/TiO2 catalysts, J. Chem. Phys. 123 (2005) 124710.

[470] H. Chiririwa, J.R. Moss, New routes to the preparation of [Ru3(CO)12], [H4Ru4(CO)12], [RuCl2(PPh3)3] and [RuCl2(COD)]n from anglo platinum refinery, Zimbabwe Journal of Science and Technology (2013) 1-8.

[471] M.R. Churchill, F.J. Hollander, J.P. Hutchinson, An accurate redetermination of the structure of triruthenium dodecacarbonyl, Ru3(CO)12, Inorg. Chem. 16 (1977) 2655-2659.

[472] R.D. Wilson, S.M. Wu, R.A. Love, R. Bau, Molecular structures of H4Ru4(CO)12 and H4Ru4(CO)10(PPh3)2, Inorg. Chem. 17 (1978) 1271-1280.

[473] F. Piacenti, M. Bianchi, P. Frediani, E. Benedetti, Preparation and reactivity of some ruthenium carbonyl hydrides, Inorg. Chem. Commun. 10 (1971) 2759-2763.

Chapter 10   Appendices

10.1 Appendix A: Instrument Maintenance and Modifications

Throughout this PhD candidature, a significant amount of effort was spent by the author (as well as the other members of Professor Andersson's research group) keeping the UHV instruments well maintained in order to produce reliable, repeatable results. Additionally, modifications were made to the instrument in order to run specific experiments or improve its capabilities. In this section, examples are given to highlight some of the work which was done.

10.1.1 UHV System Maintenance

Professor Andersson's research group at Flinders University uses two main UHV systems; one is the MIES system, while the other is the NICISS system (neutral impact collision ion scattering spectroscopy). The MIES system was the main UHV system used for this thesis (see section 3.3.1 for details on the methodologies which were used), while the NICISS system was not used for experiments in this thesis. The author was part of a small maintenance team for both UHV systems. This involved going to weekly meetings to discuss the current instrument condition and anything which needed to be fixed or improved. This work required learning how to remove and replace vacuum components which use UHV flanges. They need to be installed effectively to avoid air leaks, in order to reach the low pressure range needed for UHV experiments. Additionally, new parts often needed to be sourced and ordered for this maintenance from various suppliers. As a specific example of a maintenance/modification procedure, a new gas dosing valve was installed onto the MIES system. This involved ordering vacuum parts and gas bottles, installing the gas dosing valve and piping system onto the main chamber using the flange system, and then checking for any air leaks into the main chamber.

Some components of UHV systems require regular maintenance because they are extremely fragile or ware out with use over time. Examples of this are the filaments used for electron bombardment heating, which can crack over time due to repeated heating and cooling, and gas dosing valves which are continuously opened and closed. In some cases, the Flinders University workshop assisted with fixing components of the system which went beyond the scope of the maintenance team, such as performing repairs and maintenance on the high voltage X-ray source.

Typically, the main vacuum chamber is left under UHV at all times and is never vented to

atmosphere. However, any procedure which involves removing a vacuum flange from the main chamber requires it to be vented. Additionally, the main chamber is sometimes vented accidentally by research group members when performing operations in an incorrect order. Venting occurs when too much gas enters the main chamber at once, which triggers an automatic venting procedure to protect the turbomolecular pumps. In order to return the main chamber to UHV pressures in the range of 10^{-10} mbar, a "bakeout" must be performed. This is a multi-day procedure, which involves setting up an insulating fibreglass tent around the UHV system while the pumps are running and using heaters to heat the system up to 423 K for 1-2 days. This causes adsorbed contamination (such as water) to be desorbed from the inside walls of the chamber.

10.1.2 Designing CVD Attachment

A new attachment for the loading chamber of the MIES system was designed and built to perform CVD for a number of the experiments in this thesis. The general concept was designed by the author, which was then finished in collaboration with the Flinders University workshop. After the design was finalised, the author ordered the required parts, and the machining work was done by the workshop. The core design is a small manipulator arm attached to a vacuum flange. A metal holder for a 5 mL glass vial is welded to the manipulator arm, such that the glass vial can be moved inside the vacuum chamber. When performing CVD, a cluster material such as $Ru_3(CO)_{12}$ is loaded into the glass vial (see section 3.5.1 for further details on CVD). A sheath is attached in a fixed position to the flange, such that the glass vial can be retracted behind it to prevent the deposition of clusters onto samples outside of the intended deposition time frame.

10.1.3 Installation of New NICISS System

The basic process of a NICISS experiment involves bombarding a surface with He^+ ions and detecting backscattered neutral He using time of flight (TOF) detectors. NICISS can be used to measure an atomic depth profile of the upper layers of a surface. During this PhD candidature, the Flinders University NICISS system was upgraded to an entirely new system. This involved replacing almost the entire system and keeping only a small number of parts from the original. The new NICISS system was purchased from SPECS and was sent to Flinders University largely disassembled. A technician from the company came to Flinders to install the system, which required significant assistance and cooperation from the maintenance team. Assistance was required for installing the turbomolecular and scroll pump systems, ion guns, TOF detectors, solid and liquid sample manipulators, and various other parts. The technician stayed for approximately one week until the instrument was

competed. After this, significant effort was put into optimising the system in order to collect accurate, repeatable ion scattering data at a fast pace. This required optimising many different aspects of the system, including ion gun voltages, detector voltages, gas flow settings, and digital counting hardware settings, as well as aligning two separate TOF detectors to receive the optimum backscattered signal.

10.2 Appendix B: Ru Cluster Synthesis Data

The $Ru_3(CO)_{12}$ and $H_4Ru_4(CO)_{12}$ cluster materials used in this thesis were synthesised by Siriluck Tesana at the University of Canterbury. Tesana also performed measurements on the synthesised materials to determine their composition and lack of contaminants. The results from these measurements are presented in this section, but it should be stressed that they were performed by Siriluck Tesana, and not the author of the thesis.

Powder X-ray diffraction (PXRD) was used for confirming the identity of clusters by comparing with simulated patterns based on the crystal structure data provided by the Cambridge Crystallographic Data Centre. The Ru clusters can diffract X-rays giving distinctive diffraction patterns which correspond to the arrangement of the atoms in the crystals. If there is agreement between the PXRD of the synthesised Ru clusters and the simulated patterns, this confirms the target Ru clusters were obtained without detectable crystalline impurities. However, it should be noted that amorphous impurities do not show any peaks in PXRD. The clusters were further characterized by ^{1}H-nuclear magnetic resonance (NMR), infrared spectroscopy (IR), and thermogravimetric analysis (TGA).
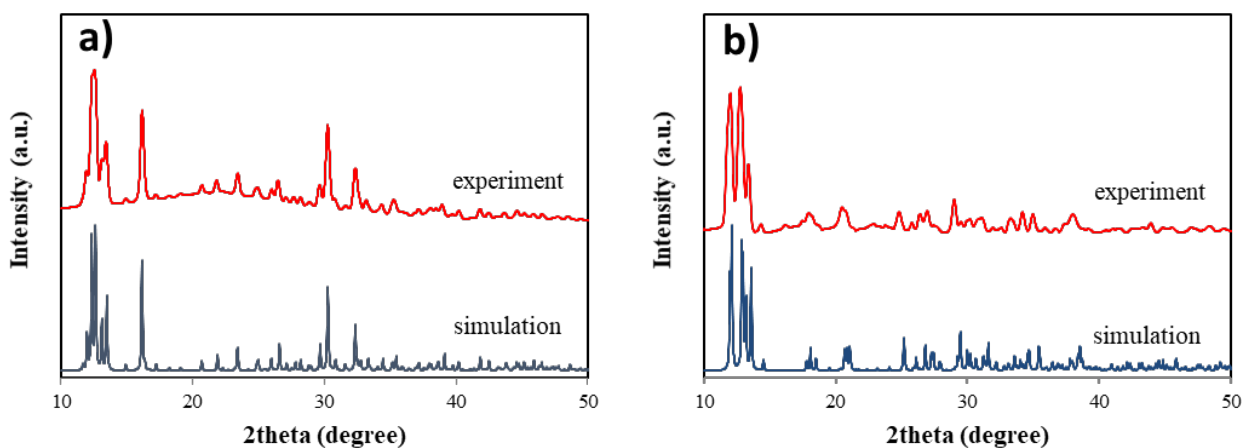
Figure 10-1: PXRD results for a) Ru₃(CO)₁₂, and b) H₄Ru₄(CO)₁₂. Performed using the Agilent Technologies SuperNova X-ray diffractometer with Mo Kα radiation. Baseline removal was performed using a polynomial fitting. All data were collected at room temperature in the 2θ range of 5 to 50 degrees. The sample powder was finely ground and packed into the end of a GC capillary column which was analysed for 40 minutes.
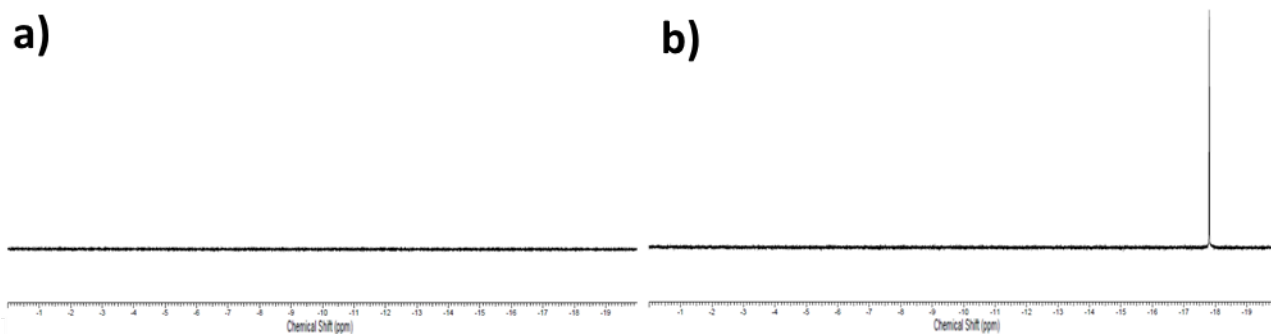
Figure 10-2: ¹H-NMR spectra for a) Ru₃(CO)₁₂, and b) H₄Ru₄(CO)₁₂. Analysis performed using CDCl₃ over silver foil.
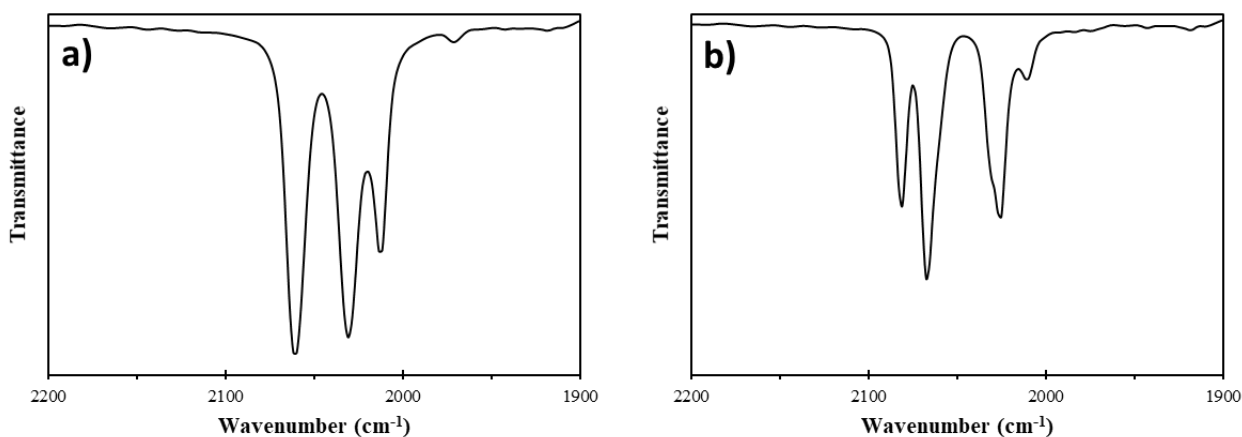
Figure 10-3: IR spectra for a) Ru₃(CO)₁₂ in hexane solvent, and b) H₄Ru₄(CO)₁₂ in cyclohexane solvent.
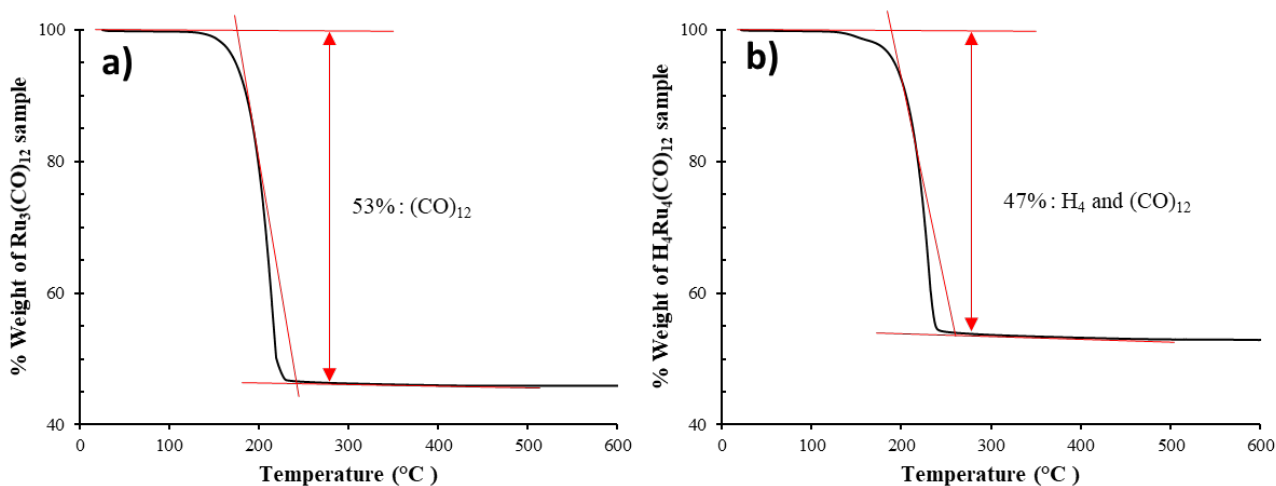
Figure 10-4: TGA spectra for a) Ru$_3$(CO)$_{12}$, and b) H$_4$Ru$_4$(CO)$_{12}$. TGA was performed using an Alphatech SDT Q600. Approximately 5 - 10 mg of samples were placed in an alumina crucible and heated under nitrogen flow (100 mL.min^{-1}) from 298 to 773 K at a heating rate of 10 K.min^{-1}.

For Ru$_3$(CO)$_{12}$ the synthesis yield was ~0.78 g (1.22 mmol), which was a 71% yield by number of Ru atoms. The PXRD spectrum (Figure 10-1a) was an excellent fit with the simulation, confirming the composition of the clusters and lack of contamination [361]. The ^{1}H-NMR spectrum of Ru$_3$(CO)$_{12}$ (Figure 10-2a) showed no peaks, confirming the absence of the possible by-product H$_4$Ru$_4$(CO)$_{12}$ [470]. The identity of the Ru$_3$(CO)$_{12}$ was supported by IR (Figure 10-3a), showing it possesses three carbonyl stretching vibrations at 2061 cm^{-1} (vs), 2031 cm^{-1} (s) and 2011 cm^{-1} (m) agreeing with reports in literature [471]. TGA (Figure 10-4a) showed 53% weight loss which matched calculated values based on the loss of ligands for Ru$_3$(CO)$_{12}$.

For H$_4$Ru$_4$(CO)$_{12}$ the synthesis yield was ~0.66 g (0.88 mmol), which was a 74% yield by number of Ru atoms. The PXRD spectrum (Figure 10-1b) was an excellent fit with the simulation, confirming the composition of the clusters and lack of contamination [362]. The ^{1}H-NMR spectrum of H$_4$Ru$_4$(CO)$_{12}$ (Figure 10-2b) showed a singlet peak at δ - 17.79 ppm corresponding to the presence of H ligands [470]. The identity of the H$_4$Ru$_4$(CO)$_{12}$ was supported by IR (Figure 10-3b), where carbonyl stretching vibrations were found at 2081 cm^{-1} (s), 2067 cm^{-1} (vs), 2030 cm^{-1} (m), 2026 cm^{-1} (s) and 2010 (w), which corresponds to previous literature [362, 472, 473]. TGA (Figure 10-4b) showed 47% weight loss which matched calculated values based on the loss of ligands for H$_4$Ru$_4$(CO)$_{12}$.